Impact of a Bearingless machine on a shaft's Rotodynamics

Control of a single winding bearingless machine



University of Nottingham

UK | CHINA | MALAYSIA

Nicolas Schneider

Department of Engineering
University of Nottingham

This dissertation is submitted for the degree of
Doctor of Philosophy

PEMC December 2019

I would like to dedicate this thesis to my loving wife Sana Sawada for her love, support and patience during the PhD.

As well as my Parents that supported me for all those years until now.

To all my Friends from INNOVATE+PEMC and the Japanese Society of Nottingham

Declaration

I hereby declare that except where specific reference is made to the work of others, the contents of this dissertation are original and have not been submitted in whole or in part for consideration for any other degree or qualification in this, or any other university. This dissertation is my own work and contains nothing which is the outcome of work done in collaboration with others, except as specified in the text and Acknowledgements. This dissertation contains fewer than 65,000 words including appendices, bibliography, footnotes, tables and equations and has fewer than 150 figures.

Nicolas Schneider
December 2019

Acknowledgements

I would like to thank all the team-members of INNOVATE Marie Skłodowska Curie project. Thank you for your help on the different works we shared together in our respective PhD and common projects. Thank you also for you friendship that has been precious during the whole duration of the project. I will be missing you all. A special thanks to all the member of the WP1 test project Shubham, Con, Andrea. I would like to thank the member of the IAT who organised this Marie Skłodowska Curie project that allowed for this project to happen and their support during the duration of the project. As well as all the people working at the ATC that helped me or kept me motivated during the duration of the PhD.

I would like to thank S2M (SKF) for allowing me to visit and stay at their facilities during 6 months for a placement.

Abstract

The aerospace industry is investigating more electrical aircraft since the early 90's. This electrification process in the aerospace industry look at replacing more and more hydraulic and mechanical actuator into electric and electromagnetic ones. The surge in electrical components in the aircraft leads to an increase in electric power consumption. For this reason there is a growing interest into the design of generator for aero-engines. Generator for turbofan are usually attached via a gear box to the high pressure shaft of the turbine. But in the last 20 years, several studies have tried to use electrical generators directly in-line with the turbine's shaft. This raised some challenges in terms of electrical machine performance, heat management as well as finding the good typologies to use for such a task.

In order to reduce even further the use of mechanical components in the aero-engine one could use an in-line electrical machine as an actuator for the starting of the turbine. However In this study will look in a different way to use an electrical generator. In addition to generate electrical power it will be able to work as actuator to reducing the impact of the vibration on the shaft. For this task the machine will be using one single winding to perform both functions.

A model of the bearingless machine will be set as well as the expressions giving the forces and the torque generated by the bearingless machine. A control system will be set up for that machine based and the model previously found. Furthermore the possibility to reduce the vibration of the shaft using the force generated by the bearingless machine will be investigated.

Looking not only at the reduction of the vibration but also the possibility of avoiding critical speeds of the shaft. Different strategies to fulfill that objectives will be proposed. Those strategies will be tested on a common test bench build in collaboration with 3 other PhD students.

Table of contents

List of figures xv

List of tables xix

Nomenclature xxi

1 In-line Starter Generators and their problematics 1
- 1.1 Starter Generators . . . 1
  - 1.1.1 Quick introduction to aero-engine . . . 1
  - 1.1.2 History of the electrical systems in aerospace . . . 2
  - 1.1.3 In-line Starter Generator . . . 5
    - 1.1.3.a Placing . . . 5
    - 1.1.3.b Temperatures . . . 5
    - 1.1.3.c Topology . . . 7
    - 1.1.3.d Torque . . . 8
  - 1.1.4 Vibrations . . . 8
- 1.2 Bearingless machine . . . 10
  - 1.2.1 Magnetic bearings . . . 10
  - 1.2.2 Introduction to bearingless machines . . . 12
  - 1.2.3 Single winding BLM . . . 13
    - 1.2.3.a Parallel Winding . . . 13
    - 1.2.3.b Bridge Winding . . . 14

2 Model of a single winding bearingless machine 17
- 2.1 Inductance matrix of the topology . . . 17
- 2.2 Voltage equation . . . 19
- 2.3 Torque equation . . . 22
- 2.4 Force equation . . . 26
  - 2.4.1 Effect of the displacement of the rotor on the air gap. . . . 26

2.4.2 Fluxes and Inductances depending on the displacement. 27
2.4.2.a Inductances depending on the displacement. 27
2.4.2.b Flux created by the magnets depending on the displacement. 28
2.4.3 Forces due to the magnet flux and current interaction. 29
2.4.3.a Choice of the angle of the Park transformation. 32
2.4.3.b Definition of the force equation in the dq0 axis reference. 34
2.4.3.c Definition of currents for a specified force. 35
2.4.4 Forces due to the Inductances. 36
2.4.5 Forces due to the Magnets. 39
2.5 Finite Element Analysis comparison. 42
2.5.1 Setting of the FEA model. 42
2.5.2 Torque comparison. 43
2.5.3 Eccentricity forces comparison. 45
2.5.3.a Displacement in a direction ε 45
2.5.3.b Static displacement in a direction ε with rotation 45
2.5.4 Currents forces comparison. 46
2.6 Control of the BLM. 47
2.6.1 Introduction to Control 48
2.6.2 Control of the currents. 50
2.6.2.a Considering a negligible suspension voltage 51
2.6.2.b Considering a non-negligible suspension voltage 56
2.6.3 Control of the Force 57
2.7 Summary 59

3 Impact of the BLM on the Rotodynamic of a shaft 61
3.1 Introduction to Rotodynamics 61
3.1.1 Single shaft system 62
3.1.2 Geared shaft system 65
3.1.2.a Model reduction 70
3.1.2.b Model construction 73
3.2 Interaction between the BLM and the shaft 75
3.2.1 Discussion about the use of the BLM 75
3.2.2 Demonstration with a simple model 78
3.2.3 Demonstration with a rotodynamic FEM 81
3.2.3.a Single shaft FEM 81
3.2.3.b Multi-shaft FEM (geared system) 86
3.3 Critical speed avoidance strategy 90

3.3.1 Critical speed push . . . 91
3.3.2 Critical speed hopping . . . 92
3.3.3 Critical speed stepping/sliding . . . 96
3.3.3.a Stepping . . . 97
3.3.3.b Sliding . . . 104
3.4 Conclusions . . . 106

4 Interaction between the electrical and mechanical control 109
4.1 Introduction to set-up . . . 109
4.2 Vibration reduction . . . 112
4.3 Rotodynamics interaction . . . 115
4.3.1 Free acceleration toward critical speeds . . . 117
4.3.2 Vibration reduction with acceleration toward critical speeds . . . 117
4.3.3 Rotodynamic control with acceleration toward critical speeds . . . 119
4.3.4 Methods Summary . . . 119

5 Application to a Test study and Experimental work 123
5.1 Test study setup . . . 123
5.1.1 Test study presentation . . . 123
5.1.2 Team's objectives . . . 124
5.1.2.a Torsional vibration. . . . 125
5.1.2.b Air-riding seal. . . . 125
5.1.2.c BLM. . . . 125
5.1.3 Material and measurement tools . . . 126
5.1.3.a Motor and Generator . . . 127
5.1.3.b Interface and Control platform . . . 127
5.1.3.c Displacement measurements . . . 128
5.1.3.d Electrical connections . . . 129
5.2 BLM set-up . . . 130
5.2.1 BLM conversion . . . 130
5.2.2 BLM performances . . . 133
5.2.3 BLM and Rotodynamics . . . 136
5.2.3.a single shaft . . . 137
5.2.3.b geared system . . . 140
5.2.3.c Summary . . . 140
5.3 Installation of the Experimental test rig . . . 143
5.3.1 General Installation . . . 143

5.3.2 BLM installation 145
5.3.2.a Installation consideration 145
5.3.2.b Installation procedure 148
5.3.2.c Installation discussion 148
5.4 Preliminary work 149
5.5 Conclusion and further work 158

Conclusion **159**

References **163**

Appendix A Control Model: Simulink **171**

Appendix B BLM rotodynamic interaction **175**
B.1 Single shaft study 176
B.2 Mutiple shaft study 178

Appendix C Test Study **181**
C.1 Single shaft study description 182
C.2 Mutiple shaft study description 183

List of figures

1.1 Turbofan diagram 1
1.2 Turbofan diagram 2
1.3 Aircrafts illustration 3
1.4 Constant speed drive diagram 4
1.5 Variable speed constant frequency diagram 4
1.6 Variable frequency diagram 5
1.7 Turbofan generator position diagram 6
1.8 S/G topologies 8
1.9 Vibration measurements 9
1.10 Campbell graph 9
1.11 Response example 10
1.12 AMB 11
1.13 Bearingless SRM 12
1.14 BLM fields 13
1.15 Single winding schematic 14
1.16 ridge single winding configuration 15

2.1 Inductance 18
2.2 Airgap 27
2.4 Direction of the forces for each phase of the BLM 31
2.5 Model on MagNet 42
2.6 BHcurve 43
2.7 Torque comparison 44
2.8 Force created by the eccentricity of the shaft 45
2.9 Force created by the eccentricity of the shaft at $10\mu m$ 46
2.10 Force created by the BLM 47
2.11 Force created by the BLM $I_s = 0.9\,A$ 48
2.12 ControlModel 48

2.13 Proposed control system 52
2.14 Abacus second order 53
2.15 Open loop diagrams 54
2.16 Close loop diagrams 54
2.17 Current control 56
2.18 Bode MIMO 56
2.19 Schematic of the force control system 57
2.20 Bode graph of the force control system 58
2.21 Step response of the force control system 58
2.22 Example of vibration reduction 59

3.1 Model vibration 1 dof 61
3.2 Model dofs 62
3.3 Element considering an axial displacement 63
3.4 Visual representation of the shafts model 65
3.5 Gear mesh model 67
3.6 Model reduction system 70
3.7 Gear connection 71
3.8 Example of a geared FEM with 2 shafts 74
3.9 Schematic of an BLM and AMB shaft system configuration 75
3.10 Schematic of an BLM and bearings shaft system configuration 76
3.11 Schematic of an BLM and its connection to the shaft 77
3.12 Schematic of an BLM Stiffness 77
3.13 Jeffcott rotor model 79
3.14 Single shaft model example 81
3.15 Campbell graph for the initial c 83
3.16 Different stiffness 84
3.17 Variation of the Critical speed of shaft for two cases 85
3.18 FEM of the geared model example 87
3.19 Geared system Campbell graph 88
3.20 Variation of the Critical speed of the 2 shafts system 89
3.21 Variation of the Critical speed of the 2 shafts system 90
3.22 Demonstration of the Strategy A. 92
3.23 Demonstration of the Strategy B. 93
3.24 Logic flow chart of the Strategy B. 94
3.25 Demonstration of the Strategy B. with overlapping 95
3.26 Strategy B. with natural frequencies with high stiffness demand. 96

3.27 Logic flow chart of the Stepping strategy 98
3.28 Stepping Strategy with Hopping comparison 100
3.29 Overlapping of natural frequencies with the stepping strategy. 100
3.30 Solution for the overlapping issue in the algorithm 102
3.31 Logic flow chart of the Stepping strategy with overlapping consideration . . 103
3.32 Overlapping of natural frequencies with the modified stepping strategy. . . 104
3.33 Overlapping of natural frequencies with the sliding strategy. 105

4.1 Combined model 109
4.2 Shaft 110
4.3 Shaft 110
4.4 Shaft vibration reduction using a BLM 113
4.5 Force created by the BLM 114
4.6 Suspension current generated by the BLM 114
4.7 Operating points for the use of a stepping strategy. 116
4.8 Critical speeds. 117
4.9 Shaft 118
4.10 Constant stiffness Vibration 118
4.11 Current 119
4.12 Stepping vibration 120
4.13 Shaft 120
4.14 Shaft 121

5.1 Illustration of Test bench 124
5.2 Illustration of the seal displacement measurement 126
5.3 BLM stator 127
5.4 ECL150 eddy current sensor 128
5.5 MicroLabBox connection 129
5.6 Panasonic servo-motor MSMA042A1C 131
5.7 BLM configuration based of the MSMA042 servo-motor 132
5.8 Old and new servo-motor's coils connection 132
5.9 PCB connecting the BLM's coils 133
5.10 Rotor with aluminium ring 133
5.11 FEA of the BLM 134
5.12 The 3 shafts and their inertias 136
5.13 The 3 shafts gear connection 137
5.14 Single shaft model (FEM) 137

5.15 Campbell graph considering that the BLM compensate for the negative stiffness of the magnets . . . 139
5.16 Critical speed variation with the stiffness . . . 139
5.17 FEM of the geared model . . . 141
5.18 Campbell graph of the 3 shafts system . . . 142
5.19 Critical speed variation with the stiffness for the geared system . . . 142
5.20 Top view of the experimental set up . . . 143
5.21 Side view of the shaft and the actuators . . . 144
5.22 Test study construction . . . 144
5.23 Air-riding seal system . . . 145
5.24 Pneumatic connection schematic . . . 145
5.25 Connection system for the BLM . . . 146
5.26 Rotor deflectio . . . 147
5.27 Stator deflection . . . 147
5.28 BLM mounting system . . . 148
5.29 Flowchart of the BLM installation . . . 151
5.30 BLM shaft misalignment illustration . . . 152
5.31 Shaft deflection . . . 152
5.32 Illustration of Test bench . . . 153
5.33 Box vibration set up . . . 153
5.34 Illustration of Test bench . . . 154
5.35 Vibration with the speed part 1 . . . 155
5.36 Vibration with the speed part 2 . . . 156
5.37 Vibration FFT of the test bench box . . . 157

A.1 BLM control . . . 172
A.2 BLM control . . . 173

List of tables

1.1 Critical speeds extracted from the Campbell graph 10

2.1 Parameter of the machine 18
2.2 Materials used in the FEA 43
2.3 Parameters of the FEA model 44
2.4 Currents $i_s(t)$ injected in the coils 46
2.5 Control loop functions 49
2.6 Value of the parameter of the PI controller 53
2.7 Margins of the open loop transfer function 54
2.8 Parameters of the force control example 57

3.1 Description of the structures used for the rotodynamics FEM calculation for a single shaft system 66
3.2 Description of the structures used for the rotodynamics FEM calculation for a geared system. 69
3.3 Components description for the single shaft system 82
3.4 Natural frequency for both cases 83
3.5 Natural frequency for a single shaft and a geared system 88
3.6 Influence of the ratio γ on the critical speeds 89
3.7 Influence of the inertia on the critical speeds 90
3.8 Look-up table for critical speed hopping 94
3.9 Look-up table for an overlapping situation 95
3.10 Stepping look-up tables 97
3.11 Power use for each strategy 106

4.1 Parameter of the machine 111
4.2 Model settings 113
4.3 PD controller settings 113
4.4 Input and Output of the Rotodynamic control block 116

5.1 Parameters of the ECL150 eddy current sensor probes 129
5.2 Summary of the different electrical component needed and their power requirements 130
5.3 Parameters of the BLM 135
5.4 Parameter of the machine 135
5.5 Components description for the single shaft system 138
5.6 3 shaft system critical speeds 140

B.1 Critical speed value for both cases at divers stiffness 177
B.2 Components description for the first shaft of the system 178
B.3 Components description for the second shaft of the system 179
B.4 Critical speeds value for the 2 shaft system 180

C.1 Critical speeds value for shaft 1 182
C.2 Components description for the first shaft of the system 183
C.3 Components description for the second shaft of the system 184
C.4 Components description for the third shaft of the system 185
C.5 Critical speeds value for the 3 shaft system 186

Nomenclature

Acronyms / Abbreviations

AC	Alternative Current
AGB	Accessory Gearbox
AMB	Active Magnetic Bearing
BLM	Bearingless machine
CAD	Computer-aided design
DC	Direct Current
DoF	Degree of Freedom.
emf	Electromotive force
FEA	Finite Elements Analysis
FEM	Finite Element Modelling/Model.
HP	High Pressure
HVDC	High Voltage Direct Current
IM	Induction machine
LP	Low Pressure
MIMO	Multiple input multiple output
PCB	Printed circuit board
PM	Permanent Magnet

V

PMSM Permanent Magnet Synchronous machine

RDS Radial Driveshaft

S/G Starter Generator

SISO Single input single output

SM Synchronous machine

Physics Constants

μ_0	Permeability of the vacuum $4\pi \cdot 10^{-7}$.	$H \cdot m^{-1}$

Electrical Parameter

$[\mathbb{E}]$	Emf Matrix	
e_M	Emf of the coils from the phase M	V
$[\mathbb{E}_{ms}]$	Emf Matrix for the bearingless configuration	
F_ε	Force in a direction ε	N
$[\mathbb{I}]$	Current Matrix	
i_{Mi}	Current of the coil number i from the phase M	A
i_{Mm}	Motor current in the coils from the phase M	A
i_{Ms}	Suspension current in the coils from the phase M	A
$[\mathbb{I}_{ms}]$	Current Matrix for the bearingless configuration	
v_{Ms}	Voltage at the suspension inverter from the phase M	V
$[\mathbb{L}]$	Inductance Matrix	
L	Self inductance of a coil	H
L_m	Motor inductance	H
$[\mathbb{L}_{ms}]$	Inductance Matrix for the bearingless configuration	
L_s	Suspension inductance	H
$M_1, M_2 ..., M_n$	Mutual inductances of a coil	H

μ_r	Relative permeability	
p	number of pairs of poles	
$[\Phi_{mag}]$	Vector of the flux created by the magnets at each coils of the BLM.	Wb
$\phi_{mag\ Mj\ 0}(\theta)$	Flux created by the magnet in the coil j of phase M with a centred rotor.	Wb
$\phi_{mag\ Mj}(\theta, \Delta_x, \Delta_y \beta)$	Flux created by the magnet in the coil j of phase M at an angle β, considering the displacement Δ_x and Δ_y of the rotor.	Wb
$[\mathbb{R}]$	Resistance Matrix	
R	Resistance	Ω
$[\mathbb{R}_{ms}]$	Resistance Matrix for the bearingless configuration	
$[\mathbb{V}]$	Voltage Matrix	
v_{Mi}	Voltage of the coil number i from the phase M	V
v_{Mm}	Voltage at the motor inverter from the phase M	V
$[\mathbb{V}_{ms}]$	Voltage Matrix for the bearingless configuration	
W	Energy	J
z	number of coils per phase	

Geometrical parameter

β	Angle of the calculated air gap considering displacement.	rad
Δ_x	Displacement of the rotor in the x direction.	m
Δ_y	Displacement of the rotor in the y direction.	m
ε	Direction	
g_0	Air gap of the BLM	m
γ_M	resulting direction of the force created by a phase of the BLM	rad
$g(\beta)$	Air gap of the BLM considering a displacement Δ_x and Δ_y of the rotor.	m
l_{mag}	Width of the magnets	m

θ	Angular position of the rotor	rad

Mechanical parameter

c_h	Connective damping between two gears.	$N \cdot s \cdot m^{-1}$
ζ	Damping factor	
D_{in}	Inner diameter	m
D_{out}	Outer diameter	m
E	Young's modulus (modulus of elasticity)	Pa
F_{axial}	Axial force	N
G	Shear modulus (modulus of rigidity)	Pa
γ	Speed ratio	
I_D	Diametral Inertia.	$kg \cdot m^2$
I_P	Polar Inertia.	$kg \cdot m^2$
k_{airgap}	Negative stiffness present in the airgap of an electrical machine.	$N \cdot m^{-1}$
k_h	Connective stiffness between two gears.	$N \cdot m^{-1}$
Φ_p	Pressure angle of the gears.	rad
R_{gear}	Gear radius	m
ρ	Material density.	$kg \cdot m^{-3}$
T	Torque	$N \cdot m$

Mathematical parameter

$b(t)$ *or* $B(s)$	Disturbance signal
$[I_n] or I_n$	Square identity matrix of size n
$\mathscr{L}\{f(t)\}$	Laplace transform of the function $f(t)$
$r(t)$ *or* $R(s)$	Reference signal
s	frequency parameter from the Laplace transform
$y(t)$ *or* $Y(s)$	Output signal

Chapter 1

In-line Starter Generators and their problematics

1.1 Starter Generators

1.1.1 Quick introduction to aero-engine

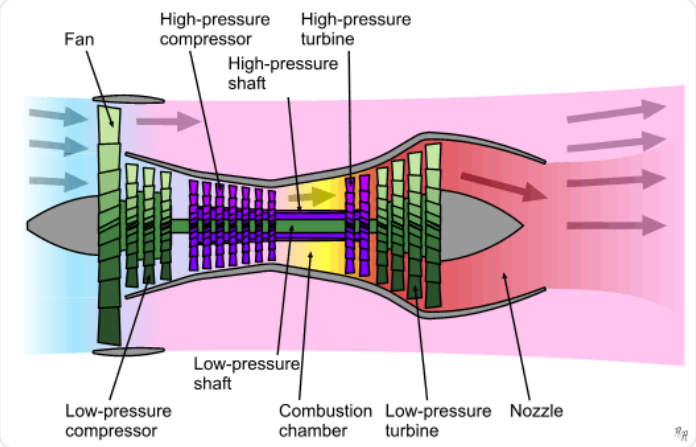


Fig. 1.1 Diagram of a turbofan ⓒⓘⓢ by *Duesentrieb*

Fig. 1.1 shows you a simplified schematic of turbofan engine used in civil passenger aircrafts. The aero-engine creates the thrust necessary to make the aircraft fly with the fan pushing air toward the back. Some of this air is then sucked into a high pressure compressor. Followed by the combustion chamber where the kerosene is injected to power the rotation of the system. The hot air is then pushed toward a low pressure turbine and ejected at the nozzle. Therefore some thrust is generated by the engine and some by the fan. A ratio between the

air that goes around the engine to the air that goes through the core is then introduced. This is called *bypass ratio*. Due to the fact that the presence of the fan does not affect much the kerosene consumption of the engine, the higher the *bypass ratio* of the engine the more fuel efficient it will be, as more thrust will be provided by the fan.

In the previous illustration Fig. 1.1 shows a turbofan with 2 distinct shafts also called spool: one for the fan one for the core. This is commonly used by GE and CFM. But some add a third intermediary spool for increased efficiency of the engine, like Rolls-Royce Trent engines.

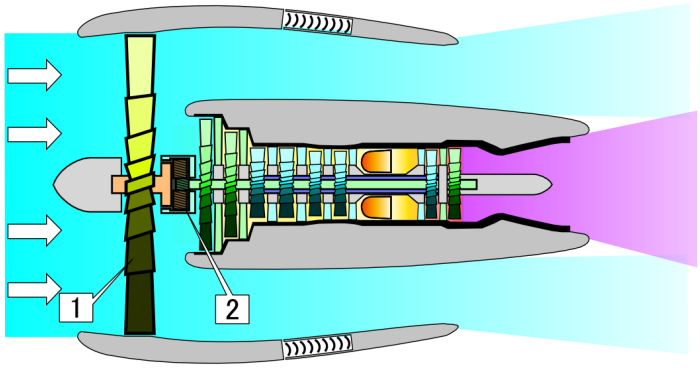
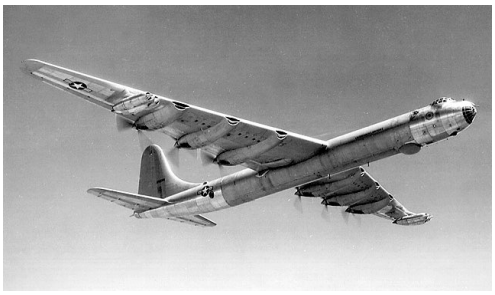


Fig. 1.2 Diagram of a geared turbofan ⓒⓘⓢ by *Tosaka*
1: fan 2: gearbox

Recently some work as been conducted regarding the use of a gearbox between the fan and the rest of the engine. The idea is to allow the fan and the engine to rotate at different speeds. Since the Low pressure shaft is connected to the fan, its speed is limited by the maximum speed that the tip of the fan blades can reach. Therefore, by decoupling them one can get rid of this constraint and allow for an increased efficiency of the engine and a higher *bypass ratio*. The main inconvenient of this solution is the losses that will be occurring at the gearbox. Furthermore, the cost of such engine will be increased due to the complexity of such a mechanical gearbox. This idea isn't new as several works has been made by Turbomeca on this in the 50's and by Honeywell later in the 70's. But this technology has seen renewed popularity with Pratt and Withney's PW1000G engine in 2008.

1.1.2 History of the electrical systems in aerospace

From the early beginning of aviation electrical systems played a significant role. From the Wright brother to the modern day aircrafts, electrical systems have always been present. At the same time their importance grew over time. In 1936 the first DC-3 used $2 \times 712.5\ W$ generator able to deliver $50\ A$ at $14.25\ VDC$. which is pretty far from the one of a $2\times$CFM



(a) Convair B-36 by *U.S. Air Force photo*



(b) Douglas DC-3 by *RuthAS*

Fig. 1.3 Aircrafts illustration

56-3 from a Boeing 737-300 each providing 136 kW in 1985. In order to reduce the weight of the future aircraft, the voltage of the DC buses has been increased with the years. In 1946 the B-36 is the first military to use AC current for its electrical power. With this they introduced the use of 400 Hz AC current as it provided the best weight solution for the increasing power demand. This has now become the standard in the aerospace industry. As it allowed to have a lighter electrical system, which was critical as the aircraft got more and more electrical energy hungry. But during the 1980's high voltage direct current (HVDC) power at 270 VDC was introduced as it prove to reduce the mass of the aircraft. It was chosen over the 400 Hz in the F-22 fight jet in 1997. In the 1980's to the 90's some other form of power were introduced like:

- High frequency 20 kHz power system [37].
- Variable frequency variable voltage VFVV.
- Variable frequency constant voltage VFCV.

VFVV being mainly used with magnet generators and VFCV using synchronous machine (SM) with an output voltage regulated to be constant at all speeds. The use of a SM as a constant speed drive as been the preferred option to generate the 400Hz power for aircraft. The constant speed drive is positioned at the accessory gearbox of the aero-engine which would change the variable speed of the engine into a constant at the synchronous speed (6000 rpm to obtain the 400Hz) Fig 1.4. Until the variable speed constant frequency VSCF system where introduced [37, 42]. They allowed to produce the 400 Hz in a more reliable way. The first of them were using cyclo-converters transforming variable high frequencies to the desired 400Hz. Even-though they provide a near sinusoidal power output, they require a very large number of semiconductors.It is also worth pointing out that the power flow can be bi-directional which would be perfect for Starter/Generator applications. Further VSCF will introduce the presence of a DC bus like standard modern drive are using. The introduction of this DC link will allow the reduction of the number of semiconductors and

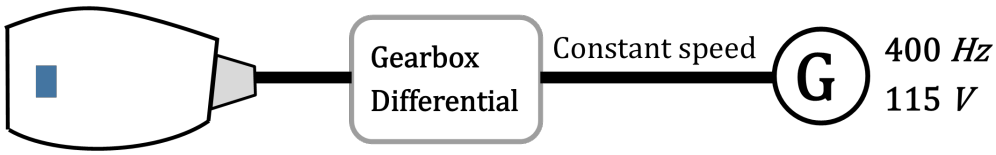


Fig. 1.4 Constant speed drive diagram

allow the possibility to use different kind of modulation to obtain the 400 Hz [71] Fig 1.5. In

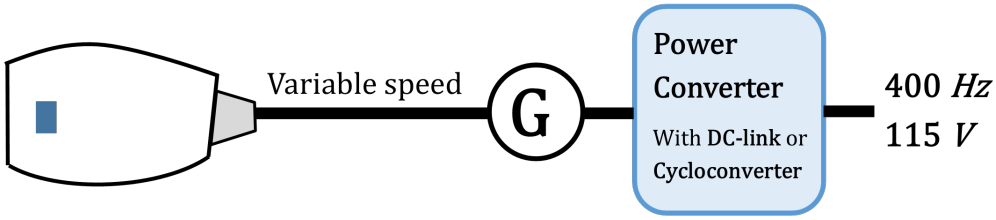


Fig. 1.5 Variable speed constant frequency diagram

the 1990's started the More Electric Aircraft (MEA) initiative which embraces the idea of replacing the different mechanic, pneumatic, hydraulic actuators or subsystems of aircrafts by electrical ones. This pushed the aircraft generator close to the engine and the distribution to the power via electrical channels instead of mechanical, pneumatic or hydraulic ones. In the recent years the addition of more and more electrical load starts to put increased strain on the generation side. At the same time the surge of the number of electrical components pushed the aerospace sector further toward replacing some of its mechanical actuator by electrical ones [73]. The A380 one of the first generation MEA proposed a system where the Constant speed Gearbox usually used in civil aircrafts Fig. 1.4 be replace by a variable frequency solution Fig. 1.6 [9]. This proposes a simple and reliable generation method but it will require that each of the aircraft's load have its own power electronics. But as most of those loads require a power converter anyway this negative aspect of the variable frequency could be dismissed. Power electronics not being too reliable, having only selected loads disconnect because of a failure instead of the whole generation system would be a clear advantage.

Since the early 1990's late 1980's some project were looking at the possibility to use in-line starter generator. The use of cyclo-converter has already been discussed to help toward this idea. In 1989 GE looked at using switch reluctant machines as an inline starter generator [53] Later on, NASA investigated the use of different topologies to be used as a

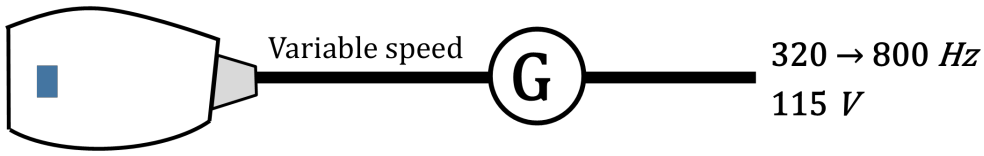


Fig. 1.6 Variable frequency diagram

starter generator [28]. More recently in 2014 Rolls-Royce with their *SEED* project used a PM brushless machine as a S/G for UAV application [13, 14].The use of such kind of technology bring its share of advantages but also inconveniences. Having a machine able to provide both the function will allow for a reduction of the weight of the engine. This fits perfectly with the drive of the aerospace industry's objectives of reducing fuel consumption.

‘

1.1.3 In-line Starter Generator

1.1.3.a Placing

To understand the reason the starter generator would need to be placed in-line with the turbine's shaft it is good to know how it is connected at the present. The starting and generating functions are for the moment usually separated. But they are both connected to an accessory gearbox (AGB). The AGB is then connected to the turbine (HP shaft in the case of the CFM56) via radial driveshaft (RDS). All this illustrated in Fig. 1.7. Therefore, using an in-line S/G would take away the need for a gearbox connecting the S/G to the turbine. In any case it would signify a reduction of its size as some other components are connected through it; like the oil pump, hydraulic pump etc. But does not come without its challenges. One of the first is the space. The aero-engine are filled with equipment and have barely any available space left for the installation of the S/G. In the same order of idea, the S/G can not just positioned at any given place on the shafts as the function of the machine has to be taken into consideration. As the starter need to be positioned at a place in the engine on a shaft that will allow the starting of the turbine.

1.1.3.b Temperatures

After finding a suitable place to position the S/G another challenge rises as most of he areas in the aero-engine are subject to high temperatures [4]. This challenge requires a study and the thermal aspect of the machine to be taken into consideration. The high temperature

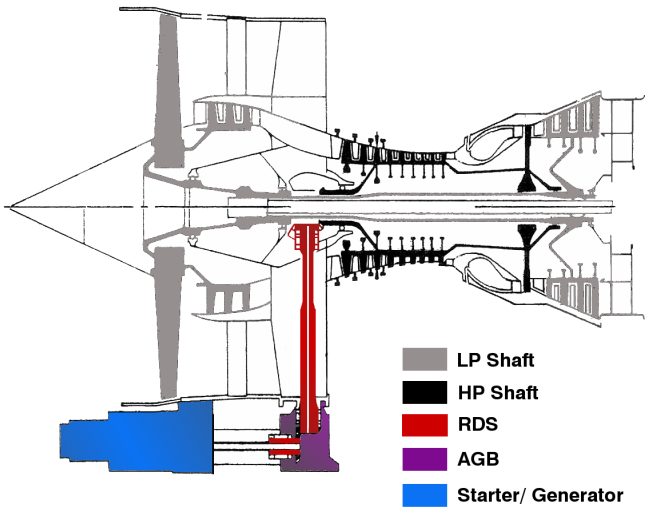


Fig. 1.7 diagram of the poition of the Generator and the starter in a CFM56 engine.

environment being definitely damaging to electrical machines [24]. the challenges posed by the high temperatures can be separated into two main categories:

1. The insulation of the winding of the electrical machine
2. The potential use of magnets

The usual temperatures limit for high performance insulation rarely exceed the $250°C$ and the risk of having electrical insulation burning in an aero-engine isn't acceptable. Furthermore, the simple degradation of the insulation might lead to short circuits that will exacerbate even further the risk of a fire. Far from the standard insulation varnish usually used in electrical machines, divers specialized solution have been proposed for the insulation of the electrical machine's winding [23]. But even with electrical insulation like ceramic or mica plated wires and aluminum oxide wires that can withstand high temperatures up to $500°C$ have been shown to degrade quite quickly overtime when subjected to those high temperatures[24].

On the other hand the use of magnets allowing for potential higher torque density could be a problem because of the deterioration of their performance with temperature. High temperatures might even lead to a complete demagnetization of the magnets. This would be obviously catastrophic for an aerospace application. Some magnets have better thermal performance than the Neodynium (NdFeB) ones like Samarium Cobalt (SmCo) or Alnico. But their magnetic performance are relatively smaller.

One could think of cooling systems to maintain the temperature of the S/G as low as possible to elude the issue with the temperature at the winding insulation and the magnets.[60]. This can be achieved by design the machine with an integrated cooling system.

1.1.3.c Topology

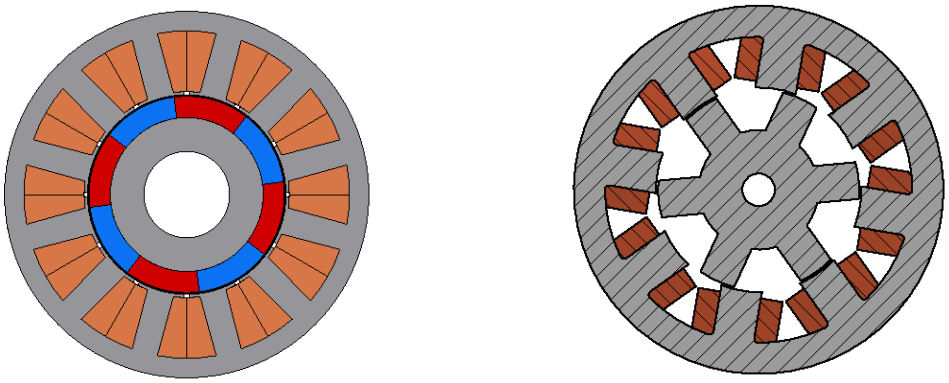
One of the aspect of the S/G is to look at the topology that might be used fill the wished function. There are several topologies thought to be potentially used as an S/G:

- Permanent magnet synchronous machines (PMSM) [13]
- Wounded synchronous machines (SM)
- Switch reluctant machine (SRM) [30]
- Induction machine (IM) [16].

But, use of SRM and PMSM machine [69] are mainly talked about. As SM machine use windings at the rotor that might lead to complex thermal issues. For IM machines the torque density being quite low compared to the other topologies will disqualify it as the aerospace industry attaches so much importance on weight reduction.

PMSM are known for having the best torque density in electrical machines [45].Even-though the potential use of PMSM machine might be problematic at high temperature as they could demagnetize, by using more temperature resistant magnets than the commonly used Neodynium (NdFeB); like Samarium Cobalt (SmCo). SmCo can resist up to 350 $^{\circ}C$ and has a temperature coefficient of grades available with a temperature co-efficient of -0.03$\% \cdot {}^{\circ}C^{-1}$ [3]. The big disadvantage of this topology is the constant presence of field in the machine due to the magnets. This could be dangerous in case of fault as there is no way to take away the field and the potential electromotive force it create. But there has been some fault tolerant machine that have been developed: using duplex machines, memory motors, Doubly salient and flux switching PMSM, auxiliary windings , mechanical flux weakening etc.[27].

One topology that has been extensively proposed for an in-line S/G application is the SRM one [57, 72, 10, 31, 36]. Their main advantages are that they are inherently fault tolerant which makes it a perfect candidate for aerospace applications. Furthermore, they have a simple laminated rotor which makes it light. The lack of any electrical or magnetic components on the rotor reduces the need for a cooling. This also makes it perfect for it use in high temperature environments up to 400 $^{\circ}C$. But one has to note that their salient shape makes them prone to windage losses [53].



(a) PMSM topology (b) SRM topology

Fig. 1.8 S/G topologies

1.1.3.d Torque

One of the other aspect of the S/G that provides some challenges are the different torque requirements for the starting and generating [53]. As the torque required is very high at the starting of the aero-engine a few questions concerning the design of the S/G arises. Does the machine design only considers the starting requirements and have overly designed S/G for the rest of the operating time? As weight in an aircraft is critical this solution does not seem viable. Especially since the starter is only used for a few minutes at the beginning of the flight and the generator part is used for all the remaining hours of the flight. On the other hand the BLM could be designed solely for the generating but take in account the over-current for the few minutes of the starting and have a cooling system allowing to sustain that stress.

1.1.4 Vibrations

In any rotating system the question of the vibration as to assessed one way or another. They are an integral part of the system and can be due to the application of external forces on the shaft and any shaft eccentricity. As well than the potential gears seals and bearings on it can create vibration. Aero-engine that can be described in vulgarized terms as a shaft assembly connected together that works as a "fan" as described in section 1.1.1. It has seals, bearings as well than a huge amount of energy transfer. Therefore, it does not escape the issue created by vibration. Any rotating system has also its natural frequencies where the vibration response of the shaft enters a resonance and tends to very high values[74, 34]. At

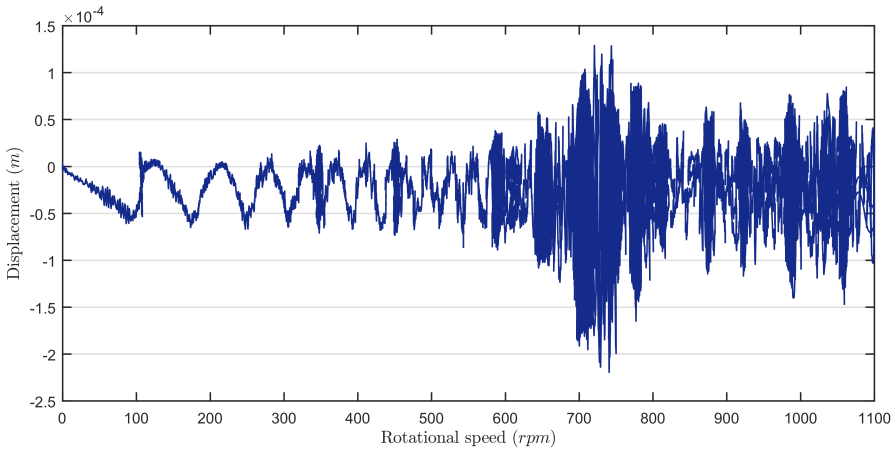


Fig. 1.9 Example of vibration measurements

those values the shaft runs a risk to loose its structural integrity and break or damage other components of the engine. Those different natural frequencies have to be studied carefully as they might put in jeopardy the integrity of the shaft assembly. Different aspect of the vibration in aero-engines have been extensively studied as they are a critical component of the aircraft [39, 75]. Fig. 1.10 shows you a Campbell graph of a shaft where one can

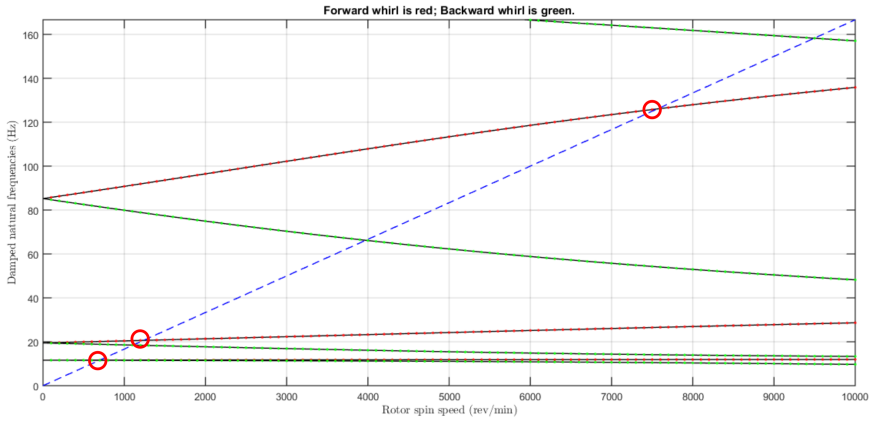


Fig. 1.10 Campbell graph highlighting the critical speeds of a shaft

extract the critical speeds by looking at the intersection between the Forward whirl curves and the curve $Damped\ frequency = \frac{Rotor\ spin\ speed}{60}$. For a bit of convenience they have been highlighted with red circles in that example. For this example one can get: Those critical speeds present issues for the good functioning of the shaft. As it is illustrated in Fig. 1.11 the increase in the response at the critical speeds of the shaft can be observed. The main strategy to avoid the negative effect of the natural frequencies is to accelerate through them

Table 1.1 Critical speeds extracted from the Campbell graph

Example	Critical speed 1	2	3
	698 *rpm*	1238 *rpm*	7563 *rpm*

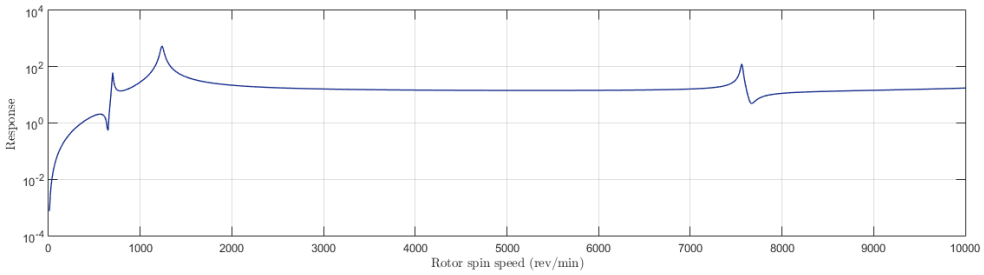


Fig. 1.11 Response at a node of the example

quickly enough so that the resonance does not increase the vibration dangerously [38]. But, the interesting part would be to find if there is a solution to avoid the effects of those critical speeds without having to accelerate through them. Or at least a solution that could reduce the overhaul vibration of the shaft. Therefore, it would be interesting to have an active or passive actuator that could act on those phenomena.

1.2 Bearingless machine

To help the reduction of vibrations one could think of changing part of the shafts using different components or changing some aspect of their design. One way to interact with the displacement of a shaft would be to use an actuator that is able to apply a force on that shaft. In order to limit the wear of the system due to friction at high speeds this force would have to be applied contact-less. For this reason an investigate the use of electromagnetic forces was pursued.

1.2.1 Magnetic bearings

One way to apply a force on a shaft and control its displacement would be to use magnetic bearings. They are actuator that have been designed to replace bearings in high speed application that would have make their use challenging or impossible For this study the use of active magnetic bearings (AMB) will be privilege n comparison to their passive counterpart,

as one wish to be able to potentially control the forces applied on the shaft. Fig. 1.12 shows you an example form of an active magnetic bearing (AMB) acting on 1 DoF. Starting by a

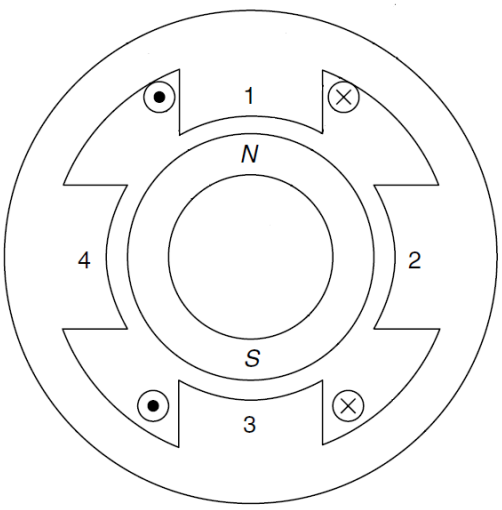


Fig. 1.12 Primitive Active magnetic bearing

small historic of the AMB. In 1939 when Werner Braunbek interpreted Samuel Earnshaw's publication *"On the Nature of the Molecular Forces which regulate the Constitution of the Luminiferous Ether"*[26] on he force equilibrium in static fields, in the sense of magnetic levitation, he managed to show that it was possible to levitate a diamagnetic object using purely permanent magnetic stabilization. Then in the 40's with the project Manhattan saw appearance of the first ideas of magnetic bearings with its use in uranium centrifuges [12]. Later on some other patents were submitted concerning the use of magnetic levitation [70]. Magnetic bearings are at their core an electromagnetic actuator that subject an object to a force and are mainly used to control 1 or several degrees of freedom (DoF) of said object. Which answers the requirement previously set. But, as for the moment they are commonly used in high speed application as a replacement for contact bearings [72, 62, 67, 11], where contact bearings would wear to fast and generate too much friction losses. But they are also used in application where the environment needs to be extremely clean (oil free) like in certain pharmaceutical applications [67]. Answering our previous the issue about the vibration, some studies have been conducted on the use of magnetic bearings as an actuator specifically dedicated to the reduction of vibration [22**?**]. Going further in the application some went to show that an electrical machine could be used to provide the torque necessary for the rotation as well as a mean to reduce the vibration of the system they are attached to [68, 43]. Those devices are electrical machines named bearingless machines (BLM.)

1.2.2 Introduction to bearingless machines

Bearingless machine (BLM), are electrical machine that are able to generate in the same time a torque and a force that levitates the rotor [20]. In order to be able to do those two functions at the time several configurations of machines exist:

- PMSM BLM [41]
- SM BLM [18]
- SRM BLM (BSRM)[77]
- IM BLM [19]
- Homopolar BLM [64]
- Conical BLM [48]
- Segmented BLM [66]

Each of those machine having their advantages and inconveniences. BSRM as shown in Fig. 1.13 has a very similar topology to the simple magnetic bearing in Fig. 1.12. The main difference is that the force created by the BLM will depend on the position θ of the rotor. For this reason more than one phase is needed on the suspension section to be able to create force in a certain direction for every position θ. The magnetic circuit of most of BLM

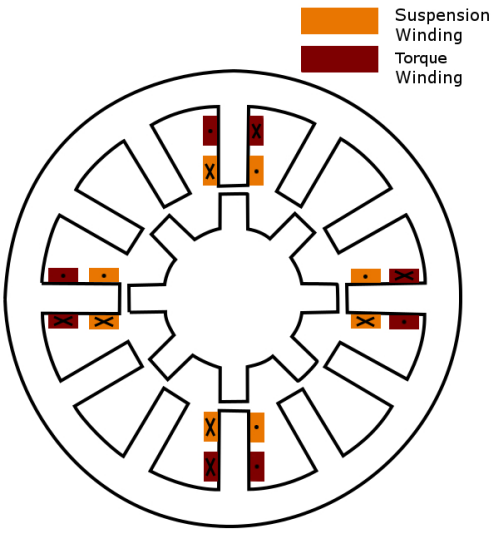


Fig. 1.13 Bearingless SRM topology

are shared by the suspension flux and the one created for the torque. This can lead to some undesirable increase of losses as well as saturation. To mitigate this some BSRM propose some flux shortening solution [76]. Push this even further some system have been proposed [46] with two separate magnetic circuits, one for each application.

From this list the attention was mainly concentrated on electrical machines that were already discussed as the potential machines used to be a S/G. But the principle behind of most of those machines are the same. They consist in creating a rotating magnetic field with a polarity p in order to create the torque. But then they could produce another magnetic field that provides the forces that will be applied to the rotor to displace it. For the PMSM this field has a polarity $p+1$ or $p-1$ [8]. This is illustrated using a PMSM BLM in Fig. 1.14 where the two fluxes Φ_m and Φ_s can be seen. For this reason most of those topologies have two separate winding that provide the two different functions sharing basically the magnetic medium.

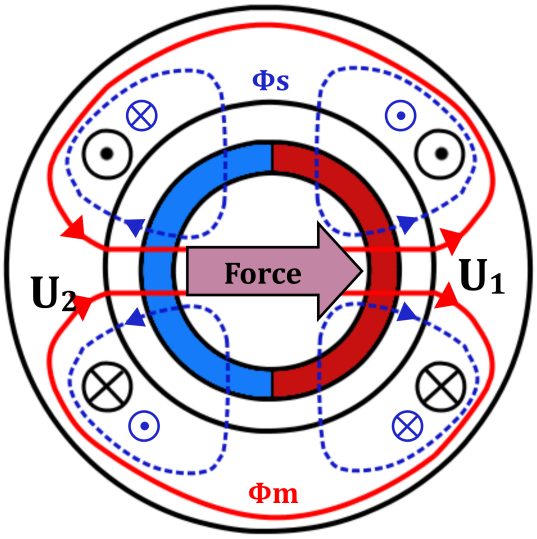


Fig. 1.14 Fields in a PMSM BLM

1.2.3 Single winding BLM

BLM use usually two separate windings but some topologies have been proposed [54, 49] using single winding ones or a single drive [68]. Those topologies generally use PMSM BLM two topology proposing a single winding PMSM BLM will be looked at more specifically.

1.2.3.a Parallel Winding

The first one proposed by Chiba [54] is illustrated in Fig.1.15.This winding using a parallel topology of windings and two power inverters. Each of the inverter will provide a current i_m and i_s respectively. The principle behind the functioning of this BLM is injecting a current i_s through the Suspension inverter that will create an unbalance in the current in each winding

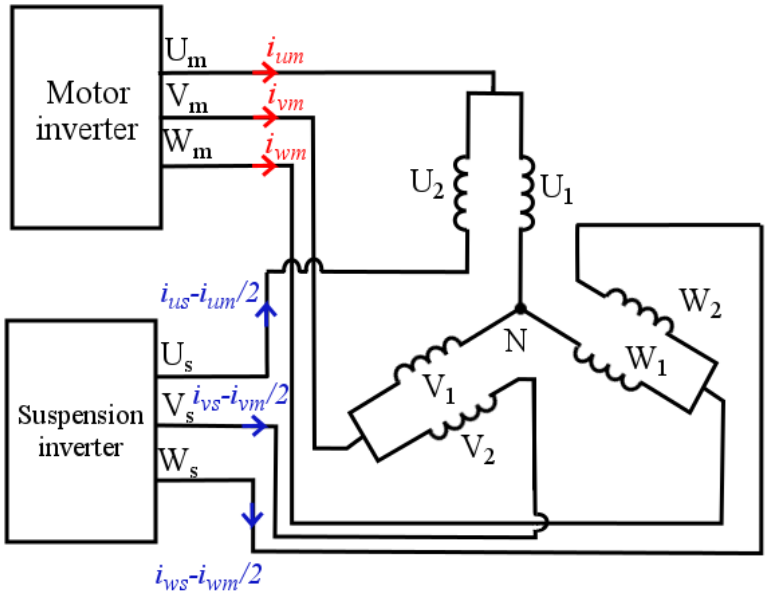


Fig. 1.15 Single winding configuration [54]

of a single phase. The currents in the two coil U_1 and U_2 will have a combination of the two currents i_m and i_s.

$$i_{U1} = \frac{i_m}{2} + i_s \qquad i_{U2} = \frac{i_m}{2} - i_s \tag{1.1}$$

This will result by the creation of a second magnetic field that has either a polarity $p+1$ or $p-1$. This is illustrated in Fig. 1.14 where you see the different fields ϕ_m and ϕ_s created by i_m and i_s respectively. As well as their interaction that leads to the creation of a force.

1.2.3.b Bridge Winding

The first one proposed by Khoo and Garvey [49] is illustrated in Fig.1.15. Instead of creating the suspension field fluxes with a parallel wing this one concentrates on the use of bridges. Each phase will be separated in 4 coils (or set of coils) that will be connected as a bridge. But this time the current i_s is injected through the middle the bridge. If considering that all the coils $U_1, \ldots, U_4$ are identical the currents in the coils can be written as:

$$i_{U1} = \frac{i_m}{2} + \frac{i_s}{2} \qquad i_{U2} = \frac{i_m}{2} - \frac{i_s}{2} \qquad i_{U3} = \frac{i_m}{2} - \frac{i_s}{2} \qquad i_{U4} = \frac{i_m}{2} + \frac{i_s}{2} \tag{1.2}$$

$$i_{U1} = i_{U4} \qquad i_{U2} = i_{U3} \tag{1.3}$$

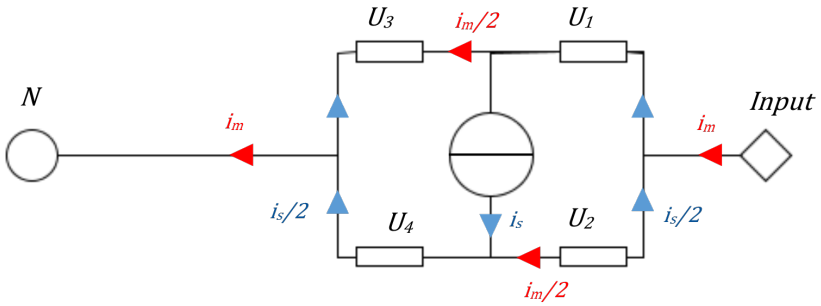


Fig. 1.16 Presentation of 1 phase of a Bridge single winding configuration

One notices that the coils work in pair as each opposite coil from the bridge have the same current. With the same principle than the one illustrated in Fig. 1.14 the current i_s will create the $p-1$ or $p+1$ field and therefore produce a force on the rotor. The main difference with the solution provided by the parallel method is the power electronics related to the functioning of the BLM. This application requires one inverter for the torque and then 1 single phase inverter for each phase.

For the rest of this study the study will then concentrate on the use of a single winding topology for its similar performance than a double winding topology. However, the main reason being that this single winding topology opens the possibility to convert easily a PMSM into a BLM without having to rewind the machine. This is true only if the PMSM has enough coils to provide the $p \pm 1$ field needed for the creation of the suspension force.

Chapter 2

Model of a single winding bearingless machine

This study will concentrate on the use of a single winding topology for it opens the possibility to convert easily a PMSM into a BLM without having to rewind the machine. Furthermore, this topology requires the use of a simple 3 phase inverter drive to control it. In this chapter will start by creating a model of the BLM that will then be used to drive it as well as evaluating its performance as a vibration reduction actuator.

2.1 Inductance matrix of the topology

To model the BLM this requires to find the inductance of its coils in order to form the inductance matrix of the machine. In this case the steel of the machine was considered to be a linear material. In order to calculate the inductance each coil of the machine was supplied with an $1A$ current one after the other and the flux on each coil was measured on FEA tool named FEMM. The different placements of the inductances calculated are represented in Fig. 2.1 where the current was fed in the coils represented by L. Knowing the equation(2.1) linking the current and inductance to the flux in the coils, all the different inductance and mutual inductance can be calculated. The extracted Inductances and the resistance of the coils are listed in Table 2.1. Considering that $M_2 \approx M_4$ and $M_3 \approx M_5$ the inductance matrix is then updated in the equation 2.2.

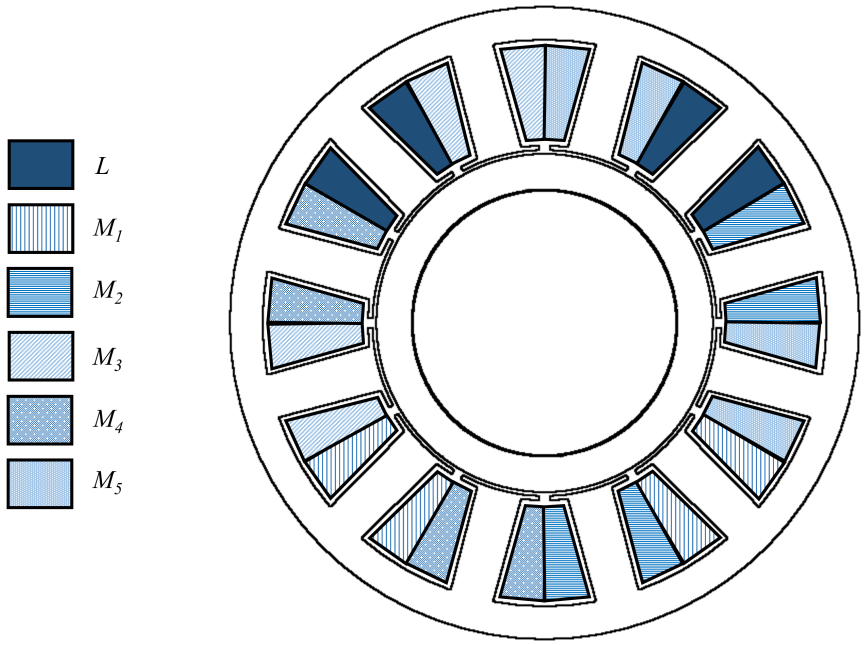


Fig. 2.1 Representation of the different inductance for one coil

Table 2.1 Parameter of the machine

Resistance in $\mu\Omega$	Inductances in μH					
R	L	M_1	M_2	M_3	M_4	M_5
219.5	42.423	5.1462	-5.1631	11.765	-5.1627	11.768

$$[\Phi] = [\mathbb{L}] \cdot [\mathbb{I}] = \begin{bmatrix} L & M_1 & M_2 & M_3 & M_4 & M_5 \\ M_1 & L & M_3 & M_2 & M_5 & M_4 \\ M_4 & M_5 & L & M_1 & M_2 & M_3 \\ M_5 & M_4 & M_1 & L & M_3 & M_2 \\ M_2 & M_3 & M_4 & M_5 & L & M_1 \\ M_3 & M_2 & M_5 & M_4 & M_1 & L \end{bmatrix} \cdot \begin{bmatrix} i_{U1} \\ i_{U2} \\ i_{V1} \\ i_{V2} \\ i_{W1} \\ i_{W2} \end{bmatrix} \tag{2.1}$$

$$[\mathbb{L}] = \begin{bmatrix} L & M_1 & M_2 & M_3 & M_4 & M_5 \\ M_1 & L & M_3 & M_2 & M_5 & M_4 \\ M_4 & M_5 & L & M_1 & M_2 & M_3 \\ M_5 & M_4 & M_1 & L & M_3 & M_2 \\ M_2 & M_3 & M_4 & M_5 & L & M_1 \\ M_3 & M_2 & M_5 & M_4 & M_1 & L \end{bmatrix} \tag{2.2}$$

2.2 Voltage equation

Following the determination of the inductance matrix of the bearingless machine, the voltage equations governing the electrical machine's behavior need to be defined.The voltage of each coil is defined by the vector $[\mathbb{V}]$ and can be expressed as show in equation (2.3) with $[\mathbb{E}]$ being the vector of the emf each winding. Developing the equation and integrating the inductance matrix from equation (2.2) the equation (2.4) was obtained. Now the currents and the voltages should be divided in two groups. One representing the motor/generator function and the other one being the suspension/actuator function of the BLM. Therefore, the currents (i_{Um}, i_{Vm}, i_{Wm}) for the motor function and (i_{Us}, i_{Vs}, i_{Ws}) for the suspension function were introduced. Their definition are given in equation (2.5) and (2.6) and represented in Fig. (1.15).The same is adapted to the voltages at each of the BLM's inverter (v_{Um}, v_{Vm}, v_{Wm}) and (v_{Us}, v_{Vs}, v_{Ws}) given in equation (2.7) and (2.8).

$$[\mathbb{V}] = [\mathbb{R}] \cdot [\mathbb{I}] + [\mathbb{L}] \cdot \frac{\mathrm{d}}{\mathrm{d}t}[\mathbb{I}] + [\mathbb{E}] \tag{2.3}$$

$$\begin{bmatrix} v_{U1} \\ v_{U2} \\ v_{V1} \\ v_{V2} \\ v_{W1} \\ v_{W2} \end{bmatrix} = R \cdot [I_6] \cdot \begin{bmatrix} i_{U1} \\ i_{U2} \\ i_{V1} \\ i_{V2} \\ i_{W1} \\ i_{W2} \end{bmatrix} + \begin{bmatrix} L & M_1 & M_2 & M_3 & M_4 & M_5 \\ M_1 & L & M_3 & M_2 & M_5 & M_4 \\ M_4 & M_5 & L & M_1 & M_2 & M_3 \\ M_5 & M_4 & M_1 & L & M_3 & M_2 \\ M_2 & M_3 & M_4 & M_5 & L & M_1 \\ M_3 & M_2 & M_5 & M_4 & M_1 & L \end{bmatrix} \cdot \frac{\mathrm{d}}{\mathrm{d}t} \begin{bmatrix} i_{U1} \\ i_{U2} \\ i_{V1} \\ i_{V2} \\ i_{W1} \\ i_{W2} \end{bmatrix} + \begin{bmatrix} e_U \\ e_U \\ e_V \\ e_V \\ e_W \\ e_W \end{bmatrix} \tag{2.4}$$

$$i_{U1} = \frac{i_{Um}}{2} + i_{Us} \qquad i_{V1} = \frac{i_{Vm}}{2} + i_{Vs} \qquad i_{W1} = \frac{i_{Wm}}{2} + i_{Ws} \tag{2.5}$$

$$i_{U2} = \frac{i_{Um}}{2} - i_{Us} \qquad i_{V2} = \frac{i_{Vm}}{2} - i_{Vs} \qquad i_{W2} = \frac{i_{Wm}}{2} - i_{Ws} \tag{2.6}$$

$$v_{Um} = v_{U1} \qquad v_{Vm} = v_{V1} \qquad v_{Wm} = v_{W1} \tag{2.7}$$

$$v_{Us} = v_{U1} - v_{U2} \qquad v_{Vs} = v_{V1} - v_{V2} \qquad v_{Ws} = v_{W1} - v_{W2} \tag{2.8}$$

The equation (2.4) is then developed further in order to search for possible simplification. For the sake of clarity, the process is demonstrated only on the phase U of the machine. The same steps will be applied on all the other phases. The equation (2.9) gives us the expression of the voltage v_{U1} as a function of all the different currents in the coils. Now the values of the suspension and motor currents can be introduced. Considering that $i_{Us} + i_{Vs} + i_{Ws} = 0$ and $i_{Um} + i_{Vm} + i_{Wm} = 0$ the equations (2.10) and (2.11) can be simplified even further. Separating the suspension and motor current in equation (2.12) and (2.13) it was observed that the derivative of the currents are multiplied by two different set of algebraic combination of the machine's inductances. Therefore L_m and L_s were introduced, defined in equation (2.14) that will represent the inductance of the BLM seen from the perspective of the motor and suspension function respectively. The assumption made here is that inductances of the BLM are not changing significantly with the angular and transverse position. As one of the main function of the machine is the reduction of vibration the impact of the eccentricity on the inductance the rotor will be neglected.

$$v_{U1} = R\, i_{U1} + L\frac{\mathrm{d}\, i_{U1}}{\mathrm{d}t} + M_1\frac{\mathrm{d}\, i_{U2}}{\mathrm{d}t} + M_2\frac{\mathrm{d}\, i_{V1}}{\mathrm{d}t} + M_3\frac{\mathrm{d}\, i_{V2}}{\mathrm{d}t} + M_2\frac{\mathrm{d}\, i_{W1}}{\mathrm{d}t} + M_3\frac{\mathrm{d}\, i_{W2}}{\mathrm{d}t} + e_U \tag{2.9}$$

$$\begin{aligned} v_{U1} = {} & R\left(\frac{i_{Um}}{2} + i_{Us}\right) + \frac{1}{2}\left(L\frac{\mathrm{d}\, i_{Um}}{\mathrm{d}t} + M_1\frac{\mathrm{d}\, i_{Um}}{\mathrm{d}t} + M_2\frac{\mathrm{d}\, i_{Vm}}{\mathrm{d}t} + M_3\frac{\mathrm{d}\, i_{Vm}}{\mathrm{d}t} + M_2\frac{\mathrm{d}\, i_{Wm}}{\mathrm{d}t} + M_3\frac{\mathrm{d}\, i_{Wm}}{\mathrm{d}t}\right) \\ & + \left(L\frac{\mathrm{d}\, i_{Us}}{\mathrm{d}t} - M_1\frac{\mathrm{d}\, i_{Us}}{\mathrm{d}t} + M_2\frac{\mathrm{d}\, i_{Vs}}{\mathrm{d}t} - M_3\frac{\mathrm{d}\, i_{Vs}}{\mathrm{d}t} + M_2\frac{\mathrm{d}\, i_{Ws}}{\mathrm{d}t} - M_3\frac{\mathrm{d}\, i_{Ws}}{\mathrm{d}t}\right) + e_U \end{aligned} \tag{2.10}$$

$$v_{U2} = R\left(\frac{i_{Um}}{2} + i_{Us}\right) + \frac{1}{2}\left(L\frac{\mathrm{d}\, i_{Um}}{\mathrm{d}t} + M_1\frac{\mathrm{d}\, i_{Um}}{\mathrm{d}t} + M_2\frac{\mathrm{d}\, i_{Vm}}{\mathrm{d}t} + M_3\frac{\mathrm{d}\, i_{Vm}}{\mathrm{d}t} + M_2\frac{\mathrm{d}\, i_{Wm}}{\mathrm{d}t} + M_3\frac{\mathrm{d}\, i_{Wm}}{\mathrm{d}t}\right) + \left(-L\frac{\mathrm{d}\, i_{Us}}{\mathrm{d}t} + M_1\frac{\mathrm{d}\, i_{Us}}{\mathrm{d}t} - M_2\frac{\mathrm{d}\, i_{Vs}}{\mathrm{d}t} - M_3\frac{\mathrm{d}\, i_{Vs}}{\mathrm{d}t} - M_2\frac{\mathrm{d}\, i_{Ws}}{\mathrm{d}t} + M_3\frac{\mathrm{d}\, i_{Ws}}{\mathrm{d}t}\right) + e_U \quad (2.11)$$

$$v_{U1} = R\left(\frac{i_{Um}}{2} + i_{Us}\right) + \frac{1}{2}\left(L + M_1 - M_2 - M_3\right)\frac{\mathrm{d}\, i_{Um}}{\mathrm{d}t} + \left(L - M_1 - M_2 + M_3\right)\frac{\mathrm{d}\, i_{Us}}{\mathrm{d}t} + e_U \quad (2.12)$$

$$v_{U2} = R\left(\frac{i_{Um}}{2} + i_{Us}\right) + \frac{1}{2}\left(L + M_1 - M_2 - M_3\right)\frac{\mathrm{d}\, i_{Um}}{\mathrm{d}t} - \left(L - M_1 - M_2 + M_3\right)\frac{\mathrm{d}\, i_{Us}}{\mathrm{d}t} + e_U \quad (2.13)$$

$$L_m = L + M_1 - M_2 - M_3 \qquad L_s = L - M_1 - M_2 + M_3 \quad (2.14)$$

The introduction of those two new inductances will allow to simplify the expressions of the voltages in the model of the BLM. The expressions of the voltages V_{Um} and V_{Us} can be obtained using equations 2.7 and 2.8 and the newly found inductances. The two resulting equations 2.15 and 2.16 will allow us the have a model of the BLM. Noting that the voltage at the suspension inverter v_{Us} does not depend on the emf of the BLM an observation that has already been made in [17]. This allow the suspension inverter's voltage to no being affected significantly by the speed of the BLM. The same procedure can be applied to each single phase of the BLM. Gathering the different equations together a new matrix system like in equation 2.3 can be created. The different part of the system are then shown in equations 2.18 and 4.5.To model the machine in Simulink, the equation to obtain an expression of the current were transformed. The obtained equation 2.20 is then implemented in a Simulink block a simple model of the BLM.

$$v_{Um} = R\left(\frac{i_{Um}}{2} + i_{Us}\right) + \frac{L_m}{2}\frac{\mathrm{d}\, i_{Um}}{\mathrm{d}t} + L_s\frac{\mathrm{d}\, i_{Us}}{\mathrm{d}t} + e_U \quad (2.15)$$

$$v_{Us} = 2R\, i_{Us} + 2L_s\frac{\mathrm{d}\, i_{Us}}{\mathrm{d}t} \quad (2.16)$$

$$[\mathbb{V}_{ms}] = [\mathbb{R}_{ms}]\cdot[\mathbb{I}_{ms}] + [\mathbb{L}_{ms}]\cdot\frac{\mathrm{d}}{\mathrm{d}t}[\mathbb{I}_{ms}] + [\mathbb{E}_{ms}] \quad (2.17)$$

$$[\mathbb{V}_{ms}] = \begin{bmatrix} v_{Um} \\ v_{Vm} \\ v_{Wm} \\ v_{Us} \\ v_{Vs} \\ v_{Ws} \end{bmatrix} \qquad [\mathbb{I}_{ms}] = \begin{bmatrix} i_{Um} \\ i_{Vm} \\ i_{Wm} \\ i_{Us} \\ i_{Vs} \\ i_{Ws} \end{bmatrix} \qquad [\mathbb{E}_{ms}] = \begin{bmatrix} e_U \\ e_V \\ e_W \\ 0 \\ 0 \\ 0 \end{bmatrix} \tag{2.18}$$

$$[\mathbb{R}_{ms}] = \begin{bmatrix} \frac{R}{2} & 0 & 0 & R & 0 & 0 \\ 0 & \frac{R}{2} & 0 & 0 & R & 0 \\ 0 & 0 & \frac{R}{2} & 0 & 0 & R \\ 0 & 0 & 0 & 2R & 0 & 0 \\ 0 & 0 & 0 & 0 & 2R & 0 \\ 0 & 0 & 0 & 0 & 0 & 2R \end{bmatrix} \qquad [\mathbb{L}_{ms}] = \begin{bmatrix} \frac{L_m}{2} & 0 & 0 & L_s & 0 & 0 \\ 0 & \frac{L_m}{2} & 0 & 0 & L_s & 0 \\ 0 & 0 & \frac{L_m}{2} & 0 & 0 & L_s \\ 0 & 0 & 0 & 2L_s & 0 & 0 \\ 0 & 0 & 0 & 0 & 2L_s & 0 \\ 0 & 0 & 0 & 0 & 0 & 2L_s \end{bmatrix} \tag{2.19}$$

$$[\mathbb{I}_{ms}] = \int [\mathbb{L}_{ms}]^{-1} \cdot [\mathbb{V}_{ms}] - [\mathbb{L}_{ms}]^{-1} \cdot [R_{ms}] \cdot [\mathbb{I}_{ms}] - [\mathbb{L}_{ms}]^{-1} \cdot [\mathbb{E}_{ms}] \mathrm{d}t \tag{2.20}$$

2.3 Torque equation

The performance evaluation and modeling of an electrical machine passes by the evaluation of its torque output. To do so Virtual works will be used. Based on equation 2.15 and considering that the current $i_{Us} = 0$ a simplified expression for v_{Um} was obtained. Then it was also changed so that it is expressed entirely in fluxes.

$$v_{Um} = R\frac{i_{Um}}{2} + \frac{L_m}{2}\frac{\mathrm{d}\, i_{Um}}{\mathrm{d}t} + e_U \tag{2.21}$$

$$v_{Um} = R\frac{i_{Um}}{2} + \frac{\mathrm{d}\, \phi_{L_{Um}}}{\mathrm{d}t} + \frac{\mathrm{d}\, \phi_{mag_{Um}}}{\mathrm{d}t} \tag{2.22}$$

Form this expression the power contained in one winding of the phase U was obtained.

$$P_{U1} = v_{Um}\frac{i_{Um}}{2} = R\frac{i_{Um}^2}{4} + \frac{i_{Um}}{2}\frac{\mathrm{d}\, \phi_{L_{Um}}}{\mathrm{d}t} + \frac{i_{Um}}{2}\frac{\mathrm{d}\, \phi_{mag_{Um}}}{\mathrm{d}t} \tag{2.23}$$

From there the variation energy $\mathrm{d}W_{U1}$ in one winding, knowing the $W = P\mathrm{d}t$, was obtained.

$$\mathrm{d}W_{U1} = P_{U1}\mathrm{d}t = R\frac{i_{Um}^2}{4}\mathrm{d}t + \frac{i_{Um}}{2}\mathrm{d}\, \phi_{L_{Um}} + \frac{i_{Um}}{2}\mathrm{d}\, \phi_{mag_{Um}} \tag{2.24}$$

the energy provided by $R\frac{i_{Um}^2}{4}$ will be converted into heat that won't be of any use to the process of torque generation. However, the ones provided by the fluxes will be able to be converted into mechanical energy and create torque. Then he equation 2.24 was simplified by taking away the part that won't provide any mechanical energy W_{meca}. Where W_Φ is the stored energy in the system.

$$\mathrm{d}W_{elec} = \mathrm{d}W_{meca} + \mathrm{d}W_\Phi \tag{2.25}$$

$$\mathrm{d}W_{elec} = i\,(\mathrm{d}\ \phi_L + \mathrm{d}\ \phi_{mag}) \tag{2.26}$$

The magnetic force resulting of this is given by $\mathrm{d}W_{meca} = F_\Phi \mathrm{dx}$. Which gives us:

$$\mathrm{d}W_\Phi = i\,(\mathrm{d}\ \phi_L + \mathrm{d}\ \phi_{mag_{Um}}) - \mathrm{d}W_{meca} \tag{2.27}$$

$$\mathrm{d}W_\Phi = i\,(\mathrm{d}\ \phi_L + \mathrm{d}\ \phi_{mag}) - F_\Phi \mathrm{dx} \tag{2.28}$$

$$\mathrm{d}W_\Phi = \frac{i}{2}\Psi - F_\Phi \mathrm{dx} \tag{2.29}$$

The co-energy W'_Φ can be calculated having it defined as:

$$W'_{\Phi_{Um}} = i\Psi - W_\Phi \tag{2.30}$$

Considering the differential of the expression 2.30 and taking in account that $\mathrm{d}(i\Psi) = i\mathrm{d}\Psi + \Psi \mathrm{d}i$ the following equation can be obtained:

$$\mathrm{d}W'_\Phi = \mathrm{d}\,(i\Psi) - \mathrm{d}W_\Phi \tag{2.31}$$

$$\mathrm{d}W'_\Phi = \Psi \mathrm{d}i + F_\Phi \mathrm{dx} \tag{2.32}$$

$$\tag{2.33}$$

Considering that the co-energy can be written has being function of two independent variables: the current i and the position x. $\mathrm{d}W'_\Phi$ was therefore expressed in this way:

$$\mathrm{d}W'_\Phi(i,x) = \frac{\partial W'_\Phi(i,x)}{\partial i}\mathrm{d}i + \frac{\partial W'_\Phi(i,x)}{\partial x}\mathrm{d}x \tag{2.34}$$

This implies that:

$$\frac{\partial W'_{\Phi}(i,x)}{\partial i} = \Psi \tag{2.35}$$

$$\frac{\partial W'_{\Phi}(i,x)}{\partial x} = F_{\Phi} \tag{2.36}$$

From the force F_{Φ} the torque T_{Φ} can be obtained. Which is given by the derivation of the co-energy with the angular position θ.

$$T_{\Phi} = \frac{\partial W'_{\Phi}(i,x)}{\partial \theta} \tag{2.37}$$

If considering in a first instance that the position x is considered constant at x_0, the co-energy can then be expressed by :

$$W'_{\Phi}(i,x_0) = \int_o^i \Psi \mathrm{d}i \tag{2.38}$$

From this the co-energy of our BLM system can be expressed by:

$$W = \frac{1}{2}[\mathbb{I}]^t[\mathbb{L}][\mathbb{I}] + [\mathbb{I}]^t[\Phi_{mag}] \tag{2.39}$$

With all the matrices being defined in equation 2.3 and 2.4. To obtain the torque the derivative of this expression in respect to the position θ of the BLM needs to be taken, like shown in equation 2.37. At first the contribution of the PM, W_{mag}, to the co-energy will be concentrated on.

$$W_{mag} = [\mathbb{I}]^t[\Phi_{mag}] \tag{2.40}$$

$$T_{mag} = \frac{\partial\ [\mathbb{I}]^t \cdot [\Phi_{mag}]}{\partial \theta} \tag{2.41}$$

For the case of a BLM with z coils per phase the expression of the torque can be expressed as follows.

$$T_{mag} = \frac{\partial}{\partial \theta} \begin{bmatrix} i_{U1} \\ \vdots \\ i_{Uz} \\ i_{V1} \\ \vdots \\ i_{Vz} \\ i_{W1} \\ \vdots \\ i_{Wz} \end{bmatrix}^t \cdot \begin{bmatrix} \phi_{mag\ U1}(\theta) \\ \vdots \\ \phi_{mag\ Uz}(\theta) \\ \phi_{mag\ Vz}(\theta) \\ \vdots \\ \phi_{mag\ V1}(\theta) \\ \phi_{mag\ W1}(\theta) \\ \vdots \\ \phi_{mag\ Wz}(\theta) \end{bmatrix} \tag{2.42}$$

It would be first, interesting to try to find an expression for $[\mathbb{I}]^t \cdot [\Phi_{mag}]$. From then the reference frame could be changed, from an *abc* frame to a $dq0$ one, using a Park transform $[P]_\alpha$ shown in equation 2.43. Where α is the reference angle of the Park transformation.

$$[\mathbb{I}_{UVW}] = [P^{-1}]_\alpha \times [\mathbb{I}_{dq0}]_\alpha = \begin{bmatrix} \cos(\alpha) & -\sin(\alpha) & 1 \\ \cos(\alpha - \frac{2\pi}{3}) & -\sin(\alpha - \frac{2\pi}{3}) & 1 \\ \cos(\alpha + \frac{2\pi}{3}) & -\sin(\alpha + \frac{2\pi}{3}) & 1 \end{bmatrix} \times [\mathbb{I}_{dq0}]_\alpha \tag{2.43}$$

Therefore, based on equation 2.42 a new expression for the torque can be extracted. However, considering that all z coil of each phase have the same current the results will be simplified even further. Moreover, considering that none of the fluxes or currents have values in the 0 axis. Meaning that $i_U + i_V + i_W = 0$ and $\phi_{mag\ U} + \phi_{mag\ V} + \phi_{mag\ W} = 0$.

$$T_{mag} = z[\mathbb{I}_{UVW}]^t \cdot \frac{\partial}{\partial \theta} \cdot [\phi_{mag}(\theta)_{UVW}] \tag{2.44}$$

$$T_{mag} = z \cdot \cdot [P^{-1}]_{\omega t} \cdot [\mathbb{I}_{dq0}]^t_{\omega t} \cdot \frac{\partial}{\partial \theta} [P^{-1}]_\theta \cdot [\phi_{mag}(\theta)_{dq0}]_\theta \tag{2.45}$$

$$T_{mag} = z \cdot \frac{3}{2} \cdot p \cdot \left[i_q \times \phi_{mag\ d} - \cdot i_d \times \phi_{mag\ q} \right] \tag{2.46}$$

Considering that the flux ϕ_{mag} generated by the magnet is only present in the d axis.

$$T_{mag} = z \cdot \frac{3}{2} \cdot p \cdot \left[i_q \times \phi_{mag\ d} \right] \tag{2.47}$$

Now an expression for the torque produced by the interaction between rotating field, created the currents in the stator ,and the field of the magnets, was obtained.

Nevertheless, an investigation on the the potential torque created by the inductance of the BLM needs to be conducted. First going back to the co-energy and express W_{ind} created by the inductances.

$$W_{ind} = \frac{1}{2}[\mathbb{I}]^t[\mathbb{L}][\mathbb{I}] \tag{2.48}$$

Following again the same process than for the energy produced by the magnets. Getting an expression for the torque T_ind create by the inductances.Considering that the currents do not depend on the position θ the definition of the torque T_ind can be simplified.

$$T_{ind} = \frac{1}{2}\frac{\partial\ [\mathbb{I}]^t[\mathbb{L}][\mathbb{I}]}{\partial\theta} \tag{2.49}$$

$$T_{ind} = \frac{1}{2}[\mathbb{I}]^t\frac{\partial\ [\mathbb{L}]}{\partial\theta}[\mathbb{I}] \tag{2.50}$$

As for all the machine considered for the study are smooth, their inductance isn't changing with the angular position θ of the rotor. Therefore T_{ind} was simplified knowing that $\frac{\partial\ [\mathbb{L}]}{\partial\theta} = 0$. So that:

$$T_{ind} = 0 \tag{2.51}$$

2.4 Force equation

The most Important part of the modeling of a BLM is to have expression linking the current and the forces applied on the rotor. To calculate the forces created the virtual energy equations was used. As show in equation 2.52 the forces in a direction ε is equal to the derivative of the energy in that same direction.

$$F_\varepsilon = \frac{\partial\ W}{\partial\varepsilon} \tag{2.52}$$

$$W = \frac{1}{2}[\mathbb{I}]^t[\mathbb{L}][\mathbb{I}] + [\mathbb{I}]^t[\Phi_{mag}] \tag{2.53}$$

In order to solve this it will require to find an expression of the air gap of the BLM function of the displacement in the direction x and y. Then the force will be separated into two parts. One dedicated to the forces created by the suspension currents, and the other concentrating on the forces created by the displacement of the rotor.

2.4.1 Effect of the displacement of the rotor on the air gap.

In order to get the derivative of the fluxes depending on the position of the rotor, there is a need to define the expression of the air gap depending on the position of the rotor. So for

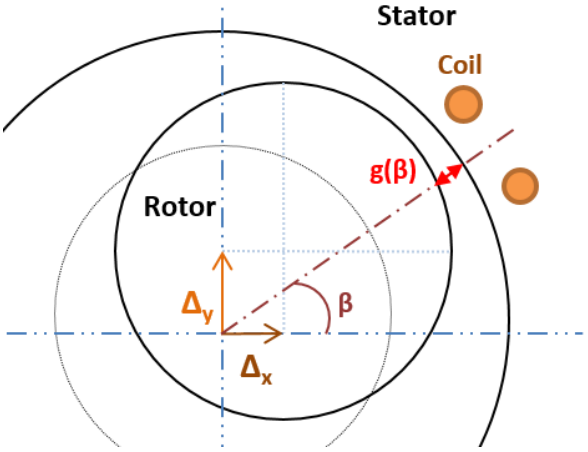


Fig. 2.2 Air gap depending on the a displacement Δ_x and Δ_y

a displacement Δ_x and Δ_y the expression of the air gap of the BLM $g(\beta)$ for each specific angle β [20] can be found. The equation 2.54 will then help us to define the expressions of the inductances and fluxes of the BLM depending on the position of the rotor.

$$g(\beta) = g_0 - \Delta_x \cdot \cos(\beta) - \Delta_y \cdot \sin(\beta) \tag{2.54}$$

2.4.2 Fluxes and Inductances depending on the displacement.

Now knowing the value of the air gap depending on of the displacement of the rotor an expression for the inductances and fluxes depending on of the position of the rotor can be found.

2.4.2.a Inductances depending on the displacement.

The inductance is defined to be inversely proportional to the size of the air-gap. so that:

$$L_0 = \frac{\lambda}{g_0} \tag{2.55}$$

Where λ_L is defined as a constant representing part of the inductance value that does not vary with the size of the air-gap. However this value can still/also be represented as a function

depending on the position θ of the rotor. From there the inductance is expressed by this:

$$L(\Delta_x, \Delta_y, \beta) = \frac{\lambda_L}{g(\beta)} \tag{2.56}$$

$$L(\Delta_x, \Delta_y, \beta) = \frac{\lambda_L}{g_0 - \Delta_x \cdot \cos(\beta) - \Delta_y \cdot \sin(\beta)} \tag{2.57}$$

$$L(\Delta_x, \Delta_y, \beta) = \frac{\lambda_L}{g_0}\left(1 + \frac{\Delta_x \cdot \cos(\beta) + \Delta_y \cdot \sin(\beta)}{g_0}\right) \tag{2.58}$$

$$L(\Delta_x, \Delta_y, \beta) = L_0\left(1 + \frac{\Delta_x \cdot \cos(\beta) + \Delta_y \cdot \sin(\beta)}{g_0}\right) \tag{2.59}$$

The same principle can be applied to the mutual inductances

$$M_{i\ j}(\Delta_x, \Delta_y, \beta_i, \beta_j) = \frac{\lambda_{M_{i\ j}}}{2g_0 - \Delta_x \cdot \big(\cos(\beta_i) + \cos(\beta_j)\big) + \Delta_y \cdot \big(\sin(\beta_i) + \sin(\beta_j)\big)\big)} \tag{2.60}$$

$$M_{i\ j}(\Delta_x, \Delta_y, \beta_i, \beta_j) = \frac{\lambda_{M_{i\ j}}}{2g_0}\left(1 + \frac{\Delta_x \cdot \big(\cos(\beta_i) + \cos(\beta_j)\big) + \Delta_y \cdot \big(\sin(\beta_i) + \sin(\beta_j)\big)}{2g_0}\right) \tag{2.61}$$

$$M_{i\ j}(\Delta_x, \Delta_y, \beta_i, \beta_j) = M_{i\ j\ 0}\left(1 + \frac{\Delta_x \cdot \big(\cos(\beta_i) + \cos(\beta_j)\big) + \Delta_y \cdot \big(\sin(\beta_i) + \sin(\beta_j)\big)}{2g_0}\right) \tag{2.62}$$

2.4.2.b Flux created by the magnets depending on the displacement.

Using the same principle than used in the previous paragraph the flux due to the magnets field is calculated.This flux created on the coils of phase M is then named $\phi_{mag\ M\ 0}(\theta)$, for a rotor that is considered centered. The value $\psi_{mag\ M}(\theta)$ represents the product $B_r(\theta) \cdot S$, where $B_r(\theta)$ is the magnetic field flux visible at the phase M at a given position θ and S the surface of the tooth in phase M. The flux $\phi_{mag\ M}(\theta, \Delta_x, \Delta_y \beta)$ is then calculated integrating the equation 2.54 into equation 2.63. In the equation 2.64 considering that the expression $\Delta_x \cdot \cos(\beta) + \Delta_y \cdot \sin(\beta)$ is going to very small compared to $l_{mag} + \mu_r g_0$, the expression has been developed into a Taylor series 2.65.This will help simplify the definition of the flux,

which reveals that the flux's expression incorporates equation 2.63.

$$\phi_{mag\ M\ 0}(\theta) = \frac{l_{mag}\psi_{mag\ M}(\theta)}{l_{mag} + \mu_r g_0} \tag{2.63}$$

$$\begin{aligned}\phi_{mag\ Mj}(\theta, \Delta_x, \Delta_y, \beta) &= \frac{l_{mag}\psi_{mag\ M}(\theta)}{l_{mag} + \mu_r\left(g_0 - \Delta_x \cdot \cos(\beta) - \Delta_y \cdot \sin(\beta)\right)} \\ &= \frac{l_{mag}\psi_{mag\ M}(\theta)}{(l_{mag} + \mu_r g_0) - \mu_r\left(\Delta_x \cdot \cos(\beta) + \Delta_y \cdot \sin(\beta)\right)}\end{aligned} \tag{2.64}$$

$$\phi_{mag\ Mj}(\theta, \Delta_x, \Delta_y, \beta) = \frac{l_{mag}\psi_{mag\ M}(\theta)}{(l_{mag} + \mu_r g_0)}\left(1 + \mu_r \frac{\Delta_x \cdot \cos(\beta) + \Delta_y \cdot \sin(\beta)}{(l_{mag} + \mu_r g_0)}\right) \tag{2.65}$$

$$\phi_{mag\ Mj}(\theta, \Delta_x, \Delta_y, \beta) = \phi_{mag\ Mj\ 0}(\theta)\left(1 + \mu_r \frac{\Delta_x \cdot \cos(\beta) + \Delta_y \cdot \sin(\beta)}{(l_{mag} + \mu_r g_0)}\right) \tag{2.66}$$

Getting in equation 2.66 an expression for the flux of the magnet $\phi_{mag\ Mj}(\theta, \Delta_x, \Delta_y\beta)$ that depends directly on the flux of the magnets, with the assumption that rotor is perfectly centered.

2.4.3 Forces due to the magnet flux and current interaction.

Based on the equation (2.53) selecting the energy W_{mag} created by the interaction between the currents in the coils and the flux of the magnets. To obtain the force created by this interaction, the derivative of the energy W_{mag} in the direction ε of the force needs to be taken. For a BLM with a z number of coil per phase the developed equation (2.68) is shown in equation (2.69). In order to get the force in the direction ε the expression of the flux derivative in that same direction was found. Applied on the directions x and y obtaining the equations (2.71) and (2.72). As already expressed in equations (2.5) and (2.6) the currents in the coils are composed of two separate components. Using those two currents a general expression of the force created by each phase M can be created. Considering the BLM machine modeled, half of the coils have to be supplied with a suspension currents of the opposite sign that the other half, leading to the choice in the equation (2.73) to consider that each second coil have a current $i_M s$ with an opposite sign. The general equation is then applied to the two directions x and y. In the model of BLM each coil of a same phase sees the same magnet flux, and due to configuration of the coils, the sum of all the $\cos(\beta j)$ and $\sin(\beta j)$ is equal to 0 as shown in Fig. 2.3a. If looking at the other sum in Fig. 2.3b it can be noted that it introduces a new angle γ_M for the resulting direction of the force created by phase M.

$$W_{mag} = [\mathbb{I}]^t[\Phi_{mag}] \tag{2.67}$$

$$F_{\varepsilon\ mag} = [\mathbb{I}]^t \cdot \frac{\partial\ [\Phi_{mag}]}{\partial \varepsilon} \tag{2.68}$$

$$F_{\varepsilon\ mag} = \begin{bmatrix} i_{U1} \\ \vdots \\ i_{Uz} \\ i_{V1} \\ \vdots \\ i_{Vz} \\ i_{W1} \\ \vdots \\ i_{Wz} \end{bmatrix}^t \cdot \frac{\partial}{\partial \varepsilon} \begin{bmatrix} \phi_{mag\ U1}(\theta, \Delta_x, \Delta_y, \beta_{U1}) \\ \vdots \\ \phi_{mag\ Uz}(\theta, \Delta_x, \Delta_y, \beta_{Uz}) \\ \phi_{mag\ Vz}(\theta, \Delta_x, \Delta_y, \beta_{V1}) \\ \vdots \\ \phi_{mag\ V1}(\theta, \Delta_x, \Delta_y, \beta_{Vz}) \\ \phi_{mag\ W1}(\theta, \Delta_x, \Delta_y, \beta_{W1}) \\ \vdots \\ \phi_{mag\ Wz}(\theta, \Delta_x, \Delta_y, \beta_{Wz}) \end{bmatrix} \tag{2.69}$$

$$\frac{\partial\ \phi_{mag\ Mj}(\theta, \Delta_x, \Delta_y, \beta)}{\partial \varepsilon} = \frac{\mu_r \phi_{mag\ Mj\ 0}(\theta)}{(l_{mag} + \mu_r g_0)} \cdot \frac{\partial\ (\Delta_x \cdot \cos(\beta) + \Delta_y \cdot \sin(\beta))}{\partial \varepsilon} \tag{2.70}$$

$$\frac{\partial\ \phi_{mag\ Mj}(\theta, \Delta_x, \Delta_y, \beta)}{\partial x} = \cos(\beta) \cdot \frac{\mu_r \phi_{mag\ Mj\ 0}(\theta)}{(l_{mag} + \mu_r g_0)} \tag{2.71}$$

$$\frac{\partial\ \phi_{mag\ Mj}(\theta, \Delta_x, \Delta_y, \beta)}{\partial y} = \sin(\beta) \cdot \frac{\mu_r \phi_{mag\ Mj\ 0}(\theta)}{(l_{mag} + \mu_r g_0)} \tag{2.72}$$

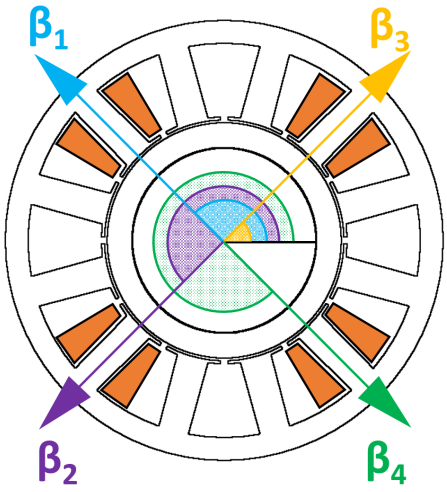
$$F_{\varepsilon\ mag\ M} = i_{Mm} \sum_{j=1}^{z} \frac{\partial\ \phi_{mag\ Mj}(\theta, \Delta_x, \Delta_y, \beta_j)}{\partial \varepsilon} + i_{Ms} \sum_{j=1}^{z} -1^{(j+1)} \frac{\partial\ \phi_{mag\ Mj}(\theta, \Delta_x, \Delta_y, \beta_j)}{\partial \varepsilon} \tag{2.73}$$

$$F_{x\ mag\ Mj} = \frac{\mu_r \phi_{mag\ Mj\ 0}(\theta)}{(l_{mag} + \mu_r g_0)} \left[i_{Mm} \sum_{j=1}^{z} \cos(\beta_j) + i_{Ms} \sum_{j=1}^{z} -1^{(j+1)} \cos(\beta_j) \right] \tag{2.74}$$

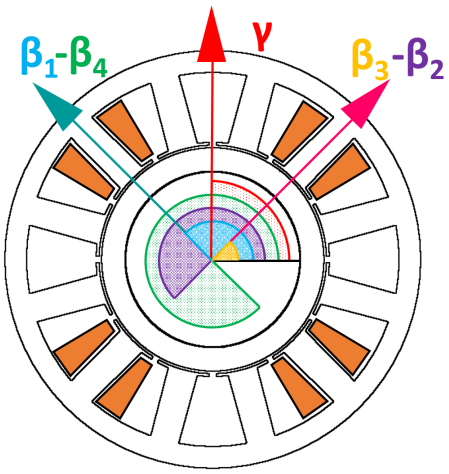
$$F_{y\ mag\ M} = \frac{\mu_r \phi_{mag\ Mj\ 0}(\theta)}{(l_{mag} + \mu_r g_0)} \left[i_{Mm} \sum_{j=1}^{z} \sin(\beta_j) + i_{Ms} \sum_{j=1}^{z} -1^{(j+1)} \sin(\beta_j) \right] \tag{2.75}$$

$$F_{x\ mag\ M} = z \cdot \frac{\mu_r \phi_{mag\ Mj\ 0}(\theta)}{(l_{mag} + \mu_r g_0)} \cdot \cos(\gamma_M)\, i_{Ms} \tag{2.76}$$

$$F_{y\ mag\ M} = z \cdot \frac{\mu_r \phi_{mag\ Mj\ 0}(\theta)}{(l_{mag} + \mu_r g_0)} \cdot \sin(\gamma_M)\, i_{Ms} \tag{2.77}$$



(a) Direction of the forces created by i_{Mm}



(b) Direction of the forces created by i_{Ms} and resulting force with a direction angle γ_M

$$\begin{bmatrix} F_x \\ F_y \end{bmatrix} = z \cdot \frac{\mu_r \cos(\frac{\pi}{p})}{(l_{mag} + \mu_r g_0)} \cdot \begin{bmatrix} \cos(\gamma) & \cos(\gamma - \frac{2\pi}{3}) & \cos(\gamma + \frac{2\pi}{3}) \\ \sin(\gamma) & \sin(\gamma - \frac{2\pi}{3}) & \sin(\gamma + \frac{2\pi}{3}) \end{bmatrix} \begin{bmatrix} \phi_{mag\ U\,j\,0}(\theta) & 0 & 0 \\ 0 & \phi_{mag\ V\,j\,0}(\theta) & 0 \\ 0 & 0 & \phi_{mag\ W\,j\,0}(\theta) \end{bmatrix} \begin{bmatrix} i_{Us} \\ i_{Vs} \\ i_{Ws} \end{bmatrix} \quad (2.78)$$

The position of the different coils of each phases is set so that each phase is shifted by $\frac{2\pi}{3}$ as shown in Fig. 2.4. This will allow us to get a force in any direction using a combination of the forces generated by each phase. With the coils set the force created by the interaction of the magnets and the suspension current can be written in a matrix form. The fluxes created by magnets in equation (2.78) will be decomposed in Fourier series in order to have manageable definition of the forces. The decomposition is presented in equation (2.79).

The next step consist to pass the currents into a *dqo* frame by using Park transform. This will allow us to get an expression of the forces cre-

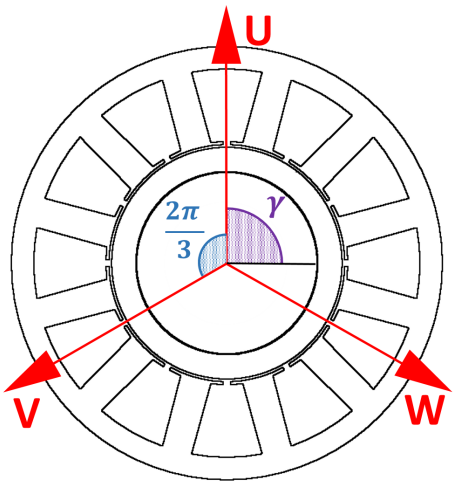


Fig. 2.4 Direction of the forces for each phase of the BLM

ated by the current which will not depend on the
position of the rotor. As a reminder the expression of the Park transform in equation set at reference angle α is given. Before jumping into the step of taking the angle α being equal to $p\theta$ as it is generally done in the electrical machine control, the possibility that this choice will not lead to undesirable results needs to be investigated.

2.4.3.a Choice of the angle of the Park transformation.

As mention previously the choice of the angle in the Park transform is not usually a major concern. However this study will show the importance of a proper selection of this angle. To do so the different possible result cases of the product of the fluxes and the currents will be considered as shown on the equations (2.81). The two angles ζ_M and η_M are respectively the phase angle of the magnets fluxes and the phase angle of the current in the coils. For the sake of simplicity here it was considered that the flux created by the magnets are defined a direct tri-phase signal as shown in equation (2.82).

$$\phi_{mag\ Mj\ 0}(\theta) = \sum_{j=1}^{\infty} \Psi_{A\ j}\cos(j\cdot p\theta + \nu_{A\ j}) + \Psi_{B\ j}\sin(j\cdot p\theta + \nu_{B\ j}) \tag{2.79}$$

$$[\mathbb{I}_{UVW}] = [P^{-1}]_\alpha \times [\mathbb{I}_{dq0}]_\alpha = \begin{bmatrix} \cos(\alpha) & -\sin(\alpha) & 1 \\ \cos(\alpha-\frac{2\pi}{3}) & -\sin(\alpha-\frac{2\pi}{3}) & 1 \\ \cos(\alpha+\frac{2\pi}{3}) & -\sin(\alpha+\frac{2\pi}{3}) & 1 \end{bmatrix} \times [\mathbb{I}_{dq0}]_\alpha \tag{2.80}$$

$$\begin{cases} 1. & \cos(p\theta+\zeta_M)\cos(p\theta+\eta_M) = \frac{1}{2}\left[\cos(\zeta_M-\eta_M)+\cos(2p\theta+\zeta_M+\eta_M)\right] \\ 2. & \cos(p\theta+\zeta_M)\sin(p\theta+\eta_M) = \frac{1}{2}\left[-\sin(\zeta_M-\eta_M)+\sin(2p\theta+\zeta_M+\eta_M)\right] \\ 3. & \sin(p\theta+\zeta_M)\cos(p\theta+\eta_M) = \frac{1}{2}\left[\sin(\zeta_M-\eta_M)+\sin(2p\theta+\zeta_M+\eta_M)\right] \\ 4. & \sin(p\theta+\zeta_M)\sin(p\theta+\eta_M) = \frac{1}{2}\left[\cos(\zeta_M-\eta_M)-\cos(2p\theta+\zeta_M+\eta_M)\right] \end{cases} \tag{2.81}$$

$$\zeta_U = 0 \qquad \zeta_V = -\frac{2\pi}{3} \qquad \zeta_W = \frac{2\pi}{3} \tag{2.82}$$

Instead of demonstrating the results for each cases the study will only concentrate on the first case (1.) from equation (2.81). Applying it to the equation (2.78). However, to simplify the result the amplitude of the signals was not considered since the main interest is the shape of the force at this point. Therefore, calculating fx representing the shape of the force created in the case (1.) in the x direction and its expression is defined in equation (2.83).

$$\begin{aligned} fx = \cos(\gamma)\,(\cos(-\eta_U) + \cos(2p\theta + \eta_U)) \\ + \cos(\gamma - \frac{2\pi}{3})(\cos(-\frac{2\pi}{3} - \eta_V) + \cos(2p\theta - \frac{2\pi}{3} + \eta_V)) \\ + \cos(\gamma + \frac{2\pi}{3})(\cos(\frac{2\pi}{3} - \eta_W) + \cos(2p\theta + \frac{2\pi}{3} + \eta_W))) \end{aligned} \quad (2.83)$$

Considering two different case for the choice of the angle α of the Park transform

1. Considering that currents are tri-phase direct $\zeta_M = \eta_M$ and setting $\alpha = p\theta$. This leads to equation (2.84). The development of the equation leads to an interesting result, as can note that resulting current depends on the position θ of the electrical machine. The same is also true for each of cases and directions. This means that if defining the currents into a $dq0$ reference the standard selection $\alpha = p\theta$ is not in any way advantageous as the main purpose to change the reference frame is to obtain "constant" values to simplify the control.

$$\begin{aligned} fx = \cos(\gamma)\,(\cos(0) + \cos(2p\theta)) \\ + \cos(\gamma - \frac{2\pi}{3})(\cos(0) + \cos(2p\theta + \frac{2\pi}{3})) \\ + \cos(\gamma + \frac{2\pi}{3})(\cos(0) + \cos(2p\theta - \frac{2\pi}{3}))) \end{aligned} \quad (2.84)$$

$$fx = \cos(\gamma)\cos(2p\theta) + \cos(\gamma - \frac{2\pi}{3})\cos(2p\theta + \frac{2\pi}{3}) + \cos(\gamma + \frac{2\pi}{3})\cos(2p\theta - \frac{2\pi}{3})) \quad (2.85)$$

$$fx = \frac{3}{2}\cos(2p\theta + \gamma) \quad (2.86)$$

2. But if taking another approach and use $\zeta_M = -\eta_M$ with $\alpha = -p\theta$. This leads to equation (2.87) which looks very similar to what was obtained previously in equation (2.84). However, the result given in equation (2.88) is drastically different, as it can observe that the result does not depend on the position θ of the rotor. This is also true for each case and direction. Which means that a simple control of the suspension current can

be obtained if considering $\alpha = -p\theta$, as the reference currents will be "constant".

$$\begin{aligned} fx = \cos(\gamma)\,(\cos(0)+\cos(2p\theta)) \\ +\cos(\gamma-\frac{2\pi}{3})(\cos(\frac{2\pi}{3})+\cos(2p\theta)) \\ +\cos(\gamma+\frac{2\pi}{3})(\cos(-\frac{2\pi}{3})+\cos(2p\theta))) \end{aligned} \quad (2.87)$$

$$fx = \cos(\gamma) - \frac{1}{2}\cos(\gamma-\frac{2\pi}{3}) - \frac{1}{2}\cos(\gamma+\frac{2\pi}{3}) \quad (2.88)$$

2.4.3.b Definition of the force equation in the dq0 axis reference.

Now that having selected the Park matrix that is the most appropriate to use the force depending on the suspension current in a $dq0$ reference can be found. Using the equation (2.78) and the results of 2.4.3.a an expression of the suspension forces depending on the $dq0$ value of the suspension current in equation 2.89 was extracted. The following is then developed into equation 2.90. Even with having selected a $-p\theta$ angle for the Park transform it was observed, that the force still depends on the position θ. This is explained by the fact the previous study concentrate on the fundamental frequency of the signals. In this case the fundamental is completely independent of the position. Since the fundamental is going to be the main actor in the creation of the force having it being independent of the position is definitely an advantage. Furthermore, considering the creation of the suspension currents with an inverter there is wish to not have any DC components in the currents. This implies that $i_{0s} = 0$. This will allow to simplify the equation of the force and also ease the inversion of the matrix when searching for the current that has to be supplied in order to obtain a specific force. Once having the equation (2.92) an expression of the currents needed to supply a desired force will be obtained.

$$\begin{bmatrix} F_x \\ F_y \end{bmatrix} = \frac{z\cdot\mu_r\cos(\frac{\pi}{p})}{(l_{mag}+\mu_r g_0)} \begin{bmatrix} \cos(\gamma) & \cos\left(\gamma-\frac{2\pi}{3}\right) & \cos\left(\gamma+\frac{2\pi}{3}\right) \\ \sin(\gamma) & \sin\left(\gamma-\frac{2\pi}{3}\right) & \sin\left(\gamma+\frac{2\pi}{3}\right) \end{bmatrix} [\Phi_{mag}][P^{-1}]_{-p\theta} \begin{bmatrix} i_{ds} \\ i_{qs} \\ i_{0s} \end{bmatrix} \quad (2.89)$$

$$\begin{bmatrix} F_x \\ F_y \end{bmatrix} = \frac{3}{4}\frac{z\cdot\mu_r\cos(\frac{\pi}{p})}{(l_{mag}+\mu_r g_0)} \begin{bmatrix} d\Phi_{a\ mag} & d\Phi_{b\ mag} & d\Phi_{c\ mag} \\ d\Phi_{d\ mag} & d\Phi_{e\ mag} & d\Phi_{f\ mag} \end{bmatrix} \begin{bmatrix} i_{ds} \\ i_{qs} \\ i_{0s} \end{bmatrix} \quad (2.90)$$

$$d\Phi_{a\ j} = \sum_{j=1}^{\infty} \Psi_{A\ j}\cos((j-1)p\theta + \nu_{A\ j} + \gamma) + \Psi_{B\ j}\sin((j-1)p\theta + \nu_{B\ j} + \gamma) \tag{2.91a}$$

$$d\Phi_{b\ j} = \sum_{j=1}^{\infty} -\Psi_{A\ j}\sin((j-1)p\theta + \nu_{A\ j} + \gamma) + \Psi_{B\ j}\cos((j-1)p\theta + \nu_{B\ j} + \gamma) \tag{2.91b}$$

$$d\Phi_{c\ j} = 2\cdot \sum_{j=1}^{\infty} \Psi_{A\ j}\cos(jp\theta + \nu_{A\ j} - \gamma) + \Psi_{B\ j}\sin(jp\theta + \nu_{B\ j} - \gamma) \tag{2.91c}$$

$$d\Phi_{d\ j} = \sum_{j=1}^{\infty} \Psi_{A\ j}\sin((j-1)p\theta + \nu_{A\ j} + \gamma) - \Psi_{B\ j}\cos((j-1)p\theta + \nu_{B\ j} + \gamma) \tag{2.91d}$$

$$d\Phi_{e\ j} = \sum_{j=1}^{\infty} \Psi_{A\ j}\cos((j-1)p\theta + \nu_{A\ j} + \gamma) + \Psi_{B\ j}\sin((j-1)p\theta + \nu_{B\ j} + \gamma) \tag{2.91e}$$

$$d\Phi_{f\ j} = 2\cdot \sum_{j=1}^{\infty} \Psi_{A\ j}\cos(jp\theta + \nu_{A\ j} - \gamma) + \Psi_{B\ j}\sin(jp\theta + \nu_{B\ j} - \gamma) \tag{2.91f}$$

$$\begin{bmatrix} F_x \\ F_y \end{bmatrix} = \frac{3}{4}\frac{z\cdot\mu_r\cos(\frac{\pi}{p})}{(l_{mag}+\mu_r g_0)} \begin{bmatrix} d\Phi_{a\ mag} & d\Phi_{b\ mag} \\ d\Phi_{d\ mag} & d\Phi_{e\ mag} \end{bmatrix} \begin{bmatrix} i_{ds} \\ i_{qs} \end{bmatrix} \tag{2.92}$$

2.4.3.c Definition of currents for a specified force.

With the equation (2.92) of the section 2.4.3.b getting an expression of the current for a specific force is made possible. In order to accomplish this the matrix composed of the different $d\Phi_{a\ mag}$, $d\Phi_{b\ mag}$, etc. was inverted as shown in the equation (2.93). Therefore, the expression of the inverse of this matrix needs to be found.

$$\begin{bmatrix} i_{ds} \\ i_{qs} \end{bmatrix} = \frac{4}{3}\frac{(l_{mag}+\mu_r g_0)}{z\cdot\mu_r\cos(\frac{\pi}{p})} \begin{bmatrix} d\Phi_{a\ mag} & d\Phi_{b\ mag} \\ d\Phi_{d\ mag} & d\Phi_{e\ mag} \end{bmatrix}^{-1} \begin{bmatrix} F_x \\ F_y \end{bmatrix} \tag{2.93}$$

$$\begin{bmatrix} d\Phi_{a\ mag} & d\Phi_{e\ mag} \\ d\Phi_{d\ mag} & d\Phi_{e\ mag} \end{bmatrix}^{-1} = \frac{\begin{bmatrix} d\Phi_{d\ mag} & -d\Phi_{b\ mag} \\ -d\Phi_{d\ mag} & d\Phi_{a\ mag} \end{bmatrix}}{d\Phi_{a\ mag}d\Phi_{e\ mag} - d\Phi_{b\ mag}d\Phi_{d\ mag}} \tag{2.94}$$

$$= \frac{\begin{bmatrix} d\Phi_{d\ mag} & -d\Phi_{b\ mag} \\ -d\Phi_{d\ mag} & d\Phi_{a\ mag} \end{bmatrix}}{\sum_{j=1}^{\infty} \Psi_{A\ j}^2 + \Psi_{B\ j}^2 - 2\Psi_{A\ j}\Psi_{B\ j}\sin(\nu_{A\ j} - \nu_{B\ j})} \tag{2.95}$$

$$\begin{bmatrix} i_{ds} \\ i_{qs} \end{bmatrix} = \frac{4\,(l_{mag}+\mu_r g_0)\begin{bmatrix} d\Phi_{e\ mag} & -d\Phi_{b\ mag} \\ -d\Phi_{d\ mag} & d\Phi_{a\ mag} \end{bmatrix}}{3z\cdot\mu_r\cos(\frac{\pi}{p})\ \sum_{j=1}^{\infty}\Psi_{A\ j}^2+\Psi_{B\ j}^2-2\Psi_{A\ j}\Psi_{B\ j}\sin(\nu_{A\ j}-\nu_{B\ j})}\begin{bmatrix} F_x \\ F_y \end{bmatrix} \tag{2.96}$$

Once the expression of the current was found, given in equation (2.96) .It enables its use for the control of the electrical machine. However, this expression can be simplified if considering that the flux created by the magnets is an even signal and therefore $\Psi_{B\ j}=0$. The simplified expression in equation (2.97) introduces a constant κ depending only on the material's property and the geometry of the BLM. Pushing the simplification even further, considering only the fundamental of the flux. The obtained expression in equation (2.99) does not depend on the position θ of the BLM's rotor anymore. But confirmation if the assumption just taken is valid will be required.

$$\begin{bmatrix} i_{ds} \\ i_{qs} \end{bmatrix} = \sum_{j=1}^{\infty}\frac{\kappa}{\Psi_{A\ j}}\begin{bmatrix} \cos((j-1)p\theta+\nu_{A\ j}+\gamma) & \sin((j-1)p\theta+\nu_{A\ j}+\gamma) \\ -\sin((j-1)p\theta+\nu_{A\ j}+\gamma) & \cos((j-1)p\theta+\nu_{A\ j}+\gamma) \end{bmatrix}\begin{bmatrix} F_x \\ F_y \end{bmatrix} \tag{2.97}$$

$$\kappa = \frac{4\,(l_{mag}+\mu_r g_0)}{3z\cdot\mu_r\cos(\frac{\pi}{p})} \tag{2.98}$$

$$\begin{bmatrix} i_{ds} \\ i_{qs} \end{bmatrix} = \frac{\kappa}{\Psi_{A\ 1}}\begin{bmatrix} \cos((\nu_{A\ 1}+\gamma) & \sin(\nu_{A\ 1}+\gamma) \\ -\sin((\nu_{A\ 1}+\gamma) & \cos(\nu_{A\ 1}+\gamma) \end{bmatrix}\begin{bmatrix} F_x \\ F_y \end{bmatrix} \tag{2.99}$$

2.4.4 Forces due to the Inductances.

The potential forces generated by the variation of the inductances of the BLM due to the displacement of the rotor was investigated. As the few previous cases it starts by calculating the energy:

$$W_{ind} = \frac{1}{2}[\mathbb{I}]^t[\mathbb{L}][\mathbb{I}] \tag{2.100}$$

From there an expression for the force in a direction ε as obtained.

$$F_{\varepsilon\ ind} = \frac{1}{2}[\mathbb{I}]^t\frac{\partial[\mathbb{L}]}{\partial\varepsilon}[\mathbb{I}] \tag{2.101}$$

For a general BLM with z coils per phase the flowing expression based on the inductance matrix from equation (2.2) was obtained.

$$F_{\varepsilon\ ind} = \begin{bmatrix} i_{U1} \\ \vdots \\ i_{Wz} \end{bmatrix}^t \cdot \frac{\partial}{\partial \varepsilon} \begin{bmatrix} L_{U1}(\Delta_x, \Delta_y, \beta_{U1}) & \cdots & M_{U1\ Wz}(\Delta_x, \Delta_y, \beta_{U1}, \beta_{Wz}) \\ \vdots & \ddots & \vdots \\ M_{Wz\ U1}(\theta, \Delta_x, \Delta_y, \beta_{Wz}, \beta_{U1}) & \cdots & L_{Wz}(\Delta_x, \Delta_y, \beta_{Wz}) \end{bmatrix} \cdot \begin{bmatrix} i_{U1} \\ \vdots \\ i_{Wz} \end{bmatrix} \tag{2.102}$$

In order to develop this expression the derivative of the different inductances and mutual inductances was defined. Starting with the inductance L_{Ui} from the i^{th} coils of the phase U. Its expression will be based on the equation (2.59).

$$\frac{\partial L_{Ui}(\Delta_x, \Delta_y, \beta)}{\partial \varepsilon} = \frac{\partial}{\partial \varepsilon} \left(L_{Ui\ 0} \left(1 + \frac{\Delta_x \cdot \cos(\beta) + \Delta_y \cdot \sin(\beta)}{g_0} \right) \right) \tag{2.103}$$

$$\frac{\partial L_{Ui}(\Delta_x, \Delta_y, \beta)}{\partial x} = L_{U1\ 0} \frac{\cos(\beta)}{g_0} \tag{2.104}$$

$$\frac{\partial L_{Ui}(\Delta_y, \Delta_y, \beta)}{\partial x} = L_{U1\ 0} \frac{\sin(\beta)}{g_0} \tag{2.105}$$

Once having the expression for $\frac{\partial L_{Ui}(\Delta_y, \Delta_y, \beta)}{\partial x}$ the same process is done using equation (2.62)

$$\frac{\partial M_{i\ j}(\Delta_x, \Delta_y, \beta_i, \beta_j)}{\partial \varepsilon} = M_{i\ j\ 0} \frac{\partial}{\partial \varepsilon} \left(1 + \frac{\Delta_x \cdot \left(\cos(\beta_i) + \cos(\beta_j) \right) + \Delta_y \cdot \left(\sin(\beta_i) + \sin(\beta_j) \right)}{2 g_0} \right) \tag{2.106}$$

$$\frac{\partial M_{i\ j}(\Delta_x, \Delta_y, \beta_i, \beta_j)}{\partial x} = M_{i\ j\ 0} \frac{\cos(\beta_i) + \cos(\beta_j)}{2 g_0} \tag{2.107}$$

$$\frac{\partial M_{i\ j}(\Delta_x, \Delta_y, \beta_i, \beta_j)}{\partial y} = M_{i\ j\ 0} \frac{\sin(\beta_i) + \sin(\beta_j)}{2 g_0} \tag{2.108}$$

From there the force $F_{x\ ind\ U1}$ created by one coil of the BLM depending on the displacement of the rotor can be evaluated.

$$F_{x\ ind\ U1} = i_{U1}\left(L_{U1\ 0}\frac{\cos(\beta_{U1})}{g_0}i_{U1} + M_{U1\ U2\ 0}\frac{\cos(\beta_{U1})+\cos(\beta_{U2})}{2g_0}i_{U2} + \cdots + M_{U1\ Uz\ 0}\frac{\cos(\beta_{U1})+\cos(\beta_{Uz})}{2g_0}i_{Uz} + \cdots + M_{U1\ Wz\ 0}\frac{\cos(\beta_{U1})+\cos(\beta_{Wz})}{2g_0}i_{Wz}\right) \quad (2.109)$$

To solve this, the study will first to concentrate on the force $F_{x\ ind\ L}$ created only by the pure inductance of the BLM. Combining the sum of each $\cos(\beta_{Uj})i_{Uj}^2$ and considering that $i_{Uj} = i_{Um} \pm i_{Us}$ this simplify the expression of the force as most of the member of the equation will cancel each other. Leading to a simple $2(\sin(\gamma)(i_{Um}i_{Us})$ where γ is an angle resulting of the combination of all the β_{Ui}.

$$F_{x\ ind\ L} = \frac{L_0}{g_0}\sum_{j=1}^{z}\cos(\beta_{Uj})i_{Uj}^2 + \cos(\beta_{Vj})i_{Vj}^2 + \cos(\beta_{Wj})i_{Wj}^2 \quad (2.110)$$

$$F_{x\ ind\ L} = \frac{2L_0}{g_0}\left(\sin(\gamma)(i_{Um}i_{Us}) + \sin(\gamma - \frac{2\pi}{3})(i_{Vm}i_{Vs}) + \sin(\gamma + \frac{2\pi}{3})(i_{Wm}i_{Ws})\right) \quad (2.111)$$

The current to produce the torque for the BLM has been defined from section 2.3 and equation (2.47) to be under the form:

$$i_{Us} = I_s \cdot \sin(p\theta) \qquad i_{Vs} = I_s \cdot \sin(p\theta - \frac{2\pi}{3}) \qquad i_{Ws} = I_s \cdot \sin(p\theta + \frac{2\pi}{3}) \quad (2.112)$$

Then injecting those values into the previous equation

$$F_{x\ ind\ L} = \frac{2L_0 I_s}{g_0}\left(\sin(\gamma)\sin(p\theta)i_{Us} + \sin(\gamma - \frac{2\pi}{3})\sin(p\theta - \frac{2\pi}{3})i_{Vs} + \sin(\gamma + \frac{2\pi}{3})\sin(\theta + \frac{2\pi}{3})i_{Ws}\right) \quad (2.113)$$

The expression can then be developed:

$$F_{x\ ind\ L} = \frac{L_0 I_s}{g_0}\left(\left[\cos(\gamma - p\theta) + \cos(\gamma + p\theta)\right] i_{Us} + \right.$$
$$\left.\left[\cos(\gamma - p\theta) + \cos(\gamma + p\theta + \frac{4\pi}{3})\right] i_{Vs} + \left[\cos(\gamma - p\theta) + \cos(\gamma + \theta - \frac{4\pi}{3})\right] i_{Ws}\right) \quad (2.114)$$

The last expression can be simplified as the sum of all the currents from the suspension inverter is equal to 0: $i_{Us} + i_{Vs} + i_{Ws} = 0$. This gives us a simple expression of the force provided by the inductances of the BLM.

$$F_{x\ ind\ L} = \frac{L_0 I_s}{g_0}\left(\cos(\gamma + p\theta) i_{Us} + \cos(\gamma + p\theta - \frac{2\pi}{3}) i_{Vs} + \cos(\gamma + \theta + \frac{2\pi}{3}) i_{Ws}\right) \quad (2.115)$$

The other mutual inductances will follow the same principle of calculation. But before pursuing the lengthy calculation of each of the expression it was decided to evaluate the force that would be generated by those inductances. First, noticing that those forces do not depend on the rotor's displacement but only on the interaction of the two currents i_s and i_m. Furthermore, if trying to estimate the maximum value of this force $F_{x\ ind\ L}$ using an inductance of 42 μH and a torque current at 0.5 A and a suspension current at 0.9 A it was founf $F_{x\ ind\ L} \approx 0.23\ N$ it was therefore decided to neglect it from our study.

2.4.5 Forces due to the Magnets.

Defining the flux created by the magnets ϕ_{mag} using a current i_{mag} representing the field created by the magnet, where having l_m the thickness of the magnets and S is the surface of a stator's tooth.

$$\phi_{mag} = \frac{i_{mag}}{\frac{l_m}{\mu_0 \mu_r S} + \frac{g_0}{\mu_0 S}} \quad (2.116)$$

$$\phi_{mag} = \frac{\mu_0 \mu_r S}{l_m + \mu_r g_0} \cdot i_{mag} \quad (2.117)$$

From the flux $\phi_{mag}$the energy W_{mag} produced by the magnets for a displacement $\Delta = \Delta_x \cos(\beta) + \Delta_y \sin(\beta)$ was calculated.

$$W_{mag} = \frac{1}{2} \cdot \frac{\mu_0 \mu_r S}{l_m + \mu_r g_0} \cdot i_{mag}^2 \tag{2.118}$$

$$W_{mag} = \frac{1}{2} \cdot \frac{\mu_0 \mu_r S}{l_m + \mu_r (g_0 + \Delta)} \cdot i_{mag}^2 \tag{2.119}$$

$$W_{mag} = \frac{1}{2} \cdot \frac{\mu_0 \mu_r S}{l_m + \mu_r g_0} \cdot i_{mag}^2 \left(1 + \frac{\mu_r \Delta}{l_m + \mu_r g_0} + \left(\frac{\mu_r \Delta}{l_m + \mu_r g_0} \right)^2 \right) \tag{2.120}$$

$$W_{mag} = \frac{1}{2} \cdot \frac{\mu_0 \mu_r^3 S}{(l_m + \mu_r g_0)^3} \cdot i_{mag}^2 \left(\frac{(l_m + \mu_r g_0)^2}{\mu_r^2} + \frac{l_m + \mu_r g_0}{\mu_r} \Delta + \Delta^2 \right) \tag{2.121}$$

From the energy, the force produced at one tooth of the BLM was extracted. Giving a general definition of the force $F_{mag\ \varepsilon}$. Following this the study will concentrate on the force in the direction x produced by a tooth j.

$$F_{mag\ \varepsilon} = \frac{1}{2} \cdot \frac{\mu_0 \mu_r^3 S}{(l_m + \mu_r g_0)^3} \cdot i_{mag}^2 \left(0 + \frac{l_m + \mu_r g_0}{\mu_r} \frac{\partial \Delta}{\partial \varepsilon} + 2\Delta \frac{\partial \Delta}{\partial \varepsilon} \right) \tag{2.122}$$

$$F_{mag\ x\ j} = \frac{1}{2} \cdot \frac{\mu_0 \mu_r^3 S}{(l_m + \mu_r g_0)^3} \cdot i_{mag\ j}^2 \left(\frac{l_m + \mu_r g_0}{\mu_r} \cos(\beta_j) + 2(\Delta_x \cos(\beta_j) + \Delta_y \sin(\beta_j)) \cos(\beta_j) \right) \tag{2.123}$$

$$F_{mag\ x\ j} = \frac{1}{2} \cdot \frac{\mu_0 \mu_r^3 S}{(l_m + \mu_r g_0)^3} \cdot i_{mag\ j}^2 \left(\frac{l_m + \mu_r g_0}{\mu_r} \cos(\beta_j) + \Delta_x (1 + \cos(2\beta_i)) + \Delta_y \sin(2\beta_j)) \right) \tag{2.124}$$

Given this expression joining those forces together in an expression for the total force in the x direction $F_{mag\ x}$. The expression was simplified by introducing a constant $\mathscr{K}$ to the previous equations.

$$\mathscr{K} = \frac{1}{2} \cdot \frac{\mu_0 \mu_r^3 S}{(l_m + \mu_r g_0)^3} \tag{2.125}$$

Having z coils per phase the force at one phase $F_{mag\ U\ x}$ is given by:

$$F_{mag\ U\ x} = \mathscr{K} i_{mag\ U}^2 \cdot \sum_{j=0}^{z-1} \left[\frac{l_m + \mu_r g_0}{\mu_r} \cos(\beta + \frac{2\pi}{z} j) + \right. \\ \left. \Delta_x (1 + \cos(2\beta + \frac{4\pi}{z} j)) + \Delta_y \sin(2\beta + \frac{4\pi}{z} j) \right] \tag{2.126}$$

Some simplification can be achieve as:

$$\sum_{j=0}^{z-1} \cos(\beta + \frac{2\pi}{z} j) = 0 \qquad \sum_{j=0}^{z-1} \cos(2\beta + \frac{4\pi}{z} j) = 0 \tag{2.127}$$

Which gives us a new expression for the force at the phase U.

$$F_{mag\ U\ x} = \mathscr{K}\, i^2_{mag\ U} \cdot \sum_{j=0}^{z-1} \Delta_x \tag{2.128}$$

$$F_{mag\ U\ x} = \frac{1}{2} \cdot \frac{\mu_0 \mu_r^3 S}{(l_m + \mu_r g_0)^3} \cdot i^2_{mag\ U} \cdot \sum_{j=0}^{z-1} \Delta_x \tag{2.129}$$

$$F_{mag\ U\ x} = \frac{z}{2} \cdot \frac{\mu_0 \mu_r^3 S}{(l_m + \mu_r g_0)^3} \cdot i^2_{mag\ U} \cdot \Delta_x \tag{2.130}$$

$$F_{mag\ x} = \frac{z}{2} \cdot \frac{\mu_0 \mu_r^3 S \Delta_x}{(l_m + \mu_r g_0)^3} \cdot \begin{bmatrix} i_{mag\ U} \\ i_{mag\ V} \\ i_{mag\ W} \end{bmatrix}^t \cdot \begin{bmatrix} 1 & 0 & 0 \\ 0 & 1 & 0 \\ 0 & 0 & 1 \end{bmatrix} \cdot \begin{bmatrix} i_{mag\ U} \\ i_{mag\ V} \\ i_{mag\ W} \end{bmatrix} \tag{2.131}$$

Considering a sinusoidal field in the air-gap:

$$\hat{i_{mag}} = \frac{\hat{B_r} l_m}{\mu_0 \mu_r} \tag{2.132}$$

$$i_{mag\ U} = \hat{i_{mag}} \cos(p\theta) \quad i_{mag\ V} = \hat{i_{mag}} \cos\left(p\theta - \frac{2\pi}{3}\right) \quad i_{mag\ W} = \hat{i_{mag}} \cos\left(p\theta + \frac{2\pi}{3}\right) \tag{2.133}$$

As for any angle α will result in $\cos(\alpha)^2 = 1/2(1+\cos(2\alpha))$ The same principle will then be applied for the y axis and will provide $F_{mag\ y}$ with a similar expression than $F_{mag\ x}$.

Finally 2 expression for the forces created by the eccentricity of the BLM's rotor were obtained:

$$F_{mag\ x} = \frac{3z}{4} \cdot \frac{\mu_r^2 S \Delta_x}{\mu_0 (l_m + \mu_r g_0)^3} \cdot (\hat{B_r} l_m)^2 \tag{2.134}$$

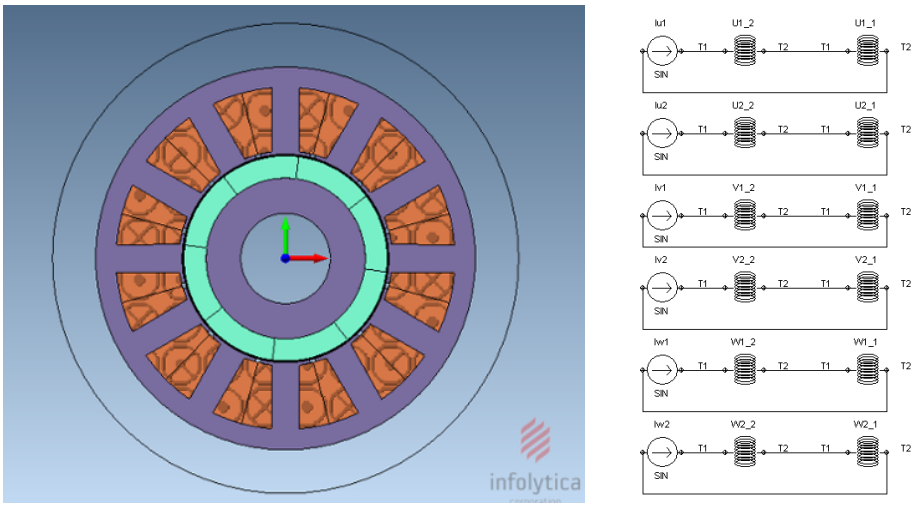
$$F_{mag\ y} = \frac{3z}{4} \cdot \frac{\mu_r^2 S \Delta_y}{\mu_0 (l_m + \mu_r g_0)^3} \cdot (\hat{B_r} l_m)^2 \tag{2.135}$$

2.5 Finite Element Analysis comparison.

Now that having set expressions for evaluating the force created by the suspension current as well as the eccentricity of the shaft and the torque, their validity needs to be confirmed by comparing them to Finite Element Analysis (FEA). To do so a model of the BLM had to be created on a FEA software.

2.5.1 Setting of the FEA model.

The model of the BLM was created using the FEA software MagNet v6.4 from Infolytica corporation. MagNet is a 2D/3D electromagnetic field software. The first step of the creation of the model is to decide of the geometry to use. Fig. 2.5a demonstrates the results of geometry created for the present comparison, using the same geometrical parameter than the BLM that wil be used in the experimental tests. In the same time the circuit of the BLM's coils was built set in the software Fig. 2.5b.



(a) Geometry model in MagNet (b) Circuit

Fig. 2.5 Model on MagNet

The different materials used for the model have been set. Table 2.2 show the materials used for the FEA model. The model can be solved either using linear equations or non-linear ones. Using a non-linear solver the behavior of the silicon iron follow a BH curve characteristic as shown in Fig. 2.6. Out of this curve he relative permeability of the iron can be obtained knowing the expression equation (2.136) which is easily transformed into

Table 2.2 Materials used in the FEA

BLM parts	Material	Properties		
		Relative Permeability	Conductivity MS/m	Coercivity kA/m
Rotor lamination	M-36 29 Ga	7,222	0	0
Rotor lamination	M-36 29 Ga	7,222	0	0
Coils	Copper	1	57.7	0
Magnets	NdFeB	1.1	0.67	-827.6
Air	Air	1	0	0

equation (2.137).

$$B_{Iron} = \mu_0 \mu_r H_{Iron} \tag{2.136}$$

$$\mu_r = \frac{B_{Iron}}{\mu_0 H_{Iron}} \tag{2.137}$$

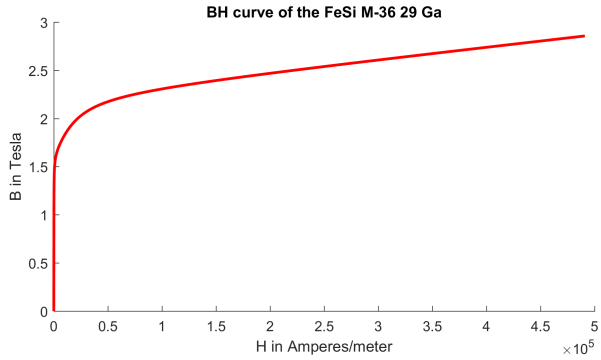


Fig. 2.6 Curve characterising the magnetic property of the Iron

All this sets the model to make comparison between the algebraic results for the Torque, forces created by the currents and the eccentricity. For each of them the comparison was done using linear and non-linear FEA. The characteristic of the model used for FEA study is given in Table 2.3. In the following calculation will not consider any eddy current effects in any elements of the machine, as well as no demagnetization on the magnets. Furthermore all the input will not include any PWM effects.

2.5.2 Torque comparison.

One important aspect of the electrical machine is the torque it generates in order to maintain or obtain the wished speed. It is therefore quite important to have a good estimate of the

Table 2.3 Parameters of the FEA model

BLM Parameter	Value	Unit
Number of pairs of poles	4	
Number of phases	3	
Number of coils per pole and per phase	2	
Number of turn per coil	200	
Length of the BLM	55.25	mm
Airgap	0.25	mm
Rotor diameter	30	mm
Back Iron diameter	56	mm
Magnet width	3.25	mm
Teeth width	4	mm
Slot depth	9.25	mm
Slot liner height	0.5	mm
Magnet span	100	%
Tooth opening	80	%

torque of the BLM. Comparing the results obtained algebraically to the one of the FEA. Fig. 2.7 shows that expression found in equation (2.47) gives us a good estimation of the BLM's torque. The difference observed with FEA is due to the fact it didn't take in account any non-linearity in the materials as well as not considering the effects that teeth harmonics have.

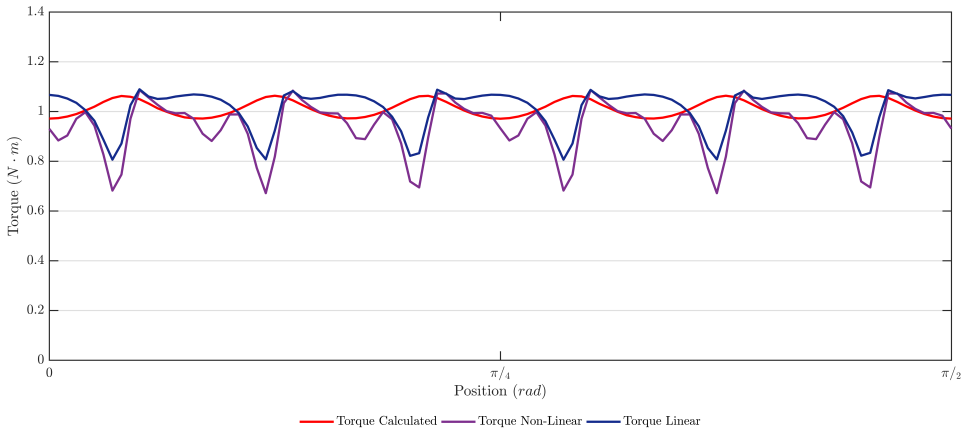


Fig. 2.7 Comparison between the calculated torque and the ones obtained by FEA

2.5.3 Eccentricity forces comparison.

As shown in 2.4.4 the displacement of the rotor in a direction ε generates a force that moves the rotor closer to the stator. Comparing the results obtained in 2.4.4 to the ones got from the FEA. To do so the different results will be compared into two scenarios. The first one will consist on displacing the rotor of the BLM in one direction ε from 0 to 20 μm. For the second will displace the rotor in a fixed direction and let it rotate around its axis. Those two comparison will allow us to have a better idea of the accuracy of the force algebraically calculated.

2.5.3.a Displacement in a direction ε .

Following the results of equation (2.134and 2.135) those results to the one proposed by the linear FEA were compared. Fig. 2.8 presents the variation of the force due to the eccentricity of the rotor. Making this eccentricity Δ_y vary from 0 to 20 μm. Observing that they are

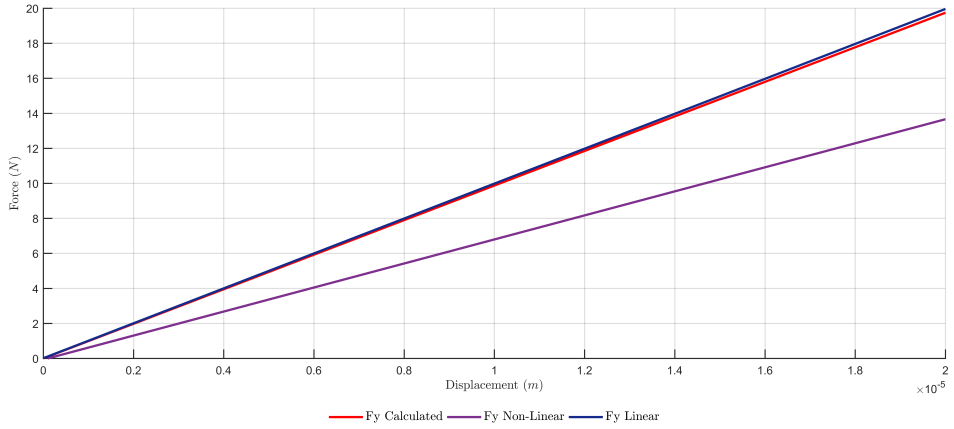


Fig. 2.8 Force created by the eccentricity of the shaft

both extremely close to each other. This force could be considered as a stiffness obtaining: $K_{FEA} = 9.98 \cdot 10^5\ N \cdot m^{-1}$ and $K_{Calc} = 9.87 \cdot 10^5\ N \cdot m^{-1}$.

Even-though the results are similar between the linear and the calculated one. The non-linear one has a quite lower force output. Which leads to a stiffness $K_{Calc} \approx 6.81 \cdot 10^5\ N \cdot m^{-1}$.

2.5.3.b Static displacement in a direction ε with rotation .

Following the same principle, displacing the rotor by $10\mu m$ but this time rotating the rotor around its axis and comparing the linear FEA results to one obtained form the algebraic

expression for a purely sinusoidal field. It can be seen from the results of Fig. 2.9 that the two forces are very close. The main reason for the difference between the results are due to the fact that it didn't take in account the specificity of the geometry and didn't consider any harmonics in the magnet's field. But if it is compared to the non-linear one, neglecting the non-linear effects in the BLM will give lower forces than expected.

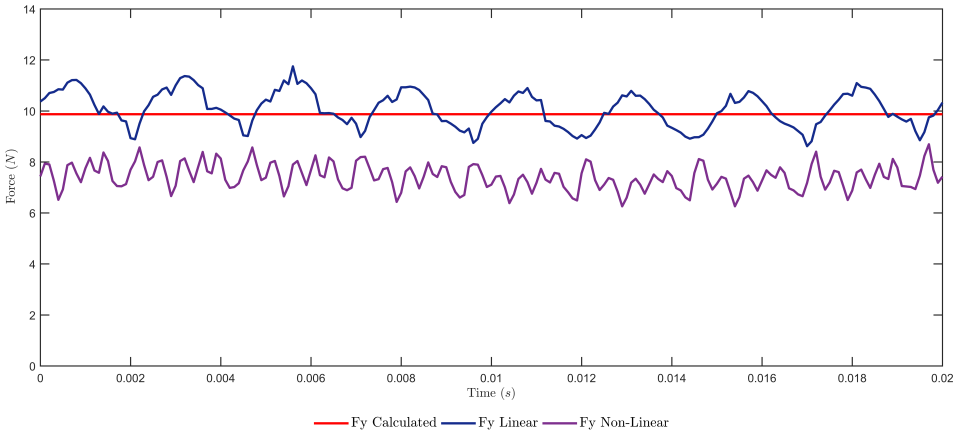


Fig. 2.9 Force created by the eccentricity of the shaft at $10\mu m$

2.5.4 Currents forces comparison.

The main objective of the BLM is to subject the rotor to a desired force in order to control its position. To do so the formulation found in section 2.4 are required to be accurate. For this injecting a certain current i_s into the BLM's FEA model and compare the results obtained to the one calculated algebraically. In the case presented here it used the following currents: The

Table 2.4 Currents $i_s(t)$ injected in the coils

Currents	$i_{Us}(t)$	$i_{Vs}(t)$	$i_{Ws}(t)$
	$0.2 \cdot \sin(2\pi 200t + 40)$	$0.2 \cdot \sin(2\pi 200t + 160)$	$0.2 \cdot \sin(2\pi 200t - 80)$

FEA was run in linear and non-linear and then plot the force acted upon the rotor depending on the position θ of the rotor. The resulting graph is given in Fig. 2.10 where the algebraic solution for the force was also added. One notice that the values of forces are quite similar. But the general shape of the force is different. This is due to the fact it didn't consider the effect of the slots on fluxes. The approximation taken by having the flux derivative by use angles β at the centre of the coils might be an over-simplification as the flux will in some

situation no mainly pass through the centre of the teeth. The difference observed with the calculated for and the non-linear one is also perfectly understandable as it didn't take in account any non-linearity in the calculation. The effect of the Saturation is even more flagrant once trying to reach high values of forces. Using a current density J_s of 4 $A \cdot mm^2$ for the suspension and only 80 N was obtained compared to the 100 expected Fig. 2.11. Therefore, for high force demand situation some care will need to be taken.

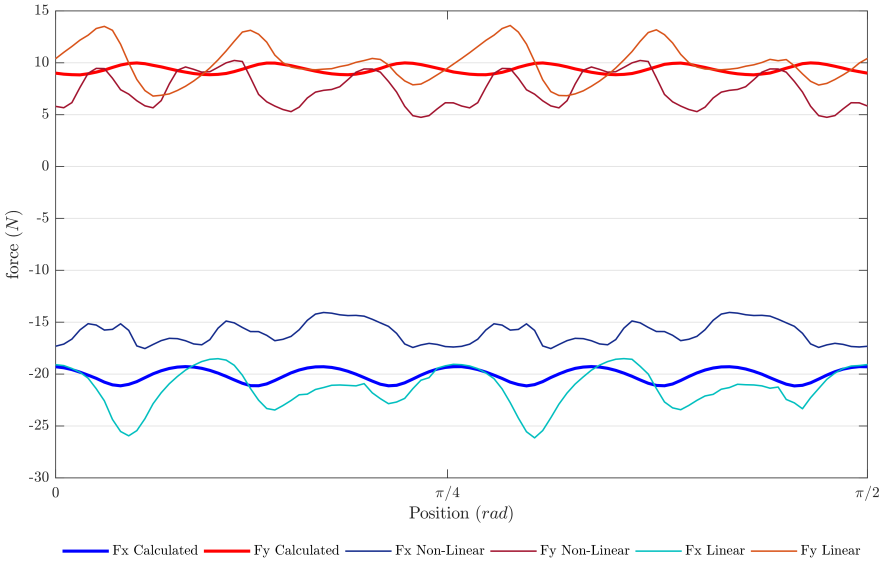


Fig. 2.10 Force created by the BLM on the shaft with a current $I_s = 0.2\ A$

2.6 Control of the BLM.

Now that a complete model of the BLM is obtained, its control can finally be considred. Using the results obtained in 2.2 the current control for the BLM can be set-up. Then the control of the speed of the BLM will be set up. Finally, a control for the position of the shaft will be proposed. The first step would be to convert the equations from the time domain to a frequency domain trough the Laplace transform $\mathscr{L}$ [25]. For a signal or function $f(t)$ is Laplace transform $F(s)$ is defined as expressed in equation (2.138) where s is a complex number representing the frequency.

$$\mathscr{L}\{f(t)\}(s) = F(s) = \int_0^\infty f(t)e^{-st}dt \tag{2.138}$$

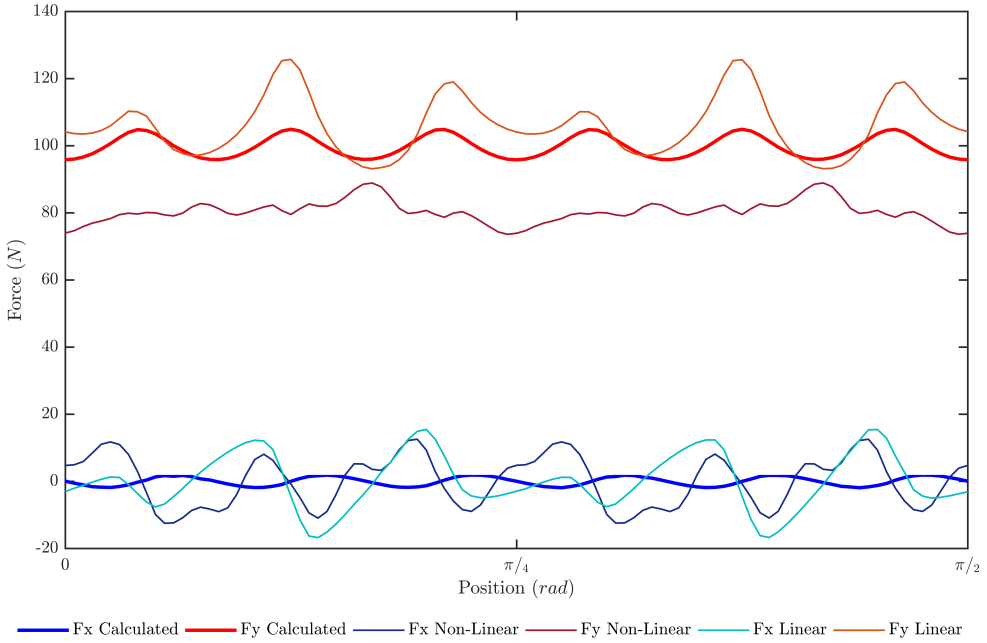


Fig. 2.11 Force created by the BLM on the shaft with a current $I_s = 0.9\ A$ and a current density $J_s = 4\ A \cdot mm^2$

2.6.1 Introduction to Control

But first the different part of the control need to be defined and some terminology based on the courses of G. Scorletti and V.Fromion [63] need to be set. Fig. 2.12 represent the base model for the control that will be used for this study. Out of this loop different transfer functions will be extracted.

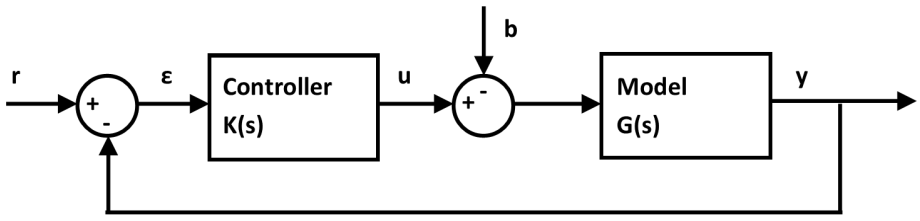


Fig. 2.12 Base model for the control

Stability The stability of the system is determined by its poles. Like shown in [32]. The system is going to be stable only if the real part of the poles of the system are negative. In the presented case the poles of the system are given by the roots of equation (2.139). In order

Table 2.5 Control loop functions

Name	
Open-loop transfer function	$L(s) = K(s)G(s)$
Sensitivity function	$T_{r\to\varepsilon} = \dfrac{1}{1+K(s)G(s)} = S(s)$
Rejection and attenuation function	$T_{b\to\varepsilon} = \dfrac{G(s)}{1+K(s)G(s)} = G(s)S(s)$
Transmission (transfer) function	$T_{r\to y} = \dfrac{K(s)G(s)}{1+K(s)G(s)} = T(s)$

to have a stable system the open loop transfer function $L(s) \neq -1$. So that the stability of the close loop system depends only on the open loop transfer function $L(s)$. This value of -1 can be translated into a gain of $0dB$ and a phase of -180°, so that this point of instability can be easily spotted on a Bode and/or Nyquist plot. Assuming that the modeled system does not describe perfectly the real system some margin can be introduced. Those margins are known as: phase margin and gain margin. The phase margin $\Delta\varphi$ correspond to an angle of which has to make the phase plot move in order to have -180° at the frequency ω_c where the gain is $0dB$. The gain margin ΔG is the opposite; it is the gain one has to add or subtract to the gain plot in order to have $0dB$ at point where the phase is equal to -180°. Those two margins can bee also observed on a Nyquist plot. Some system can have an infinite gain and phase margin, which means that the system should always be "stable". However, in fact this last statement is not always true. That is why another term is introduced; named sensitivity which corresponds to the minimal distance between the open loop transfer function $L(S)$ and the point of instability -1 as shown in equation (2.142). This value has to be as small as possible in order to have a stable system. This opens the possibility of some systems to have an infinite gain and phase margin but a very high sensitivity. Another margin that can be used to quantify the stability of the system is the delay margin ΔD. It is defined using the pulsation ω_c where the open loop system $L(s)$ has a $0dB$ gain.

$$1 + K(s)G(s) = 0 \tag{2.139}$$

$$\Delta G = \frac{1}{\mid L(j\omega_{-180^\circ}) \mid} \tag{2.140}$$

$$\Delta\varphi = arg\,(L(j\omega_c)) + 180^\circ \tag{2.141}$$

$$Sensitivity = max\ _{0<\omega<\infty} \mid S(s) \mid \tag{2.142}$$

$$\Delta D = \frac{\Delta\varphi}{\omega_c} \tag{2.143}$$

Tracking The tracking means that the system is going to follow a desired input command, like a step, a ramp etc. In order to do so, the system needs to have the limit of $\varepsilon(t)$ towards the infinite equal to 0 for a specific input $r(t)$ as expressed in equation (2.144).Based on the Table 2.5 and Fig. 2.12 an expression of $E(s)$ depending on the sensitivity function $S(s)$ can be found. Using the resulting equation (2.145) and the final value Theorem [32] equation (2.146) was obtained, which is stetting the condition needed to track a signal $r(t)$.

$$lim\ _{t\to\infty}\varepsilon(t) = 0 \tag{2.144}$$

$$E(s) = R(s)T_{r\to\varepsilon} = R(s)S(s) \tag{2.145}$$

$$\lim_{t\to\infty}\ \varepsilon(t) = lim\ _{s\to 0}\ sE(s) = lim\ _{s\to 0}\ sR(s)S(s) = 0 \tag{2.146}$$

Rejection In order to have a system able to reject some defined perturbation b(t). It needs to make sure that the limit of $\varepsilon(t)$ tends to 0 as shown in equation (2.147).The expression of $E(s)$ using the rejection function is given in equation (2.148). From there the condition that our systems and controller need to fulfill in order to reject a disturbance signal $b(t)$ can be defined in equation (2.149).

$$\lim_{t\to\infty}\ \varepsilon(t) = 0 \tag{2.147}$$

$$E(s) = B(s)T_{b\to\varepsilon} = B(s)G(s)S(s) \tag{2.148}$$

$$lim\ _{t\to\infty}\varepsilon(t) = lim\ _{s\to 0}\ sE(s) = lim\ _{s\to 0}\ sB(s)G(s)S(s) = 0 \tag{2.149}$$

2.6.2 Control of the currents.

With the equations (2.15) and (2.16) defined in 2.2, the process of model the BLM was started. The equations that model the BLM are converted to the frequency domain. The results are the two equations(2.150) and(2.151). Combining the two expressions equation (2.150) was simplified into the equation (2.152). In order to be able to control the two parts of the BLM the two models will be decoupled. $\underline{V_{Us}}$ depends only on the current $\underline{I_{Um}}$, which will make its control easier than the one of $\underline{V_{Um}}$. The main issue with the expression of $\underline{V_{Um}}$ is that he depends on the emf $\underline{E_U}$ as well as $\underline{V_{Us}}$. The problematic can be seen in two

ways: either the voltage generated by the suspension is negligible compared to the one of the current or a multi-variable control has to be set.

$$\underline{V_m} = R\left(\frac{\underline{I_m}}{2} + \underline{I_s}\right) + s\,\frac{L_m}{2}\,\underline{I_m} + s\,L_s\,\underline{I_s} + \underline{E_U} \tag{2.150}$$

$$\underline{V_s} = 2R\,\underline{I_s} + s\,2L_s\,\underline{I_s} \tag{2.151}$$

$$\underline{V_m} = R\frac{\underline{I_m}}{2} + s\,\frac{L_m}{2}\,\underline{I_m} + \frac{\underline{V_s}}{2} + \underline{E} \tag{2.152}$$

2.6.2.a Considering a negligible suspension voltage

Considering that voltage suspension of the BLM is negligible compared to the voltage for the torque, the expression of the BLM model for the control can be simplified to the two equations 2.153 and 2.154. This chapter is going to demonstrate only the control of $\underline{I_{Um}}$ as the setting of control of $\underline{I_{Us}}$ will be done in the same fashion. The first step is to transform the equation 2.153 into a transfer function $\underline{T_{Im}}$ equation 2.156. Obtaining a first order transfer function with a gain G_{Im} and a time constant τ_m detailed in equation 2.157. The Control of the currents will be done by a PI controller as shown on Fig. 2.153.

$$\underline{V_m} = \frac{1}{2}\left[R\,\underline{I_m} + s\,L_m\,\underline{I_m}\right] \tag{2.153}$$

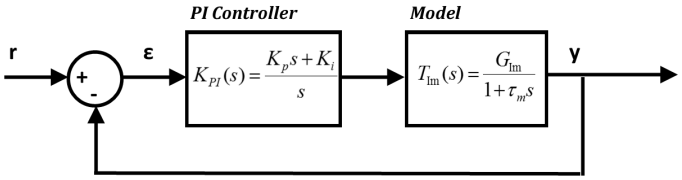
$$\underline{V_s} = 2\left[R\,\underline{I_s} + s\,L_s\,\underline{I_s}\right] \tag{2.154}$$

$$\frac{\underline{I_m}}{\underline{V_m}} = \frac{2}{R + s\,L_m} = \frac{\frac{2}{R}}{1 + s\,\frac{L_m}{R}} \tag{2.155}$$

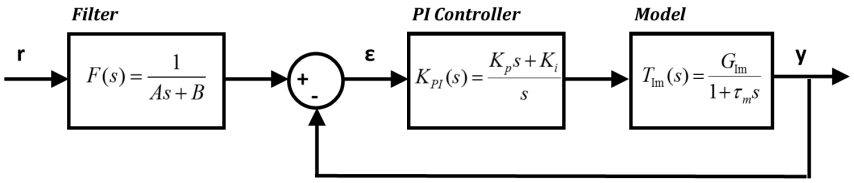
$$\underline{T_{Im}} = \frac{G_{Im}}{1 + \tau_m s} \tag{2.156}$$

$$G_{Im} = \frac{2}{R} \qquad \tau_m = \frac{L_m}{R} \tag{2.157}$$

In order to control the current, the system needs to be able to follow a step input. To do so a PI controller with its expression K_{PI} described in equation (2.158) will be used. The closed loop control system that will then be studied is represented in the Fig. 2.13a The resulting transfer function $T_{CL}(s)$ of this close loop system is then calculated in equation (2.160). Observing that the system results in a well-known second order system described by equation (2.161) with ω_0 the cutting pulsation of the filter and ξ the damping. The behavior of



(a) Standard PI control system



(b) PI control system with a filter

Fig. 2.13 Proposed control system

the system using a well-known abacus Fig. 2.14 for second order systems, can be found. For this system choosing to have a response time at 5% of the final value of a step to be $100\mu s$ with a damping ξ of 0.7. The values of the parameters of the PI controller were obtained as shown in Table 2.6.

The second step is to observe the open loop transfer function $T_{OL}(s)$ of the system with the PI controller. As discussed in 2.6.1 $T_{OL}(s)$ will allow us to have some information about the stability of the system. Equation (2.159) gives us the expression of $T_{OL}(s)$. From that transfer function the Bode Fig. 2.15a and Nyquist diagram Fig. 2.15b were drawn. The system will be stable as the Nyquist diagram does not pass by the point $(-1,0)$ nor does the Bode diagram have $0dB$ at a phase $-180°$. But as mention in 2.6.1 to have a better understanding of the stability of the close loop system the different margins of the open loop transfer function should be looked at. Those margins are all described in Table 2.7. The result of the margins obtained for this controller are pretty good, with an infinite gain margin and the phase margin of 66° is significant enough to make the system safe from instability. Even the overall sensibility of the system is only $5.2 \cdot 10^{-3} dB$.

$$K_{PI}(s) = \frac{K_p s + K_i}{s} \tag{2.158}$$

$$T_{OL}(s) = \frac{K_p s + K_i}{s} \cdot \frac{G_{Im}}{1 + \tau_m s} = \frac{G_{Im}(K_p s + K_i)}{s + \tau_m s^2} \tag{2.159}$$

$$T_{CL}(s) = \frac{\dfrac{G_{Im}}{1+\tau_m s}\cdot\dfrac{K_p s+K_i}{s}}{1+\dfrac{G_{Im}}{1+\tau_m}\cdot\dfrac{K_p s+K_i}{s}} = \frac{\dfrac{G_{Im}}{\tau_m}(K_p s+K_i)}{s^2+s\left(\dfrac{1+K_p G_{Im}}{\tau_m}\right)+\dfrac{K_i G_{Im}}{\tau_m}} \tag{2.160}$$

$$T_{CL}(s) = \frac{\omega_0^2\,(As+B)}{s^2+2\xi\,\omega_0 s+\omega_0^2} \tag{2.161}$$

$$\omega_0 = \sqrt{\frac{K_i G_{Im}}{\tau_m}} \qquad \xi = \frac{1+K_p G_{Im}}{2\omega_0\tau_m} \qquad A = \frac{K_p}{K_i} \qquad B = 1 \tag{2.162}$$

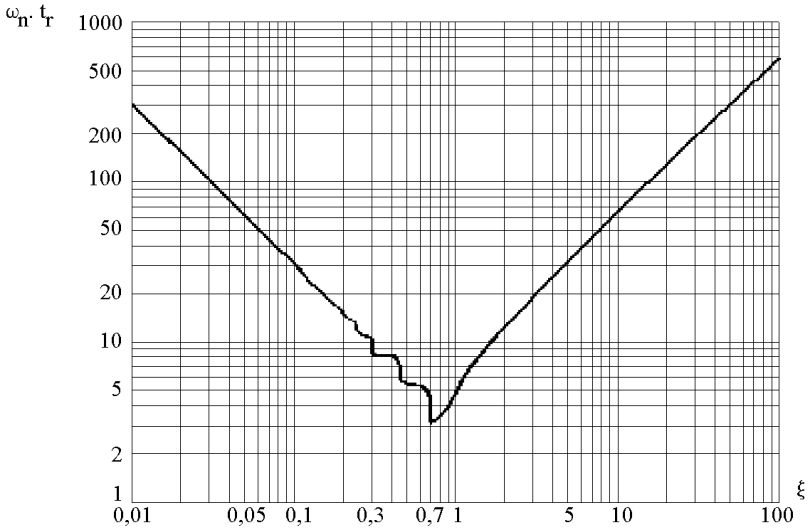


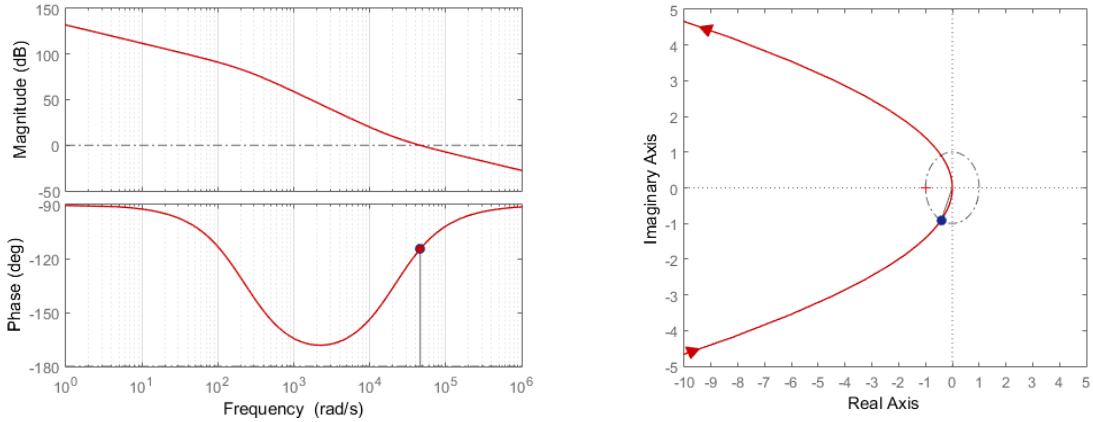
Fig. 2.14 Abacus of second order

Table 2.6 Value of the parameter of the PI controller

System constraint	Value
Response time at 5%	$100\ \mu s$
Damping ξ	0.7
Cutting frequency ω_0	$30,000\ rad.s^{-1}$
PI parameter	**Value**
K_i	$\dfrac{\tau_m\omega_0^2}{G_{Im}} = 2.439\cdot 10^7$
K_p	$\dfrac{2\xi\,\tau_m\omega_0 - 1}{G_{Im}} = 1.132\cdot 10^3$

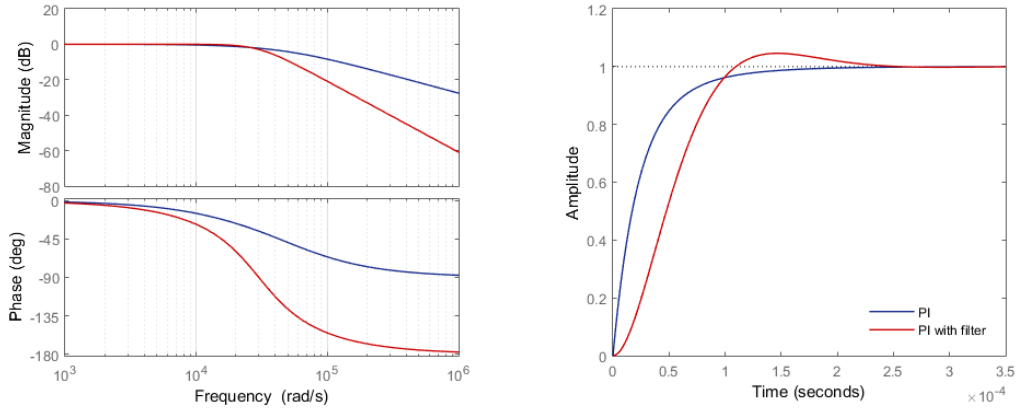
Table 2.7 Margins of the open loop transfer function

Margin	Value	
Gain Margin	∞	dB
Phase Margin	66	$^\circ$
Delay Margin	$2.59 \cdot 10^{-4}$	s
Sensitivity	$5.2 \cdot 10^{-3}$	dB



(a) Bode diagram (b) Nyquist diagram

Fig. 2.15 Open loop diagrams



(a) Closeloop Bode diagram (b) response to a step

Fig. 2.16 Close loop diagrams

But one can notice that a zero $(As+B)$ appears in the expression of $T_{CL}(s)$ which will influence the control of the current as it won't be a pure second order response. This can be observed on Fig. 2.16a. Using the controller topology of Fig. 2.13a the system does not behave like wanted . The bode diagram clearly show that the system is behaving closer to a first order system. Even Fig. 2.16b shows a lack of oscillation expected from a second order system. To counteract this a filter that will cancel the zero $(As+B)$ of the close loop system was introduced. In equation (2.162) it can be observed that the component of the zero that needs to be compensated depend only on the PI corrector's parameter. Which facilitates the compensation as there won't be any incertitude in the parameters involved, therefore not potentially affect the stability of the system. The expression of the filter $F(s)$ is given in equation (2.163). Looking at Fig. 2.16b and Fig. 2.16a the systems now behaves like a second order as planed. The new close loop transfer function $T_{CL}(s)$ of the system including the filter $F(s)$ is given in equation (2.164).

$$F(s) = \frac{1}{As+B} = \frac{K_i}{K_i + K_p s} \tag{2.163}$$

$$T_{CL}(s) = \frac{\dfrac{K_i G_{Im}}{\tau_m}}{s^2 + s\left(\dfrac{1+K_p G_{Im}}{\tau_m}\right) + \dfrac{K_i G_{Im}}{\tau_m}} = \frac{\omega_0^2}{s^2 + 2\xi\,\omega_0 s + \omega_0^2} \tag{2.164}$$

The Same exact process will be used for the suspension current,the only difference being the values of the PI parameters and the gain G_{Is} and time constant τ_s. The expression of the different parameter of the system are given in equation (2.166).

$$\underline{T_{Is}} = \frac{G_{Is}}{1+\tau_s s} \tag{2.165}$$

$$G_{Is} = 2R \qquad \tau_s = \frac{L_s}{R} \tag{2.166}$$

The resulting control system for the currents of the BLM is then illustrated in Fig. 2.17. The emf of the BLM is added on the result of the control of v_m as well as $\frac{1}{2}v_s$ as they have been discarded of the control from equation (2.152) to equation (2.153). The overhaul control of the BLM can be found in Appendix A.

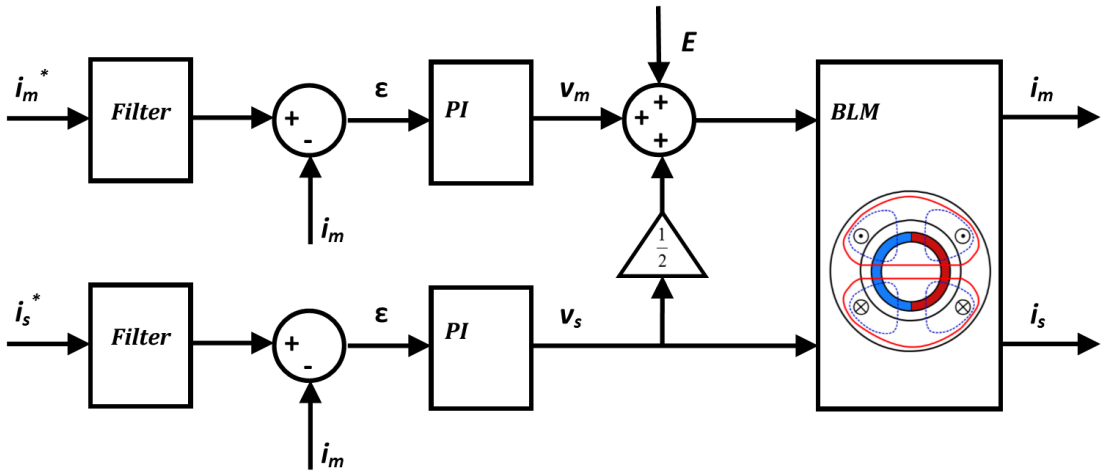


Fig. 2.17 Diagram illustrating the control of the currents for the BLM

2.6.2.b Considering a non-negligible suspension voltage

For the previous study it was considered that the suspension voltage of the BLM is low/ negligible compared to the one for the torque. This is true for our case study but in further work it would be interesting to look into a MIMO study for this system. Fig. 2.18 highlight the fact that the suspension current input has an effect on the output of the torque current by about 9 dB. It would be therefore interesting in further work to look at the MIMO control of the BLM

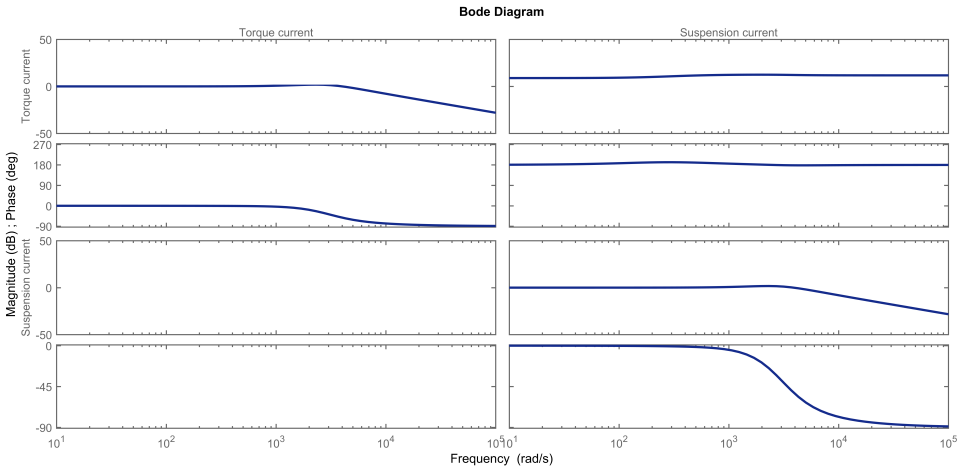


Fig. 2.18 Bode Diagram of the close loop system if we consider it as a MIMO

2.6.3 Control of the Force

The control of the force generated by the BLM will be studied in order to ensure that the system stay stable through process of vibration control. For this, it was decided that a PD controller will be used to achieve that function. That control have been chosen because it perfectly reflects parameter of the rotodynamics of a shaft. The PD controller is also a great solution to reject any input, which would make it perfect for vibration reduction. The equation representing a shaft can be written as follows:

$$m\ddot{x} + d\dot{x} + kx = f(t) \tag{2.167}$$

with m representing the mass of the object, k its stiffness and d its damping. x being the displacement of the object/shaft and $f(t)$ the forces applied to it. The transfer function $H_{PD}$of the PD controller being expressed as follows:

$$H_{PD}(s) = K_{P\ PD} + s \cdot K_{D\ PD} \tag{2.168}$$

WThe parallel between the PD controller and the rotodynamic model can easily be found by stating that $K_{P\ PD}$ would represent a given stiffness k_{BLM} produced by the BLM and $K_{D\ PD}$ would represent a damping d_{BLM}.

The next step is going to study the impact of that PD controller on the system previously controlled. The model is represented in Fig. 2.19. From this the Bode diagram resulting of

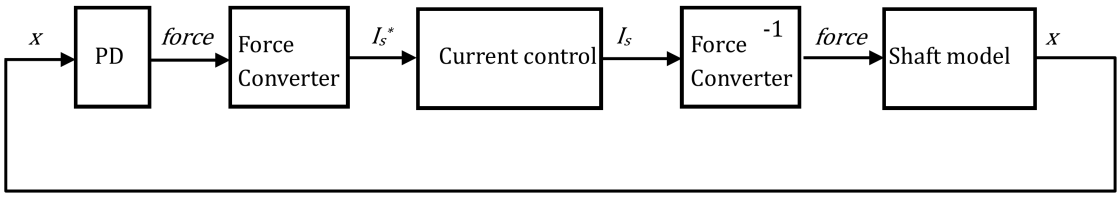


Fig. 2.19 Schematic of the force control system

that close loop system will be studied. For this an example with the following parameters was used: The resulting Bode diagram is displayed on Fig. 2.20. it can be seen that the

Table 2.8 Parameters of the force control example

Parameters	m	d	k	$K_{P\ PD}$	$K_{D\ PD}$
Values	$0.4\ kg$	$1\ N \cdot s \cdot m^{-1}$	$7.8 \cdot 10^8\ N \cdot m^{-1}$	$5 \cdot 10^5$	10

output of the response has an amplitude of about $-60\ dB$ which promises a reduction of the displacement x of the shaft. But one has to note the spike appearing at $4 \cdot 10^4\ rad/_s$ which is due to the natural frequency of the shaft $\omega_{nat} = \sqrt{\frac{k}{m}} \approx 4 \cdot 10^4\ rad/_s$. The response of the system to an step in put of 1 has been reduced to a displacement of about $0.7 \cdot 10^{-3}$.

As an example Fig. 2.22 highlights the vibration of a shaft and at the middle of the data sample activating the control through the PD controller. The change of behavior of the shaft's displacement can clear be observed.

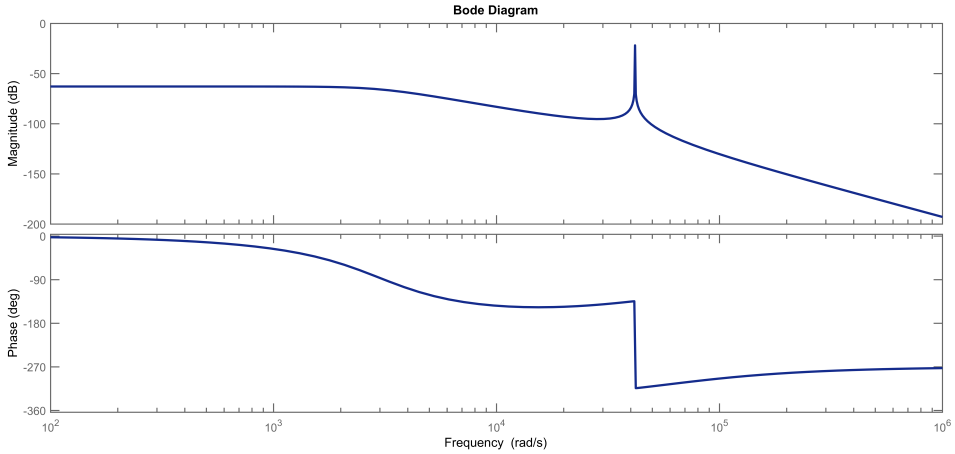


Fig. 2.20 Bode graph of the force control system

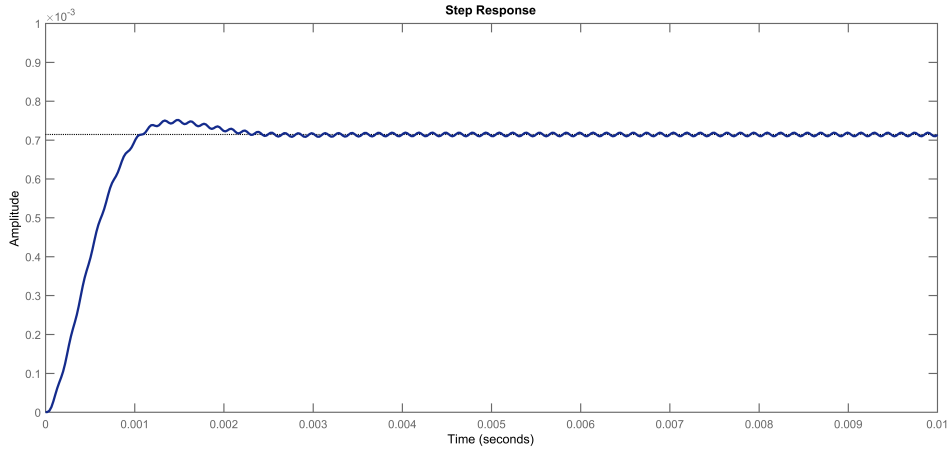


Fig. 2.21 Step response of the force control system

However, the idea, now, would be to see if that control could be used not only to reduce vibrations but also to act on the critical speeds of a shaft. Instead of constantly regulate

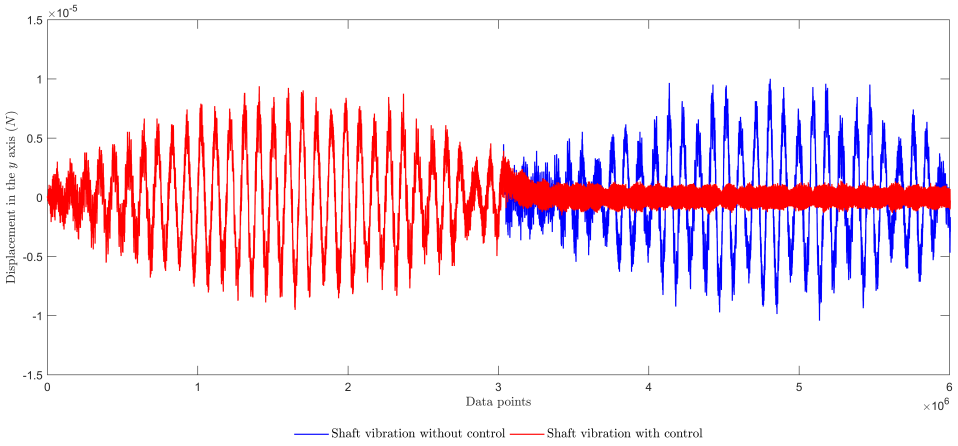


Fig. 2.22 Example of vibration reduction

the position of the shaft it would be interesting to apply forces on the shaft only for certain situation and during a limited period of time.

2.7 Summary

Having now a model of the single winding BLM as well as expressions that allow us to know what current to inject in order to obtain a certain torque or force output. Those expressions have been verified through an FEA. The results in the using linear materials gave similar results to the one obtained through algebraic calculations. But on the other hand the non-linear ones aren't too similar. This might require a more extensive study of the non-linear effect in the BLM and the creation of non-linear BLM model.

Simplifying the control expression and model of BLM by introducing 2 parameters L_m and L_s that are a combination of the different inductances of the BLM's coils. The control is stable if it consider that the voltage injected into the suspension inverter is small compared to the one needed for the torque. But a more extensive study should be done on the effect of that voltage in case of a high V_s using MIMO control. For the same reason it would be interesting to look at a non-linear model it would be interesting to looks at the improvement of the control through a non-linear control like H_∞ or LMI.

Now knowing that the idea gives the possibility to act on the shaft via the BLM and apply forces on the rotor in a controlled manner. But the question now is: couldn't the BLM be used more efficiently by not trying to constantly to reduce the vibration but by acting only in specific period that requires it. Furthermore, it would be interesting to look at the possibilities it has in acting on the rotodynamic of a shaft using this controlled BLM.

Chapter 3

Impact of the BLM on the Rotodynamic of a shaft

3.1 Introduction to Rotodynamics

To see the potential impact of a BLM on the rotodynamics of a shaft or set of shafts it is important to have a model of it. The basics governing the behavior of vibrations is given by the single degree of freedom (DoF) example shown in Fig. 3.1 of a mass in the direction x is given in equation (3.1). The behaviour of the system is characterized by 4 main parameters.The mass m at that DoF as well as the damping d and the stiffness k. The forces $f(t)$ applied at that DoF.

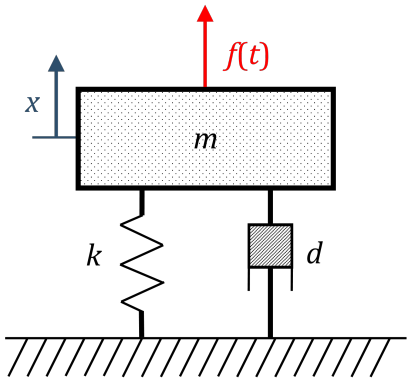


Fig. 3.1 Vibration model for 1 DoF

$$m\ddot{x} + d\dot{x} + kx = f(t) \tag{3.1}$$

This is the basis for the rotodynamics study that will follow in this chapter. The model that will be developed for this study will take in account 5 DoF as well as gyroscopic and shear effects. The said model will be described using finite element modeling (FEM) based on an existing Matlab FEM code [1], issued by the authors of the book Dynamics of Rotating Machines [33].The FEM code is limited transversal vibration studies and the functionality to connect several shafts to one another via gears was added as this part was missing in the base code. As Fig. 3.1 represents only one DoF for the shaft model,Fig. 3.2 illustrates all 6 of them. Having 3 transversal $(x,\ y,\ z)$ and 3 rotational $(\theta,\ \psi,\ \phi)$ axis. But in this study any effect on the z DoF won't be taking into account as it was considered that the bearings will be stiff enough to hold firmly the shaft in place and therefore generate a negligible displacement in z. Furthermore, this study will concentrate on the transversal effect as the BLM mainly acts on the 2 traversal DoF $(x,\ y)$. This leave use with 5 DoF $(x,\ y)$ and $(\theta,\ \psi,\ \phi)$.

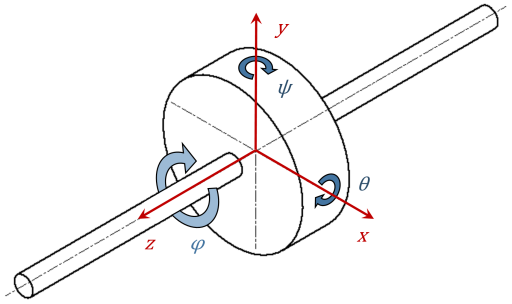


Fig. 3.2 The different DoF if a shaft

3.1.1 Single shaft system

A single shaft can be described as different elements in order to obtain the different matrices needed to describe it's rotodynamic behavior. First the different DoF the study is interested in, will need to be defined. In the case of single shafts system the study is looking for 4 DoF: 2 transversal (x and y), and the two rotations around those axes (Φ and θ). The FEM of a shaft will be performed into 4 steps:

- **Define the mesh** The shaft needs to be divided into several elements. The shafts will be divided into small beam connected between each other with nodes. The more subdivision the model has the more the number of DoF of the system increases. If n_{node} is the number of node, in our case it would have a total number of DoF of $4 \times n_{node}$.

- **Express the elasticity, inertia and external forces** For each element the force and moment should be applied to them in terms of their local coordinates.
- **Assemble the elements** All the elements of the system must be assembled together with their respective forces and moments in order to produce the general force or moment of the simulated shaft.
- **Perform the analysis** With the equations of motion generated form the different element of the shaft it allows to solve them together.

The detail for the definition of element of the matrices is given in [33] The different elements of the shaft are obtained by approximating the kinetic and strain energies. Giving for a single element beam with E_e the young modulus of, its cross-section A_e, density ρ_e and its length ℓ_e a mass matrix M_e and stiffness matrix K_e. Pursuing the study of the axial displacement, w_{e1} and w_{e2}, of a single element shaft with its forces f_{e1} and f_{e2} as illustrated in Fig.3.3 it was found that:

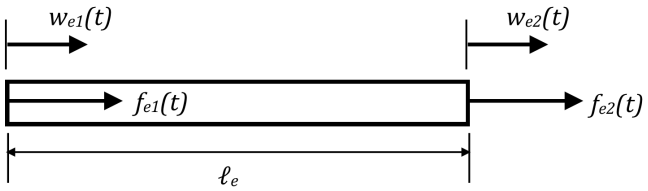


Fig. 3.3 Element considering an axial displacement

$$M_e = \frac{\rho_e A_e \ell_e}{6} \begin{bmatrix} 2 & 1 \\ 1 & 2 \end{bmatrix} \tag{3.2}$$

$$K_e = \frac{E_e A_e}{\ell_e} \begin{bmatrix} 1 & -1 \\ -1 & 1 \end{bmatrix} \tag{3.3}$$

Assuming a system with 3 components having the same length ℓ_e the resulting stiffness matrix K would be given by:

$$K = \frac{E_e A_e}{\ell_e} \left(\begin{bmatrix} 1 & -1 & 0 & 0 \\ -1 & 1 & 0 & 0 \\ 0 & 0 & 0 & 0 \\ 0 & 0 & 0 & 0 \end{bmatrix} + \begin{bmatrix} 0 & 0 & 0 & 0 \\ 0 & 1 & -1 & 0 \\ 0 & -1 & 1 & 0 \\ 0 & 0 & 0 & 0 \end{bmatrix} + \begin{bmatrix} 0 & 0 & 0 & 0 \\ 0 & 0 & 0 & 0 \\ 0 & 0 & 1 & -1 \\ 0 & 0 & -1 & 1 \end{bmatrix} \right) \tag{3.4}$$

$$K = \frac{E_e A_e}{\ell_e} \begin{bmatrix} 1 & -1 & 0 & 0 \\ -1 & 2 & -1 & 0 \\ 0 & -1 & 2 & -1 \\ 0 & 0 & -1 & 1 \end{bmatrix} \tag{3.5}$$

The same principle will then be applied to all the other matrices even for more complex systems. The FEM code will be able to take in account the different effect which will each influence on the general resulting matrices. Starting with the mass matrix $[\mathbb{M}]$:

- M_e The mass matrix of the shaft elements
- M_d The mass matrix of the disc
- M_s The mass matrix of the seals

The stiffness matrice $[\mathbb{K}]$:

- K_e The stiffness matrix of the shaft elements
- K_d The stiffness matrix of the disc
- K_s The stiffness matrix of the seals
- K_b The stiffness matrix of the bearings
- $K_T e$ The stiffness matrix due the torque on an element
- $K_F e$ The stiffness matrix due axial forces on an element

The damping matrice $[\mathbb{C}]$:

- C_e The damping matrix of the shaft elements
- C_s The damping matrix of the seals
- C_b The damping matrix of the bearings

On top of this the gyroscopic effects can also be taken into account, which will add a matrix $[\mathbb{G}]$.

The previous definition gave the different element of the matrices describing the shafts rotodynamic model. In order to enable the user input a shaft model, a structure based modeling was set in place. The structure created is described in Table.3.1, as it describes the different parts of the shaft to model. A potential result of the software is given in Fig. 3.4

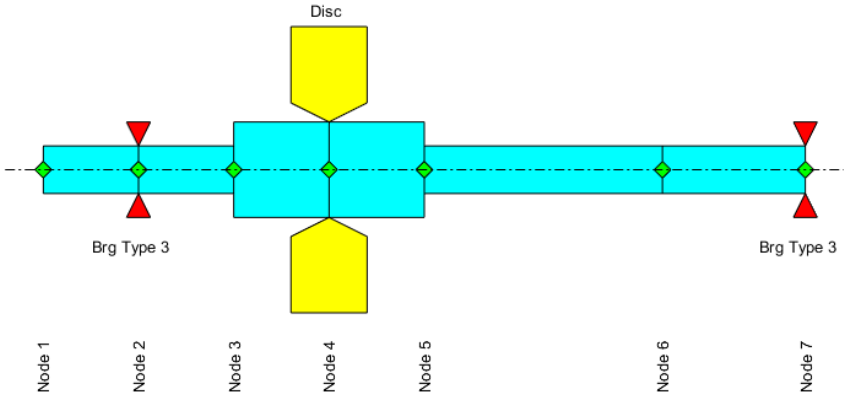


Fig. 3.4 Visual representation of the shafts model

3.1.2 Geared shaft system

The previous discussion showed how the model of shaft is achieved using FEM. However, this concentrate only on the transversal vibration of the shaft it does not allow taking in account the possibility to connect several shafts to one another. For this purpose the FEA model will need to integrate a new DoF to model the shaft system. This was done because on gears the torsional vibration of the shafts affect the transversal ones and vice-versa. The model of the connected shafts was then modified based on the works of Rao [7, 59]. This effect is illustrated in Fig. 3.5 where it can seen that any displacement in (x_1, y_1) will induce a displacement in (x_2, y_2) and vice-versa, through a stiffness k_h, damping c_h via a pressure

Table 3.1 Description of the structures used for the rotodynamics FEM calculation for a single shaft system

Structure name	Data	Description
Model	node	This parameter represent all the nodes of the shaft. It contains the node numbers as well as the position of the node on the shaft. Considering a shaft with n nodes the parameter will be represented by a $n \times 2$. Where each row is represented by: $[\, n_{Node} \;\; p_{Node}]$
	shaft	This Matrix represent the different parameter of the shaft's section. For shaft with n node it will have a maximum of $n-1$ shaft section. Each row of the shaft matrix will defined as follows: $[\, Type_{shaft} \;\; Node_{start} \;\; Node_{end} \;\; D_{outer} \;\; D_{inner} \;\; \rho \;\; E \;\; G \;\; \zeta \;\; F_{axial} \;\; T_{node}]$
	disc	This matrix represent all the discs of the model. They are separated in to two definition type: Type 1: $[\, 1 \;\; Node \;\; \rho \;\; thickness \;\; D_{outer} \;\; D_{inner}]$ Type 2: $[\, 2 \;\; Node \;\; M_{disc} \;\; I_D \;\; I_P]$
	bearing	This matrix represent all the bearings of the model. They are separated in 2 main categories each including different types of bearing. The first category considers Rigid bearings (pinned or clamped boundary condition): Type 1:$[\, 1 \;\; Node]$ Pinned Boundary Type 2:$[\, 2 \;\; Node]$ clamped Boundary The second category considers bearings specified with constant damping and stiffness properties : Type 3: $[\, 1 \;\; Node \;\; k_{xx} \;\; k_{yy} \;\; c_{xx} \;\; c_{yy}]$ Type 4: $[\, 1 \;\; Node \;\; k_{xx} \;\; k_{yy} \;\; k_{\theta\theta} \;\; k_{\psi\psi} \;\; c_{xx} \;\; c_{yy} \;\; c_{\theta\theta} \;\; k_{\psi\psi}]$ Type 5: $[\, 1 \;\; Node \;\; k_{xx} \;\; k_{xy} \;\; k_{yx} \;\; k_{yy} \;\; c_{xx} \;\; c_{xy} \;\; c_{yx} \;\; c_{yy}]$ Type 6: $[\, 1 \;\; Node \;\; k_{xx} \;\; k_{xy} \;\; k_{x\theta} \;\; k_{x\psi} \;\; \ldots \;\; etc]$
	em	This parameter of the Model structure will allow the definition of electrical machines with their negative stiffness in the air gap k_{airgap}. Considering m electrical machine connected on the model, em will be represented by a $m \times 4$ matrix. Where each row is represented as follows: $[\, Node_{start} \;\; Node_{end} \;\; B_{airgap} \;\; Airgap]$

angle Φ_p. Introducing the 2 parameter S and C defined in equation (3.6) the stiffness matrix was expressed as $[\mathbb{K}_{gear\ 1,2}]$.

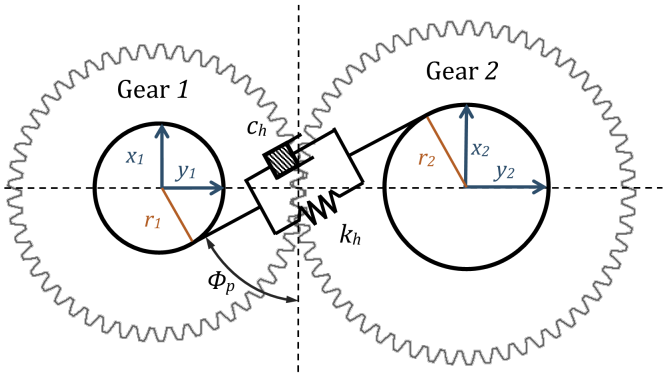


Fig. 3.5 Gear mesh model

$$S = \sin(\Phi_p) \qquad C = \cos(\Phi_p) \tag{3.6}$$

$$[\mathbb{K}_{gear\ 1,2}] = k_h \cdot \begin{bmatrix} S^2 & SC & 0 & 0 & r_1S & -S^2 & -SC & 0 & 0 & r_2S \\ SC & C^2 & 0 & 0 & r_1C & -SC & -C^2 & 0 & 0 & r_2C \\ 0 & 0 & 0 & 0 & 0 & 0 & 0 & 0 & 0 & 0 \\ 0 & 0 & 0 & 0 & 0 & 0 & 0 & 0 & 0 & 0 \\ r_1S & r_1C & 0 & 0 & r_1^2 & -r_1S & -r_1C & 0 & 0 & r_1r_2 \\ -S^2 & -SC & 0 & 0 & -r_1S & S^2 & SC & 0 & 0 & -r_2S \\ -SC & -C^2 & 0 & 0 & -r_1C & SC & C^2 & 0 & 0 & -r_2C \\ 0 & 0 & 0 & 0 & 0 & 0 & 0 & 0 & 0 & 0 \\ 0 & 0 & 0 & 0 & 0 & 0 & 0 & 0 & 0 & 0 \\ r_2S & r_2C & 0 & 0 & r_1r_2 & -r_2S & -r_2C & 0 & 0 & r_2^2 \end{bmatrix} \tag{3.7}$$

The use of the definition of geared system will therefore require that each shafts be modeled using 5 DoF in order to include the torsional effects. At the same time the program should be fitted with a function allowing the different shafts of the system to be connected to one another. The Table 3.2 describes the structure used to define the system composed with different shafts and how they are connected together. In order to take in account the fact that shaft will be rotating at different speed it will be important that the system considers this in the definition of each shaft set of matrices. Considering a set of i shafts each with n_i DoF the base of the representation of the system will be defined using different matrices$[\mathbb{M}_{1\to i}]$,$[\mathbb{C}_{1\to i}]$,$[\mathbb{G}_{1\to i}]$,$[\mathbb{K}_{1\to i}]$,$[\mathbb{S}_{1\to i}]$ and the vectors $[\mathbb{F}_{1\to i}]$,$[q_{1\to i}]$. All the matrices, for a selected shaft i, being the same size $\sum_{j=1}^{i} n_j$. With $[\mathbb{M}_{1\to i}]$ being the mass matrix,

$[\mathbb{C}_{1\to i}]$and$[\mathbb{G}_{1\to i}]$ corresponding to the damping. $[\mathbb{K}_{1\to i}]$and$[\mathbb{S}_{1\to i}]$ corresponding to the stiffness.$[\mathbb{F}_{1\to i}]$ is the force applied at each DoF for every shaft. $[q_{1\to i}]$ represents the different DoF of the system. Those matrices do not take yet in account the presence of the gears of the system. One can understand this by the fact the resulting matrix do not show any interaction between the shaft. The matrix defining the gears as specified in equation(3.7) were inserted, that highlight the stiffness at the gear. This will introduce the first interactions between shafts. But since the shaft are going to be connected together the rotation of each shaft are therefore interdependent. For this purpose the concept of matrix reduction was introduced.

$$[\mathbb{M}_{1\to i}] = \begin{bmatrix} [M_1]_{n_1\times n_1} & [0]_{n_1\times n_2} & \cdots & [0]_{n_1\times n_i} \\ [0]_{n_2\times n_1} & [M_2]_{n_2\times n_2} & \cdots & [0]_{n_2\times n_i} \\ \vdots & \vdots & \ddots & \vdots \\ [0]_{n_i\times n_1} & [0]_{n_i\times n_2} & \cdots & [M_i]_{n_i\times n_i} \end{bmatrix} \tag{3.8}$$

$$[\mathbb{C}_{1\to i}] = \begin{bmatrix} [C_1]_{n_1\times n_1} & [0]_{n_1\times n_2} & \cdots & [0]_{n_1\times n_i} \\ [0]_{n_2\times n_1} & [C_2]_{n_2\times n_2} & \cdots & [0]_{n_2\times n_i} \\ \vdots & \vdots & \ddots & \vdots \\ [0]_{n_i\times n_1} & [0]_{n_i\times n_2} & \cdots & [C_i]_{n_i\times n_i} \end{bmatrix} \tag{3.9}$$

$$[\mathbb{G}_{1\to i}] = \begin{bmatrix} [G_1]_{n_1\times n_1} & [0]_{n_1\times n_2} & \cdots & [0]_{n_1\times n_i} \\ [0]_{n_2\times n_1} & \dfrac{\Omega_2}{\Omega_1}[G_2]_{n_2\times n_2} & \cdots & [0]_{n_2\times n_i} \\ \vdots & \vdots & \ddots & \vdots \\ [0]_{n_i\times n_1} & [0]_{n_i\times n_2} & \cdots & \dfrac{\Omega_i}{\Omega_1}[G_i]_{n_i\times n_i} \end{bmatrix} \tag{3.10}$$

$$[\mathbb{K}_{1\to i}] = \begin{bmatrix} [K_1]_{n_1\times n_1} & [0]_{n_1\times n_2} & \cdots & [0]_{n_1\times n_i} \\ [0]_{n_2\times n_1} & [K_2]_{n_2\times n_2} & \cdots & [0]_{n_2\times n_i} \\ \vdots & \vdots & \ddots & \vdots \\ [0]_{n_i\times n_1} & [0]_{n_i\times n_2} & \cdots & [K_i]_{n_i\times n_i} \end{bmatrix} \tag{3.11}$$

$$[\mathbb{S}_{1\to i}] = \begin{bmatrix} [S_1]_{n_1\times n_1} & [0]_{n_1\times n_2} & \cdots & [0]_{n_1\times n_i} \\ [0]_{n_2\times n_1} & \dfrac{\Omega_2}{\Omega_1}[S_2]_{n_2\times n_2} & \cdots & [0]_{n_2\times n_i} \\ \vdots & \vdots & \ddots & \vdots \\ [0]_{n_i\times n_1} & [0]_{n_i\times n_2} & \cdots & \dfrac{\Omega_i}{\Omega_1}[S_i]_{n_i\times n_i} \end{bmatrix} \tag{3.12}$$

Table 3.2 Description of the structures used for the rotodynamics FEM calculation for a geared system.

Structure name	Data	Description
Model	id	number identifying the shaft. Considering n shafts, id is generally defined with: $model_1.id = 1,\ model_2.id = 2,\ \ldots\ model_n.id = n.$
	node	
	shaft	
	disc	Those parameters have already been described in Table 3.1
	bearing	
	em	
	gear	Defines the gears on the shaft's model. The gear's definition was based on the one of the disc. There are two possible definition. Type 1: $[\ 1\ \ Node\ \ \rho\ \ thickness\ \ D_{outer}\ \ D_{inner}]$ Type 2: $[\ 2\ \ Node\ M_{gear}\ \ I_D\ \ I_P\ \ R_{gear}]$ *Note*: Compared to the Type 2 disc the radius was added, which is necessary in the definition of the coupled stiffness in equation(**??**)
System	models	Table containing the model structures of the shafts in the geared system. Considering n shafts, the table will be: $[\ model_1\ \ model_2\ \ \ldots\ model_n]$
	gamma	Table containing the speed ratios of each shafts. Considering n shafts, the table will be: $[\ \gamma_1\ \ \gamma_2\ \ \ldots\ \ \gamma_n]$
	connection	Matrix containing the links between the different shafts. Considering a system m geared connections. The matrix will have m row. For the connection between 2 shafts a and b the row will be: $[\ model_a.id\ \ \sharp_{Gear\ a}\ \ model_b.id\ \ \sharp_{Gear\ b}\ \ \Phi_p\ \ k_h]$

$$[\mathbb{M}_{1\to i}][\ddot{q}_{1\to i}] + [[\mathbb{C}_{1\to i}] + \Omega_1[\mathbb{G}_{1\to i}]][\dot{q}_{1\to i}] + [[\mathbb{K}_{1\to i}] + \Omega_1[\mathbb{S}_{1\to i}]][\dot{q}_{1\to i}] = [\mathbb{F}_{1\to i}] \quad (3.13)$$

3.1.2.a Model reduction

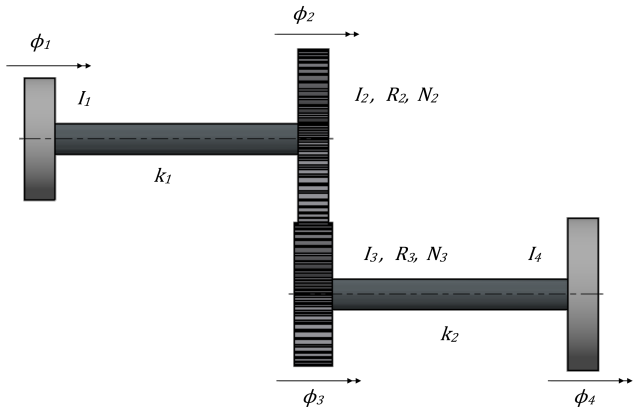


Fig. 3.6 Simple geared system

To be able to connect two or more shafts together there is a need to link each of them with a certain amount of constraints. For the example as illustrated in Fig. 3.6 it will concentrate on a simple example using only the torsional DoF. This will lay down the basis of the model reduction that will be used for more complex system afterwards. In order to simplify further the system no damping will be considered. The model can be represented by the equation (3.14) using $q = [\phi_1\ \phi_2\ \phi_3\ \phi_4]^T$ the torsional position at each node. Q correspond to the applied torque at each node and $[M]$ and $[K]$ are respectively the mass and stiffness matrices.

$$[M]\ddot{q} + [K]q = Q \quad (3.14)$$

The angular displacement ϕ_3 and ϕ_4 on the gears are coupled and cannot be considered independent. They are both connected through the gear's mesh as shown in Fig.3.7. One see that the Torque T_2 and T_3 create a force on the connection between the two gears F_{23}. To the equation (3.14) Q_C was introduced that enforces the constraint on the unconnected DoF.

$$[M]\ddot{q} + [K]q = Q + Q_C \quad (3.15)$$

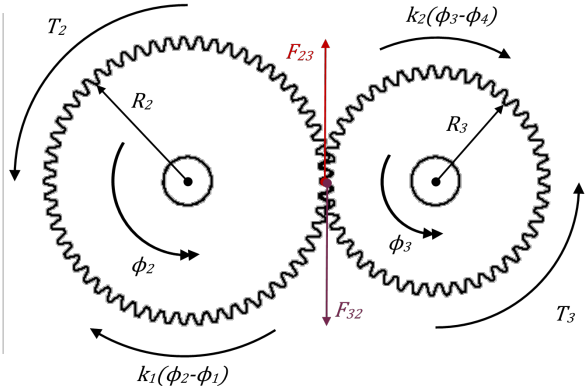


Fig. 3.7 Forces and torque at the gears

$$Q_C = \begin{bmatrix} 0 \\ R_2 \\ R_3 \\ 0 \end{bmatrix} F_{23} \tag{3.16}$$

Considering the tangential velocity at the gears $R_3\dot{\phi}_3 = -R_2\dot{\phi}_2$ was obtained. This constraint can then be set into a constraint matrix E through:

$$E^T\dot{q} = 0 \tag{3.17}$$

If the constant of integration was set to zero, the equation can be integrated (3.17) to

$$E^T q = 0 \tag{3.18}$$

These constraints will lead to the creation of transformation matrix T that will reduce the length of the vector q. This mean a reduction of the number of DoF in the model. Through this transformation a new vector q_R was obtained with:

$$q = Tq_R \tag{3.19}$$

If integrateing the transformation to the constraint vector and for any q_R:

$$E^T q = E^T T q_R = 0 \tag{3.20}$$

$$E^T T = 0 \tag{3.21}$$

At the same time this also ensures that $T^T Q_C = 0$, and that the resulting length of q_R is the same as the resulting constraint system. This can be expressed mathematically by having $Y = [ET]$ full rank. Which is equivalent to saying that YY^T is non-singular. Using this matrix T the whole model can be reduced.

$$[M_R] = T^T[M]T \qquad [K_R] = T^T[K]T \qquad Q_R = T^T Q \tag{3.22}$$

$$[M_R]\ddot{q}_R + [K_R]q_R = Q_R \tag{3.23}$$

But one should first find an expression for the transformation matrix T. Using a well know method commonly used in FEA [33]. The algorithm used applies each constraint one by one creating p intermediate transformation T_i, where p is equal or fewer than the number of constraint. The final transformation$T$ is obtained by the product of all those T_i.

$$T = T_1 \times T_2 \times \cdots \times T_p \tag{3.24}$$

Each one of those transformations will reduce the constraint vector. Therefore, for each intermediate constraint it needs to recalculate the constraint matrix E_i for each step i.

$$E_i = T_i^T E_{(i-1)} \tag{3.25}$$

E_0 is the original constraint matrix for the system. If considering n_0 the number of DoF of the non-constraint system, the number of DoF reduces at each applied constraint. So that, at the i^{th} constraint the number of DoF is now $n_i = n_0 - i$. The procedure to obtain each T_i is as follows:

1. Set $T_i = I_{n_i+1}$
2. Define k so that $E_{i-1}(k,i) = max_{j:1\to n_i}|E_{(i-1)}(j,i)|$
3. Replace the k^{th} row of T_i with the transposed column i from E_{i-1}
4. Divide this row by $-E_{(i-1)}(k,i)$
5. Strike out the column k from the matrix T_i
6. calculate the new constraint matrix $E_i = T_i^T E_{(i-1)}$

If applying this to the system illustrated in Fig.3.6, starting with the assumption that $R_2 > R_3$. E_0 is then defined based on the results of equation(3.16):

$$E_0 = \begin{bmatrix} 0 & R_2 & R_3 & 0 \end{bmatrix}^T \tag{3.26}$$

Applying the three first steps of the algorithm obtained

$$T_1 = \begin{bmatrix} 1 & 0 & 0 & 0 \\ 0 & R_2 & R_3 & 0 \\ 0 & 0 & 1 & 0 \\ 0 & 0 & 0 & 1 \end{bmatrix} \tag{3.27}$$

Following step 4. and 5. transforming T_1 and as it only has one constraint the resulting matrix $T_1 = T$.

$$T = \begin{bmatrix} 1 & 0 & 0 \\ 0 & -\dfrac{R_3}{R_2} & 0 \\ 0 & 1 & 0 \\ 0 & 0 & 1 \end{bmatrix} \tag{3.28}$$

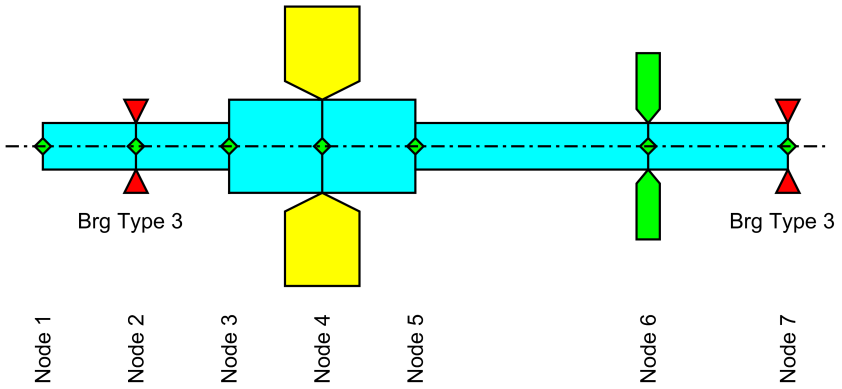
This will allow to obtain the different matrices and vector: $[M_R]$,$[K_R]$,Q_R and q_R. This provides now a way to apply constraint on a system and therefore apply it to model the gears and create a model of system with multiple interconnected shafts.

3.1.2.b Model construction

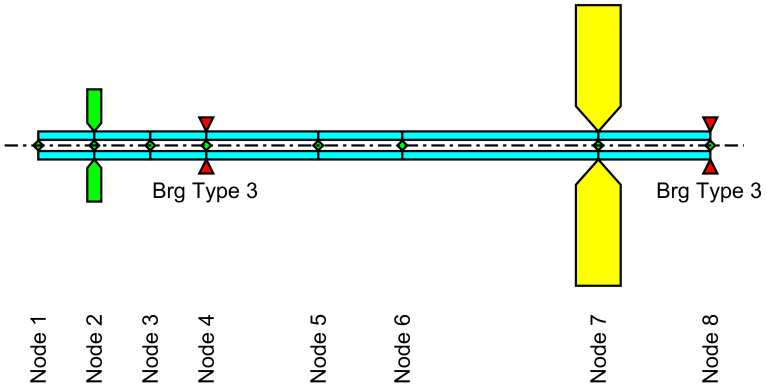
The resulting FEM model of the shaft system can be obtained as shown on Fig. 3.8 where the green disc represents the gears of the system. As introduced in Table. 3.2 an overall structure will contain the data of each shaft's model. Furthermore, it will require each shaft to be identified and a connection matrix. In the example of Fig. 3.8 this matrix would be: $\begin{bmatrix} Shaft\ 1 & 1 & Shaft\ 2 & 1 & \Phi_p & k_h \end{bmatrix}$. In the same time each shaft should be given its speed ratio. As a convention the driving shaft was kept with a ratio of 1 given the following matrix for our example: $\begin{bmatrix} 1 & 8 \end{bmatrix}$. From this FEM it will be able to obtain the different matrices characterizing the system. Considering a system with a total of *i* DoF, the following matrices can be obtained:

- Mass matrix $\mathbb{M}_{1\to i}$
- Stiffness matrix $\mathbb{K}_{1\to i}$
- Damping matrix $\mathbb{C}_{1\to i}$
- Gyroscopic matrix$\mathbb{G}_{1\to i}$
- Speed dependent stiffness matrix $\mathbb{S}_{1\to i}$

Using those definitions the previous model of a single shaft can be extended , as showed in Table.3.2. Then applying the constraints through a reduction transformation on the base



(a) Shaft 1



(b) Shaft 2

Fig. 3.8 Example of a geared FEM with 2 shafts

given in equation(3.13) the new representation of our geared system can be obtain to represent a multiple shaft sytem.. This new system obtained through the reduction equation (3.30) will then be used to obtain the critical speeds of the shaft system and plot the Campbell graph of it.

$$T^T[\mathbb{M}_{1\to i}]T\ddot{q}_{1\to i} + T^T\left[[\mathbb{C}_{1\to i}] + \Omega_1[\mathbb{G}_{1\to i}]\right]T\dot{q}_{1\to i} + T^T\left[[\mathbb{K}_{1\to i}] + \Omega_1[\mathbb{S}_{1\to i}]\right]Tq_{1\to i} = T^T[\mathbb{F}_{1\to i}] \quad (3.29)$$

$$[\mathbb{M}_{R\ 1\to i}]\ddot{q}_{R\ 1\to i} + [\mathbb{C}_{R\ 1\to i}\ (\Omega_1)]\,\dot{q}_{R\ 1\to i} + [\mathbb{K}_{R\ 1\to i}\ (\Omega_1)]\,\dot{q}_{R\ 1\to i} = [\mathbb{F}_{R\ 1\to i}] \tag{3.30}$$

3.2 Interaction between the BLM and the shaft

3.2.1 Discussion about the use of the BLM

Now that an idea of the model and the functioning of the BLM was obtained, the study can concentrate on the application of that technology. BLM and Magnetic bearings are already in use in divers industrial applications [52]. BLM are used in application that require ultra clean environments. The system being friction-less it does not necessitate any lubricant which might contaminate any chemical or pharmaceutical processes. Products like Centrifugal pumps and blood pump have already been developed and used. On the other hand AMB are also used in high speed application where the use of bearings would be impossible or very costly [67, 11, 72]. Some BLM and AMB are used principally to reduce the vibrations in a rotating system [68, 19, 43].

BLM are usually used in a bearingless system (Fig. 3.9); meaning that the system in question use magnetic bearings in order to have a contact-less rotation of the shaft for application where the speed or environmental condition do not allow the use of bearings. In this instance the BLM's objective is to maintain the shaft centered and levitated it as well as restrict 2 DoF of the shaft. In this case the BLM will act like a bearing. Which means it can be defined as having a Stiffness and Damping. But this requires a constant control of the current in order to maintain the levitation of the shaft.

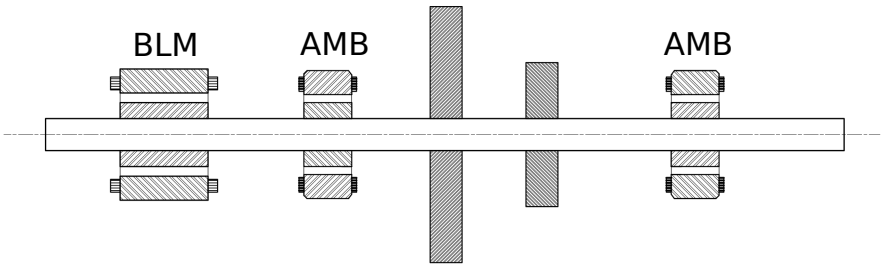


Fig. 3.9 Schematic of an BLM and AMB shaft system configuration

On the other hand if considering a shaft where there is no need for magnetic levitation (Fig. 3.9), with a system containing an electrical machine, the motor could be replaced by a BLM. In this instance the BLM would have for only function to reduce the amount of

transversal vibration on the shaft and the bearings would maintain the shaft. Concentrating our attention on this kind of scenario, for the following reasons. The first one is the fact the BLM does not need to provide any kind of levitation reducing the strain on the BLM. Therefore, allowing it to be designed for a lower current rating. Not concentrating on the levitation of the shaft, the BLM can also be used as a variable "bearing" by dynamically changing the values of the apparent stiffness and damping of the BLM. Furthermore, using the BLM as a simple actuator could be used in two ways.

1. Control the BLM for reducing the shaft's vibration. The system will then counteract the displacement of the shaft by providing a force opposing the movement via a PD controller.

2. Control the BLM to affect the rotodynamic properties of the system for only specificity time frames where it is needed. Like affecting the critical speeds of a rotating shaft as they have a potential hazardous effect on the integrity of the shaft and the overhaul rotating system.

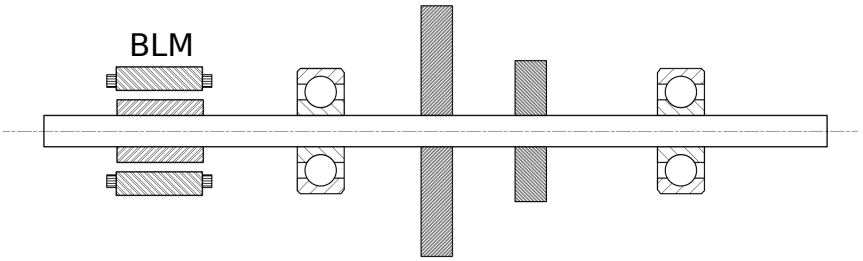


Fig. 3.10 Schematic of an BLM and bearing shaft system configuration

The first method has received already some significant attention and has shown to work [68, 19, 43]. However, has it was stated previously the presence of the critical speeds of a rotating system brings some challenges once the rotating speed approaches those specific points. Methods to alleviate the impact of those frequencies using an actuator has yet to be proposed. Therefore, it seemed logical to pursue the second approach and investigate if the BLM could be used in such a way.

First a simple model of shaft will be used to study and demonstrate the principle that the BLM could potentially impact the rotodynamics of the shaft. This will be done by concentrating on the study of the critical speeds of the model.

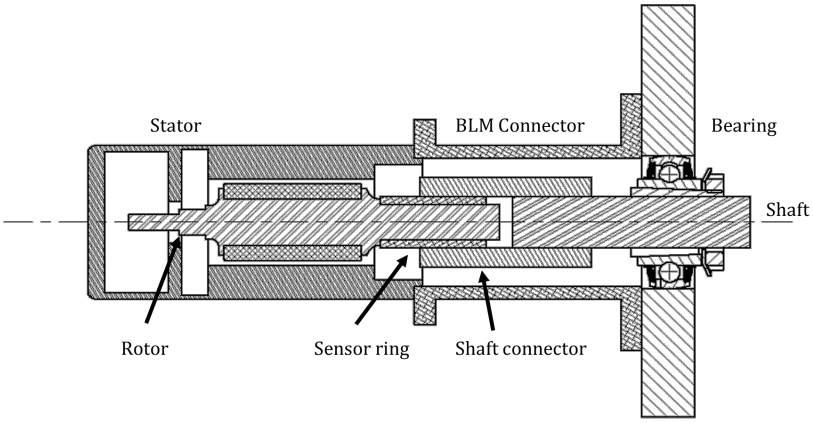


Fig. 3.11 Schematic of an BLM and its connection to the shaft

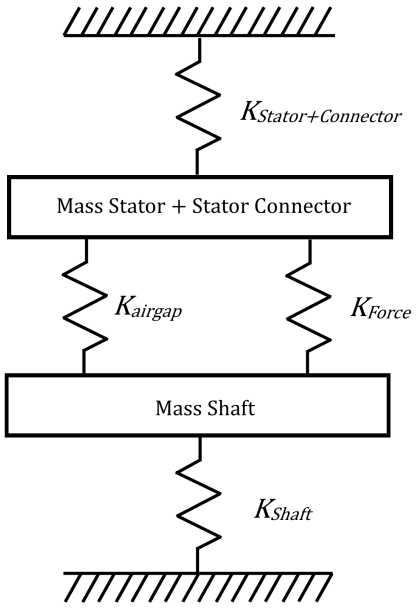


Fig. 3.12 [Schematic of an BLM's Stiffness

3.2.2 Demonstration with a simple model

$$M\ddot{q} + D\dot{q} + Kq = F \tag{3.31}$$

Based on the rotodynamic model developed in 3.1 and illustrated in equation(3.31),the effect of the BLM could be evaluated on the shaft. But to do this it would need a study of the connection of the BLM to the rest of the shaft model. Based on the primitive model illustrated in Fig. 3.10. The connection solution of BLM Fig. 3.11 attaches the machine from the flanges to the support for the bearings holding the system. For the rotodynamic modeling of the BLM one could consider the forces applied by the BLM on the shaft as a stiffness. This assumption is derived from the results of 2.4.4 where it showed that the eccentricity of the rotor induced a force proportional to the displacement of the rotor in a direction q.T his can then be transformed into a stiffness K_{airgap}:

$$F_{eccentricity} = Constant \times q \tag{3.32}$$

$$F_{eccentricity} = K_{airgap} \times q \tag{3.33}$$

Furthermore, the BLM will be generate forces F_{BLM} through controlled currents. The produced forces were arranged so that they oppose to the one generated by $F_{eccentricity}$. By having, it under the form:

$$F_{BLM} = -K_{Force} \times q \tag{3.34}$$

From there the attention was focused on to the stiffness connection between the BLM and the shaft and a schematic summarizing all the different stiffness involved in the connection was established. In this case it was assumed that the structure holding the bearings and the BLM is fixed and that the stiffness of the bearing is very large so that it can actually be ignored Fig. 3.12. The BLM will be providing two different stiffness: K_{airgap} representing the negative stiffness generated by the magnets of the BLM and K_{Force} the useful stiffness provided by the BLM. The connection of the BLM to the system's structure or ground will also imply a stiffness $K_{Stator+Connector}$ that the system will have to take in account. From those combinations of stiffness it is possible to obtain a resulting stiffness K_{BLM}.

$$K_{BLM} = \frac{K_{Stator+Connector} \times (K_{airgap} + K_{Force})}{K_{Stator+Connector} + (K_{airgap} + K_{Force})} \tag{3.35}$$

This result can then reintegrated into equation(3.31). Giving us new expression for the rotodynamic behaviour of the shaft.

$$M\ddot{q} + D\dot{q} + Kq = F - K_{BLM}q \tag{3.36}$$

$$M\ddot{q} + D\dot{q} + (K + K_{BLM})q = F \tag{3.37}$$

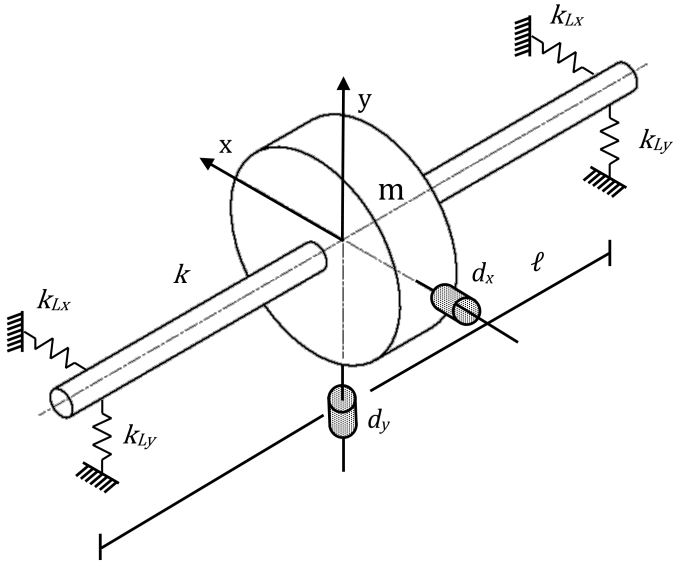


Fig. 3.13 Jeffcott rotor model

From this expression one could conceive the possibility to stiffen the shaft at the rotor's position. Taking the example of a simple Jefcott Rotor [61, 74, 35]. The model Fig. 3.13 is composed of a shaft of length ℓ and stiffness k. In the middle sits a cylindrical disc of mass m with a damping d_x and d_y at each respective direction x and y. The shaft is hold at both ends by two identical bearings with a stiffness k_{Lx} and k_{Ly}. The total stiffness k_x and k_y can be evaluated in each respective direction x and y.

$$k_x = \frac{2k\,k_{Lx}}{k + 2k_{Lx}} \tag{3.38}$$

$$k_y = \frac{2k\,k_{Ly}}{k + 2k_{Ly}} \tag{3.39}$$

From this ithe rotodynamic model of the Jeffcott rotor based on equation(3.31) was obtained. The force f_g due to the weight of the disc was also introduced in the model.

$$m\ddot{x} + d_x\dot{x} + k_x x = 0 \tag{3.40}$$

$$m\ddot{y} + d_y\dot{y} + k_y y = f_g \tag{3.41}$$

Therefore the natural frequency ω of the system can be calculated to be:

$$\omega_x = \sqrt{\frac{k_x}{m}} \tag{3.42}$$

$$\omega_y = \sqrt{\frac{k_y}{m}} \tag{3.43}$$

As well as the natural frequency of the damped system frequency ω_d depends on the damping factor D

$$\omega_{dx} = \omega_x\sqrt{1 - D_x^2} \tag{3.44}$$

$$\omega_{dx} = \omega_y\sqrt{1 - D_y^2} \tag{3.45}$$

$$D_x = \frac{d_x}{2\sqrt{k_x m}} \tag{3.46}$$

$$D_y = \frac{d_y}{2\sqrt{k_y m}} \tag{3.47}$$

Looking at the critical frequencies of that simple Jeffcott rotor, it was observed that the stiffness has a direct impact on the natural frequency of the system. Even in more complex system this will stay true even though it might not look as explicit that the results given equations(3.42 to 3.47) [34, 21]. Therefore, one can think about injecting the forces created by the BLM under the form of a stiffness k_{BLM} as presented earlier in equation(3.35). Applied to the Jeffcott rotor obtained a resulting natural frequency ω_{BLM} that increases as the value of k_{BLM} increases.

$$\omega_{BLM\ x} = \sqrt{\frac{k_x + k_{BLM}}{m}} \tag{3.48}$$

$$\omega_{BLM\ y} = \sqrt{\frac{k_y + k_{BLM}}{m}} \tag{3.49}$$

Following this one could oven consider the addition of a damping from the BLM d_{BLM}.

$$\omega_{BLM\ dx} = \omega_{BLM\ x}\sqrt{1 - D_{BLM\ x}^2} \tag{3.50}$$

$$\omega_{BLM\ dx} = \omega_{BLM\ y}\sqrt{1 - D_{BLM\ y}^2} \tag{3.51}$$

$$D_{BLM\ x} = \frac{d_x + d_{BLM}}{2\sqrt{(k_x + k_{BLM})m}} \tag{3.52}$$

$$D_{BLM\ y} = \frac{d_y + d_{BLM}}{2\sqrt{(k_y + k_{BLM})m}} \tag{3.53}$$

But that impact does not necessary change the value of the natural frequencies as much as the stiffness. But they will reduce the amplitude of the response at those frequencies.

Now that the study has illustrated on this simple model how the BLM could change the critical speeds of a shaft by injecting a force that can be associated to stiffness, it still needs to demonstrate its application with the FEM model.

3.2.3 Demonstration with a rotodynamic FEM

3.2.3.a Single shaft FEM

Using rotodynamic FEM introduced in 3.1.1 a single shaft system is going to be used with the BLM Fig. 3.14. In this model it was considered that the BLM is firmly attached to the system's structure. Resulting in a stiffness $K_{Stator+Connector}$ being so big that it won't influence on the value of K_{BLM} presented in equation (3.35). So that it can be simplified to $K_{BLM} = K_{airgap} + K_{BLM}$. The model used is illustrated in Fig. 3.14 and its different components are described in Table 3.3. The system will be operating between a rotating speed of 0 to 3000 rpm.

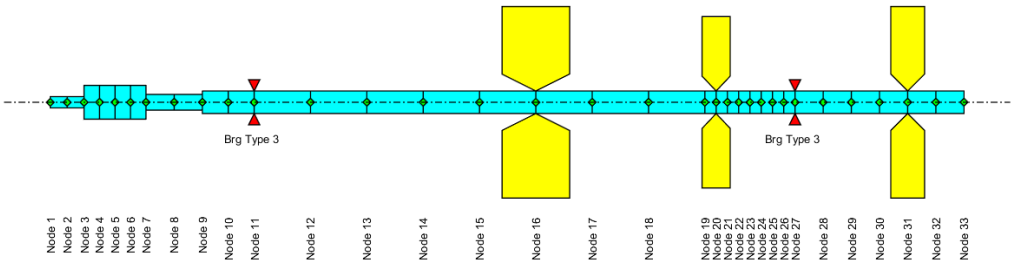


Fig. 3.14 Single shaft model example

Table 3.3 Components description for the single shaft system

Element	Nodes	Parameters					
		D_{outer}	D_{inner}	$\ell_{element}$	E	G	ρ
Shaft	1→3	10 mm	0 mm	15mm	$1.9 \cdot 10^{11}\ Pa$	$7.6 \cdot 10^{10}\ Pa$	$8000\ kg/m^3$
	3→7	30 mm	0 mm	13.75 mm			
	7→9	14 mm	0 mm	25 mm			
	9→11	20 mm	0 mm	23 mm			
	11→19	20 mm	0 mm	50 mm			
	19→27	20 mm	0 mm	10 mm			
	27→33	20 mm	0 mm	25 mm			
		D_{outer}	D_{inner}	Thickness			ρ
Discs	16	170 mm	20 mm	60 mm			$8000\ kg/m^3$
	20	152 mm	20 mm	25 mm			
	31	170 mm	20 mm	30 mm			
		k_x and k_y			d_x and d_y		
Bearings	11	$1 \cdot 10^{10}\ N \cdot m^{-1}$			$300\ N \cdot s \cdot m^{-1}$		
	27	$1 \cdot 10^{10}\ N \cdot m^{-1}$			$300\ N \cdot s \cdot m^{-1}$		
		k_{airgap}		max k_{BLM}	d_{BLM}		
BLM	3→7	$-8 \cdot 10^5\ N \cdot m^{-1}$		$9.44 \cdot 10^5\ N \cdot m^{-1}$	$10\ N \cdot s \cdot m^{-1}$		

Table 3.4 Natural frequency for both cases

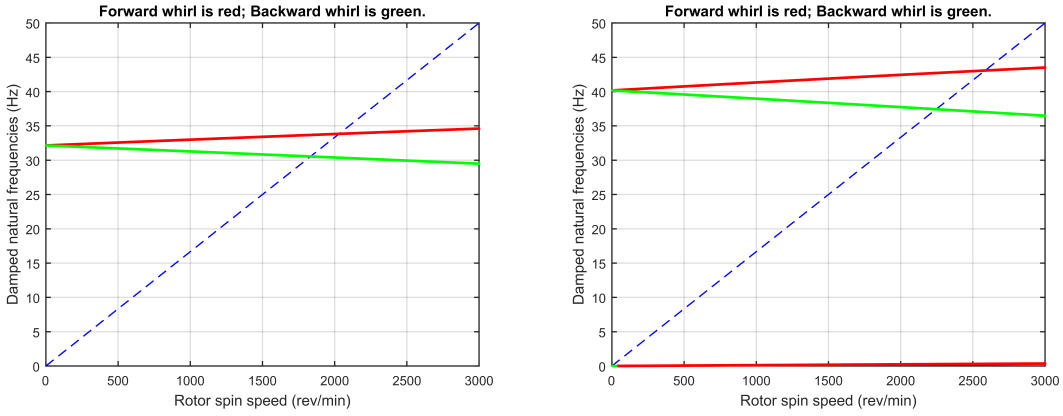
Mode	Case A		Case B	
	backward whirl	forward whirl	backward whirl	forward whirl
1	1800 rpm	2020 rpm	2246 rpm	2584 rpm

From then on one can study the impact of BLM through the implementation of a stiffness K_{BLM} on the shafts in two ways:

A. Consider a permanent compensation for k_{airgap}. Therefore, having $k_{BLM} \in [\,0;\ max\, k_{BLM}]$

B. Not compensate the effect of k_{airgap}. Therefore, having $k_{BLM} \in [\,k_{airgap};\ max\, k_{BLM}]$

So first step of the study will be to obtain the Campbell graph for model. This will allow us to know the critical speeds or natural frequencies of the shaft.This for both cases enumerated before. The first thing that was noticed from those two Campbell graph in Fig. 3.15 is that their natural frequencies are different as shoen in Table. 3.4. This demonstrates again the possibility of impacting the natural frequencies of the shaft via a BLM. As in case A it started with a stiffness at the BLM of $0\ N \cdot m^{-1}$ and B with $-8 \cdot 10^5\ N \cdot m^{-1}$.



(a) Case A (b) Case B

Fig. 3.15 Campbell graph for the initial c

The next step is to introduce a variation of the stiffness k_{BLM}. For each of the cases a graph representing the critical speeds evolving with the stiffness was created. On the same graph the amplitude of the response of shaft at node 16 at the center of the shaft were added. To do so, first k_{BLM} will need to be defined for both cases A and B Fig. 3.16. As both case overlap between $[0;\ max\, k_{BLM}]$ the case B will only be studied on stiffnesses between $[k_{airgap};\ 0]$. For this purpose parabolic curves were used as described in equation(3.54) with

31 data points n so that $n \in \mathbb{N} \in [0,\ 30]$. The functions for the two cases have been selected to illustrate the best some points of the next paragraphs. Inserting this value of k_{BLM} into the described model. So that for each value of stiffness the critical speed and the response at node 16 was calculated. The result is then compiled in Fig. 3.17 highlighting the results for both cases.

$$K_{BLM}(n) = \begin{cases} 9.44 \cdot 10^5 \cdot \dfrac{e^{\,0.1n} - 1}{e^{\,3} - 1} & \text{Case A} \\ -\frac{8 \cdot 10^3}{9}\, n^2 + \frac{16 \cdot 10^3}{6}\, n - 8 \cdot 10^5 & \text{Case B} \end{cases} \tag{3.54}$$

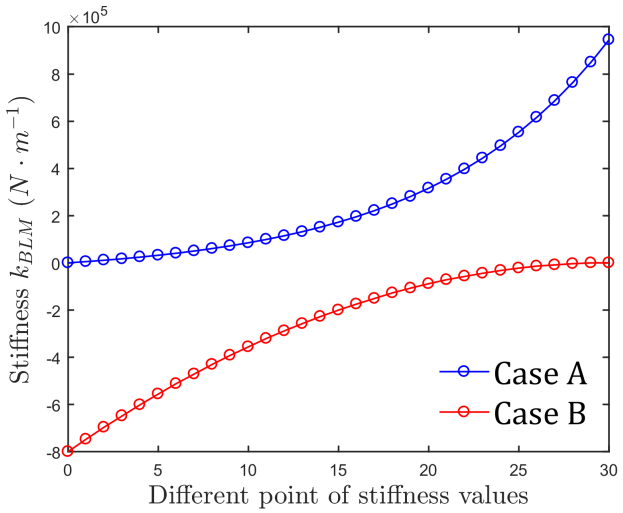
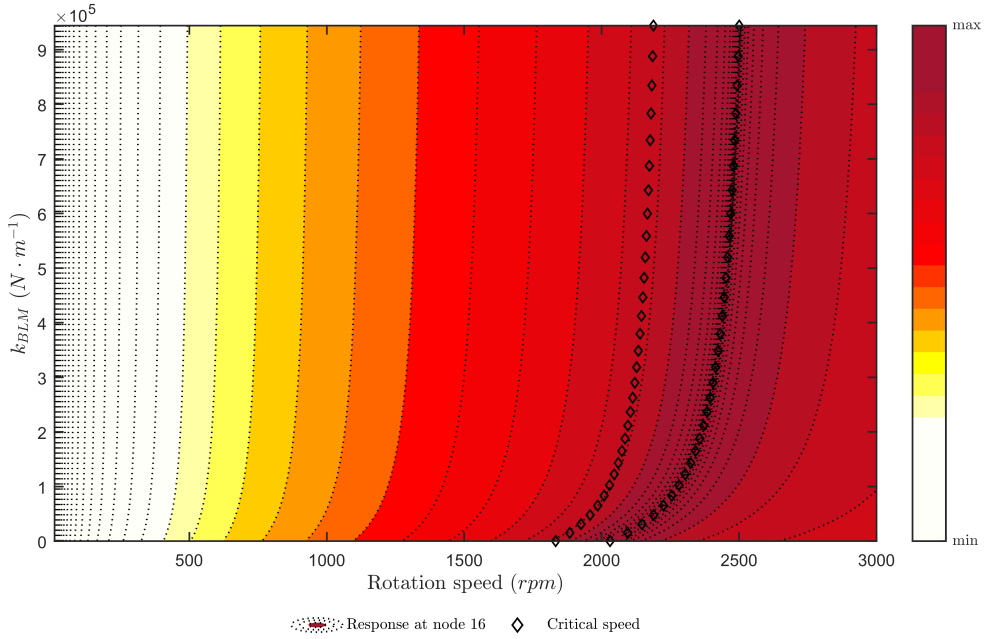


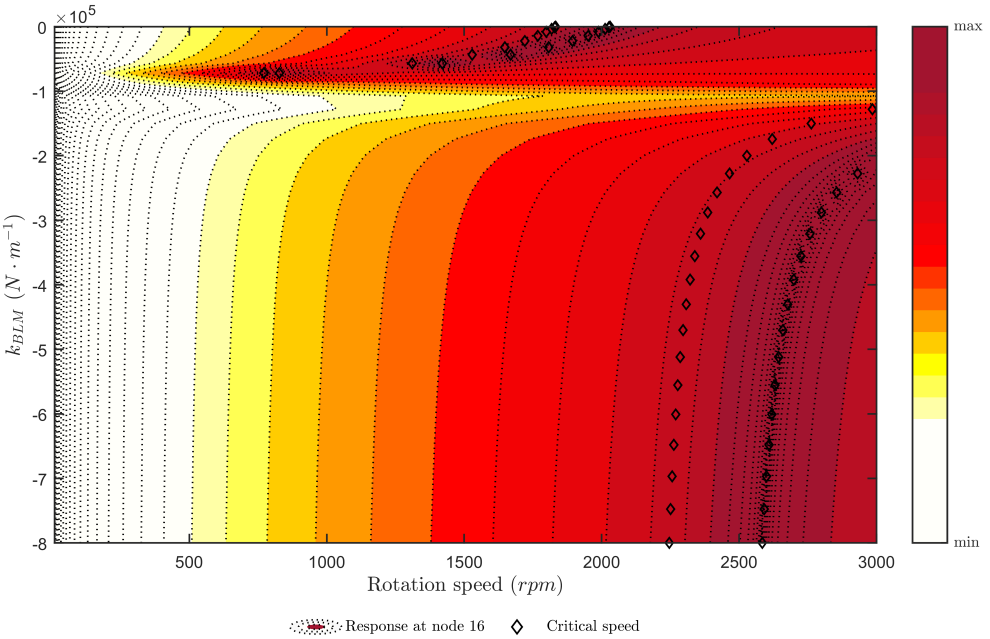
Fig. 3.16 Variation of the stiffness k_{BLM} for case A and B

For the two cases described in Fig. 3.17 one can observe that the peaks of frequencies are obtained on forward whirl natural frequencies. Therefore, the attention will be concentrated on the effect of the BLM mainly on those types of natural frequencies. At first for Case A Fig. 3.17a it can be observed that a shift of the natural frequency of the shaft toward higher frequency values happens. However, the increase of the stiffness required for the displacement of a natural frequency is exponential. Meaning that only $k_{BLM} \in [0;\ 4 \cdot 10^5\ N \cdot m^{-1}]$ will have a significant effect on the push of the shaft's critical speed. The results are quite encouraging as they show that the system can push the natural frequency of shaft by applying a stiffness k_BLM.

On the other hand in case B the critical speed starts at a higher values of speed 2584 rpm. This was already show on the Campbell graph of Fig. 3.15b. Like previously the increase of the stiffness k_{BLM} results in a push of the critical speed. However, in contrary to case A, now the effect of k_{BLM} seems to affect the push of the critical speeds at an exponential rate.



(a) Case A



(b) Case B

Fig. 3.17 Variation of the Critical speed of shaft for two cases

Furthermore, around a stiffness of $-1 \cdot 10^5\ N \cdot m^{-1}$ it was noticed that the critical speeds shifts suddenly to lower values (around 800 rpm). From then the critical speeds are push again like they are in case A. The presence of that sudden shift is due to the apparition of a new natural frequency at lower rotation speeds. On the other hand the previously observed critical speed from $[-8 \cdot 10^5;\ -1 \cdot 10^5]\ N \cdot m^{-1}$ is still continuing to increase. But the apparition of this new Critical speed will potentially lead to some challenges. If by inadvertence a stiffness too high is applied, pushing the newly appeared critical speed toward the operating rotating speed this could have catastrophic results.

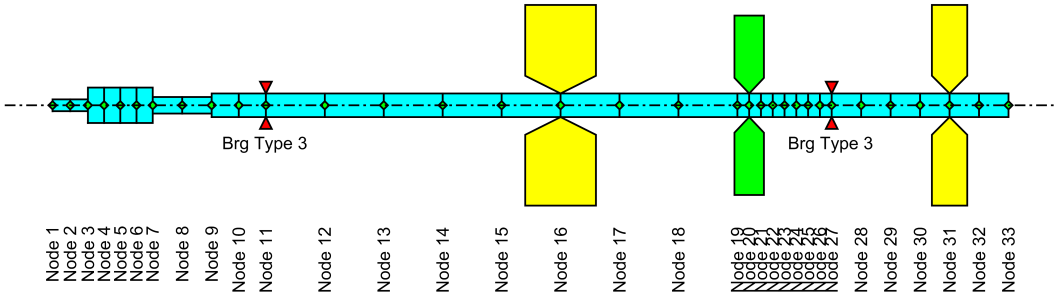
A more precise description of the critical speeds variation with the stiffness can be found in B.1 Table. B.1

Based on those observation it can be concluded that the BLM can effectively provide an impact on the rotodynamic of a shaft, using the forces F_{BLM} applied by the BLM so that it is under the form $F_{BLM} = k_{BLM} \times q$. As discussed two choices are available: either to permanently compensate for the negative stiffness created by the magnets in the air gap or to allow the possibility to keep this negative stiffness in place. On one hand the constant compensation of the negative stiffness could add a strain on the BLM or would require to dimension it so that it is capable to produce this compensation. On the other hand by having no compensation it runs into the risk of the apparition of new critical speeds that might overlap with the current operating speed. Furthermore the variation rate of the critical speed value is more advantageous in the case of magnet compensation requiring less stiffness injection. The next step is now to investigate the impact the BLM will have, using this methodology, on a geared system.

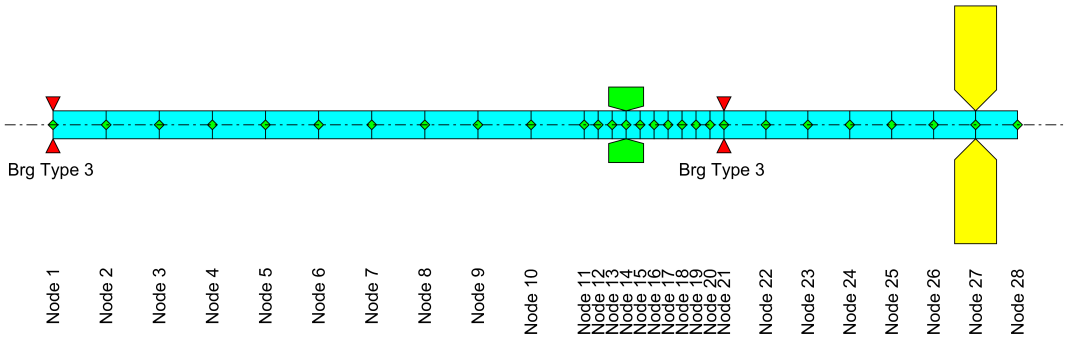
3.2.3.b Multi-shaft FEM (geared system)

From here on it will be assumed that the system (BLM) compensates for the negative stiffness created by the magnets in the air-gap. In order to observe the effect of the BLM on a geared system the same shaft than in 3.2.3.b was used and connect it to a second shaft. Going through the same procedure an FEM of the geared system was created Fig. 3.18. The model is also described in detail in B.2, Table. B.2 and B.3. The speed ratio matrix γ for this model has been set as $\begin{bmatrix} 1 & 3 \end{bmatrix}$, so that if the first shaft has an operating speed of $0 \rightarrow 3000\ rpm$ the second one has it from $0 \rightarrow 9000\ rpm$. As usual the first step is to draw the Campbell graph of the system. This will allow to have a view of the different natural frequencies of our system as well as potentially identify which one are forward or backward whirls.

In Fig. 3.19 it can be observed that adding another shaft to the system changed completely the Campbell graph from the one shown in Fig. 3.15a. Furthermore, the figures highlights



(a) Shaft 1



(b) Shaft 2

Fig. 3.18 FEM of the geared model

that all the natural frequencies are mixed whirls. Comparing the critical speeds of the shaft in Table 3.5 confirms even further the impact of adding the second shaft.

Following this will look at the impact that the BLM will have on the geared system with the stiffness injection. Fig. 3.20 illustrates the impact of the BLM on the 2 shafts. The main remarks that can be done regarding those results are again the difference from the one obtained for a single shaft. However, what is even more striking is that some the natural frequencies do not seem to be affect significantly by the stiffness injection. The first natural frequency varies only from 1728 $rpm \rightarrow 1737\ rpm$, changing the natural frequency by only 0.5 %, which can fairly be assumed as being a negligible variation. From this it could therefore be concluded that with the connection of the shafts the BLM's interaction with critical speeds will potentially be mitigated. However, the study wants to investigate the

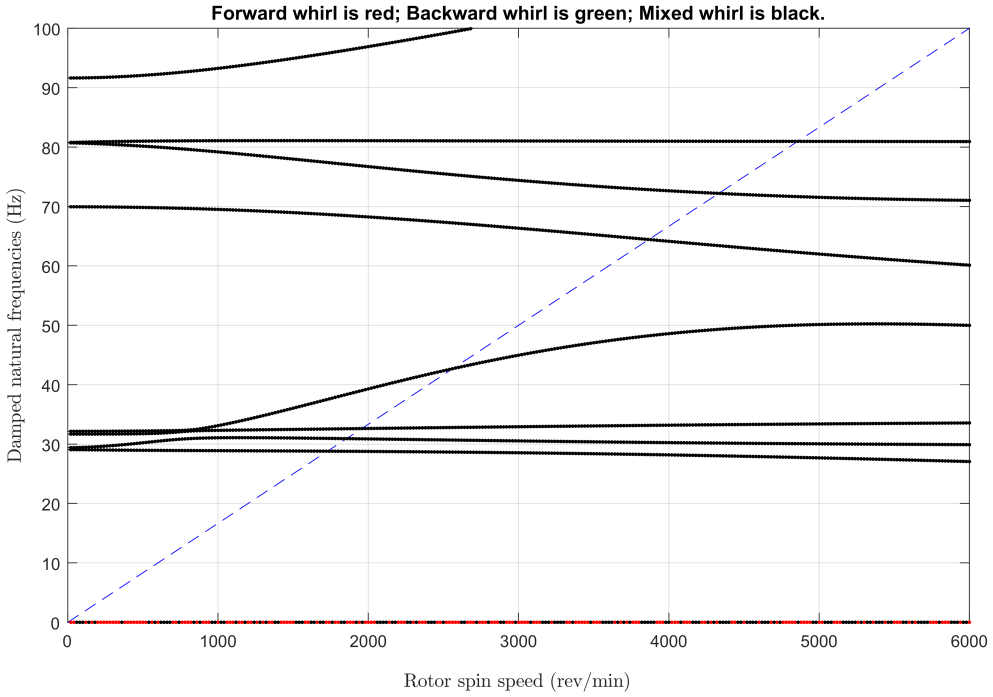


Fig. 3.19 Geared system Campbell graph.

Table 3.5 Natural frequency for a single shaft and a geared system

Critical speeds	Whirl	Single shaft			Geared system (2 shafts)		
		backward	forward	mixed	backward	forward	mixed
		1800 *rpm*					0 *rpm*
			2020 *rpm*				1728 *rpm*
							1855 *rpm*
		Out of operating range					1957 *rpm*
							2561 *rpm*

reason leading to the ineffectiveness of the BLM with a geared system. To investigate this the impact of changing either the inertia on shaft 2 or the gear ratio γ_2 of the gears on the effectiveness of the proposed strategy will be studied.

First the effect of the speed ratio γ_2 on the system was investigated. Fig. 3.21 show the response of our system with a $\gamma_2 = 2$. From the results presented on Table. 3.6 it can be assumed that the speed has a small impact on the variation of the critical speeds. However, for a lower gear ratio one of the last critical speeds seems to increase its variation potential.

Looking at the effect of the inertia in the second shaft, Table. 3.7 shows the critical speeds and their variation with the change of the inertia's diameter. The reduction of the

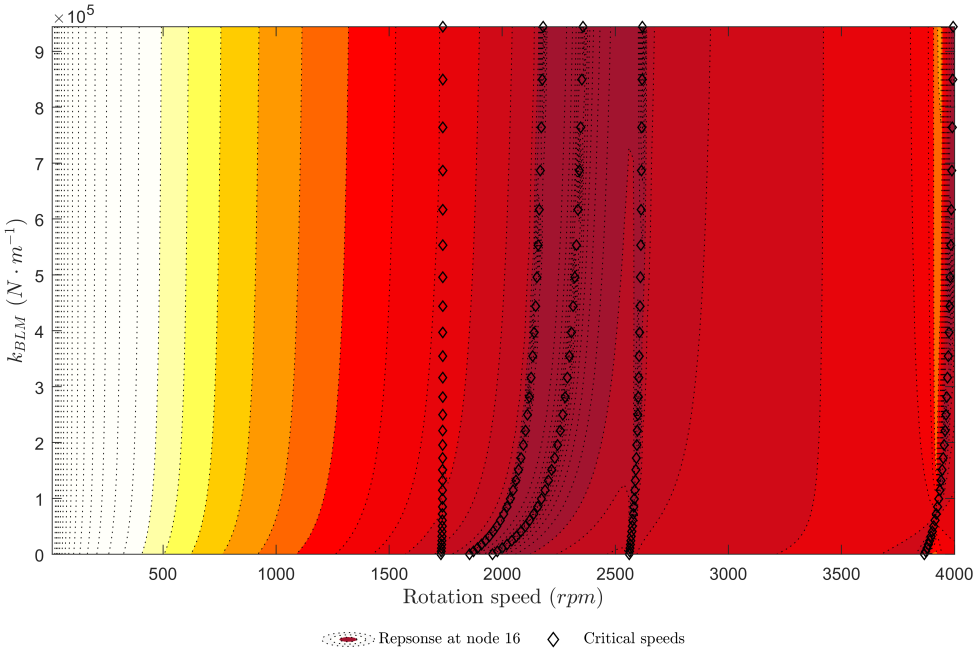


Fig. 3.20 Variation of the Critical speed of the 2 shafts system

Table 3.6 Influence of the ratio γ on the critical speeds

γ_2	Critical speeds in rpm											
	1			2			3			4		
	min	max	diff	min	max	diff	min	max	diff	min	max	diff
4	1728	1737	9	1856	2205	349	1957	2358	401	2945	2983	38
3	1728	1737	9	1855	2181	326	1957	2357	400	2561	2620	59
2	1729	1737	8	1852	2052	200	1957	2318	361	2144	2364	220

inertia brought an increase of the values of the critical speeds. But it also allowed for an increase in the variation of the critical speeds that were previously low. But one must note that parallel to this the ones with higher variation did decrease. However, reducing the inertia it further only exacerbated the issue and created 2 new unusable natural frequency for the critical speed push. This investigation showed that certain configuration of system won't allow for the optimal use of the BLM as a critical speed changing actuator. Which means some consideration should be taken on the when the BLM is used on connected shafts. For example the inertia of the shafts connect to one where the BLM is located have to be ensure to not be too high.

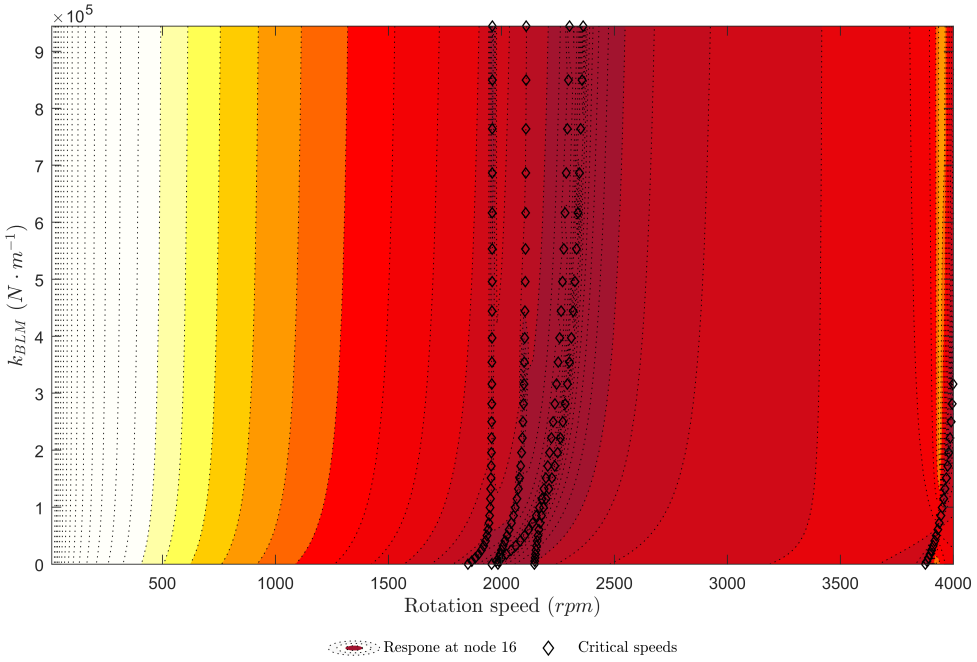


Fig. 3.21 Variation of the Critical speed of the 2 shafts system with $\gamma_2 = 2$

Table 3.7 Influence of the inertia on the critical speeds

Inertia's diam *mm*	Critical speeds in *rpm*											
	1			2			3			4		
	min	max	diff	min	max	diff	min	max	diff	min	max	diff
170	1728	1737	9	1855	2181	326	1957	2357	400	2561	2620	59
150	1846	1957	110	1956	2160	204	1984	2342	358	2251	2373	86
120	1880	2244	364	1956	2358	402	2422	2442	20	2710	2725	25
100	1897	2288	391	1958	2361	403	2850	2854	4	2710	2725	15

3.3 Critical speed avoidance strategy

I was shown in 3.2.3 that the BLM could help to "push" the critical speed of the shaft. In 3.2.3 two different case of use of the BLM where shown and their impact on the natural frequencies of the shaft. Now that those option are available a a strategy to use that functionality advantageously will have to be found. Two main possible use of this BLM interaction have been identified:

A. Permanently push the natural frequencies outside of the band of operational speeds.

B. Push the natural frequencies away from the current operating speed, as it approaches a critical speed.

Stemming from those two propositions different strategy variations can be imagined and they will be discussed in the following paragraphs

.

3.3.1 Critical speed push

The first one (A.) has the advantage that it is simple. It only requires to find out the stiffness needed to be added to the shaft in order to set all critical speeds of the shaft away from the band of speeds used during the process. However, this means that the BLM will have to be able to provide the stiffness required to push all the natural frequencies out of the used band. This might lead to a large increase in the dimension of the BLM as the force/stiffness provided by it directly depends on the current I_s feed in its coils. So that for a constant displacement q in order to increase the stiffness k_{BLM} it will require to increase the current equation (3.57).

$$f_{BLM} = k_{BLM} \times q \tag{3.55}$$

$$f_{BLM} = Cst_{\ BLM} \times I_s \tag{3.56}$$

$$k_{BLM} = \frac{Cst_{\ BLM}}{q} \times I_s \tag{3.57}$$

So from this a strategy can be defined following those simple steps:

1. Set a model of the shaft or shaft system you wish to control.
2. Obtain the variation of the shaft's natural frequencies with the stiffness.
3. Choose a stiffness so that no critical speeds are in the selected operational speed range.
4. Apply the stiffness in the BLM's control.

The search for that particular stiffness k_{BLM} that will fulfill the requirement of step 3. of strategy A. is illustrated in Fig. 3.22. Where in a purely illustrative example it can be seen that it would need a permanent injection of $3.8 \cdot 10^{\,5} N \cdot m^{-1}$ with the BLM.

The clear advantage of this strategy is that you only need to find the particular stiffness you need for any situation and do not need to worry about any changes to your controller. This solution being quite simple is quiet inefficient as it will require a constant application of

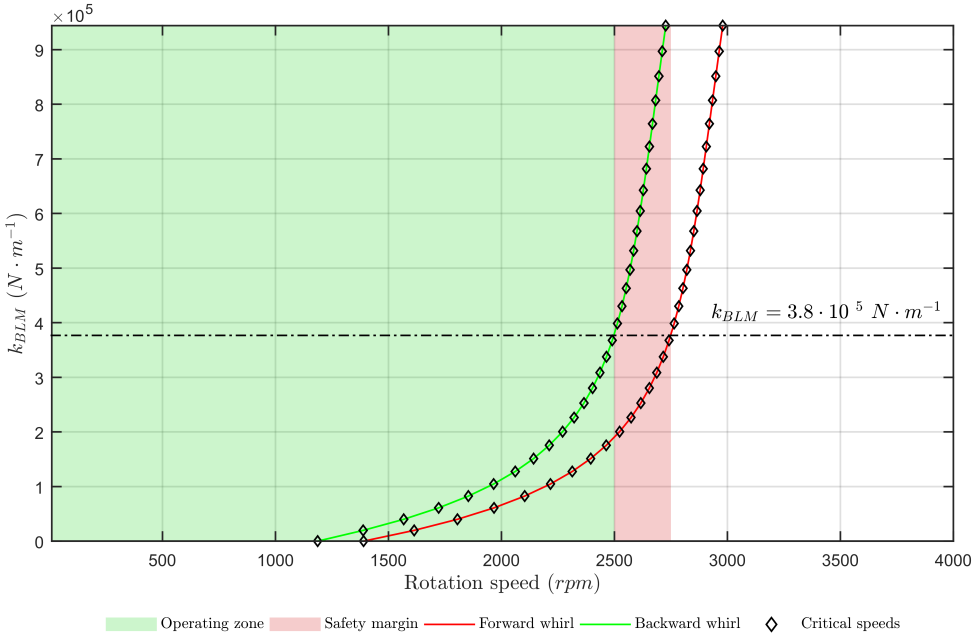


Fig. 3.22 Demonstration of the Strategy A.

a potentially high stiffness to the shaft. This would mean that possibly high currents will be demanded to the BLM. Furthermore, for all the moments where there wouldn't have been any natural frequency in the operational speed band, it is injecting a stiffness that wouldn't have been necessary in the first place. Looking at this it can be suggested to not add any stiffness in bands where there wouldn't be natural frequency. This leads naturally to the second strategy (B.) proposed previously .

3.3.2 Critical speed hopping

Following the previous discussion, a control strategy that involves applying stiffness to a shaft only as it approaches critical speeds will be considered. In the same way some controllers propose to set some critical speeds where the devices avoids the speed by suddenly accelerating or decelerating through them, the BLM is going to inject a stiffness around the natural frequencies of the shaft. However, with the use of the stiffness only around natural frequencies there should be a margins so that shaft can hop the frequency before it reaches the critical speed, and at the same time also allowing for the possibility that the actual critical speed might deviate a bit from the one found in the theory. Therefore, for each natural frequencies the BLM will has to decide which stiffness it will have to inject. Furthermore,

the sign of the acceleration will matter in that strategy, so that the BLM will have to switch the stiffness on and off at different speeds depending on the acceleration's sign/direction. This is illustrated in Fig. 3.23 where the different lines (blue dashed) where the stiffness injection system is turn on or off at each crossing are drawn. The strategy is defined in detail as follows:

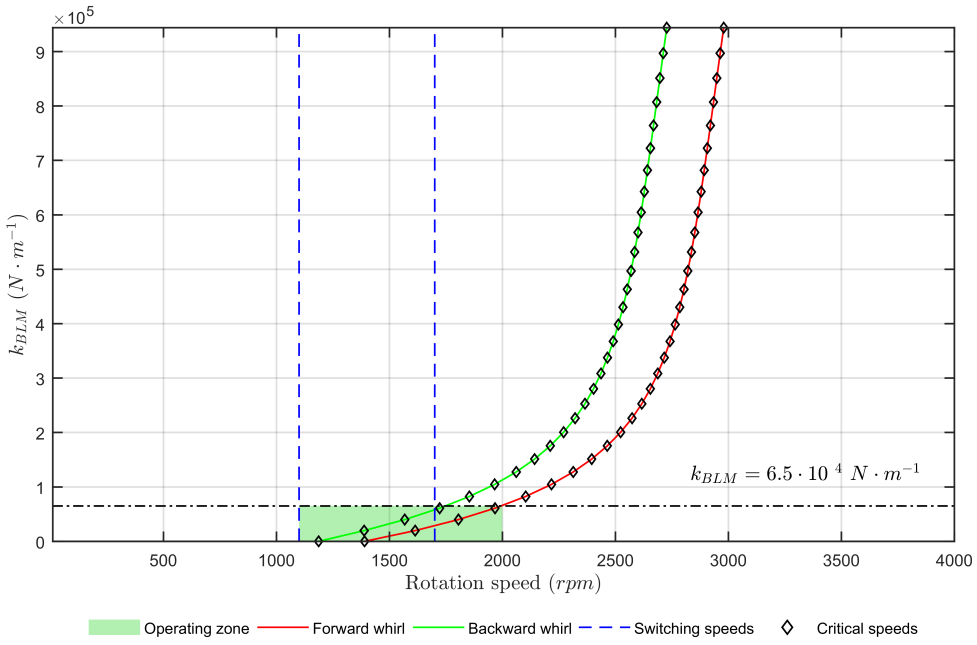


Fig. 3.23 Demonstration of the Strategy B.

1. Set a model of the shaft or shaft system you wish to control.
2. Obtain the variation of the shaft's natural frequencies with the stiffness.
3. Choose a stiffness to inject for each natural frequency of the shaft to create a safe "hopping".
4. Prepare a look up table with all the stiffness and their respective speed bands and switches as shown in Table 3.8.
    - Switch_ID are the indices of the two following look-up tables.
    - Switch_speed is filled with all the switching speeds that have been defined like in Fig. 3.23.

- Stiffness contains all the values of k_{BLM} for the different band of critical speed hopping.

5. Implement the algorithm given in Fig. 3.24 as a Logic Flowchart to the control. This will enable the BLM to perform the critical speed hopping.

For the purpose of illustration the margin in Fig. 3.23 around the critical speed has been set very large. Nevertheless, the stiffness k_{BLM} required by this strategy is significantly lower than the one proposed in 3.3.1.

Table 3.8 Look-up table for critical speed hopping

Look-up table	Data points					
Switch_ID	1	2	3	4	...	end
Switch_speed (rpm)	$Speed_1$	$Speed_2$	$Speed_3$	$Speed_4$	...	$Speed_{end}$
Stiffness $(N \cdot m^{-1})$	0	$Siffness_1$	$Siffness_2$	$Siffness_3$	...	$Siffness_{end}$

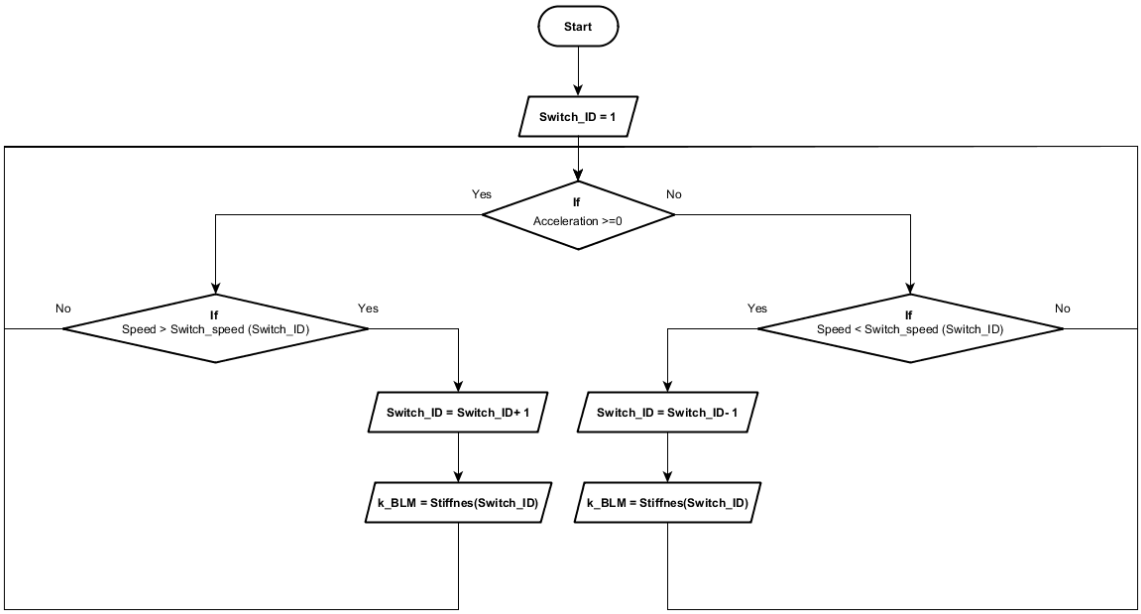


Fig. 3.24 Logic flow chart of the Strategy B.

However, one has to be careful that the stiffness injected will not push another critical speed near the current operating point. Moreover, there is a need to pay attention that the shaft won't fall on the new critical speed after having passed a critical speed and stopped the stiffness injection. This will therefore require some sort of countermeasure during the

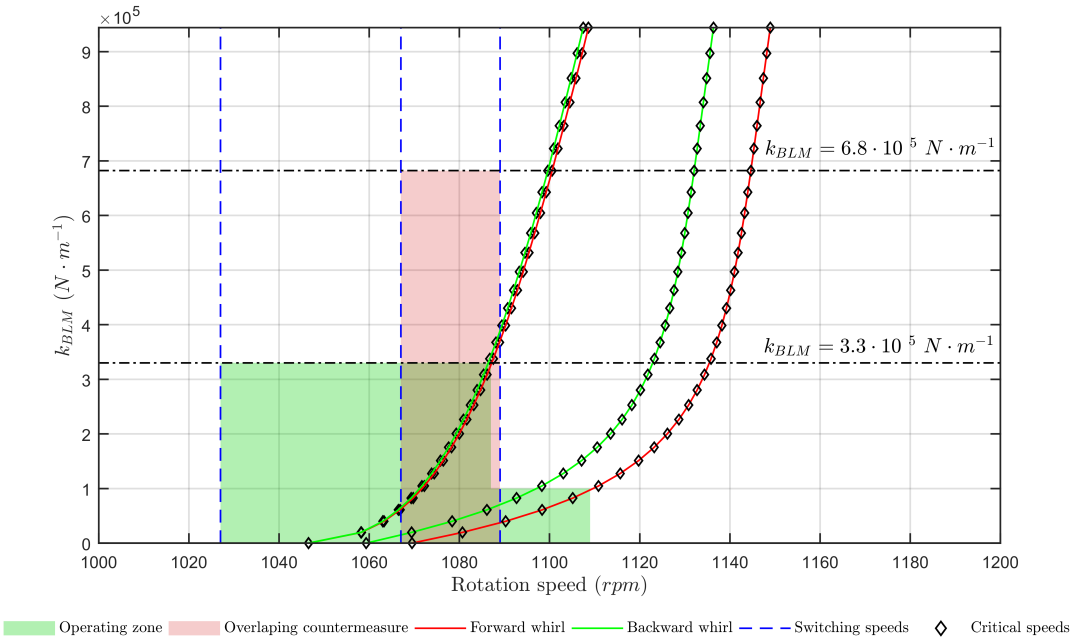


Fig. 3.25 Demonstration of the Strategy B. with overlapping

Table 3.9 Look-up table for an overlapping situation

Look-up table	Data points			
Switch_ID	1	2	3	4
Switch_speed (rpm)	1028	1067	1087	$Speed_{end}$
Stiffness $(N \cdot m^{-1})$	0	$3.3 \cdot 10^5$	$6.8 \cdot 10^5$	0

stiffness injection. This means injecting a higher stiffness at the overlapping zone so that at no point the shafts ends up resting on either of the critical speed. This is illustrated in Fig. 3.25 where the problem occurring with 2 overlapping critical speeds is illustrated. To solve this the look-up table associated to the system has to be changed to take in account this overlapping as illustrated in Table. 3.9.

Nevertheless as shown Fig. 3.26 this strategy might lead to the abrupt injection of high amount of stiffness to pass a critical speed. In order to mitigate those large sudden stiffness injection a gradual increase of stiffness by the BLM is proposed. This can be obtained either by allowing more detail in the lookup table or implementing a restriction on the slope speed of the stiffness change. Furthermore, using a gradual increase of the stiffness the BLM will be more efficient since there is a direct link between the stiffness and the value of the

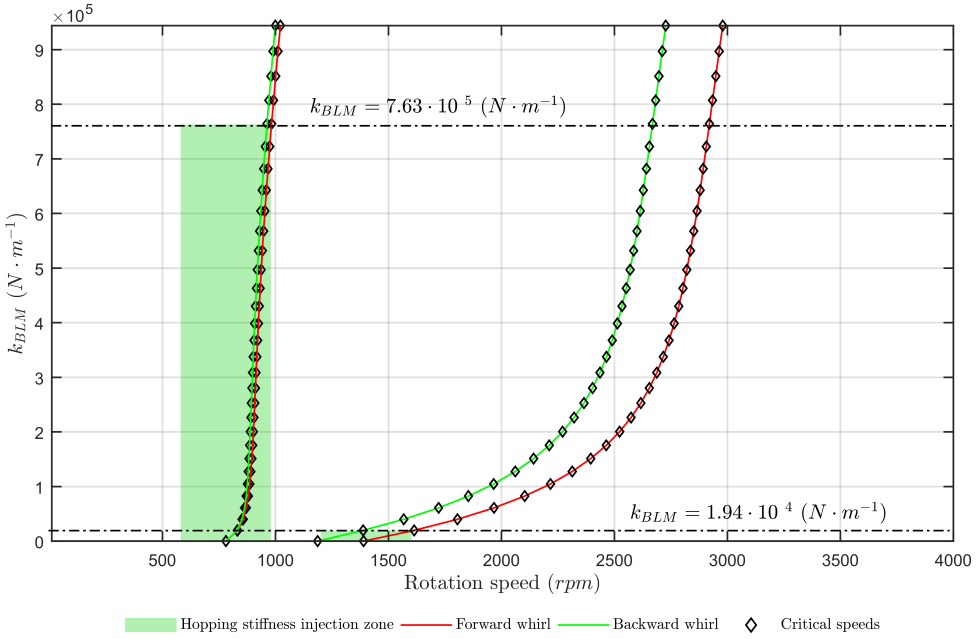


Fig. 3.26 Strategy B. with natural frequencies with high stiffness demand.

current I_s injected in the BLM as discussed in 3.3.1 . Moreover, the acceleration at which the shafts pass through the critical speeds as been shown to affect the output of the shaft's vibration [38, 44]. This incites to pay further attention at a target "speed" at which the natural frequencies of the shaft will be changed. Because as well as passing critical speeds the ideas is to maintain the vibration of the shaft as low as possible.

3.3.3 Critical speed stepping/sliding

As already pointed out in the previous section, one could think of a more efficient and safer way to change of the natural frequencies of a shaft. But as stated previously the look up table used for the control of the shaft's natural frequencies will need to be improved. They will need to include all the different possible changes on the critical speeds in order be able to vary continuously to the stiffness injected by the BLM and not suddenly inject a large amount of stiffness. This won't require more preparation work than any of the strategies presented previously in 3.3.1 and 3.3.2. As they all need a great understanding of the rotodynamic effects the BLM has on the shaft with curves like the one represented in Fig. 3.26. To answer the challenge set by the limitation of the speed hopping strategy two new methods are proposed:

1. Integrate many intermediate steps in the BLM stiffness value injection for passing a critical speed [Stepping]
2. Have a continuous various of the injected stiffness when passing a critical speed [Sliding].

3.3.3.a Stepping

Different smaller steps to push gradually the critical speed of the shaft away of the current operating speed could be used. So that instead of having a major input of stiffness for each give natural frequency, the BLM will provide smaller ones that will gradually increase (or decrease) with operating speed. From there one can describe the strategy with the following steps:

1. Set a model of the shaft or shaft system you wish to control.
2. Obtain the variation of the shaft's natural frequencies with the stiffness.
3. Prepare a look up table with all the critical speeds depending on the different values of stiffness injected in them. Considering a n natural frequencies and m different values of stiffness an $m \times n$ matrix is obtained illustrated in Table 3.10.
   - Crit_contain all the n critical speeds depending on the m values of stiffness applied by the BLM.
   - Stiffness contains all the m values of k_{BLM} applied on the shaft.
4. Implement the algorithm given in Fig. 3.27 as a Logic Flowchart to the control. This will enable the BLM to perform the critical speed stepping.

Table 3.10 Stepping look-up tables

Look-up tables				
Crit_speed	1	2	...	m
1	$Speed_{1\,1}$	$Speed_{1\,2}$	...	$Speed_{1\,m}$
2	$Speed_{2\,1}$	$Speed_{2\,2}$	...	$Speed_{2\,m}$
⋮	⋮	⋮	⋱	⋮
n	$Speed_{n\,1}$	$Speed_{n\,2}$	...	$Speed_{n\,m}$
Stiffness	$Siffness_{1}$	$Siffness_{2}$	...	$Siffness_{m}$



Fig. 3.27 Logic flow chart of the Stepping strategy

The algorithm used for this strategy, shown in Fig. 3.27 ,is decomposed into two main branches:

- acceleration
- deceleration

Both of them work on the similar principles; the principal change being the margins applied is set differently in the two branches. Therefore, for the sake of simplicity here only the acceleration phase is illustrated as the deceleration just requires a change in the margins. Furthermore, the graph presenting the stiffness injection for an acceleration scenario are much easier to read and have a better clarity.

- The first step is to check if the operating speed (Speed) is not too small compared to the next critical speed. If this is the case no stiffness injection is needed and set Stiff_ID to 1.
- If the first statement isn't true it will have to verify if the current operating speed (Speed) is high enough compared to the natural frequency. If this is the case it can consider the natural frequency passed and increase Crit_ID by 1.
- If the previous statement isn't true it are lead to two possibilities
  - If the Operating speed (Speed) is too small compared to the current natural frequency's critical speed it will reduce the stiffness infected by the BLM by decreasing Stiff_ID by 1.
  - If the Operating speed (Speed) is too big compared the current natural frequency's critical speed it will reduce the stiffness infected by the BLM by decreasing Stiff_ID by 1.
- Finally it sets $k_{BLM} = \text{Stiffness}(\text{ Stiff\_ID})$

The algorithm presented here works taking in account a list of margins m_1, m_2, ..., m_6. Those margins are user defined but in order to work properly some rules have to be applied first.

- 0 < m_1, 2, 7 and 8 < 1 $\rightarrow$ Margins before a critical speed < 1
- m_3, 4, 5 and 6 > 1 $\rightarrow$ Margins after a critical speed > 1

However, one could consider to adapt each margin of every single natural frequencies differently. So that if a system with n critical speeds is studied, the margin m_1 is described with a table: $\text{m\_1} = [\text{m\_1}_1\ \text{m\_1}_2\ \ldots\ \text{m\_1}_n]$. The margin used can be decided by looking at the theoretical response of the shaft. The margins can be chossen so that they minimize the vibration response of the shaft during the process.

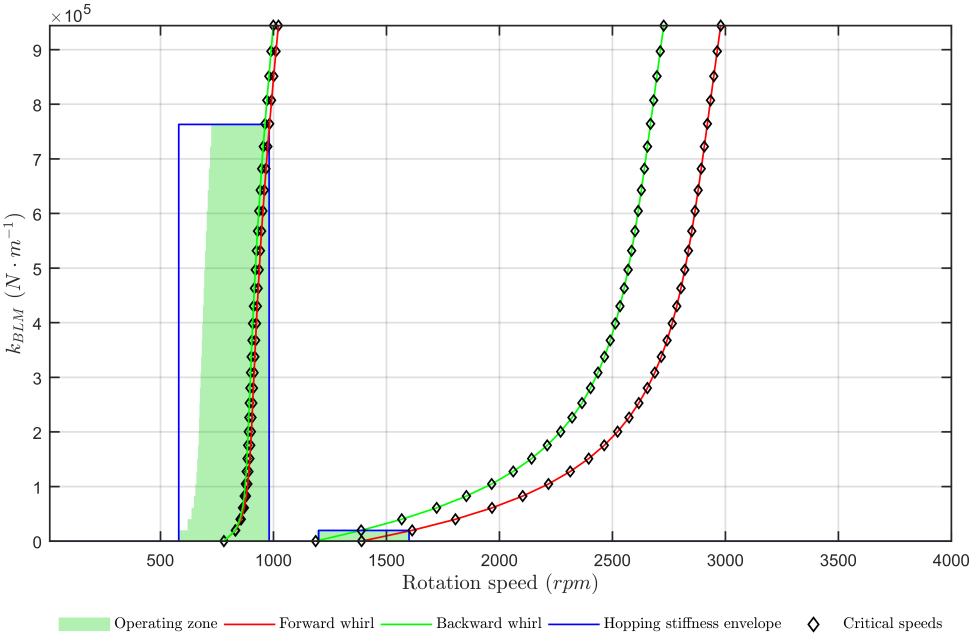


Fig. 3.28 Stepping Strategy with Hopping comparison

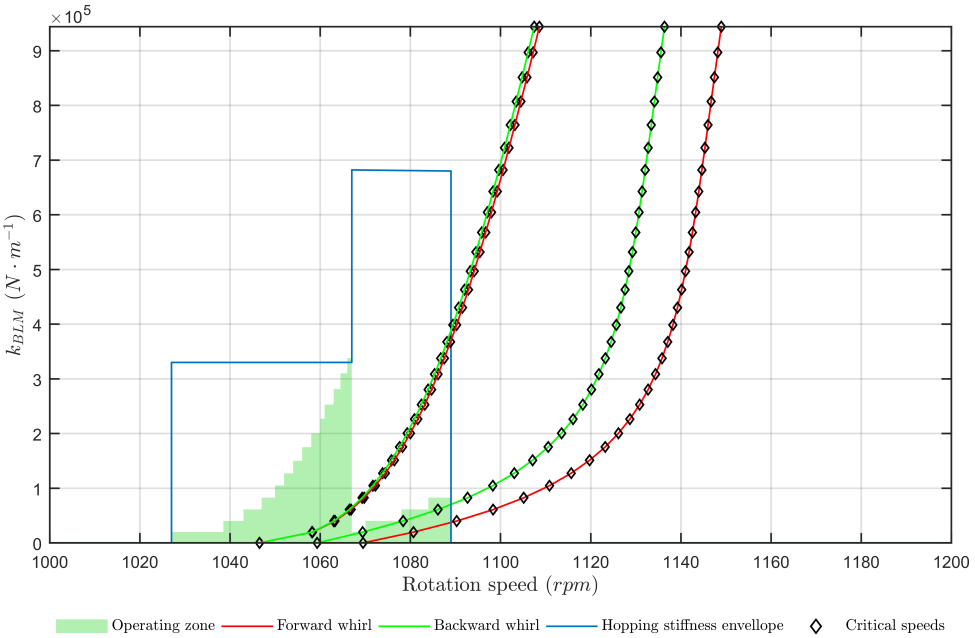


Fig. 3.29 Overlapping of natural frequencies with the stepping strategy.

One can see on Fig. 3.28 that the maximum stiffness applied is not reduced. However, one notice the band of speeds concerned by this high stiffness is significantly reduced. Looking at Fig. 3.29 it can be note that although the stiffness is reduced, the strategy does not take in account overlapping of natural frequencies. To mitigate this the logic flow chart of Fig. 3.27 has been modified. The issue with the first algorithm is that although it operates fine in most situation it does not take in consideration the values of the past natural frequencies. In Fig.3.30a it shows part of the previously used algorithm. One can see that the increase or decrease of the stiffness injected by the BLM does only depend on the critical speed values of the current natural frequency Crit_ID. This as shown in Fig. 3.29 leads to the overlapping issues. Fig.3.30b presents a solution for that problem, by integrating the critical speed of the natural frequency Crit_ID-1 into the algorithm. For the increase of the stiffness the respect the following condition will have to be verified:

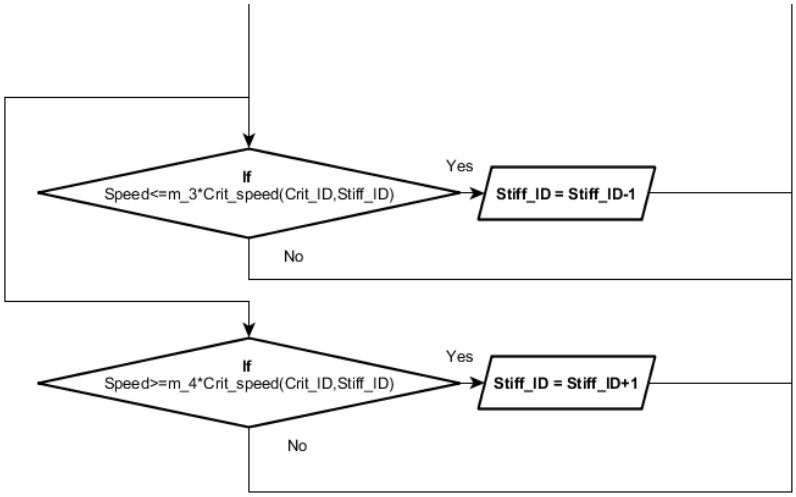
$$\begin{aligned} &\text{Speed} \geq \text{m\_4a} \times \text{Crit\_speed}(\text{Crit\_ID}, \text{Stiff\_ID}) \\ &\qquad\qquad\qquad\qquad \textbf{or} \\ &\text{Speed} \geq \text{m\_4b} \times \text{Crit\_speed}(\text{Crit\_ID-1}, \text{Stiff\_ID}) \end{aligned} \tag{3.58}$$

So that the shaft is ensured to not be too close from the current natural frequency's critical speed **or** too close from the previous natural frequency's critical speed. The same issue comes when considering the decrease of the stiffness injected by the BLM. However, this time it have to make sure the critical speed from the current natural frequency is far enough **and** the same for the previous natural frequency.

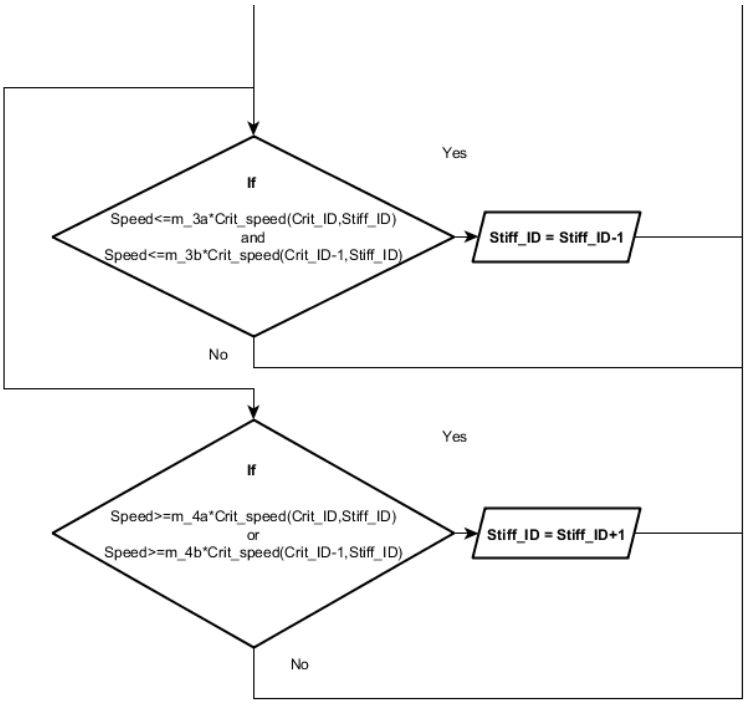
$$\begin{aligned} &\text{Speed} \leq \text{m\_3a} \times \text{Crit\_speed}(\text{Crit\_ID}, \text{Stiff\_ID}) \\ &\qquad\qquad\qquad\qquad \textbf{and} \\ &\text{Speed} \leq \text{m\_3b} \times \text{Crit\_speed}(\text{Crit\_ID-1}, \text{Stiff\_ID}) \end{aligned} \tag{3.59}$$

Changes proposed have then been implemented to the algorithm presented in Fig. 3.31 and will replace Fig. 3.27 in the control strategy for the Critical speed stepping.

With the new algorithm the overlapping scenario was reproduced, firstly to compare it to the one previously obtained in Fig. 3.29. The results of Fig. 3.32 show a clear shift compared to the previous version as the overlapping issue is now resolved. Furthermore, if comparing this result to the hopping strategy in Fig. 3.25 a clear improvement concerning the stiffness needed to be applied by the BLM to the shaft can be noted. Only a significantly smaller portion of the speed band require large stiffness injections.



(a) Algorithm with overlapping issues



(b) Algorithm to solve the overlapping

Fig. 3.30 Solution for the overlapping issue in the algorithm

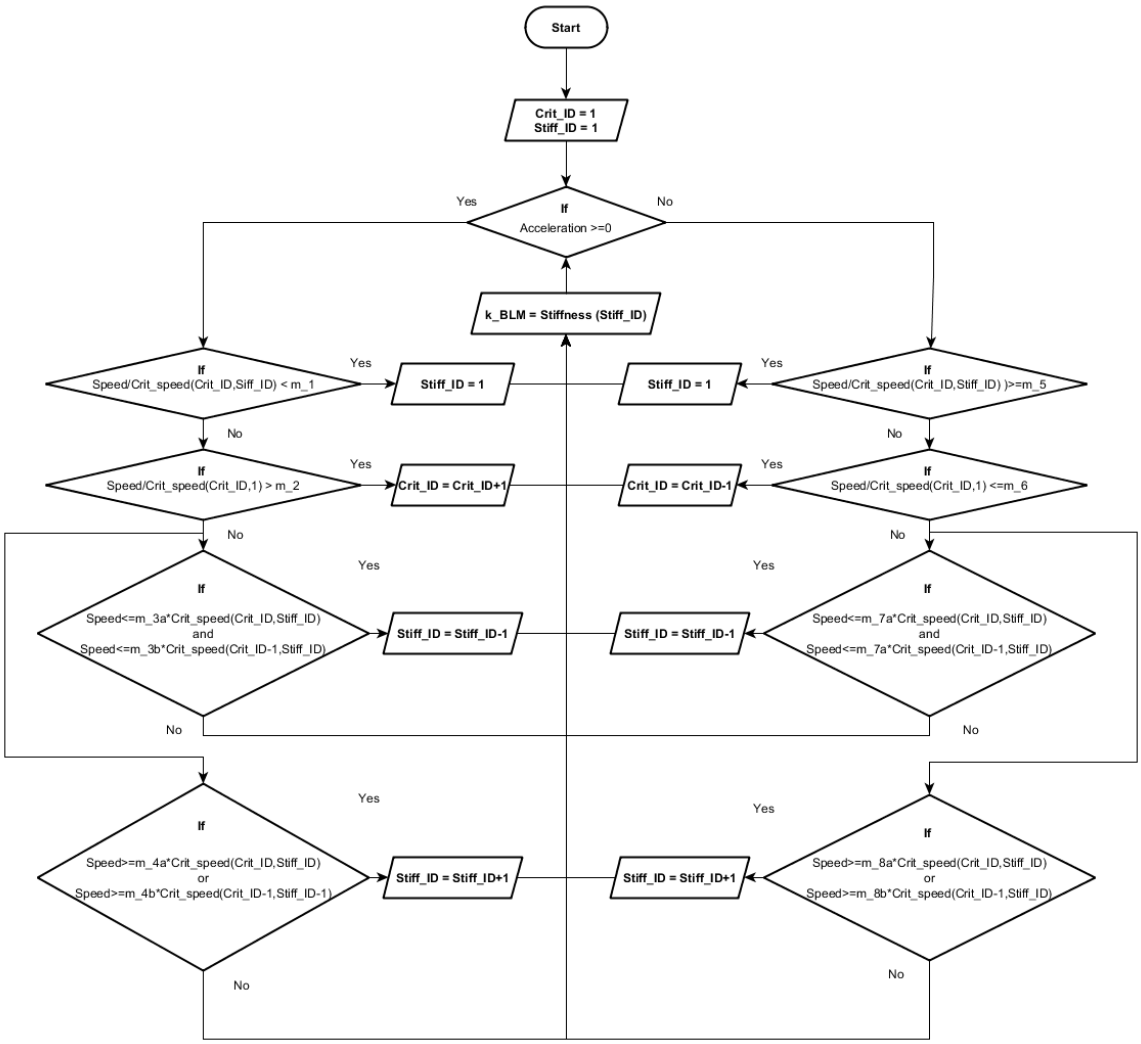


Fig. 3.31 Logic flow chart of the Stepping strategy with overlapping consideration

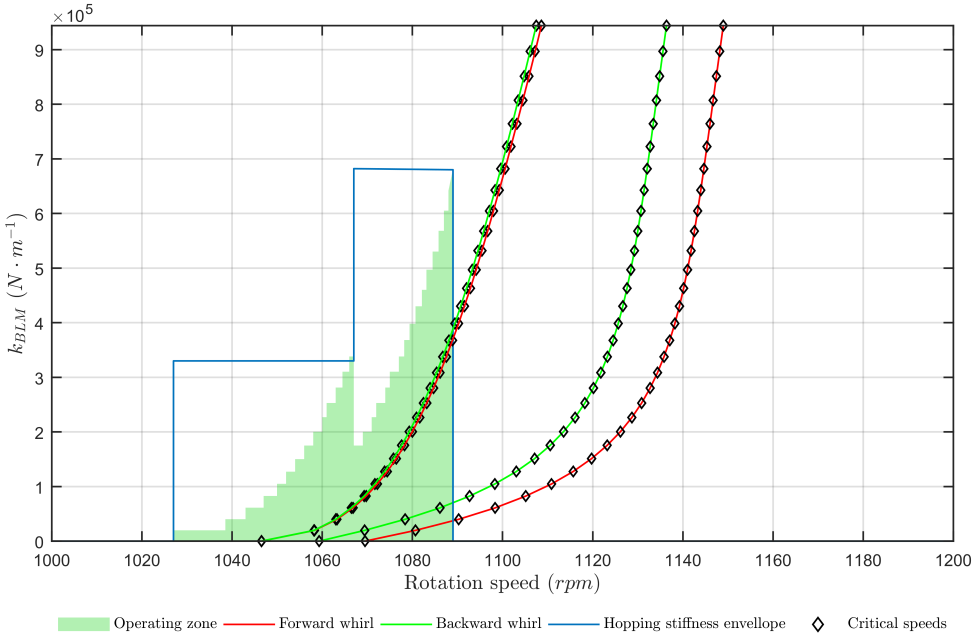


Fig. 3.32 Overlapping of natural frequencies with the modified stepping strategy.

One see that even-though this system is quite an improvement compared to the frequency hopping, the result seem to depend on the number of point m in the look-up table. The higher the number the better the precision of the system will be. But at the same time the bigger the matrix $Crit\_speed$.To mitigate that kind of problem and furthermore increase the efficiency of the system one could consider a continuous change of said stiffness. Not using a 2D look-up table but functions describing the behaviour of each natural frequency.

3.3.3.b Sliding

Following the discussion in 3.3.3.b one could imagine a continuous flow of stiffness injection instead of the previously presented steps. This will potentially improve further the efficiency at which the BLM is used. However, on the other hand this will also increase the complexity of the process needed for the control of the shaft's rotodynamic. Two ways to achieve this goal are proposed here:

1. Finding a function defining the behaviour of the critical speed with the stiffness for each natural frequency.

2. For each natural frequency the look-up table defined in Table. 3.10 could be used and use divers interpolation methods, like Spline [29, 15], to obtain piece wise functions defining the behaviour of the critical speeds with the stiffness inject in the shaft.

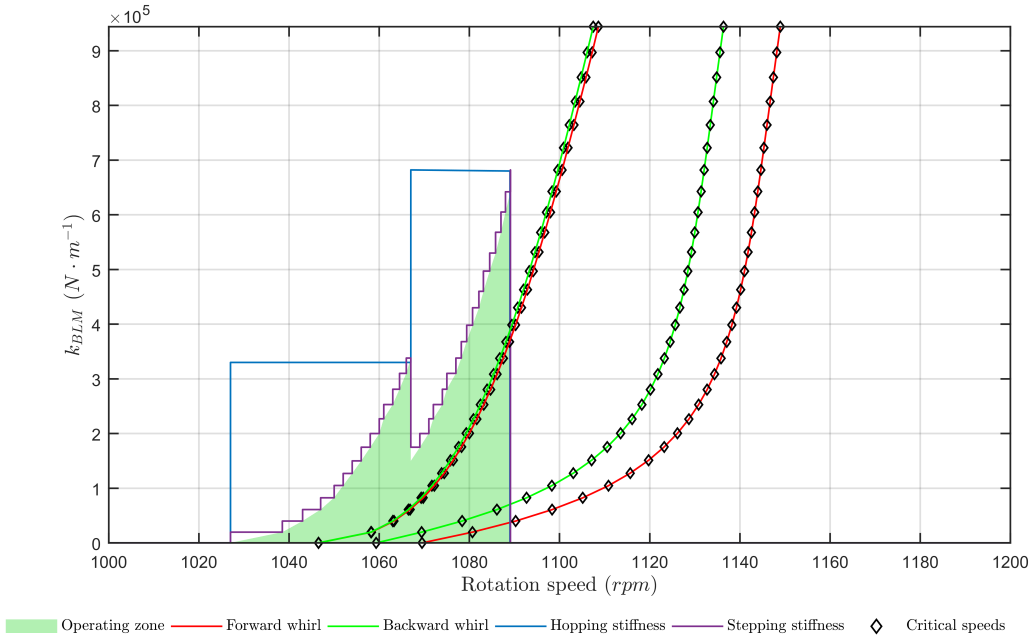


Fig. 3.33 Overlapping of natural frequencies with the sliding strategy.

Finding specific functions that would characterize each natural frequency's behaviour when subjected to a stiffness k_{BLM} was not studied further as it would require that for any changes made to a system a whole new set of function should be defined. This process will be hazardous and unpractical to automate. Due to this major reduction in flexibility it was decided to concentrate on the use of interpolations that can be easily automated from a look-up table in a software like Matlab©. Furthermore the advantage of this method is that it does not require any new strategy elaboration as it is based on the strategy and the look-up table from the stepping method.

In Fig. 3.33 the improvement given by a simple linear interpolation strategy that reduces again the requirement for stiffness injection of the BLM can be observed. It can be foresee that the use of more elaborated interpolation will further improve this.

Table 3.11 Power use for each strategy

Situation	Strategy			
	Push	Hop	Step	Slide (linear)
Overlapping	$7.4 \cdot 10^8$	$2.8 \cdot 10^7$	$1.25 \cdot 10^7$	$1.18 \cdot 10^7$

3.4 Conclusions

To sum up the different results of this chapter dedicated to the interaction of the BLM and the rotodynamics of a shaft. First a model of the shaft using FEM, based on the work of *Michael I. Friswell, Seamus D. Garvey, John E. T. Penny, Arthur W. Lees* [33, 1], was established. From this base the capability of the code was improved by including the possibility to connect divers shafts together via gears. From there the possibility to inject stiffness on the shaft using the BLM as an actuator was discussed and demonstrated in a simple example. Furthermore it was found that the injection of stiffness is able to "push" the critical speeds of a shaft. This was demonstrated on a simple example and in the FEM model. Then the most appropriate way to use this capability of the BLM to pass critical speeds of a shaft system was searched. From there several strategies to use that possibility to push critical speeds of a shaft, were devised. Each of them described in this chapter and sorted in order of simplicity.

1. Critical speed push
2. Critical speed hopping
3. Critical speed stepping
4. Critical speed sliding

Even though the strategies are becoming more and more complex they also provide a better usage of the BLM by having an economy of energy spent. If considering the area of operating stiffness for each strategy a good idea of what the power requirement of each strategy will be can be obtained. In Table. 3.11 one can observe a clear improvement of the power usage of the BLM. at the end there is almost 2 orders of magnitude of difference between the push strategy and the slide one. Using more complex strategies will therefore have a benefit on the use of the BLM by having less unnecessary strain put on it for the same result. But one has to note that regardless of the improvement of the use of the BLM, the maximum values of stiffness required are the same on the last 3 presented strategies. This will have to be taken in account during the setting up of the system.

Now that it was showed that the BLM can be used to impact the shaft's rotodynamic and pass critical speeds thanks to the different strategy proposed in this chapter. The next logical is to combine the work of Chapter.2 with the one presented in this chapter. In other words combine the electromagnetic model of the BLM and its control with the rotodynamic modeling and critical speed passing strategies.

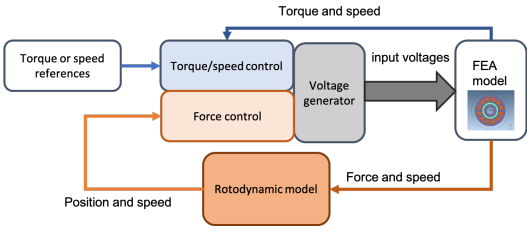
Chapter 4

Interaction between the electrical and mechanical control

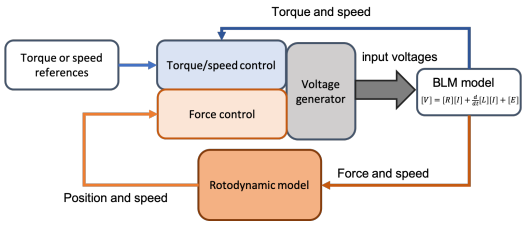
4.1 Introduction to set-up

Following the work done in the Chapter 2 and 3, the chapter will combine their two studies together in order to have a system approach to the use of the BLM as a rotodynamic actuator. To do this a simulation environment was created, where both systems can be introduced. Using Matlab Simulink it is possible to use the electrical model of the BLM to generate the control currents to obtain a specific torque and forces. Furthermore, we will be able to integrate the forces from the BLM as an input into the rotodynamic model of the shafts. This gives us two possibilities:

- Direct coupling between an FEA model and the Simulink model (Fig. 4.1a)
- Generate an algebraic model or look-up table define the machine and combine it to the Simulink model.



(a) Set-up including the use of an FEA model



(b) Set-up including the use of an voltage equation based model of the BLM

Fig. 4.1 Combined model

The first solution will require a large amount of data space and calculation time to do the target simulation. On the other hand, the second step would be quite fast to run and wouldn't require much data space. As illustrated in previous chapters the relative accuracy of the model created for the BLM it was therefore decided to focus on the use of a matrix model of the machine in this study. The resulting combined controlled model is shown in shown in Fig. 4.2.

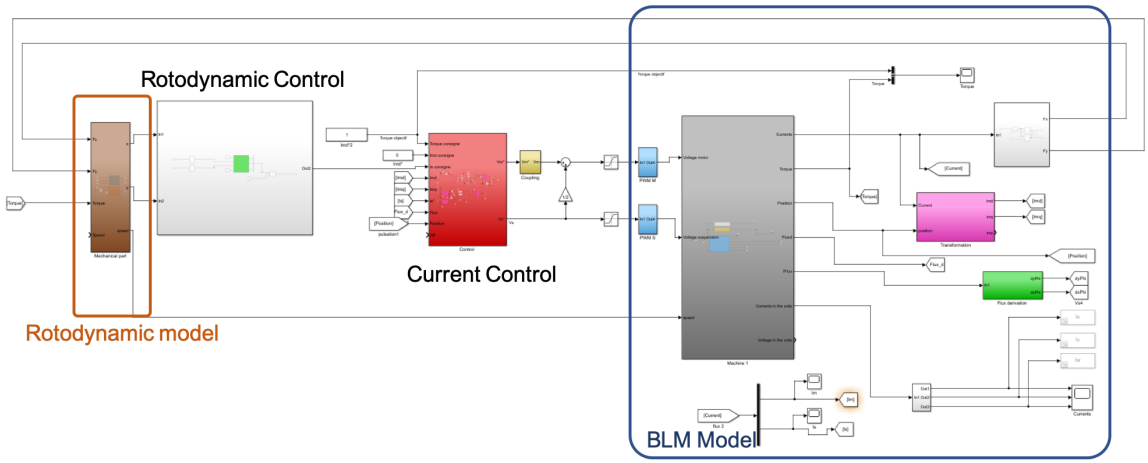


Fig. 4.2 Simulink control model combining the rotodynamic and the BLM modeling.

The example set in place will represent 1 shaft of the model previously present in Chapter 3. In this case the gear was set as a simple disk inertia, Fig.4.3. This simple model will give us an insight on the behavior of the combination of our two models. This will also allow for the confirmation of the validity of the methods used in this study so far.

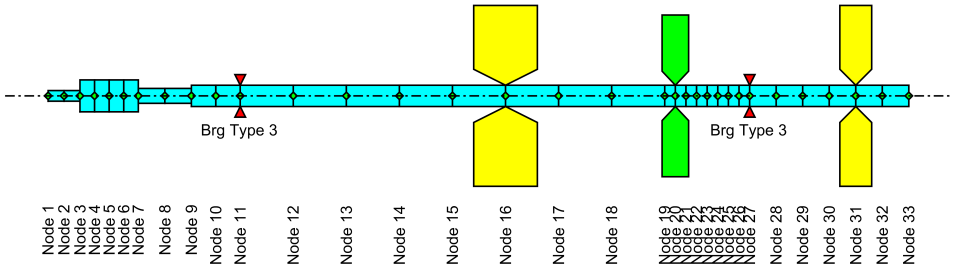


Fig. 4.3 Shaft used for the interaction modeling

The model as shown in Fig.4.3 can be separated in to two parts:

Table 4.1 Parameter of the machine

Resistance in $\mu\Omega$	Inductances in μH	
R	L_S	L_M
219.5	54.2049	40.9673

- The BLM model
- The shaft model

BLM model The model of the BLM will use the identical model created in Chapter 2. The BLM will be modeled using its voltage equation and based on the inductances of the machine as shown in equation 4.1 and 4.2. Furthermore, the formulation will be using matrices as illustrated in equation 4.4, with each matrix's content being illustrated in the equations that follow. The value of each component of the model will be given in Table. 4.1.

$$v_{Um} = R\left(\frac{i_{Um}}{2} + i_{Us}\right) + \frac{L_m}{2}\frac{\mathrm{d}\, i_{Um}}{\mathrm{d}t} + L_s\frac{\mathrm{d}\, i_{Us}}{\mathrm{d}t} + e_U \tag{4.1}$$

$$v_{Us} = 2R\, i_{Us} + 2L_s\frac{\mathrm{d}\, i_{Us}}{\mathrm{d}t} \tag{4.2}$$

$$[\mathbb{V}_{ms}] = [\mathbb{R}_{ms}]\cdot[\mathbb{I}_{ms}] + [\mathbb{L}_{ms}]\cdot\frac{\mathrm{d}}{\mathrm{d}t}[\mathbb{I}_{ms}] + [\mathbb{E}_{ms}] \tag{4.3}$$

$$[\mathbb{V}_{ms}] = \begin{bmatrix} v_{Um} \\ v_{Vm} \\ v_{Wm} \\ v_{Us} \\ v_{Vs} \\ v_{Ws} \end{bmatrix} \qquad [\mathbb{I}_{ms}] = \begin{bmatrix} i_{Um} \\ i_{Vm} \\ i_{Wm} \\ i_{Us} \\ i_{Vs} \\ i_{Ws} \end{bmatrix} \qquad [\mathbb{E}_{ms}] = \begin{bmatrix} e_U \\ e_V \\ e_W \\ 0 \\ 0 \\ 0 \end{bmatrix} \tag{4.4}$$

$$[\mathbb{R}_{ms}] = \begin{bmatrix} \frac{R}{2} & 0 & 0 & R & 0 & 0 \\ 0 & \frac{R}{2} & 0 & 0 & R & 0 \\ 0 & 0 & \frac{R}{2} & 0 & 0 & R \\ 0 & 0 & 0 & 2R & 0 & 0 \\ 0 & 0 & 0 & 0 & 2R & 0 \\ 0 & 0 & 0 & 0 & 0 & 2R \end{bmatrix} \qquad [\mathbb{L}_{ms}] = \begin{bmatrix} \frac{L_m}{2} & 0 & 0 & L_s & 0 & 0 \\ 0 & \frac{L_m}{2} & 0 & 0 & L_s & 0 \\ 0 & 0 & \frac{L_m}{2} & 0 & 0 & L_s \\ 0 & 0 & 0 & 2L_s & 0 & 0 \\ 0 & 0 & 0 & 0 & 2L_s & 0 \\ 0 & 0 & 0 & 0 & 0 & 2L_s \end{bmatrix} \tag{4.5}$$

Shaft model The shaft model will be based on the rotodynamic model presented in Chapter3.

$$m\ddot{x} + d\dot{x} + kx = f(t) \tag{4.6}$$

The base of the rotodynamic model is describe by the equation 4.6, where q is any displacement direction. The variables m,d and q are respectively the mass, damping and stiffness. With the FEM software introduced those different elements of equation 4.6 can be extracted for the shaft's modeling.

At first the model was tested in a simple scenario. Where the BLM will rotated at a fixed speed and will apply a simple torque target to provide. At the same time the BLM will be used to reduce the vibration of the shaft via a simple PD control. Once it manages to illustrate the effect the BLM can have on the shaft vibration it will be extended to the study of the proposed method discuss in Chapter 3. This will help demonstrate the feasibility of the use of BLM as rotodynanmic actuator.

4.2 Vibration reduction

As mentioned previously, the model was set in a simple scenario. The model used for the calculation is presented in Fig. The controller will be set so that the vibration of the shaft around the BLM is reduce. This will serve a as a simple example on how the BLM can help, in a simple way, to reduce vibrations in a shaft system. In order to achieve this the force in the BLM will be controlled using a PD controller as described in Chapter 2 2.6.3. But this time the shaft model won't be a Jefcott rotor. This will make the simulation more representative of a real system. The control of the vibration will be tested combined with the torque control. For this application as the study are not interested in the rotodynamic behaviour of the machine the simulation will be operated at fixed speed. The settings of the model's simulation will be descried in Table.4.2.

The controller will have it's value recalculated based on the previously example using a Jefcott rotor and the values of the PD parameters will be displayed in Table.4.3. The values of the PD parameter are selected to add a $5cdot\ 10^5 N \cdot m^{-1}$ stiffness to the shaft and a damping of $1000\ N \cdot s \cdot m^{-1}$.

in order to obverse the impact of the BLM the model will be set to rotate freely without any vibration compensation for the first part of the simulation. In the second part it will engage the vibration compensation from the BLM.

The looking at Fig. 4.4 showing the vibration at the BLM it can conclude that the BLM does have a significant impact on the vibration of rotor as the vibration amplitude reduced from a 400 μm to only a couple of μm. This was obtained by applying a force with an

Table 4.2 Model settings

Parameter	Value	Unit
Speed	3000	rpm
Torque	1	$N \cdot m$
DC Voltage	270	V
Max suspension current	10	A

Table 4.3 PD controller settings

Parameter	Value
P	$5 \cdot 10^5$
D	1000

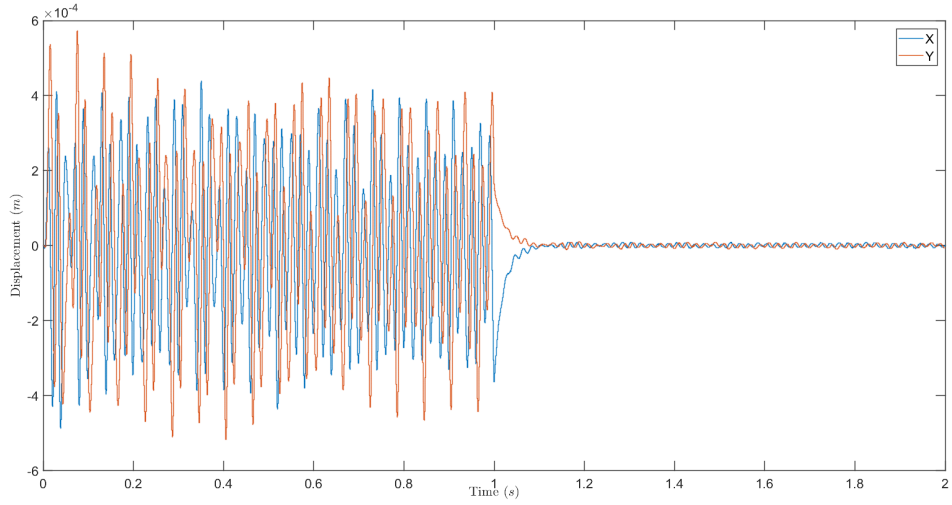


Fig. 4.4 Shaft vibration reduction using a BLM

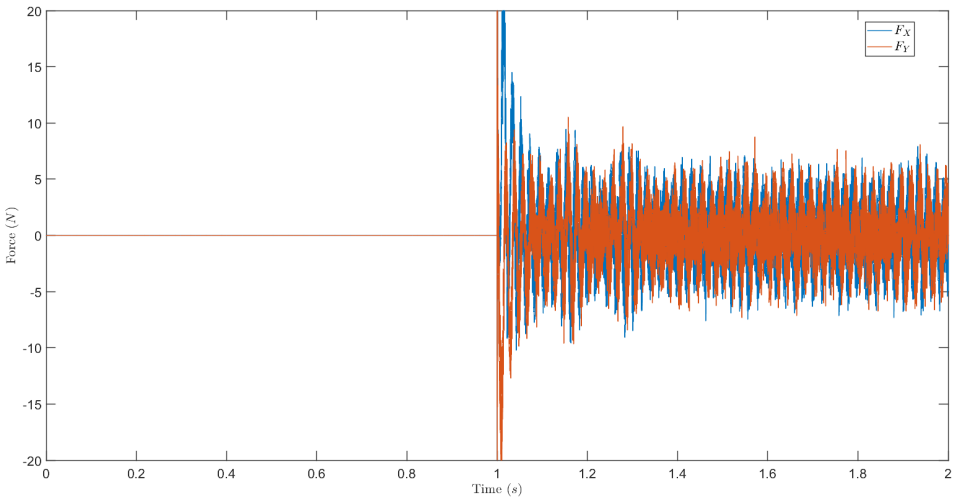


Fig. 4.5 Force created by the BLM

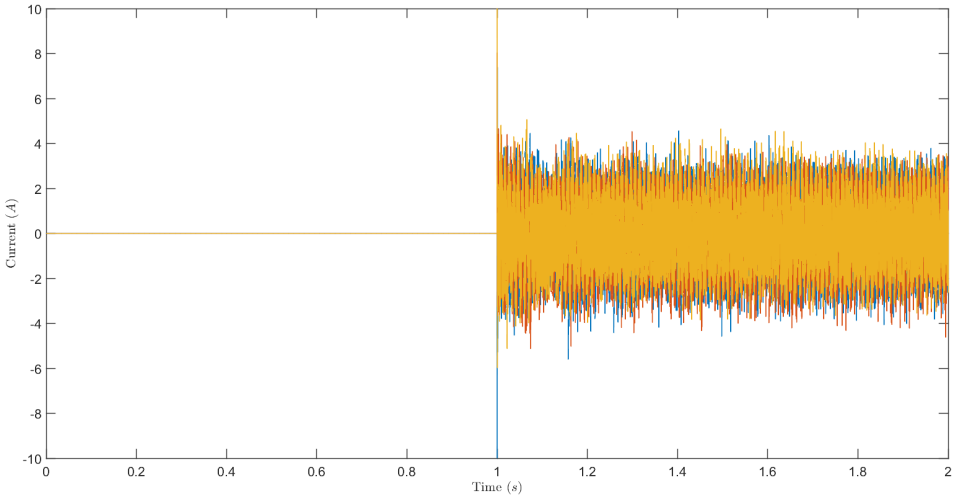


Fig. 4.6 Suspension current generated by the BLM

amplitude 100 N during steady state as illustrated in Fig. 4.5. This force was generated by the BLM 's suspension current of 4 A for the steady state behaviour of the controller as shown in Fig.4.6. However, when applying this vibration reduction on a critical speed it might allow to observe some limitation of this method. The next paragraphs will be highlighting this particular point.

4.3 Rotodynamics interaction

Now that it was established that the proposed system can reduce the vibration of a shaft, the study will investigate how this system can handle the rotodynamic interaction strategies presented in Chapter 3. For this purpose the PD controller previously used in 4.2 will be replaced by a block that will include the strategy proposed as illustrated in Fig. 4.2. The blocks input and output are described in Table. 4.4. The block will require information on the current rotation speed of the shaft and the stiffness that was injected so far in the shaft by the BLM. This will help to localize the operating point on the control maps (Fig. 4.7)like the ones created previously. Fig.4.8 shows the critical speed that where extracted from the selected shaft. It was observed that in this case 2 critical speed have to be passed at 1000 rpm and 2600 rpm. Furthermore, the acceleration of the shaft's rotation speed will need to be identified, in order to set the appropriate margins for the control strategy. As defined in our proposed strategies for an operating point it will extract a stiffness to inject. This stiffness will be output by the block together with the force to apply in the X and Y direction based on the current displacement of the shaft in the respective direction. In order identify the operating point and the stiffness, the block will contain look-up tables for the different critical speeds as well as the injected stiffness depending the acceleration direction. Therefore, the block will be connected directly to the force to current estimator/converter that will supply the proper current i_s in the BLM for the wished forces/stiffness.

In order to observe the validity of the proposed methods scenario where the rotor is accelerating slowly toward a critical speed of the shaft was simulated. The position of the shaft will be monitored at the BLM rotor and at all the inertia on the shaft. The simulation will be focused around the first critical speed at 1800 rpm. Therefore, the simulation will have the shaft start at 1200 rpm and accelerate up to 1900 rpm. The speed profile will be set as illustrated in Fig. where the acceleration is set lower around the critical speed to exacerbate the negative effects of the natural frequency of the system. Furthermore, a torque of 1 $N\dot{m}$ was maintained on the shaft. So in the first case the force control of the BLM will be deactivated in order to observe the increase of vibration resulting to the approach toward a critical speed. The next step will illustrate the limitation of the simple stiffness and damping

Table 4.4 Input and Output of the Rotodynamic control block

Type	Parameter	Unit
Input	X position	m
	Y position	m
	Rotation speed	rpm or $rad \cdot s^{-1}$
	Acceleration	$rad \cdot s^{-2}$
	Current supplied stiffness	$N \cdot m^{-1}$
Output	Force X	N
	Force Y	N
	Supplied stiffness	$N \cdot m^{-1}$

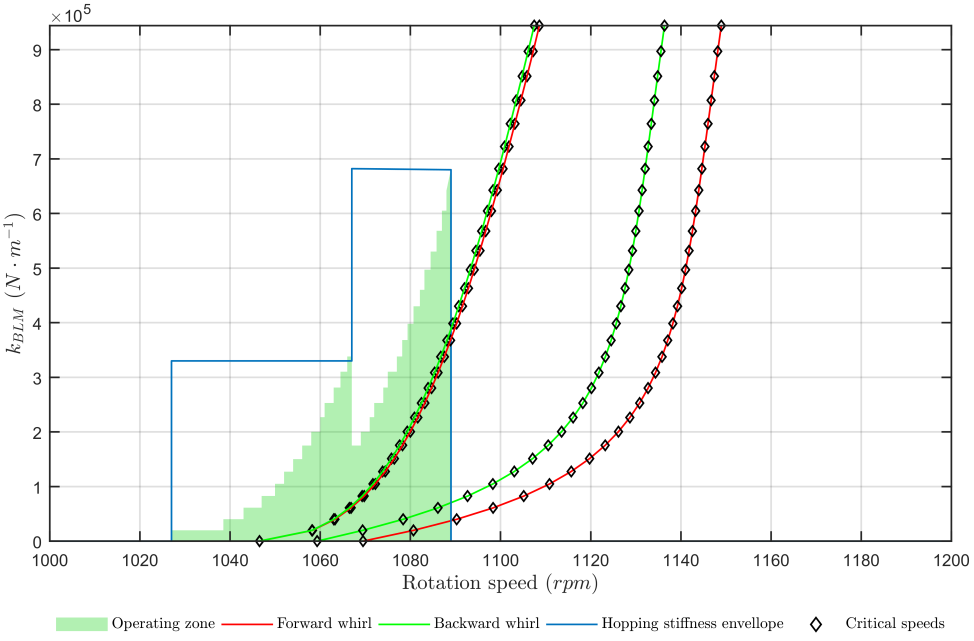


Fig. 4.7 Operating points for the use of a stepping strategy.

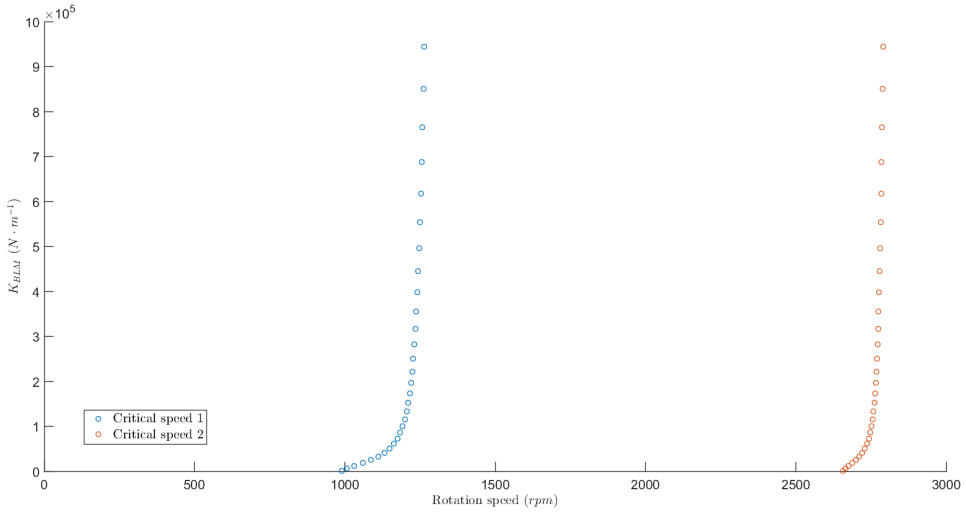


Fig. 4.8 Critical speeds of the shaft

for reducing the vibration. Then finally it will illustrate the impact and advantages of the using the proposed method to pass critical speeds. In order to illustrate clearly the impact of the stiffness injection on the shaft the damping will be set to 0 so that it won't interfere with the results.

4.3.1 Free acceleration toward critical speeds

The model will left to rotate freely without the action of the BLM on the shaft. The machine will be set to pass through the first critical speed changing the rotation speed of the shaft from 0 rpm to 3750 rpm. during a time period of 10 seconds. Figure 4.9 shows the increase in vibration at the BLM, around the critical speeds of the machine. This is especially significant at around 2600 rpm where the vibration is expected to be of an amplitude of 2.56mm. This peak represent 10 times the size of the BLM's air-gap and will result in a collision between rotor and stator leading to a potential destruction of the BLM and the shaft. It was also noticed that after a critical speed the vibration of the shaft stay quite high due to the lack of damping in the shaft, with the clear understanding that this will lead to even larger vibration.

4.3.2 Vibration reduction with acceleration toward critical speeds

Like in section 4.2the study will simply apply a constant damping and stiffness on the shaft for the whole simulation. The vibration was reduced on most of the speeds. However, when pass toward a critical speed the displacement of the shaft increases sharply and following

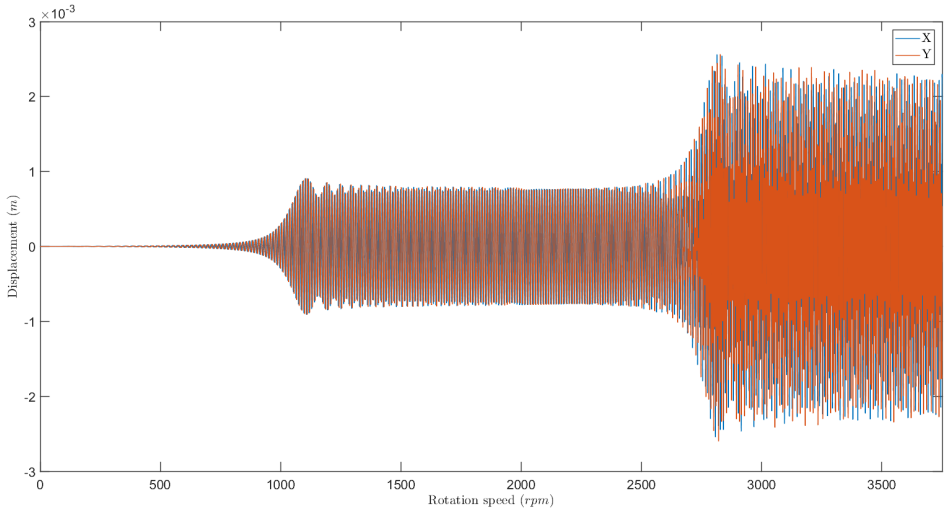


Fig. 4.9 Free vibration of the shaft from 0 to 3750 rpm

resulting vibration is bigger that during the free vibration.This is due to the fact that the added stiffness pushed the first critical speed to a higher speed (1300 rpm), which could lead to a larger excitation due to the critical speed. However, the vibration is only reduced and the critical speeds have still an effect on them. This illustrates quite well how the use of constant stiffness bring only limited benefits. Furthermore the constant stiffness injection lead to a constant flow of current to the BLM as it can be observed in the Fig. 4.11.

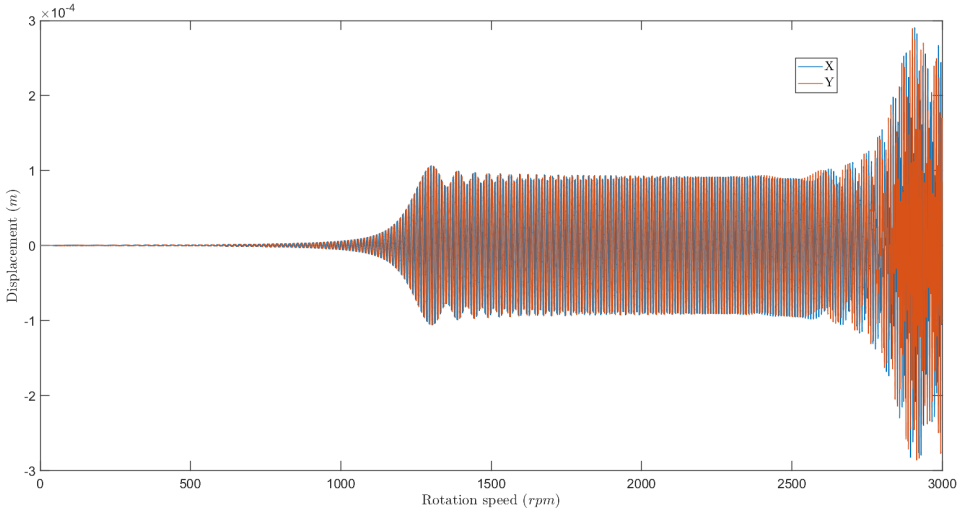


Fig. 4.10 Vibration of the shaft from 0 to 3750 rpm for a constant $5 \cdot 10^5\ N \cdot m^{-1}$ stiffness

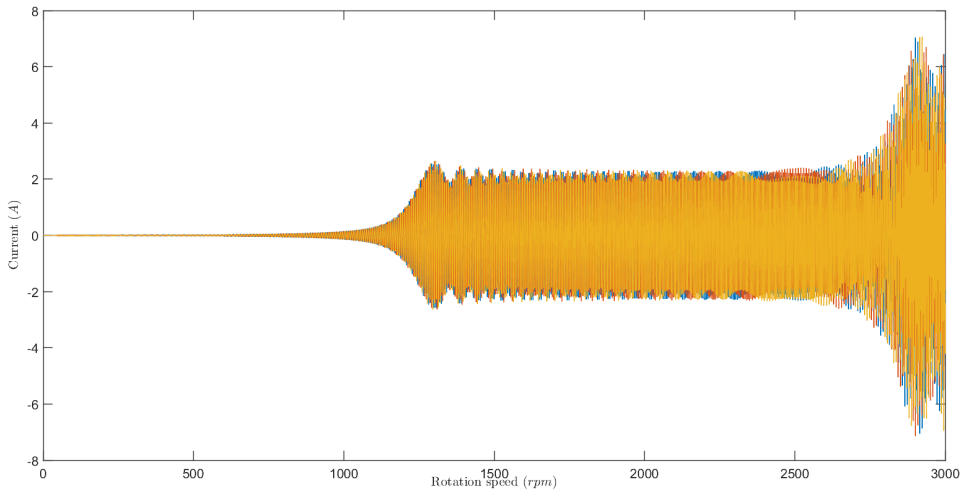


Fig. 4.11 Suspension current in the BLM from 0 to 3750 rpm for a constant $5 \cdot 10^5$ $N \cdot m^{-1}$ stiffness

4.3.3 Rotodynamic control with acceleration toward critical speeds

Now applying the methods proposed in Chapter 3.3 on the simulation model to illustrate there validity and advantages other simple vibration reductions. This simulation will concentrate on only the best method proposed: *Stepping*. The algorithm of the *Stepping* strategy is described in detail in 3.3.3, where the main idea is apply the stiffness gradually as the shaft's speed approaches a critical speed. The first advantage observed compared to the simple vibration reduction is the current used during the operation. As the stiffness shown in Fig.4.14 is not applied during the whole process the current is only generated for those selected periods of time Fig.4.13. Although, the current applied is similar to than the previous method; in overall the power consumption and energy use is lower. Looking at Fig.4.12 it was observe that the vibration has been reduced compared the previous method especially around the critical speed. However, one can notice that the vibration increases dramatically after the critical speed. This is due to a margin potentially set too small or the potential requirement for a smooth reduction transition after passing the critical speed.

4.3.4 Methods Summary

After a look the divers simulation conduced to illustrate how the BLM can be used in interacting with the rotodynamic of a shaft, a conclusion on the divers result provided will b e done First it was established to show that the combination between the BLM and rotodynamic model is possible and that the reduction of the vibration is feasible. However it does not help

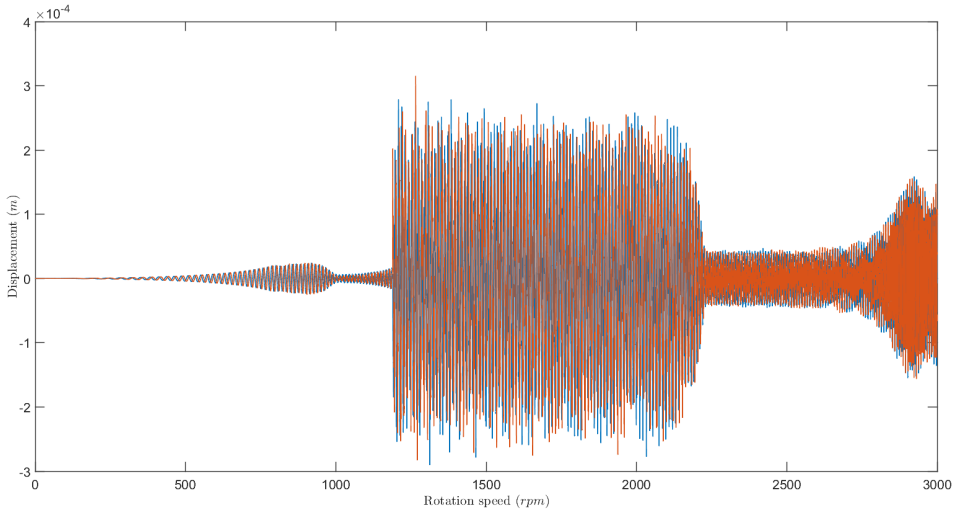


Fig. 4.12 Vibration of the shaft from 0 to 3750 *rpm* for a Stepping strategy

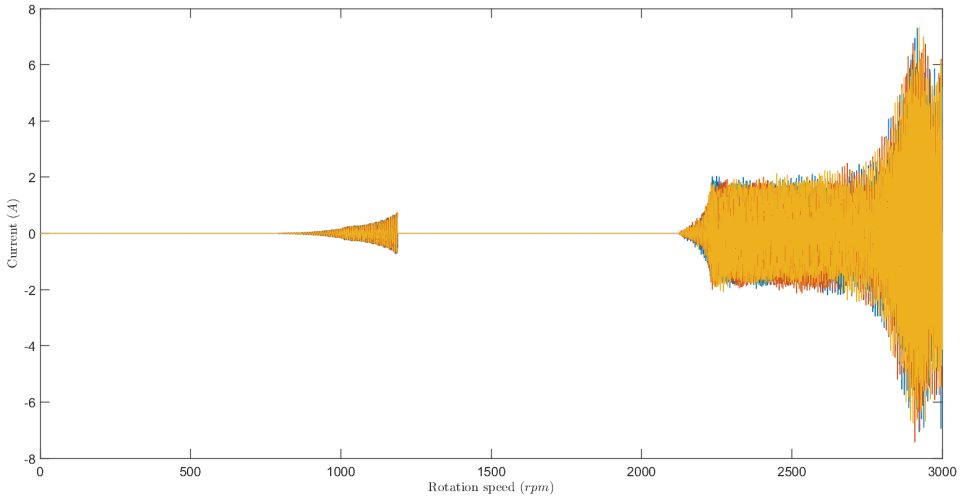


Fig. 4.13 Suspension current in the BLM from 0 to 3750 *rpm* for a Stepping strategy

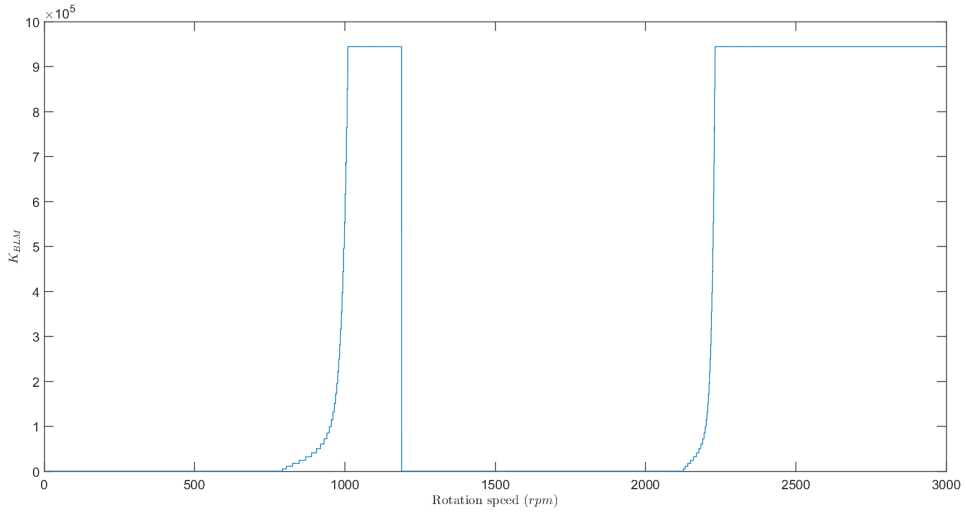


Fig. 4.14 Stiffness in the BLM from 0 to 3750 *rpm* for a stepping strategy

with the critical speeds of the machine. On the other hand, the study managed to illustrate that with the strategy proposed in the previous chapter, a reduction of the vibrations as well as passing critical speeds with a low current usage is possible. So by having a good understanding of the properties of the BLM's behaviour as well as having an accurate model of your shaft system, it is possible to control a shaft 's vibration with more flexibility than previous paper presented [68, 19, 43]. The next step now is to try those on a test bench.

Chapter 5

Application to a Test study and Experimental work

5.1 Test study setup

5.1.1 Test study presentation

For the test study and the following experiential test rig it was decided to combine the work of 3 different research project under the Marie Skłodowska Curie project INNOVATE, which each of the team member are part of. The aim of the study was to show the interaction and benefits between each of our respective works. As well as be a demonstrator for the application of future technologies for the aerospace industry. In that regard our common goal was the reduction of torsional and traversal vibration and see its implication and impact on a new type of air ridding seal. With the aerospace sector going toward the re-evaluation of their technology and its move towards More Electric Aircraft (MEA), several mechanical or hydraulic components will be replace by electrical ones[47, 65, 73]. As well as the integration of new technologies the team wanted to illustrate how the interconnection of each new element, mean that it required to re-think the way of designing systems. The optimization of the system is no longer the simple optimization of each single component but taking in account the divers elements together. As the action might affect one and the other in positive or negative way which warrants the need for combined studies and observations.

The different parts that will be studied are as follows:

1. Novel air-riding seal. by *S.Kumar*

2. The electromechanical interaction between the shaft and the generator and how to reduce the torsional vibration created by the application of electrical load. by *C.Ahumada Sanhueza*

3. The impact of an in-line BLM S/G a on the rotoynamics of the engine shaft. by *N.Schneider*

For this a test bench was devised together with the help of Prof. *S.Gravey*,our colleague *A.Bristot* and *M.Goodyer* from SAS engineering. In order to be able to test each of the different part of the system the bench was designed so that it stays modular and that some parts of the system can be disconnected at any moment for the convenience of each member of the team. The test rig has been separate into 3 shafts with each of them connected to

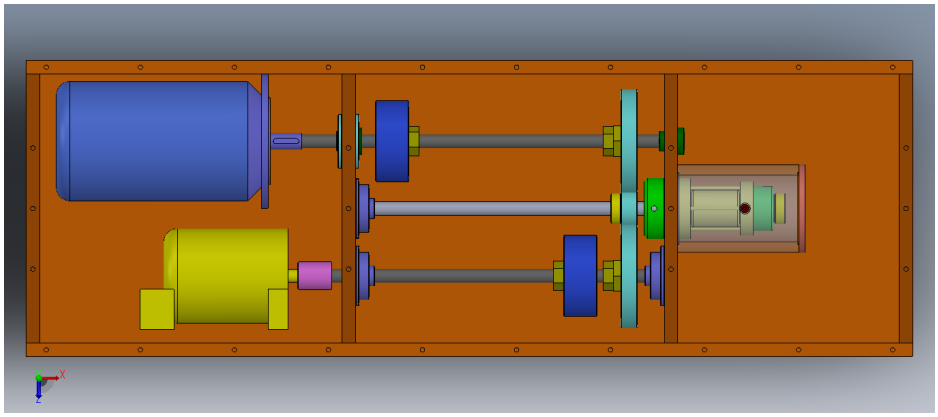


Fig. 5.1 Illustration of Test bench

one of the system developed by the member of the team Fig. 5.1. Each of them requiring a different rotating speed fit for their test requirements. The center shaft has been set to have a max speed to around 9000rpm to get realistic rotation speed around the novel seal [4]. The other shaft have their speed limited mechanically by the devices connected to them. The Servo motor used for the BLM has a maximum speed around 3000 rpm and the universal motor used for the torsional vibration control is limited to 4000 rpm.

5.1.2 Team's objectives

Each of the members of the team have different objectives that have to be met and combined to appreciate the interaction between the different parts of the system. This will be conveyed through several measurements. Therefore, a need to evaluate the needs of the test study will have regarding this aspect. But first the objectives of each of the team members needs to be identified .

5.1.2.a Torsional vibration.

Starting with the work on the electro-mechanical interaction and the torsional vibration [6]. In order to visualize the impact of her novel load control with load pulse timing [5] the angular position of the shaft at different parts of the shaft system needs to be observed. So that when putting a load on the rotating shaft a torsion of the shaft can be observed. At the same time this torsion should be negligible or small when the novel control is applied. At the same time there is a need to measure the functioning of the control by observing the currents and voltages on the load and the generator. In order to simplify the load control a DC generator will be used. To make the effect of the control more visible the effects of torsional vibration will be exacerbated using inertias. They will help also to keep the torsional natural vibration frequencies low.

- DC Generator + drive
- Motor+ drive
- Electrical loads
- Inertias
- 2 incremental or absolute encoders. To measure the torsion.
- Current and voltage transducer (Lem)

5.1.2.b Air-riding seal.

For the demonstration of the novel air riding seal [51]. An air-tight chamber will be set to which compressed air will be feed through a pressure regulator. This will allow us to monitor the behaviour of the seal at different pressures. At the same time the position of the seal compared to the shaft will be monitored to have an idea of the air-gap present in the seal Fig. 5.2. As well as the potential deflection created by the weight of the seal structure.

- Seal system
- Air compressor
- Compressed air connection system
- Pressure regulator
- 4 displacement sensors.
- Flow-metre

5.1.2.c BLM.

For the demonstration of the impact of a BLM on the rotodynamics of a shaft, measuring the position the rotor will be needed. This is a requirement for the control of the stiffness of the

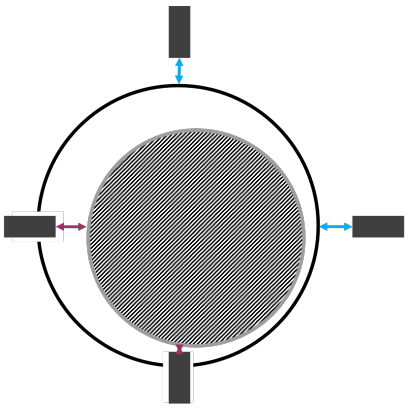


Fig. 5.2 Illustration of the seal displacement measurement

shaft and compensate the negative stiffness in the air-gap. At the same time it will require measuring the angular position of the rotor for the control of the current. For the control of the system it will need to be able to measure the currents to control them. To ensure that the natural frequencies of the transversal vibration are low enough so that the BLM can affect them.

- BLM + 2 drives
- Absolute or incremental encoder
- Current and voltage transducer (Lem)
- 3 4 displacement sensors
- inertias
- generator
- electrical loads

5.1.3 Material and measurement tools

The previous section highlighted the needs for the different parts of the test study. With this a list of the different measurements and instruments the test bench, associated with the study, will need, was obtained .Combining the needs of each team members the use of the measurement tool was shared and it was decided to use a common control/measuring platform. As well as, the main actuator for the good functioning of the test bench will need to be found, fulfilling each team member's objective. The main aspect of the rig, which is to have the 3 shafts rotate together was the main target.

5.1.3.a Motor and Generator

For all the 3 combined project there is a need for a rotation of the shafts. It will need a motor that would act as the turbine in order to simulate an aero-engine. Conjointly it needs a generator to simulate the generation aspect of the aero-engine. Those two aspects being the main interest of the two projects of *C.Ahumada Sanhueza* and *N.Schneider*. Both looking at the interaction of the generator on the vibration of the shafts. To keep the overall test bench modular it was decided to start with the system using a IM to provide the motor torque. In order that *C.Ahumada Sanhueza* could independently start her research on the torsional vibration at the generator. The generator that was used will be a Universal motor as they are easy to control and allow us to use simple DC loads.

For our project involving the BLM, the IM by will be replaced the BLM. It will then be able to use the BLM as a motor and a magnetic bearing. Complementary the already connected universal machine can be used as a motor or generator depending on the situation wished to be studied. As the starting point of the study was the development of starter generator this test rig will allow taking account for it. The BLM will either been built at the PEMC Fig. 5.3 or convert an existing machine to a BLM.

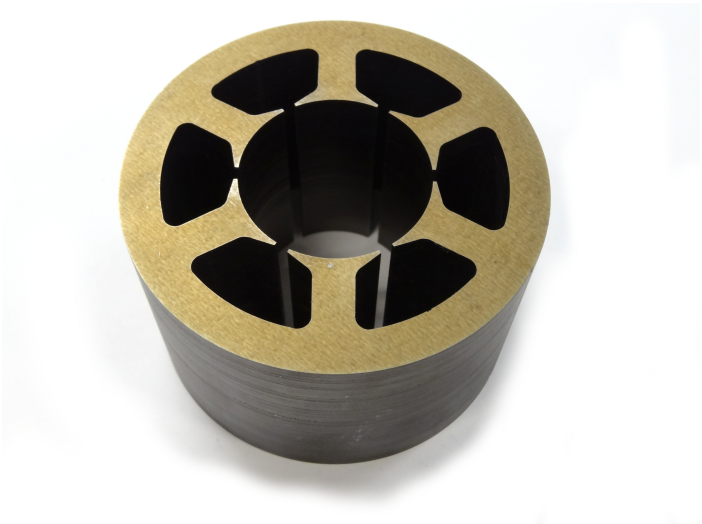


Fig. 5.3 BLM laminated stator sheets

5.1.3.b Interface and Control platform

For the measurement/control platform it was decided to opt for a DSP/fpga structure provided by dSpace GmbH. The MicroLabBox provided the necessary input-output in analogue as well as digital.This will allow connecting our different measurement tools to one system.

It will allow us to monitor in real-time the different outputs of the test bench. But it also allows the control of different actuator or inverters as well as preparing a control system under Matlab/SIMULINK.

5.1.3.c Displacement measurements

For the measurements of the different displacement a common system was used as it will reduce the cost of the test bench. The main requirements came from the precision needed as well as the output format. The air-gap of the novel air-ridding seal is about $40\mu m$ and the one of the BLM is $250\mu m$. To obtain a decent idea of the position in those gaps it was required to have system able to measure value under the μm. For this there was two available solutions:

- Eddy current sensors
- Capacitive sensors

The capacitive one being more precise as well as having no restriction on the material of the measured object. But in the other hand the eddy current solution is more affordable and restricts the measured object being a conductive metal (preferably not ferrous [50]). The test benches main restriction was on the budget, it was therefore decided to use the eddy current ones and add aluminium rings at the position of displacement measurement. The ECL150 multi-channel eddy-current displacement system with 2 U3 probes and 4 U5 probes Fig .5.4 supplied by Lion Precision was chosen. It will allow to connect all the 6 sensor probes Fig. 5.4a to the same amplification unit Fig. 5.4b. Having the amplifier set at a 15 KHz bandwidth by the manufacturer (as recommended by them for our application) It was expected to have a resolution of about 65 *nm* at the BLM and 150 *nm* at the seal air-gap [58].



(a) Eddy current sensor probe U5 (b) Eddy current sensor amplificator

Fig. 5.4 ECL150 eddy current sensor

Table 5.1 Parameters of the ECL150 eddy current sensor probes

Probe model	range (mm)	Min. target size (mm)	Material type	Resolution (nm)			
				250 Hz	1 KHz	10 KHz	15 KHz
U3	$0.05-0.55$	6	Non-ferrous	35	45	60	65
			Ferrous	60	80	100	110
U5	$0.25-1.50$	10.2	Non-ferrous	75	100	140	150
			Ferrous	130	180	240	260

5.1.3.d Electrical connections

Following the description of the requirements for each team-member and the measurement tools needed. Preparing a schematic describing how the different elements will be connected to the MicroLabBox was required. At the same time a similar schematic for the electrical connection of to power each element of test bench was prepared.

The MicroLabBox connection is going to enable us to have record the measurements from divers sensors and process them in real-time. As well as export the recorded data for post-processing. Fig. 5.5 present the connection of the different sensors and the actuator of the test rig. For each element number of connections needed for the good transmission of the data was indicated.

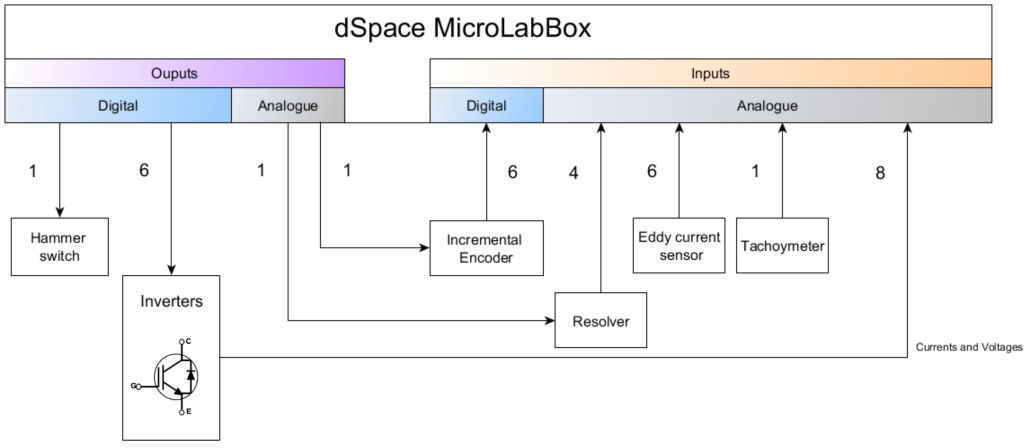


Fig. 5.5 Connection schematic of the MicroLabBox and the measurement tools

The Power connection of each element had to be taken in account in the design of the test rig. Actuators and sensor have each different power requirement that will have to be meet.

It was imperative to make sure that the Test bench will be able to provide enough power for the system. But at the same time make sure that enough inputs to convert the different power requirement of each device are there. For this an exhaustive list of each device used is needed:

Table 5.2 Summary of the different electrical component needed and their power requirements

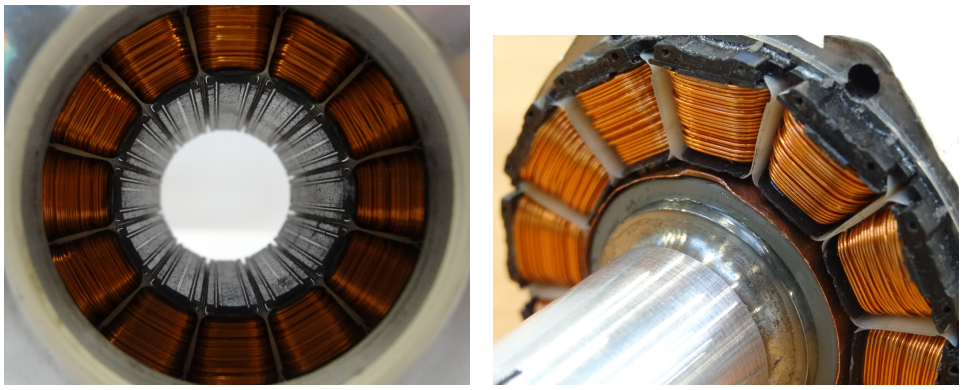
Device	Voltage	Power	Connection to Power
AC Motor + Drive	230 *VAC* 3Ph.	2.2 *KW*	Monophase power socket (16*A*)
BLM + Drives	$2\times$ 230 *VAC* 3Ph.	$2\times$ 2 *KW*	$2\times$ Monophase power socket (16*A*)
Eddy current sensors	$12 \rightarrow 24$ *VDC*	4.5 *W*	Charger to a standard (5*A*) socket
MicroLabBox	230 *VAC*	125 *W*	Isolated (5*A*) socket
Solenoid	12 *VDC*	12 *W*	Charger to a standard (5*A*) socket
Generator control	5 *VDC*	12 *W*	Charger to a standard (5*A*) socket
	12 *VDC*	12 *W*	Charger to a standard (5*A*) socket
Oscilloscope + probes	3×230 *VAC*	Not relevant	$3\times$ standard (5*A*) socket
Computer	$2\times$ 230 *VAC*	Not relevant	$2\times$ standard (5*A*) socket

Table.5.2 Illustrates not exhaustively all the components that may have to be used during the process of the Test-bench. It was concluded that at least 2 16 *A* single phase *AC* sockets were needed . As well as around 10 5 *A* sockets with one of them isolated with an isolation transformer to connect the MicrolabBox to the inverters. (See Annex **??**) The construction and wiring of the system was done by the PEMC technical staff in accordance to BS 7671 [2].

5.2 BLM set-up

5.2.1 BLM conversion

For the part of the project concerning the rotodynamic interaction using a BLM a few preliminary challenges were encountered. The BLM needs to be set up as well as making sure that our installation will have at least one natural frequency inside the operating speed of the said BLM. For this it was decided to start the conversion of a servo motor into a BLM machine. The servo-motor used for this conversion is a MSMA042A1C by Panasonic© [56]. The first step of the conversion was to take apart the different parts of the PMSM. The main structure, the 2 bearings that maintained the rotor in place needed to be separated. So that the rotor could be extracted and have access to the stator's winding for the conversion.



(a) Servo-motor MSMA042A1C (b) Servo-motor coils

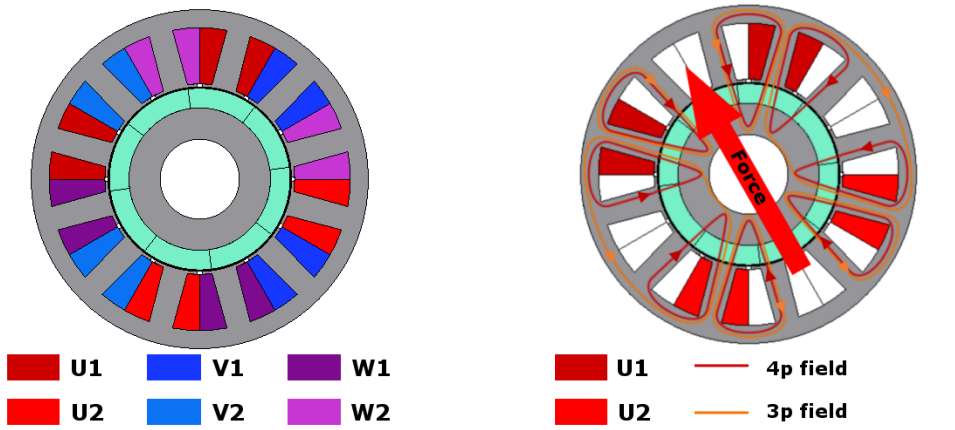
Fig. 5.6 Panasonic servo-motor MSMA042A1C

Based on the coils setting of the servo-motor the possibility to transform it into a BLM needed to be verified. The machine is a PMSM machine with 12 coils and slots. BLM is set to be 4 pairs of pole machine. The system will needed to be able to provide a 4 pairs of pole field and also will need supply the torque. As discussed previously in chapter 2 in order to be able to supply a force on the rotor a field that has one pole pair difference between the one that provides the torque[55, 18] needs to be created. This leads to the two following solution:

- the field created by the suspension current is 5 pole pairs
- the field created by the suspension current is 3 pole pairs

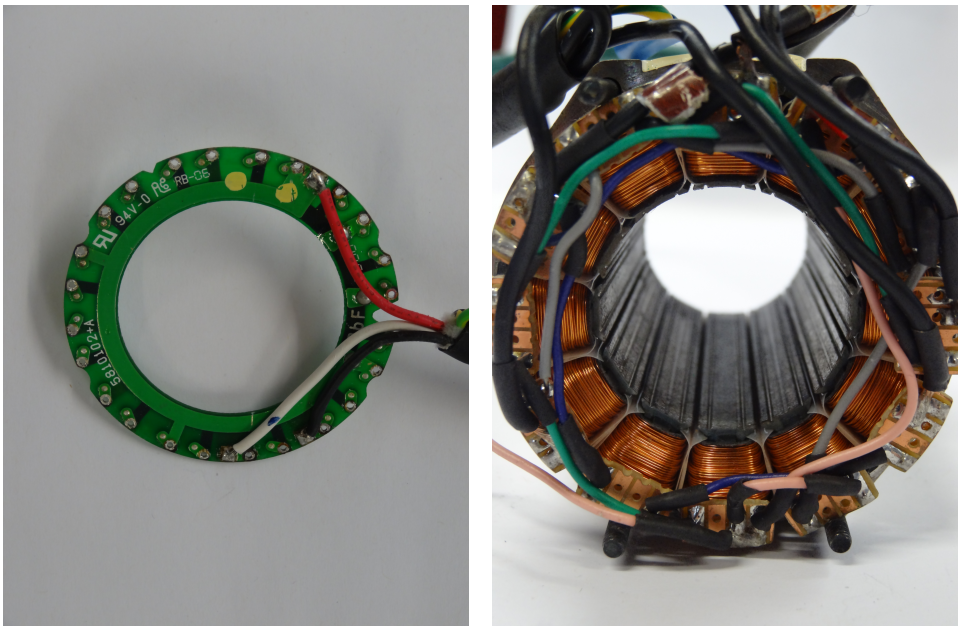
But looking at the number of coils (12) it cannot support any field with a higher number of pole pair than 4. Due to the fact that it has 3 phases and if considering that it has 8 poles the normal amount of coils needed is 24, but as it has a concentrated winding with 2 conductor per slots it can reach a minimum of 12. Therefore, the winding of the servo-motor needs to be changed so that it can be accommodate to create that required 3 pole pairs field. At the same time the objective was to make as few modifications as possible to the existing winding in order to not face a costly and lengthy winding change. The Servomotor having its coils created as separate assemblies like show in Fig. 5.6b are connected together via a small printed circuit board (PCB) Fig. 5.8a This Fig. 5.7a shows the solution used to obtain the 3 pair of poles field as well as the 4 pairs of poles one. Fig. 5.7b illustrates the 2 fields created by the phase U of the BLM and their interaction to create a force on the rotor.

The connection shown in Fig.5.8b has been created on the coil's arrangement previously found.This has been achieved using small PCB section that have been cut and sanded to the proper dimension Fig. 5.9. The cable that will be connected to the inverter have then been solder to it. For the use of several future test the neutral point of the winding was kept



(a) Configuration of the coils to form the BLM (b) interaction between the 3p and 4p field

Fig. 5.7 BLM configuration based of the MSMA042 servo-motor



(a) PCB connector (b) New coils connection

Fig. 5.8 Old and new servo-motor's coils connection

accessible. This will allow for example the testing of the forces generated by one phases in the future.

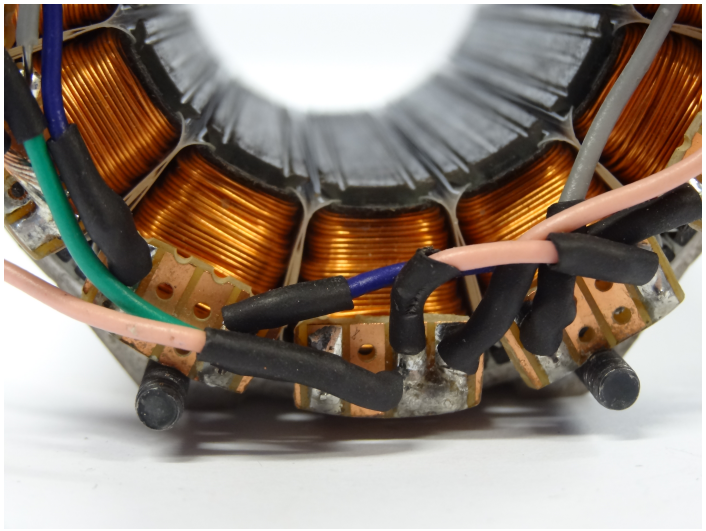


Fig. 5.9 PCB connecting the BLM's coils

In order to be able to measure the position of the rotor using the eddy current probes discussed in 5.1.2.b an aluminum ring will be be added Fig. 5.10 around the rotor's shaft. This is due to fact that the shaft is made out of steel that is not an ideal material to be used for the measuring with eddy current sensors [50].



Fig. 5.10 Rotor with aluminium ring

5.2.2 BLM performances

Once the connection of the servo-motor's coils was established so that it is converted to a BLM, it is possible to test how it will perform. It is important to have an idea of currents and

voltages needed by the BLM to supply the torque and the forces. As well as the maximum torque and/or maximum force that the BLM can provide on the shaft. This will be useful for the understanding of how much this BLM will be able to impact the rotodynamic of the shaft in the manner described in 3.3. For this purpose the different results of our previous

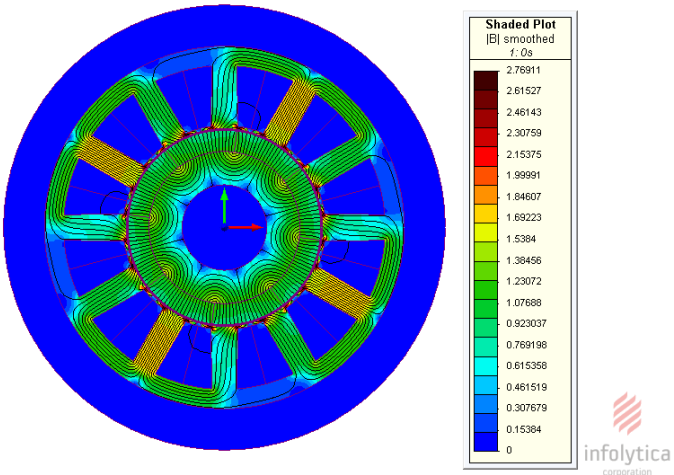


Fig. 5.11 FEA of the BLM

study on the modeling of a BLM in 2 will be used. First all the geometrical parameters of the BLM will need to be measured in order to get an idea of the system used in Table. 5.3. The different values have been either measured using a caliber or using the information included in the data-sheet of the MSMA042A1C servo-motor [56].

To evaluate the control and the behaviour of the BLM its inductances where measured and compiled them in Table. 5.4. Those are the values used from the beginning of the study in order to have the control done on the values of the real BLM. It was found that the magnet of the BLM provide a negative stiffness of about $1 \cdot 10^6\ N \cdot m^{-1}$. Using the FEA model and the equations of chapter 2 it was found that machine is capable to produce a force of about 100 N while still maintaining an acceptable suspension current density J_s of 4 $A \cdot mm^2$. If considering that the vibration of the shaft won't exceed 100 μm it will be producing at least a maximum stiffness k_{force} of $1 \cdot 10^6\ N \cdot m^{-1}$ which will at least cover the magnetic pull of the PM of the machine and still help to maintain the rotor to the center position. For this study it was observed that the vibration at the center of the shaft mainly is confined around $100 \sim 150 \mu m$. Considering that the BLM will be trying to reduce those and is located close to a stiff bearing, we will set k_{force} at $2 \cdot 10^6\ N \cdot m^{-1}$. This will imply that after compensating the PM's negative stiffnessthe resulting stiffness k_{BLM} of $2 \cdot 10^6\ N \cdot m^{-1}$ can be obtained.

Table 5.3 Parameters of the BLM

BLM Parameter	Value	Unit
Number of pairs of poles	4	
Number of phases	3	
Number of coils per pole and per phase	2	
Number of turn per coil	~ 200	
Length of the BLM	55.25	mm
Airgap	0.25	mm
Rotor diameter	30	mm
Back Iron diameter	56	mm
Magnet width	~ 4	mm
Teeth width	~ 4	mm
Slot depth	9.25	mm
Slot liner height	0.5	mm
Magnet span	100	%
Tooth opening	~ 80	%

Table 5.4 Parameter of the machine

Resistance in $\mu\Omega$	Inductances in μH					
R	L	M_1	M_2	M_3	M_4	M_5
219.5	42.423	5.1462	-5.1631	11.765	-5.1627	11.768

For the torque, it was estimated the BLM is capable to produce a torque of 1 $N \cdot m$ with a current of I_m of 0.34 A. This will create a current density J_m in the coils of 2.3 $A \cdot mm^2$.

But one notice in Fig. 5.11 that already for achieving the 1 $N \cdot m$ torque the BLM's teeth are highly saturated ($\sim 1.8T$) care will be taken with the potential increase of losses in the BLM that might lead overheating of the BLM and reduction of its efficiency.

5.2.3 BLM and Rotodynamics



Fig. 5.12 The 3 shafts and their inertias

For the purpose of transversal and the torsional study of the vibration it was important to have a good idea of the different natural frequencies of our system. In order to force them into acceptable position for our elements, inertias were added to have the low torsional frequencies that would represent with a certain fidelity the frequencies encountered in an aero-engine. But at the same time it was important that those inertia set the transversal natural frequency low enough so that interacting with it using the BLM was possible but not too much such as it overcrowds the spectrum with critical speeds. Furthermore, all those inertia were made relatively easily adjustable in there position on the shaft.

As described in the set-up of the test 5.1 three independent shafts are set, that have the possibility to be connected to each other via a set of spur gears [40]. As already discussed in Chapter3.1.2 the presence of the gears will have an impact on the rotodynamic response of the shafts. Therefore, the system will be studied in two cases:

- Just the single shaft connected to the BLM.
- All the 3 shafts connect together via the gears.

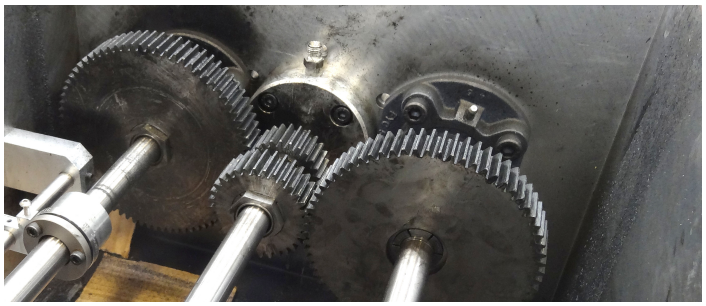


Fig. 5.13 The 3 shafts gear connection

For both cases an FEM model was created using the same methodology as in Chapter3.1.2. This will allow at first to identify if its possible obtain a natural frequency in the range of operating speeds of the system. Then in a second step verify how well the BLM will interact with the shaft's rotodynamics.

5.2.3.a single shaft

Based on the geometry presented in 5.1.1 a FEM of the single shaft where the BLM is connected was created. The gear connected to it will be considered has a simple disc as it won't interact with any of the other ones. The bearings of the test study have been considered here as being close to infinitely stiff. Therefore giving them a value of stiffness $k_x = k_y = 1 \cdot 10^{10}\ N \cdot m^{-1}$. But concerning the damping at those bearing it was decided to start with an arbitrary $d_x = d_y = 300\ N \cdot s \cdot m^{-1}$. But those values will have to change in accordance to future experimental results to improve the model of the shaft. Table. 5.5 defines the different part of the single shaft connected to the BLM.

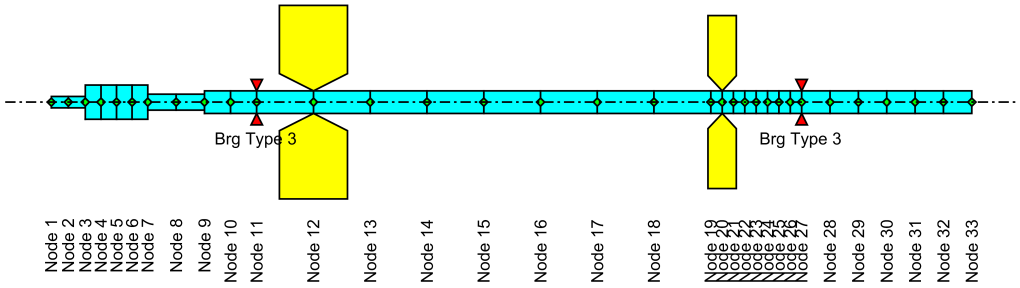


Fig. 5.14 Single shaft model (FEM)

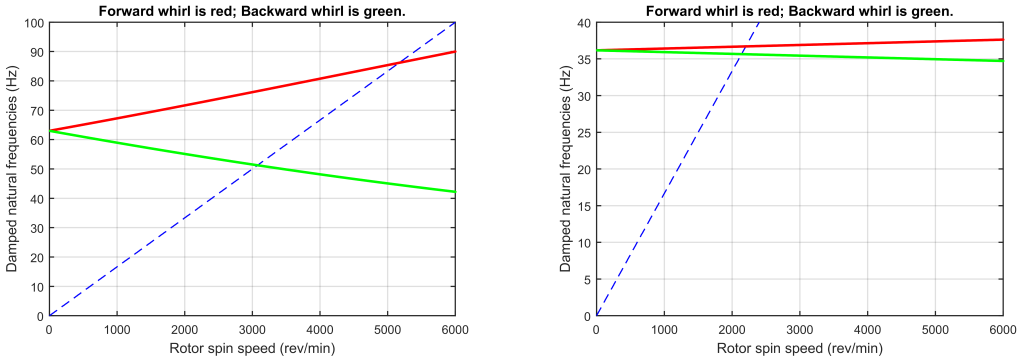
After the definition of the shaft Fig. 5.14 we will firstly check for the natural frequencies of the system using the Campbell graph. With the results observed on the Campbell graph Fig. 5.15 it can be said that keeping the inertia at node 12 Fig. 5.15a will note serve us. As the the first critical speed appear at 5100 rpm way beyond the max 3000 rpm of the BLM. For this reason it was proposed to displace it more toward the center at node 16 Fig. 5.15b.This reviled a more acceptable critical speed at 2210 rpm which is in the operating speeds of the BLM.

Table 5.5 Components description for the single shaft system

Element	Nodes	Parameters					
		D_{outer}	D_{inner}	$\ell_{element}$	E	G	ρ
Shaft	1→3	10 mm	0 mm	15mm	$1.9 \cdot 10^{11}\ Pa$	$7.6 \cdot 10^{10}\ Pa$	$8000\ kg/m^3$
	3→7	30 mm	0 mm	13.75 mm			
	7→9	14 mm	0 mm	25.00 mm			
	9→11	20 mm	0 mm	23.00 mm			
	11→19	20 mm	0 mm	50.00 mm			
	19→27	20 mm	0 mm	10.00 mm			
	27→33	20 mm	0 mm	25.00 mm			
Discs		D_{outer}	D_{inner}	Thickness			ρ
	12	170 mm	20 mm	60 mm			$8000\ kg/m^3$
	20	152 mm	20 mm	25 mm			
Bearings		k_x and k_y				d_x and d_y	
	11	$1 \cdot 10^{10}\ N \cdot m^{-1}$				$300\ N \cdot s \cdot m^{-1}$	
	27	$1 \cdot 10^{10}\ N \cdot m^{-1}$				$300\ N \cdot s \cdot m^{-1}$	
BLM		k_{airgap}		max k_{BLM}		d_{BLM}	
	3→7	$-8 \cdot 10^5\ N \cdot m^{-1}$		$9.44 \cdot 10^5\ N \cdot m^{-1}$		$10\ N \cdot s \cdot m^{-1}$	

From there it will be seen how the BLM can interact with this critical speed with the injecting of stiffness and damping. Injecting a permanent damping of $10\ N \cdot s \cdot m^{-1}$ and have a maximum stiffness supply of $9.44 \cdot 10^5\ N \cdot m^{-1}$. From this a graph illustrating the shifting of the critical speeds of the shaft with the injection of a stiffness k_{BLM} by the BLM was obtained. For this example it was assumed that the negative stiffness generated by the magnets was already compensated.

Looking the results given by Fig. 5.16 it can be observed that with this configuration the BLM will be able to shift the critical speeds of the shaft by more than 500 rpm. The idea now will be to test, using the test bench that will be developed, if by using any of the



(a) Inertia at node 12 (b) Inertia at node 16

Fig. 5.15 Campbell graph considering that the BLM compensate for the negative stiffness of the magnets

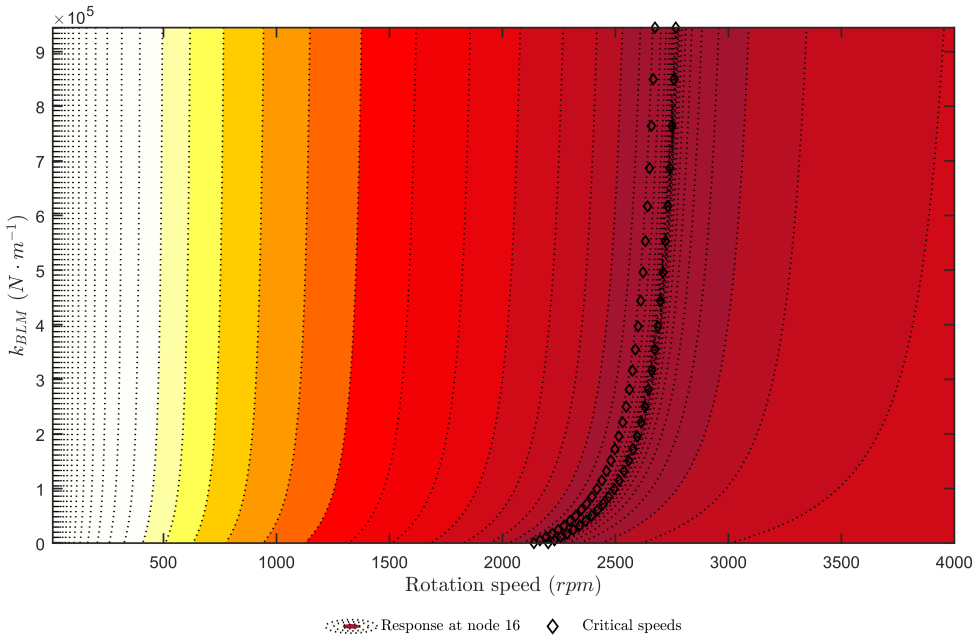


Fig. 5.16 Variation of the critical speed of the shaft with the injected stiffness k_{BLM}

strategies presented in Chapter 3.3 wa significant impact on the rotodynamics of the shaft can be established.

5.2.3.b geared system

In continuation of the previous section the same review was applied with the 3 shafts connected together. Using the work previously done in Chapter 3.1.2 an FEM model was created to describe the system Fig. 5.17. The detailed description of the 3 shafts can be found in C.2 for further information. As done in the previous chapter a matrix reduction of the system was determined so that it conveys the forcing forces due to the presence of the gears. Again the first step of the study will be to obtain a Campbell graph of the shaft system. In order to asses the different critical speeds that will be present.Looking at Fig. 5.18 it was observed that the Critical speeds in the operating speed range of the test study are displayed in Table. 5.6. Still critical speeds relatively close to the one observed in the single shaft study were observed in the present configuration.

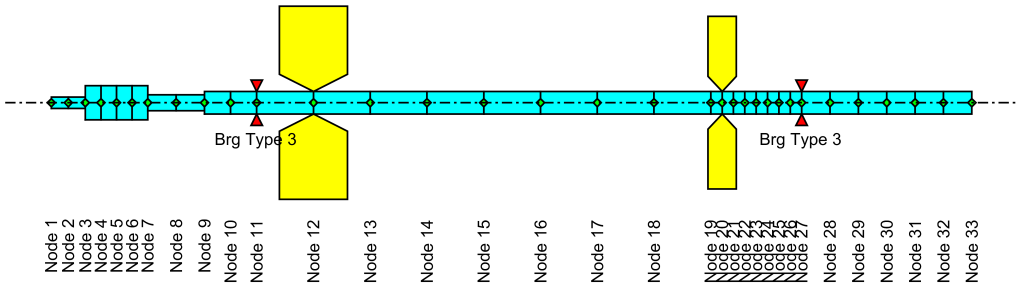
Table 5.6 3 shaft system critical speeds

3 shafts system	Critical speeds		
	2102.6 rpm	2187 rpm	2739.2 rpm

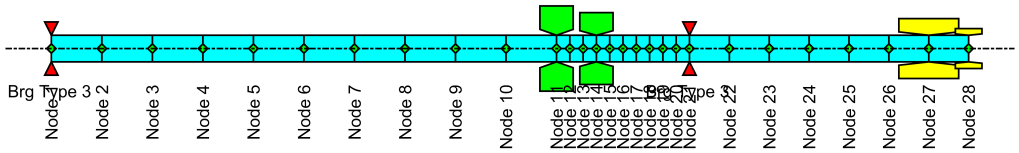
Following the study of Campbell graph it was decided to look at the impact of the stiffness k_{BLM} on the deviation of the critical speeds of the system. As for all the previous examples so far a figure describing the deviation of all the critical speeds of the system within its operating range will be produced. Fig. 5.19 shows the clear change of all the critical speeds of the system. For the two first natural frequency a similar behaviour than the one observed in the one on single shaft was obtained. From which one can assume that the inertia present in the first shaft are responsible of them. The third one that appears at 2739.2 rpm probably is introduced by the inertia in the third shaft. And in contrary to the first two its deviation with the stiffness is relatively smaller. The two first have a variation of 414 and 521 rpm respectively. Compared to the 170 rpm of the third one. A more detailed description of the values of the critical speeds are given in Table. C.5 in Appendix C.2.

5.2.3.c Summary

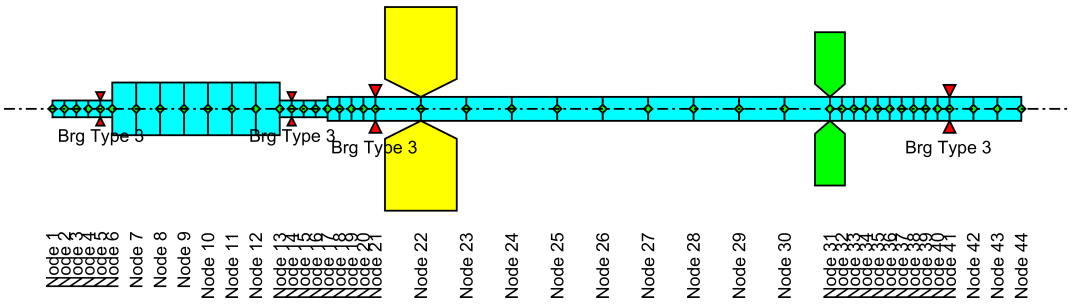
Looking at the results of the two previous section, it can are confidently said that it is possible to use the BLM as an actuator to avoid critical speeds of the system. Using a few of the different strategies presented in 3.3. It will even provide the added benefit to able to observe



(a) Shaft 1



(b) Shaft 2



(c) Shaft 3

Fig. 5.17 FEM of the geared model

the behaviour of the strategies confronted to overlapping. This will allow comparing in practice the strategies in varied conditions.

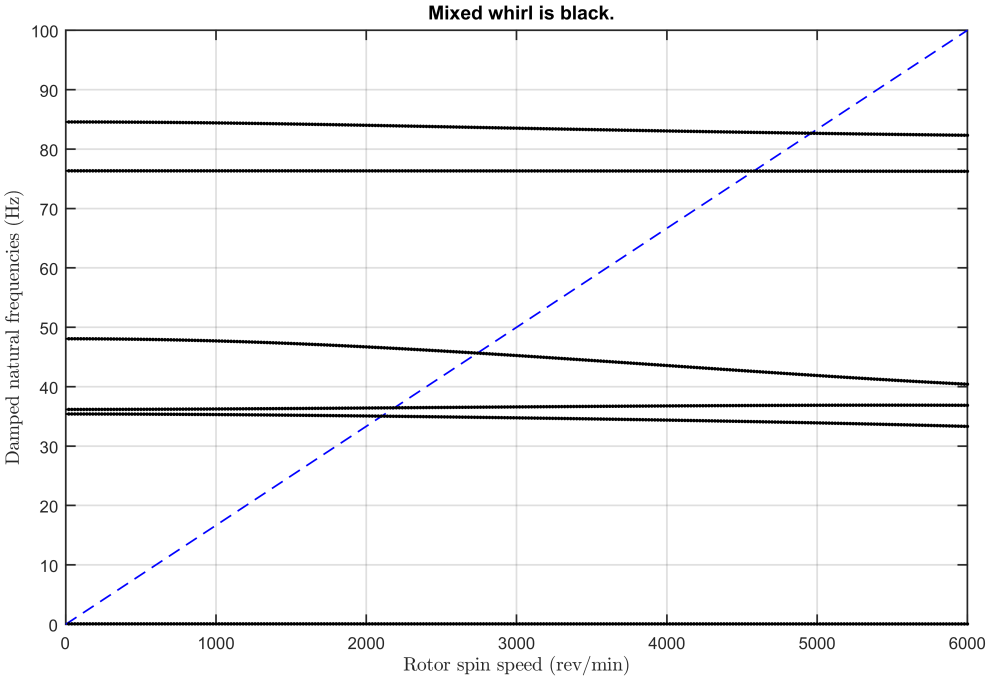


Fig. 5.18 Campbell graph of the 3 shafts system

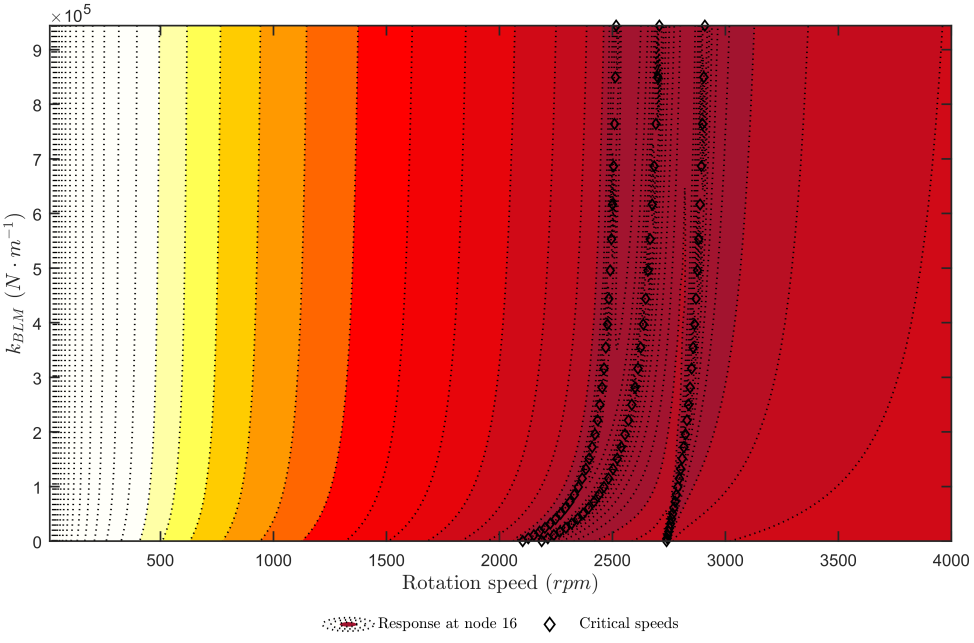


Fig. 5.19 Critical speed variation with the stiffness for the geared system

5.3 Installation of the Experimental test rig

The General idea of the case study has been lay down on the previous section. Going on the more practical approach of the building of the test rig; a detailed description of it was given. Furthermore, highlights of each part of the teams experimental work process will be added. But first the installation process and test bench setting needs to be discussed.

5.3.1 General Installation

With the idea behind the test study discussed in 5.1.1. The practical aspect of the building of the test rig related to the study has to be explained. The Test bench was built on the

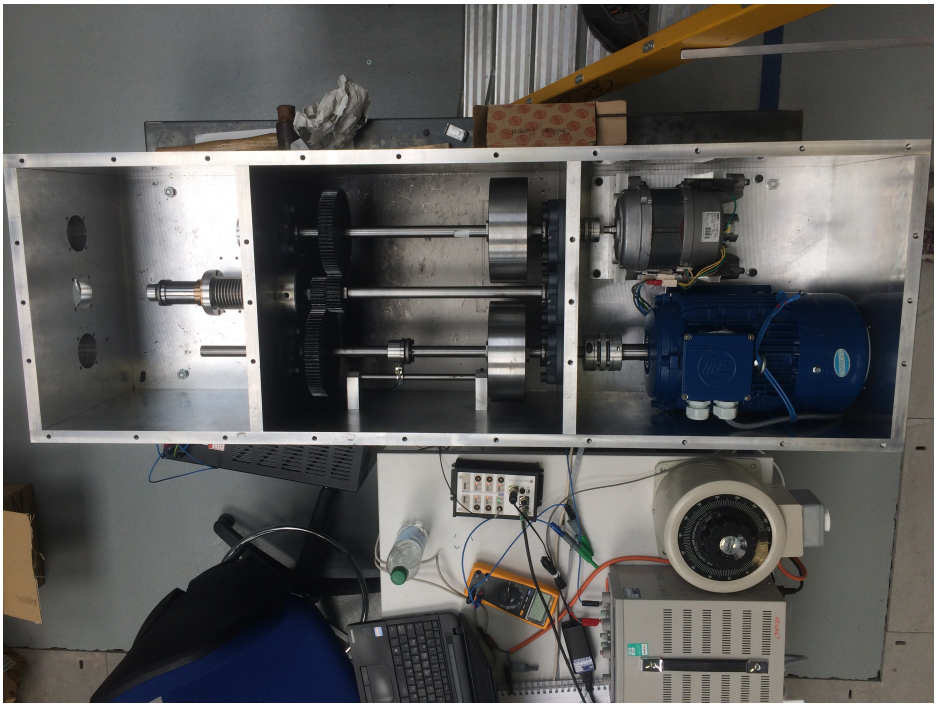
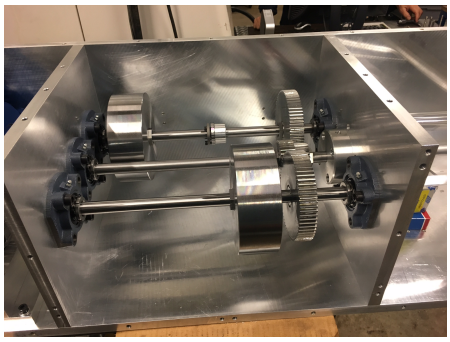


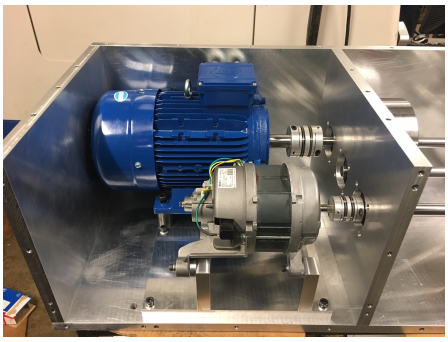
Fig. 5.20 Top view of the experimental set up

specifications and CAD drawing. Fig. 5.20 gives you a top view of the Test bench. The three shafts have been set in the test bench and hold each by SKF Y bearings Fig. 5.21a. The two shafts holding the generator and the motor have there inertia installed. The gears of each shaft has also been mounted. Fig. 5.21b highlights the position of the IM used as the motor and the generator. The last one being a salvaged universal motor from a commercial washing machine refitted by *C.Ahumada Sanhueza* to be used as a generator. The motor and the generator will be connected to the other shaft with disc couplings. They allow for a

torsionally rigid coupling with an angular backlash free transfer of the motion. All this while retaining a certain flexibility accommodating for shaft misalignment.



(a) Side view of the 3 shafts with their inertias



(b) Side view of the motor and generator

Fig. 5.21 Side view of the shaft and the actuators

The whole system is then put on a table hold by damper in order to maintain the system in place and limit as much as possible the impact of external vibration on the behaviour of the system. Pictures of the said table and damper can be found on the Fig. 5.22.



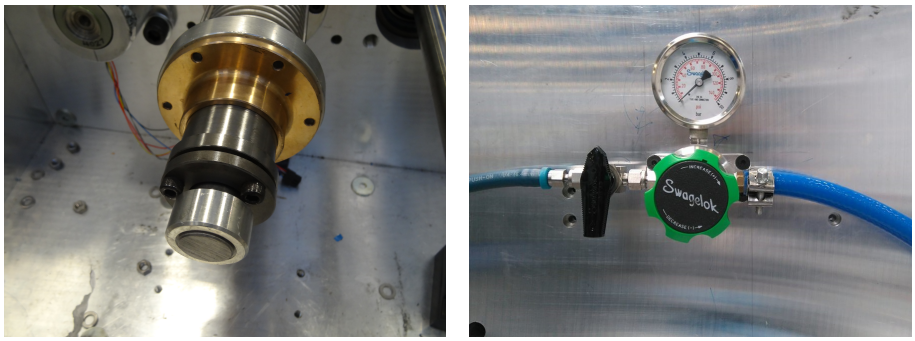
(a) Side view of the test rig before being mounted to the Table



(b) Damper set between the test rig and the bench

Fig. 5.22 Test study construction

Following this the pneumatic instrumentation for the test bench was installed to prepare the system to be feed with compressed air up to 10 *Bar*. First the seal and its below contained in a Plexiglas bell. Followed by the installation of the Swagelok pressure regulator and the pressure valve. The pneumatic system is connected to the Test bench via a hole in the protection shield.



(a) Air riding Seal and below (b) Swaglok Pressure regulator

Fig. 5.23 Air-riding seal system

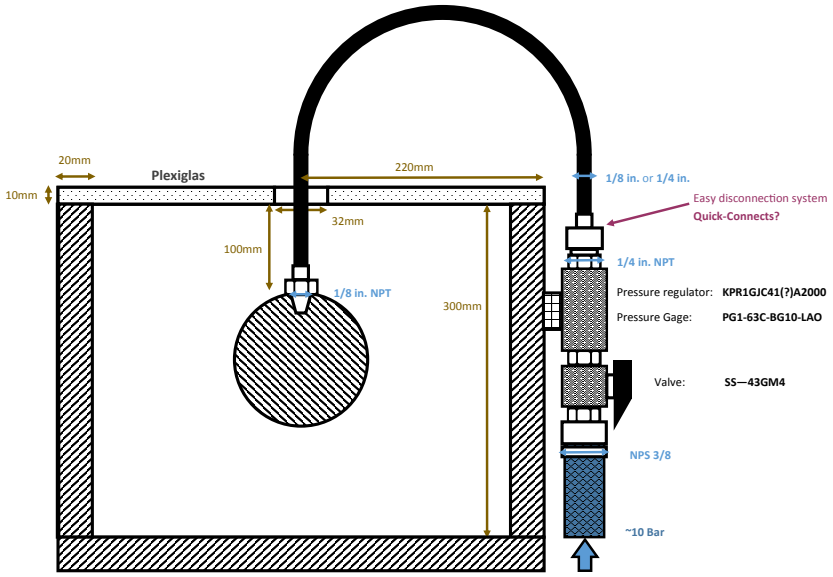


Fig. 5.24 10 *Bar* Pneumatic connection schematic

5.3.2 BLM installation

5.3.2.a Installation consideration

At the moment the way to hold in place the stator of the BLM in order to connect the BLM to the test bench was not discussed so far Fig. 5.25. On the Rotor an aluminum ring was mounted and force fitted so that it will help for measurements of the Rotor's displacement as discussed in section.5.1.3.c. To connect the shaft of the BLM with the one of the test bench a

solid coupling was installed. In order that the connection behaves as much as possible as they would be both part of the same shaft. To increase even further the stiffness of the connection the two shafts will be glued to the coupling using an epoxy glue.

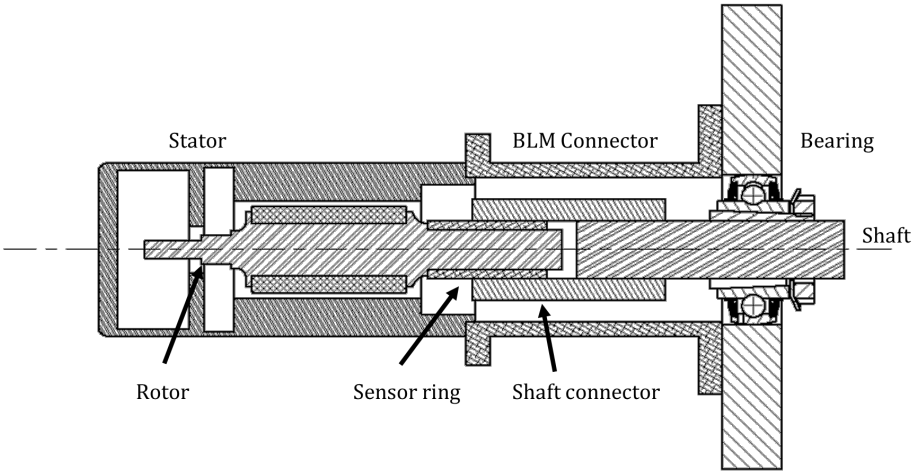


Fig. 5.25 Connection system for the BLM

But it was imperative to make sure that the deflection caused by the PM and the weight of the rotor won't deflect the rotor too far and have the magnets stuck on the stator. It was decided to model this using an FEA software (AutoDesk Inventor). Simulating a part of the shaft extending out of the bearing. Considering that the shaft is fix at the bearing position, like it would be stuck at a wall. From there it was found that the deflection due to the weight of the rotor is maximum 3.2 μm in the air-gap area. Combining this deflection and the magnetic pull in the air-gap it was found that the deflection in that area shouldn't exceed 138 μm Fig. 5.26 which far from the 250μm the air-gap of the BLM has.

The BLM's stator will also have to be hold in place. For this a cylindrical flange hold was designed and built. It will take advantage of the hole created to insert the bearing to attach itself to it with a spigot and screws. On the side of the BLM it will again use a spigot and screw to hold the BLM in place. Fig. 5.28b illustrates the connection of the connector to the main frame of the test bench as well as to the flange of the BLM. Like for the solid coupling he deflection of the BLM connector under its own weigh and external forces was investiagted. From the FEA results we can estimate the stiffness $K_{Stator+Connector}$ as discussed in section 3.2.2. By place a force f_{stiff} on the stator and measure its deflection d. Then getting the $K_{Stator+Connector}$ with the equation:

$$K_{Stator+Connector} = \frac{f_{stiff}}{d} \tag{5.1}$$

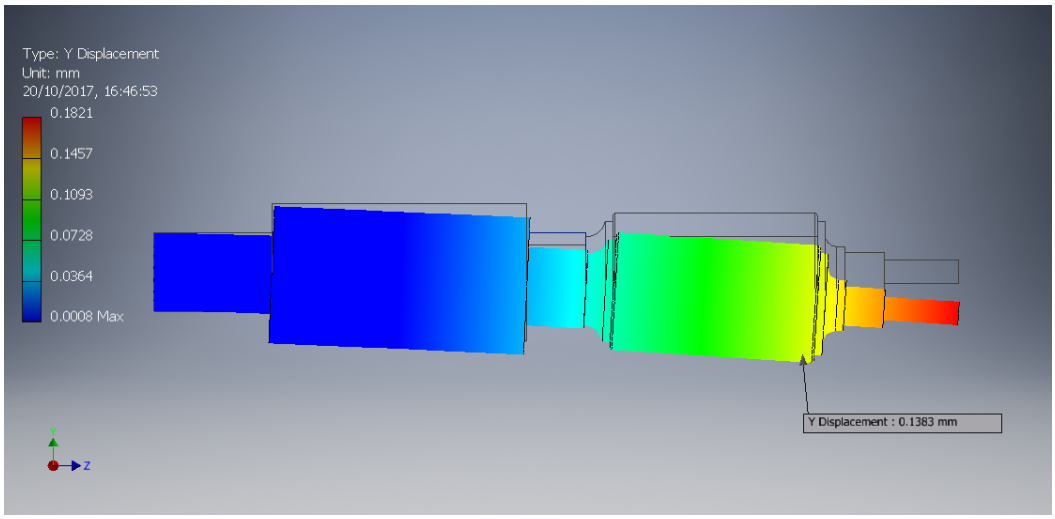


Fig. 5.26 Rotor deflection

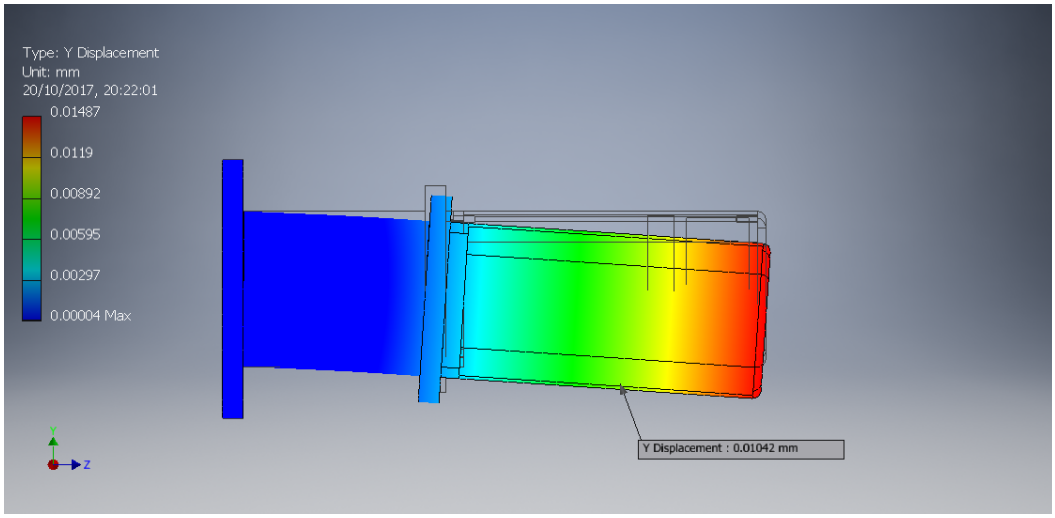


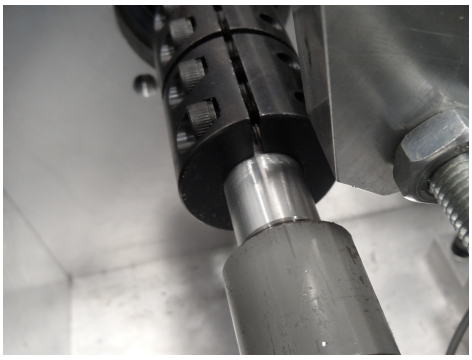
Fig. 5.27 Stator deflection

It was found that $K_{Stator+Connector} = 2.22 \cdot 10^7\ N \cdot m^{-1}$. Based on the equation 3.35 and the fact that $MAX(K_{airgap} + K_{force}) = 9.44 \cdot 10^5$ it can be considered that:

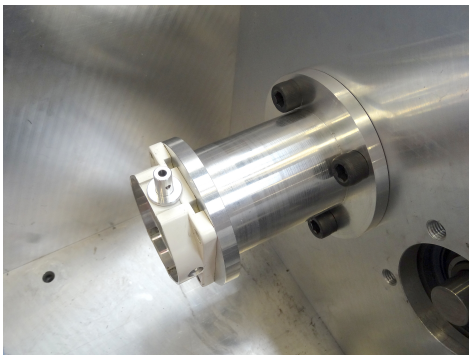
$$k_{BLM} \approx K_{airgap} + K_{force} \tag{5.2}$$

Like on the previous case the connector was fixed so that it is fix on the frame wall. From there the deflection due to the weight of the stator was found to be 0.8 μm in the air-gap area. Combining this deflection and the magnetic pull in the air-gap it was found that the deflection in that area shouldn't exceed 10.4 μm. This shows that even when combing the two maximum deflection it will not be possible to touch the stator as $132 + 10.4 = 142.4\ \mu m < 250\ \mu m$.

Therefore, if considering that the shaft is perfectly aligned there won't be any issue due to the magnet pull.



(a) Solid coupling



(b) BLM stator flange connector

Fig. 5.28 BLM mounting system

5.3.2.b Installation procedure

A procedure to install the whole BLM holding system will need to be found. Since the magnets will attract the stator structure and potentially create a misalignment. At the same time the stator flange holder will not allow access to the solid coupling. At the same time the BLM's rotor needs to be fixed in the good position so that the rotor and the stator are perfectly aligned. So with those considerations in mind, the following procedure in Fig. 5.29 was set in place for the installation of the BLM.

To decrease the possibility of a mistake, it is recommended that this process is first applied dry (no use of glue) a couple of time.

5.3.2.c Installation discussion

The process described previously has been applied dry with a cooper sleeve of 210 μm.Fig. 5.30a show the state of our system at step 11. After the extraction of the sleeve the result is far from what was hoped. Fig. 5.30b shows that the rotor of the BLM is stuck to its stator. The procedure has been restarted a couple of time but yield the exact same result. The first idea that sprung to our mind was that our previous study in section 5.3.2.a was wrong. Meaning that the shaft and the BLM holding system isn't stiff enough. Therefore, if one would approach the rotor sufficiently close to another side of the stator it will get stuck to the stator in that position.

Therefore in a first instance pushed manually the rotor to one side of the stator. As expected it was stuck at the other side, but as soon as it was released the rotor went back

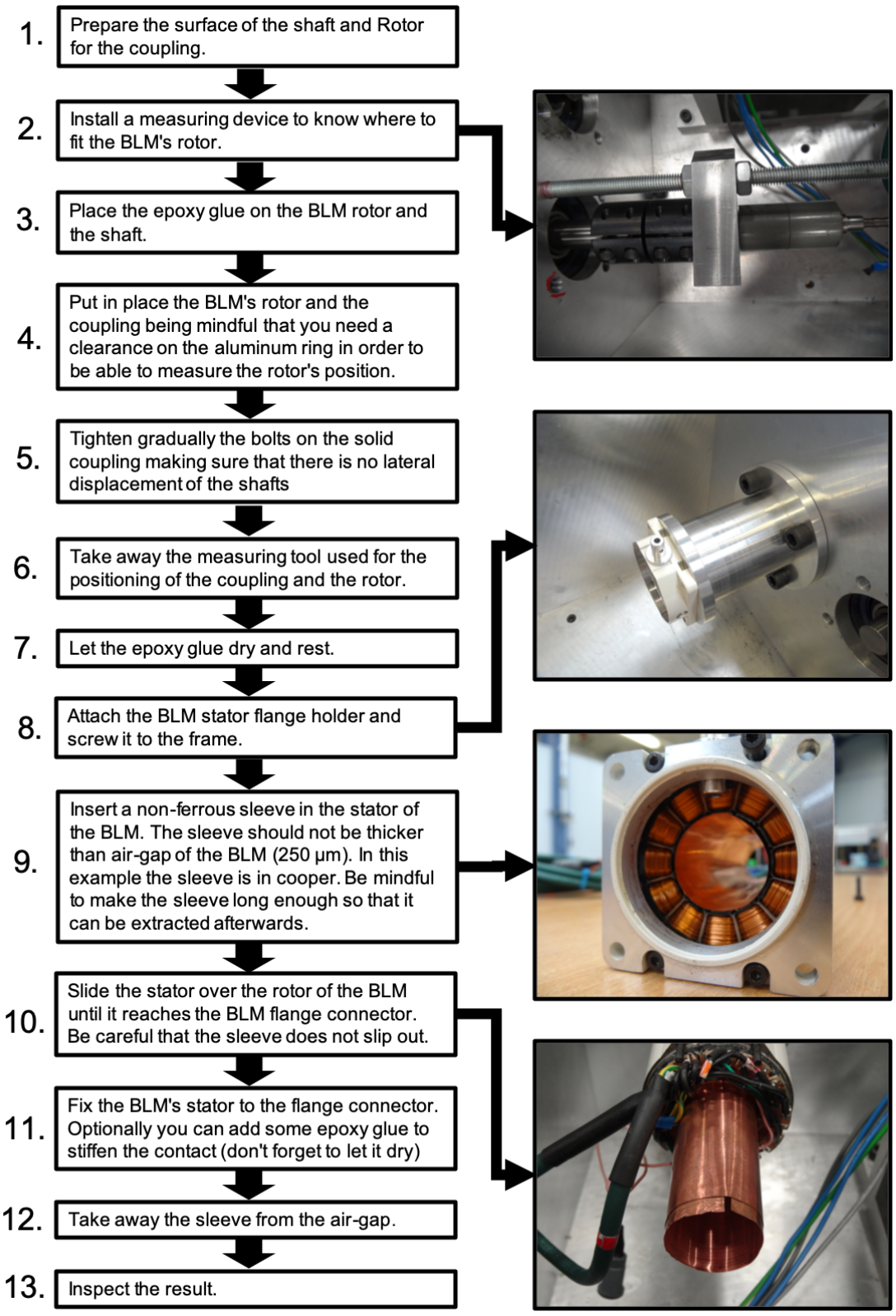
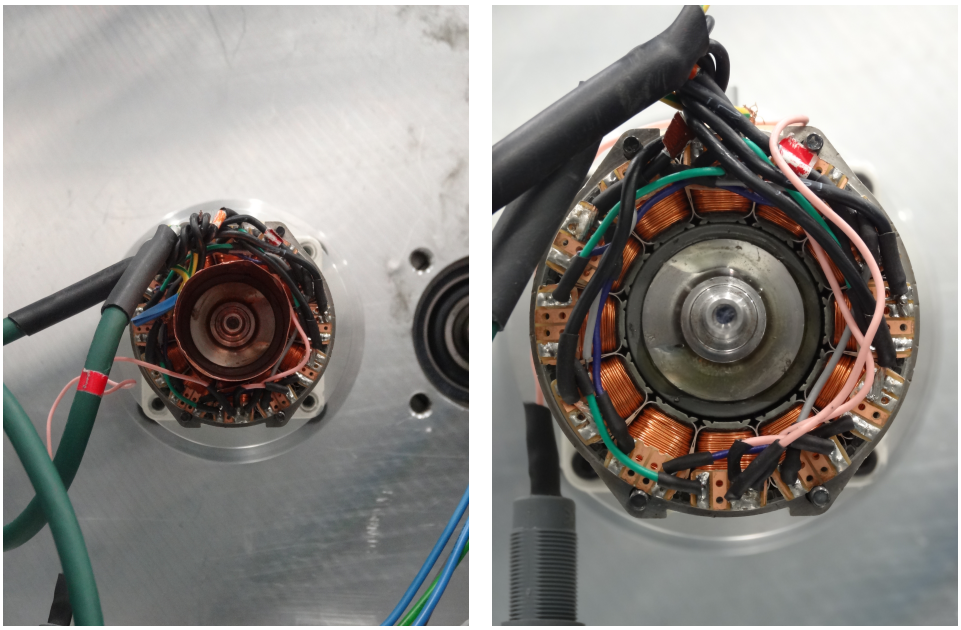


Fig. 5.29 Installation procedure of the BLM to the test rig



(a) System with the sleeve (b) BLM shaft misalignment

Fig. 5.30 Pictures illustrating the misalignment of the shaft in the BLM.

to it's initial position. Which lead us to the conclusion that the phenomenon is due to a big misalignment of the BLM shaft.

This obviously raises a few questions and the reason for this misalignment could be due to:

1. The process created isn't adequate to the system.
2. Are there some manufacturing errors
3. The shaft isn't centred.
4. All of them combined

This could be due to the fact while it was connect the coupling, the position of it along the shaft's axis was assessed. But this is not done regarding any potential deviation in the other axes. Looking at the potential deviation of the shaft due to the weight of the inertias and discs attached to it at the moment the BLM was attached, it was found that they significantly impact the shaft. Fig. 5.31 created with the FEM created in Chapter. 3 illustrates that the shaft could deviate up to 80 μm at the BLM. Combining this to possible defect in the manufacturing of the frame or non-alignment of the bearings this could clearly lead to the result obtained previously. To counteract this, a centering system should be devised to compensate for any defects and deflection of the shaft. But also it should compensate for the imperfections of the

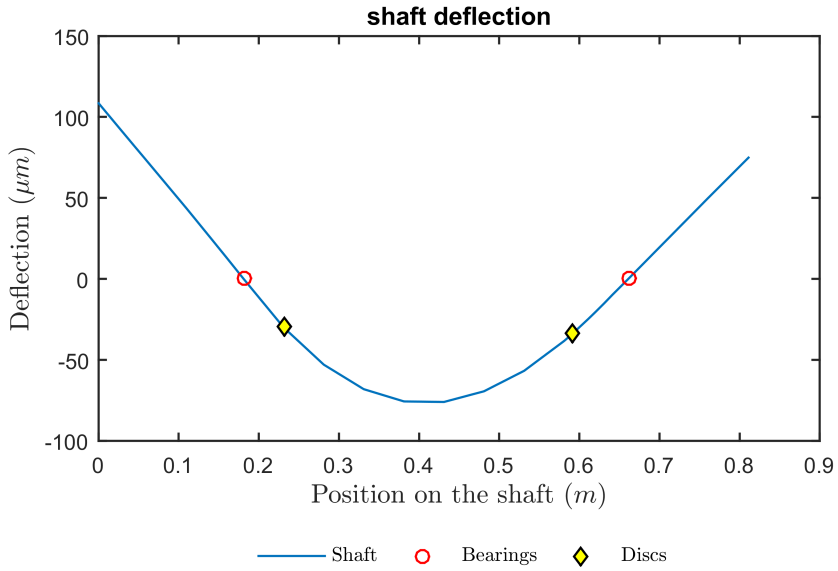


Fig. 5.31 Deflection of the shaft with the weight of the different components attached to it

divers components of the holding system. Sadly a lack of time and resources didn't allow for the design and creation of this said device. Wish lead to the impossibility to test the BLM's function as a rotodynamic actuator. But the preparation of the centering device is going to be pursued after this project.

5.4 Preliminary work

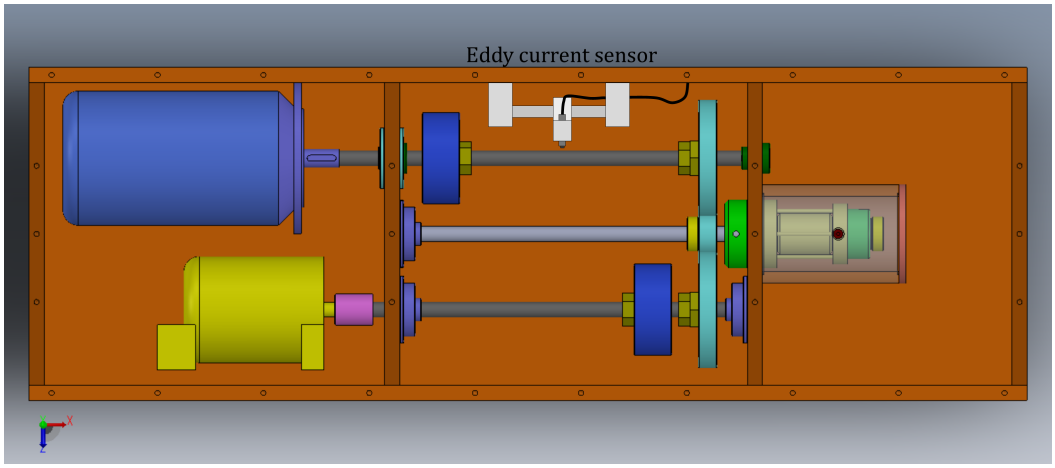


Fig. 5.32 Illustration of Test bench with the position of the eddy current sensor

Regardless of the success of the fact that the connection of the BLM being a failure, some work has been conducted. The main idea was first to confirm the critical speeds obtained through the rotodynamics FEM. For this the system was span using the IM. An eddy-current sensor was placed in the middle of the shaft and measured the displacement of the shaft at this point. Fig. 5.32 displays where and how the displacement sensor has been mounted. So to test out the vibration in the system the speed of the IM was slowly increased and the speed of the shaft, using a resolver, and the displacement of the shaft, using the eddy current sensor were measured. But as the system is slightly different because of the presence of the IM a new rotodynamic FEM for the system was created. From this FEM the critical speeds of the system were obtained. The only one is present at 2301 rpm. Care will be required around this speed during this experimental test. Doing so this the displayed measurement in Fig. 5.35 were obtained. Those results raise certain amount of questions concerning the system and the rotodynamic FEM. A sudden increase of vibration around 720 rpm is not present on the FEM response. As well as an oscillation with increase of vibration around 1440 rpm. The same happens again at 1525 rpm. Furthermore at the first test at around 2240 rpm the system decoupled the gears spontaneously. After a couple more test this happened again at roughly 2380 rpm as shown in Fig. 5.36. Concerning the gear issue; it was first thought that the gears where not set properly to the shaft. But after a few installations it was made sure that they are tightly set on the shaft, they still decoupled.

All those set-back indicate that certain factors of our study were overlooked. The first and principal suspect was the table and bench assembly of the test rig. The whole study considered that the Test bench is stiffly secured and damped to the ground. But this might have been an exaggeration.To verify this a test to observe the vibration at the box only was set Fig. 5.33. For this the box was hit in divers direction and measure the vibration the displacement of the box in different directions. The results of that experiment has been passed through a FFT in order to identify the frequencies at which the box resonate. Those result have been compiled in Fig. 5.37.

In Fig.5.37 one can observe that the frequency that appears the most is around 7 Hz, as well as 12 Hz and 25 Hz. If set into rpm those values would refer to 420 rpm, 720 rpm and 1500 rpm respectively. There is no way to say that some of them correlate with the unexpected behaviour of the shaft. This would be unreasonable as the interaction between the box and the shaft is probably more complicated. The rotodynamic FEM should take in account this phenomenon by inserting those data as a constraint at the bearings of the system or to find a stiffness K_{box} and a damping C_{box} representing the behaviour of the test bench as illustrated in Fig. 5.34. Another solution to this issue would to improve the stiffness of the connection of the test-bench. The way the system is installed at the moment isn't optimal for

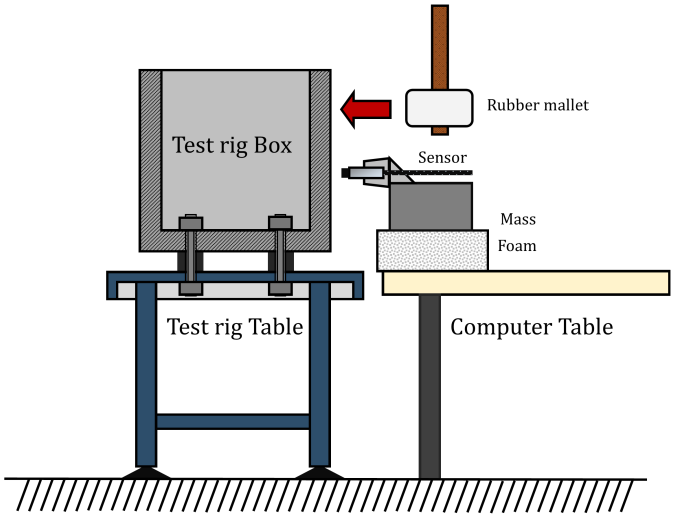


Fig. 5.33 Box vibration set up

the measurement of the vibration. The table at which the bench is fixed should be made way heavier and propose more damping to isolate even more the box from the ground. Probably also looking at way to isolate the measurement of the shaft from the box itself might be needed. As for the moment the sensor are sensible of the displacement of the box. This might make it hard to distinguish the vibration of the shaft from the one of the box.

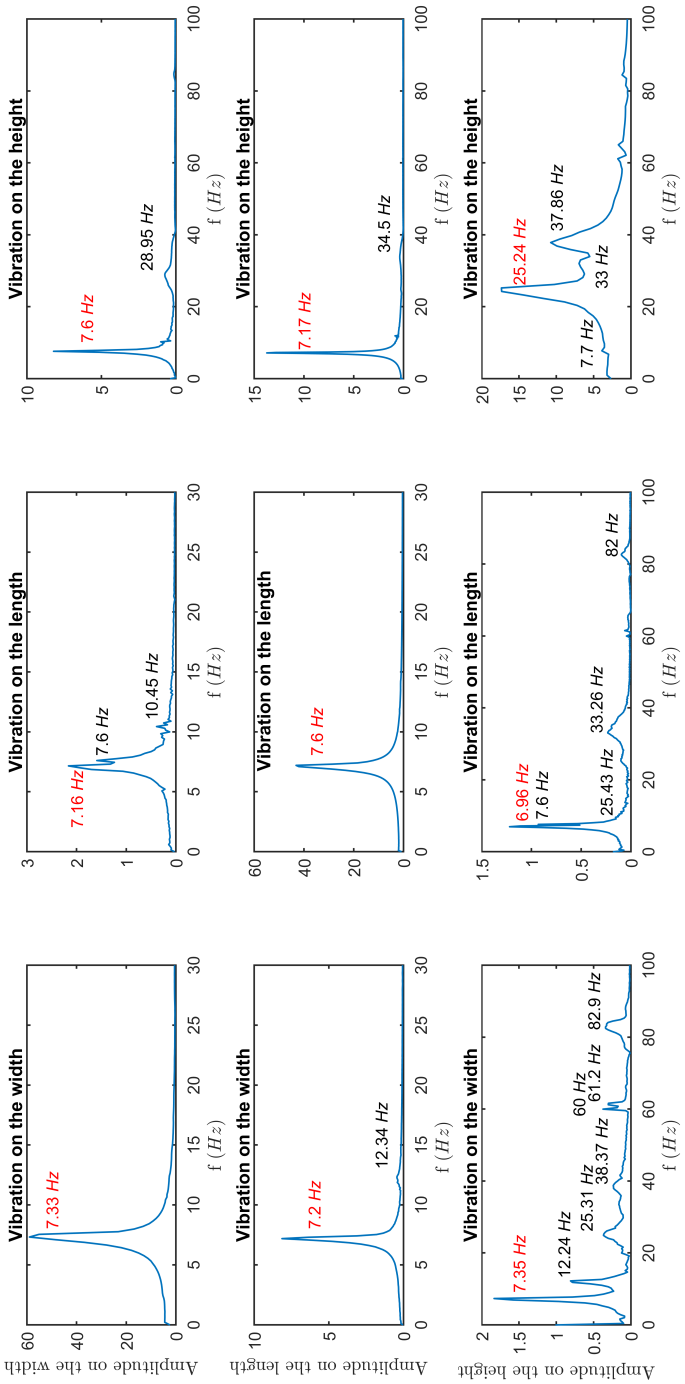


Fig. 5.34 FFT of the vibration of the test bench box

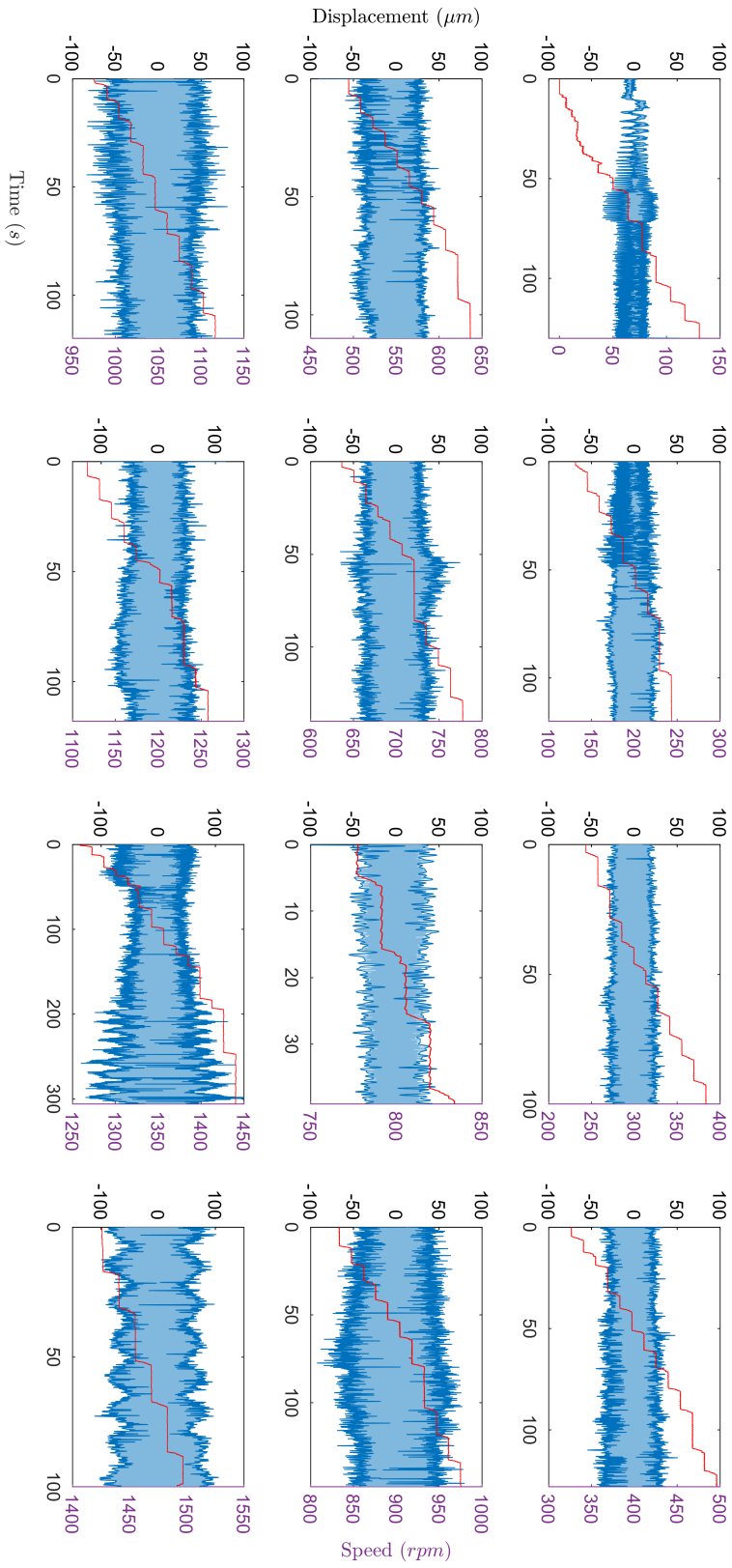


Fig. 5.35 Vibration with the speed

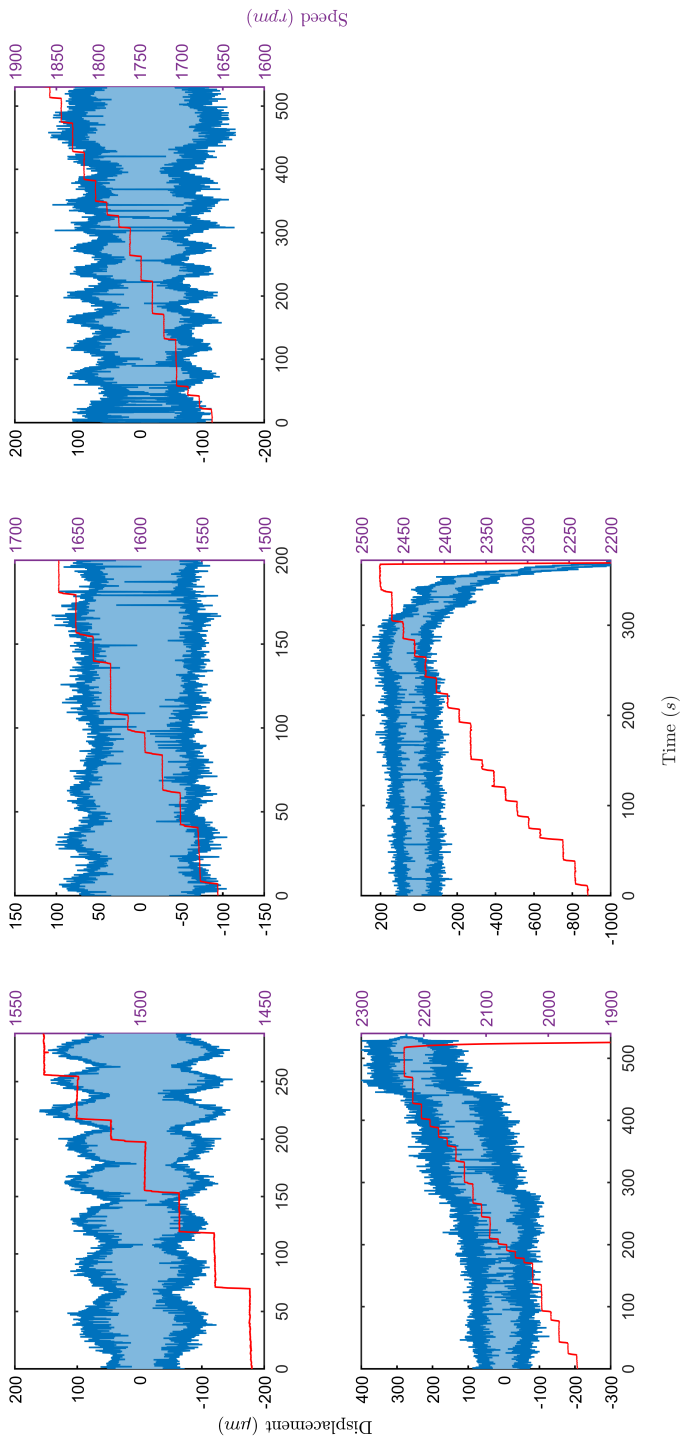


Fig. 5.36 Vibration with the speed

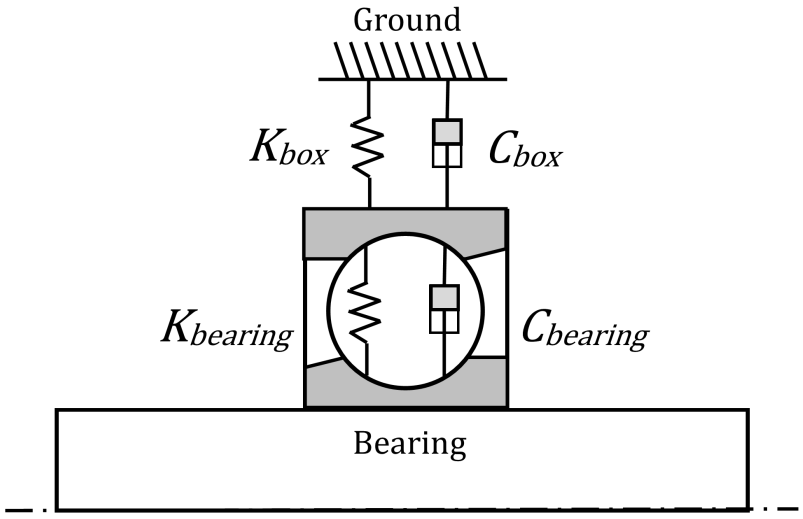


Fig. 5.37 Illustration of Test bench with the position of the eddy current sensor

5.5 Conclusion and further work

An experimental set up for a collaborative work has been set with C.Ahumada Sanhueza, S.Kumar, A.Bristot and N.Schneider. It combines together their PhD work as part of Marie Curie Project. The test rig has been design to provide each of the team-members a platform to test work from his/her PhD. As well as highlight the interaction the PhD works have between each other. Once the test bench was built it was analysand and tested. During its analysis a few challenges arouse. From those it was realized that some flaws in the design procedure of certain element like the air-riding seal and the support platform for the BLM are present. To our biggest regret those challenges couldn't be addressed in the available time frame the team had. Which leaves the test bench with some future work in order to address those challenges. Here will be listed the ones more specific to the present study:

- BLM connection
- FEM analysis of the test-bench
- Vibration of the test-bench structure
- Isolation of the measurement tools

After already discussing about the different solution for those challenges in their respective sections. But as a conclusion the required work for each of them will be summarized.

The BLM connection needs to be reviewed. Some defect in the manufacturing of the connector or even the overhaul design of the connection might be the reason for the high eccentricity of the BLM's rotor.

The FEM analysis of the test-bench should probably include the vibration of the test-bench structure in order to properly represent it. But this could be avoided if those vibrations would be avoided.

The vibration of the test-bench structure could be reduced by introducing a new structure where to sit the test-bench. Buy firmly grounding the box to a heavy and damped body it could avoid that the vibration of the box has an impact on the shaft's one.

The isolation of the measurement tools could be an advantage to the system so that the measurements of the shaft's displacement would not be polluted by the vibration of the test-bench's structure.

Conclusion

The aerospace industry has been investigating on more electrical aircraft since the 90's, trying to convert an increasing amount of mechanical actuators into electrical one. This lead to the need to generate more and more power for the ever-increasing electrical actuator in the aircraft. For this reason there is a growing interest into the study and design of electrical generator for aero-engines. Generator for turbofan are usually attached via a gear box to the high pressure shaft of the turbine. However, in the last 20 years several studies are trying to use electrical generators directly in-line with the turbine's shaft. This raised some challenges in finding the best topologies to use in such a task, as the generator must meet some strict requirements. Being used in the aerospace industry the topology should be most likely fault-tolerant. Furthermore, the use of the machine directly on the turbine' shaft will expose the machine to very high temperature. This will require the use of specific material and insulation as well as a designed cooling system for the machine. Out of this came two potential topologies that could fit the requirement stated previously: The PMSM or the BRM.

In order to reduce even further the use of mechanical components some studies looked at the use of this in-line electrical machine as an actuator for the starting of the turbine. Which leads to some design challenges regarding the difference between the starting torque and the generating one.

This study looked at the possibility to take advantage of the presence of this kind of electrical in-line machine to looks at the possibility to use it as an actuator to reduce the vibration in the turbine as well as generating power for the aircraft. To do this using a BLM to apply magnetic forces on the shaft that would lead to a reduction in shaft vibration was proposed.

To reach that goal a single winding PMSM BLM topology was studied ,that would be used for that role. A model of that BLM was made based on its voltage equation. An expressions for the force produced by the machine due to potential eccentricity as well as the interaction between the magnetic field of the PM and the currents injected by the suspension inverter, has been found. This model was then tested against and FEA mode, which showed a good correlation. However, the assumption that the iron in the BLM behaves as a magnetically

linear material can be limiting as most of high power dense PMSM are highly saturated. In future projects this model should be adapted to be able to take in account magnetic saturation. Based on this a control of the BLM allowing for reduction of the vibration and the potential injection of a stiffness K_{BLM} and a damping C_{BLM} on the shaft was created.

Based on this control and the model, the possibility to not only affect the vibration of the shaft but additionally the natural frequencies of the shaft, was investigated. The main objective was to investigate if the BLM could push/ avoid certain critical speeds of the shaft by injecting a specific amount of stiffness K_{BLM} into it. To be able to investigate if the BLM could affect the rotodynamic of the shaft a FEM simulation toll was used and improved in order to implement the effect of shafts connected with gears. Through this rotodynamic FEM and a simple algebraic example it was possible to show that it was possible to reduce the vibration of the shaft. Moreover, it demonstrated that the BLM could be used to shift/push critical speeds. Furthermore, several strategies in order to avoid critical speeds of a shaft were proposed.

- Critical speed push
- Critical speed hopping
- Critical speed stepping
- Critical speed sliding

The two last one, Critical speed stepping and Critical speed sliding, have been shown to be largely more efficient that the two first ones as they require much less stiffness during the overhaul use of the strategy. Following the demonstration of the validity of the BLM model with FEA comparison and the proposed rotodynamic strategy, teh combination of the two can be put in place. So that the BLM can have an interaction with the shaft's behaviour the FEM rotodynamic model has been combined with the control model of the BLM. In a first step has showed that the BLM was able to reduce the vibration of a shaft using a simple PD controller. Moreover, the limitation of this approach when facing critical speeds due to the large vibration created by the natural frequency has been presented. As simply trying reducing the vibration in this occasion has little to no effect on the rising of the vibration in the shaft. Once the interaction has been shown to be feasible in a combined model the validity of the proposed strategies to push critical speeds was confirmed. The combined model validated that it was indeed possible and validated the previous conclusion on the energy efficiency of the Critical speed stepping and Critical speed sliding. Furthermore it was possible to observe that critical speeds could be passed safely. However, one section that would require further study is the impact of the acceleration at which the critical speed is

pushed on the vibration of the shaft. There is a possibility that there could be an optimal acceleration to be found.

Finally once the models have been show to validate the proposed method, using a test-bench that was designed as part of the Marie Skłodowska Curie INNOVATE, the proposed technology should be tested. With 3 other PhD student the test bench was designed and built so that each of us could use it as a test platform of our PhD work as well as combining them and look at their interaction. Due to some manufacturing and design challenges no significant results were obtained form this test-bench that would confirm the feasibility of the use of the BLM coupled to a critical speed avoidance strategy.

Furthermore, this test bench highlighted one important aspect of the methodology presented in this thesis. The FEM rotodynamic model in this case was not matching well with reality. As this method is based on the assumption that the FEM model is accurate, there is a definite need to correct the FEM model based on measurements to be close to reality. Further studies should be done concentrating on the impact of the accuracy of the critical speed table generated from the FEM model on the proposed method.

In general this thesis highlighted that the use of BLM could not only be limited to the simple reduction of vibration, but could be used as rotodynamics actuator. Instead of having to accelerate through critical speeds the BLM will change the properties of the shaft. However the challenges that will arise from the proposed methods is that it is much more complex than the one used for vibration reduction as it requires a good understanding of the electromagnetic forces generated by the BLM as well as a detailed model of the shaft. A better understanding of the impact of the accuracy of those models is needed. Even-though the setting up of such a sytem in more complex than the one proposed in [22**?**], this thesis has shown clear limitation of this method when reaching critical speeds, which is going to be the case in most turbine applications.

References

[1] URL http://www.rotordynamics.info/.

[2] URL http://electrical.theiet.org/wiring-regulations/index.cfm.

[3] High performance permanent magnets. *Magnet Sales and Manufacturing Inc.*, 7:68, 2007.

[4] 2017. URL https://www.easa.europa.eu/system/files/dfu/TCDS%20E%20036%20issue%2008.pdf.

[5] S Constanza Ahumada, Seamus Garvey, Tao Yang, Patrick Wheeler, and Herve Morvan. The importance of load pulse timing in aircraft generation. In *Electrical Machines and Systems (ICEMS), 2015 18th International Conference on*, pages 1339–1345. IEEE. ISBN 1479988057.

[6] Constanza Ahumada S, Seamus Garvey, Tao Yang, Patrick Wheeler, and Herve Morvan. Impact of electric loads on engine shaft dynamics within more electric aircraft. SAE International. doi: 10.4271/2015-01-2409. URL https://doi.org/10.4271/2015-01-2409.

[7] M. Ananda Rao, J. Srinivas, V. B. V. Rama Raju, and K. V. S. S. Kumar. Coupled torsional–lateral vibration analysis of geared shaft systems using mode synthesis. *Journal of Sound and Vibration*, 261(2):359–364, 2003. ISSN 0022-460X. doi: http://dx.doi.org/10.1016/S0022-460X(02)01240-3. URL http://www.sciencedirect.com/science/article/pii/S0022460X02012403.

[8] N. Ando, M. Nakao, K. Hijikata, and Y. Tanaka. A proposal of a novel identification method of radial force parameters for bearingless motors. In *Electrical Machines and Systems (ICEMS), 2014 17th International Conference on*, pages 2305–2309. doi: 10.1109/ICEMS.2014.7013883.

[9] CR Avery, SG Burrow, and PH Mellor. Electrical generation and distribution for the more electric aircraft. In *Universities Power Engineering Conference, 2007. UPEC 2007. 42nd International*, pages 1007–1012. IEEE. ISBN 1905593368.

[10] J. B. Bartolo and C. Gerada. The electromagnetic design of a high speed, 45kw, switched reluctance machine having a novel rotor geometry for aerospace application. In *2014 International Conference on Electrical Machines (ICEM)*, pages 2513–2519. doi: 10.1109/ICELMACH.2014.6960540.

[11] T. Baumgartner, R. M. Burkart, and J. W. Kolar. Analysis and design of a 300w 500,000 rpm slotless self-bearing permanent-magnet motor. *Industrial Electronics, IEEE Transactions on*, 61(8):4326–4336, 2014. ISSN 0278-0046. doi: 10.1109/TIE.2013.2284159. URL http://ieeexplore.ieee.org/ielx7/41/6734701/06616583.pdf?tp=&arnumber=6616583&isnumber=6734701.

[12] J.W. Beams and F.T. Holmes. Suspension of rotatable bodies, 1941. URL https://www.google.com/patents/US2256937. US Patent 2256937 A.

[13] B. S. Bhangu and K. Rajashekara. Control strategy for electric starter generators embedded in gas turbine engine for aerospace applications. In *Energy Conversion Congress and Exposition (ECCE), 2011 IEEE*, pages 1461–1467. doi: 10.1109/ECCE.2011.6063953. URL http://ieeexplore.ieee.org/ielx5/6056715/6063732/06063953.pdf?tp=&arnumber=6063953&isnumber=6063732.

[14] B. S. Bhangu and K. Rajashekara. Electric starter generators: Their integration into gas turbine engines. *IEEE Industry Applications Magazine*, 20(2):14–22, 2014. ISSN 1077-2618. doi: 10.1109/MIAS.2013.2288398.

[15] Garrett Birkhoff and Henry L. Garabedian. Smooth surface interpolation. *Journal of Mathematics and Physics*, 39(1-4):258–268, 1960. ISSN 1467-9590. doi: 10.1002/sapm1960391258. URL http://dx.doi.org/10.1002/sapm1960391258.

[16] A. Cavagnino, A. Tenconi, G. Rizzoli, M. Mengoni, and G. Serra. Multiphase induction machine for aero-engine shaft-line-embedded starter/generator: Scaled prototypes testing. In *2014 International Conference on Electrical Machines (ICEM)*, pages 2107–2113. doi: 10.1109/ICELMACH.2014.6960475.

[17] A. Chiba, S. Horima, and H. Sugimoto. A principle and test results of a novel bearingless motor with motor parallel winding structure. In *Energy Conversion Congress and Exposition (ECCE), 2013 IEEE*, pages 2474–2479. doi: 10.1109/ECCE.2013.6647019. URL http://ieeexplore.ieee.org/ielx7/6624149/6646663/06647019.pdf?tp=&arnumber=6647019&isnumber=6646663.

[18] A. Chiba, M. A. Rahman, and T. Fukao. Radial force in a bearingless reluctance motor. *Magnetics, IEEE Transactions on*, 27(2):786–790, 1991. ISSN 0018-9464. doi: 10.1109/20.133292.

[19] A. Chiba, T. Fukao, and M. Azizur Rahman. Vibration suppression of a flexible shaft with a simplified bearingless induction motor drive. *Industry Applications, IEEE Transactions on*, 44(3):745–752, 2008. ISSN 0093-9994. doi: 10.1109/TIA.2008.921401.

[20] Akira Chiba, Tadashi Fukao, Osamu Ichikawa, Masahide Oshima, Masatsugu Takemoto, and David G. Dorrell. *Magnetic Bearings and Bearingless Drives*. Newes, 2005. ISBN 0-7506-5727-8.

[21] D. R. Chivens and H. D. Nelson. The natural frequencies and critical speeds of a rotating, flexible shaft-disk system. *Journal of Engineering for Industry*, 97(3):881–886, 1975. ISSN 1087-1357. doi: 10.1115/1.3438696. URL http://dx.doi.org/10.1115/1.3438696.

[22] MOT Cole, PS Keogh, and CR Burrows. Vibration control of a flexible rotor/magnetic bearing system subject to direct forcing and base motion disturbances. *Proceedings of the Institution of Mechanical Engineers, Part C: Journal of Mechanical Engineering Science*, 212(7):535–546, 1998. ISSN 0954-4062.

[23] D. Cozonac, V. Mihaila, G. Velu, S. Duchesne, J. P. Lecointe, and D. Roger. Performance comparision of winding wires for high-temperature rotating machines. In *Solid Dielectrics (ICSD), 2013 IEEE International Conference on*, pages 318–321. ISBN 2159-1687. doi: 10.1109/ICSD.2013.6619771. URL http://ieeexplore.ieee.org/ielx7/6596174/6619651/06619771.pdf?tp=&arnumber=6619771&isnumber=6619651.

[24] S. Duchesne G. Velu D. Cozonac, J-Ph. Lecointe. Material characterization and geometry of a high temperature induction machine. 2014.

[25] P.S. de Laplace. *Des Fonctions génératrices*, book section Chapter I. Ve. Courcier, 1812. URL https://books.google.co.uk/books?id=nQwAAAAAMAAJ.

[26] Samuel Earnshaw. On the nature of the molecular forces which regulate the constitution of the luminiferous ether. *Trans. Camb. Phil. Soc*, 7:97–112, 1842.

[27] AM El-Refaie. Fault-tolerant permanent magnet machines: A review. *IET Electric Power Applications*, 5(1):59–74, 2011. ISSN 1751-8679.

[28] M. E. Elbuluk and M. D. Kankam. Potential starter/generator technologies for future aerospace applications. In *Aerospace and Electronics Conference, 1996. NAECON 1996., Proceedings of the IEEE 1996 National*, volume 1, pages 75–82 vol.1. ISBN 0547-3578. doi: 10.1109/NAECON.1996.517619. URL http://ieeexplore.ieee.org/ielx3/3788/11049/00517619.pdf?tp=&arnumber=517619&isnumber=11049.

[29] James Ferguson. Multivariable curve interpolation. *J. ACM*, 11(2):221–228, 1964. ISSN 0004-5411. doi: 10.1145/321217.321225.

[30] C. A. Ferreira, S. R. Jones, and W. S. Heglund. Performance evaluation of a switched reluctance starter/generator system under constant power and capacitive type loads. In *Applied Power Electronics Conference and Exposition, 1995. APEC '95. Conference Proceedings 1995., Tenth Annual*, pages 416–424 vol.1. doi: 10.1109/APEC.1995.468982. URL http://ieeexplore.ieee.org/ielx2/3292/9884/00468982.pdf?tp=&arnumber=468982&isnumber=9884.

[31] C. A. Ferreira, S. R. Jones, W. S. Heglund, and W. D. Jones. Detailed design of a 30-kw switched reluctance starter/generator system for a gas turbine engine application. *Industry Applications, IEEE Transactions on*, 31(3):553–561, 1995. ISSN 0093-9994. doi: 10.1109/28.382116. URL http://ieeexplore.ieee.org/ielx1/28/8658/00382116.pdf?tp=&arnumber=382116&isnumber=8658.

[32] G.F. Franklin, J.D. Powell, and A. Emami-Naeini. *Finale Value Theorem*, pages 102–105. Addison-Wesley, 1994. ISBN 0201527472. URL https://books.google.co.uk/books?id=wBIoAQAAMAAJ.

[33] M. I. Friswell. *Dynamics of rotating machines*. Cambridge aerospace series. Cambridge University Press, Cambridge ; New York, 2010. ISBN 9780521850162 (hardback) 0521850169 (hardback).

[34] M. I. Friswell, S. D. Garvey, J. E. T. Penny, and M. G. Smart. Computing critical speeds for rotating machines with speed dependent bearing properties. *Journal of Sound and Vibration*, 213(1):139–158, 1998. ISSN 0022-460X. doi: https://doi.org/10.1006/jsvi.1998.1503. URL http://www.sciencedirect.com/science/article/pii/S0022460X98915036.

[35] G. Genta. *Jeffcott rotor*, book section 1, pages 35–91. Springer New York, 2005. ISBN 9780387209364. URL https://books.google.co.uk/books?id=_dGQ9hdJA88C.

[36] R. Hall, A. G. Jack, B. C. Mecrow, and A. Mitcham. Design and initial testing of an outer rotating segmented rotor switched reluctance machine for an aero-engine shaft-line-embedded starter/generator. In *Electric Machines and Drives, 2005 IEEE International Conference on*, pages 1870–1877. doi: 10.1109/IEMDC.2005.195975. URL http://ieeexplore.ieee.org/ielx5/10252/32672/01531593.pdf?tp=&arnumber=1531593&isnumber=32672.

[37] Irving G Hansen and Gale R Sundberg. Space station 20-khz power management and distribution system. In *Power Electronics Specialists Conference, 1986 17th Annual IEEE*, pages 676–683. IEEE. ISBN 9996323277.

[38] H. L. Hassenpflug, R. D. Flack, and E. J. Gunter. Influence of acceleration on the critical speed of a jeffcott rotor. *Journal of Engineering for Power*, 103(1):108–113, 1981. ISSN 0742-4795. doi: 10.1115/1.3230680. URL http://dx.doi.org/10.1115/1.3230680.

[39] R Holmes and MM Dede. Non-linear phenomena in aero-engine rotor vibration. *Proceedings of the Institution of Mechanical Engineers, Part A: Journal of Power Engineering*, 203(1):25–34, 1989. ISSN 0954-4046.

[40] HPC. Heavy duty spur gear: Yg2. Report, 2013. URL https://shop.hpceurope.com/pdf/gb/YG2.pdf.

[41] Zhu Huangqiu, Tan Er, Wang Chengbo, Huang Zhenyue, and Jia Haolai. Direct torque and direct suspension force control of bearingless permanent magnet synchronous motor. In *Control and Decision Conference (CCDC), 2010 Chinese*, pages 2411–2415. doi: 10.1109/CCDC.2010.5498804.

[42] D.J. Hucker. Variable speed constant frequency generating system, 1986. URL https://www.google.com/patents/US4625160. US Patent 4625160 A.

[43] Y. Iiyama, K. Soutome, and A. Chiba. A novel middle-point current-injection type bearingless motor for vibration suppression. In *Energy Conversion Congress and Exposition (ECCE), 2010 IEEE*, pages 1693–1698. doi: 10.1109/ECCE.2010.5618114. URL http://ieeexplore.ieee.org/ielx5/5606065/5617696/05618114.pdf?tp=&arnumber=5618114&isnumber=5617696.

[44] Yukio Ishida, Takashi Ikeda, and Toshio Yamamoto. Transient vibration of a rotating shaft with nonlinear spring characteristics during acceleration through a major critical speed : Vibration, control engineering, engineering for industry. *JSME international journal*, 30(261):458–466, 1987. doi: 10.1299/jsme1987.30.458.

[45] Alan G Jack, Barrie C Mecrow, and James A Haylock. A comparative study of permanent magnet and switched reluctance motors for high-performance fault-tolerant applications. *IEEE transactions on industry applications*, 32(4):889–895, 1996. ISSN 0093-9994.

[46] Liu Jianfeng, Wang Huijun, Bao Junfang, Zhou Guangxu, and Zhang Fengge. A novel permanent magnet biased bearingless switched reluctance motor. In *Energy Conversion Congress and Exposition (ECCE), 2013 IEEE*, pages 4342–4347. doi: 10.1109/ECCE.2013.6647281. URL http://ieeexplore.ieee.org/ielx7/6624149/6646663/06647281.pdf?tp=&arnumber=6647281&isnumber=6646663.

[47] RI Jones. The more electric aircraft—assessing the benefits. *Proceedings of the Institution of Mechanical Engineers, Part G: Journal of Aerospace Engineering*, 216 (5):259–269, 2002. ISSN 0954-4100.

[48] P. Kascak, R. Jansen, T. Dever, A. Nagorny, and K. Loparo. Motoring performance of a conical pole-pair separated bearingless electric machine. In *Energytech, 2011 IEEE*, pages 1–6. doi: 10.1109/EnergyTech.2011.5948515. URL http://ieeexplore.ieee.org/ielx5/5937410/5948497/05948515.pdf?tp=&arnumber=5948515&isnumber=5948497.

[49] W. K. S. Khoo. Bridge configured winding for polyphase self-bearing machines. *Magnetics, IEEE Transactions on*, 41(4):1289–1295, 2005. ISSN 0018-9464. doi: 10.1109/TMAG.2005.845837. URL http://ieeexplore.ieee.org/ielx5/20/30696/01420685.pdf?tp=&arnumber=1420685&isnumber=30696.

[50] Byron Knapp, Dave Arneson, and Don Martin. Electrical runout using an eddy-current sensor for roundness measurements. Report, Lion Precision, 2017. URL http://www.lionprecision.com/tech-library/technotes/tech-pdfs/article-PI-electrical-runout-ASPE.pdf.

[51] Shubham Kumar, Seamus Garvey, and Hervé Morvan. An investigation in radial gap air-riding seals for aero-engines. *ARPN Journal of Engineering and Applied Sciences*, 11(12):5, 2016. ISSN 1819-6608.

[52] B. Liu. Survey of bearingless motor technologies and applications. In *2015 IEEE International Conference on Mechatronics and Automation (ICMA)*, pages 1983–1988. ISBN 2152-7431. doi: 10.1109/ICMA.2015.7237790.

[53] Stephen R. MacMinn and W. D. Jones. A very high speed switched-reluctance starter-generator for aircraft engine applications. In *Aerospace and Electronics Conference, 1989. NAECON 1989., Proceedings of the IEEE 1989 National*, pages 1758–1764 vol.4. doi: 10.1109/NAECON.1989.40453. URL http://ieeexplore.ieee.org/ielx5/837/1552/00040453.pdf?tp=&arnumber=40453&isnumber=1552.

[54] R. Oishi, S. Horima, H. Sugimoto, and A. Chiba. A novel parallel motor winding structure for bearingless motors. *Magnetics, IEEE Transactions on*, 49(5):2287–2290, 2013. ISSN 0018-9464. doi: 10.1109/TMAG.2013.2240279. URL http://ieeexplore.ieee.org/ielx7/20/6514491/06514703.pdf?tp=&arnumber=6514703&isnumber=6514491.

[55] M. Oshima, S. Miyazawa, T. Deido, A. Chiba, Fukuzo Nakamura, and T. Fukao. Characteristics of a permanent magnet type bearingless motor. In *Industry Applications Society Annual Meeting, 1994., Conference Record of the 1994 IEEE*, pages 196–202 vol.1. doi: 10.1109/IAS.1994.345479.

[56] Panasonic. Ac servo motor driver minas a-series. Report, 2007. URL https://industrial.panasonic.com/content/data/MT/PDF/minas_a_e.pdf.

[57] D. J. Powell, G. W. Jewell, D. Howe, and K. Atallah. Rotor topologies for a switched-reluctance machine for the 'more-electric' aircraft engine. *Electric Power Applications, IEE Proceedings* -, 150(3):311–318, 2003. ISSN 1350-2352. doi: 10.1049/ip-epa:20030121.

[58] Lion Precision. Eddy-current sensors. Report, 2017. URL http://www.lionprecision.com/manuals/lit-pdfs/EddyCurrentSensorCatalog_LionPrecision.pdf.

[59] J. S. Rao, T. N. Shiau, and J. R. Chang. Theoretical analysis of lateral response due to torsional excitation of geared rotors. *Mechanism and Machine Theory*, 33(6):761–783, 1998. ISSN 0094-114X. doi: http://dx.doi.org/10.1016/S0094-114X(97)00056-6. URL http://www.sciencedirect.com/science/article/pii/S0094114X97000566.

[60] A. La Rocca, S. J. Pickering, C. Eastwick, and C. Gerada. Enhanced cooling for an electric starter-generator for aerospace application. In *7th IET International Conference on Power Electronics, Machines and Drives (PEMD 2014)*, pages 1–7. doi: 10.1049/cp.2014.0373.

[61] G. Schweitzer, H. Bleuler, E.H. Maslen, M. Cole, P. Keogh, R. Larsonneur, E. Maslen, r Nordmann, Y. Okada, and G. Schweitzer. *Magnetic Bearings: Theory, Design, and Application to Rotating Machinery*. Springer Berlin Heidelberg, 2009. ISBN 9783642004964. URL https://books.google.co.uk/books?id=m369jwEACAAJ.

[62] Maslen Eric H. (Eds.) Schweitzer, Gerhard. *Magnetic Bearings Theory, Design, and Application to Rotating Machinery*. 2009. ISBN 978-3-642-00497-1.

[63] G. Scorletti and V. Fromion. Introduction à la commande multivariable des systèmes: méthode de synthèse fréquentielle h infinie. *Université de Caen/Basse Normandie*, 1: 201, 2007.

[64] E. Severson, R. Nilssen, T. Undeland, and N. Mohan. Analysis of the bearingless ac homopolar motor. In *Electrical Machines (ICEM), 2012 XXth International Conference on*, pages 570–576. doi: 10.1109/ICElMach.2012.6349926. URL http://ieeexplore.ieee.org/ielx5/6330482/6349821/06349926.pdf?tp=&arnumber=6349926&isnumber=6349821.

[65] Jennifer Catherine Shaw, SDA Fletcher, PJ Norman, and SJ Galloway. More electric power system concepts for an environmentally responsible aircraft (n+ 2). In *Universities Power Engineering Conference (UPEC), 2012 47th International*, pages 1–6. IEEE. ISBN 1467328561.

[66] T. Stallinger, W. Gruber, and W. Amrhein. Bearingless segment motor with a consequent pole rotor. In *Electric Machines and Drives Conference, 2009. IEMDC '09. IEEE International*, pages 1374–1380. doi: 10.1109/IEMDC.2009.5075382. URL http://ieeexplore.ieee.org/ielx5/5069086/5075166/05075382.pdf?tp=&arnumber=5075382&isnumber=5075166.

[67] D. Steinert, T. Nussbaumer, and J. W. Kolar. Slotless bearingless disk drive for high-speed and high-purity applications. *Industrial Electronics, IEEE Transactions on*, 61(11):5974–5986, 2014. ISSN 0278-0046. doi: 10.1109/TIE.2014.2311379. URL http://ieeexplore.ieee.org/ielx7/41/6827271/06766196.pdf?tp=&arnumber=6766196&isnumber=6827271.

[68] H. Sugimoto, S. Tanaka, and A. Chiba. Vibration reduction of one-axis actively position regulated single-drive bearingless motor with repulsive passive magnetic bearings. In *Energy Conversion Congress and Exposition (ECCE), 2014 IEEE*, pages 1799–1805. doi: 10.1109/ECCE.2014.6953636.

[69] Martin van der Geest, Henk Polinder, Jan A Ferreira, and Dennis Zeilstra. Machine selection and initial design of an aerospace starter generator. In *Electric Machines and Drives Conference (IEMDC), 2013 IEEE International*, pages 196–203. IEEE. ISBN 1467349747.

[70] B.J. W, K.E. E, and N.B.T. Peoples. Magnetically supported rotating bodies, 1954. URL https://www.google.com/patents/US2691306. US Patent 2691306 A.

[71] Joseph Weimer. *Past, present and future of aircraft electrical power systems*. Aerospace Sciences Meetings. American Institute of Aeronautics and Astronautics, 2001. doi: doi: 10.2514/6.2001-114710.2514/6.2001-1147. URL https://doi.org/10.2514/6.2001-1147.

[72] Ding Wen, Liu Ling, and Lou Jianyong. Design and control of a high-speed switched reluctance machine with conical magnetic bearings for aircraft application. *Electric Power Applications, IET*, 7(3):179–190, 2013. ISSN 1751-8660. doi: 10.1049/iet-epa.2012.0319.

[73] Patrick W Wheeler, Jon C Clare, Andrew Trentin, and Serhiy Bozhko. An overview of the more electrical aircraft. *Proceedings of the Institution of Mechanical Engineers, Part G: Journal of Aerospace Engineering*, 227(4):578–585, 2013. ISSN 0954-4100.

[74] S.Y. Yoon, Z. Lin, and P.E. Allaire. *Introduction to Rotor Dynamics*, book section 2, pages 17–55. Springer London, 2012. ISBN 9781447142393. URL https://books.google.co.uk/books?id=PvrvugAACAAJ.

[75] Chaoping Zang and DJ Ewins. Model validation for structural dynamics in the aero-engine design process. *Frontiers of Energy and Power Engineering in China*, 3(4):480–488, 2009. ISSN 1673-7393.

[76] Xu Zhenyao, Lee Dong-Hee, Zhang Fengge, and Ahn Jin-Woo. Hybrid pole type bearingless switched reluctance motor with short flux path. In *Electrical Machines and Systems (ICEMS), 2011 International Conference on*, pages 1–6, . doi: 10.1109/ICEMS.2011.6073473. URL http://ieeexplore.ieee.org/ielx5/6059525/6073288/06073473.pdf?tp=&arnumber=6073473&isnumber=6073288.

[77] Xu Zhenyao, Zhang Fengge, and Ahn Jin-Woo. Design and analysis of a novel 12/14 hybrid pole type bearingless switched reluctance motor. In *Industrial Electronics (ISIE), 2012 IEEE International Symposium on*, pages 1922–1927, . ISBN 2163-5137. doi: 10.1109/ISIE.2012.6237386. URL http://ieeexplore.ieee.org/ielx5/6230783/6237048/06237386.pdf?tp=&arnumber=6237386&isnumber=6237048.

Appendix A

Control Model: Simulink

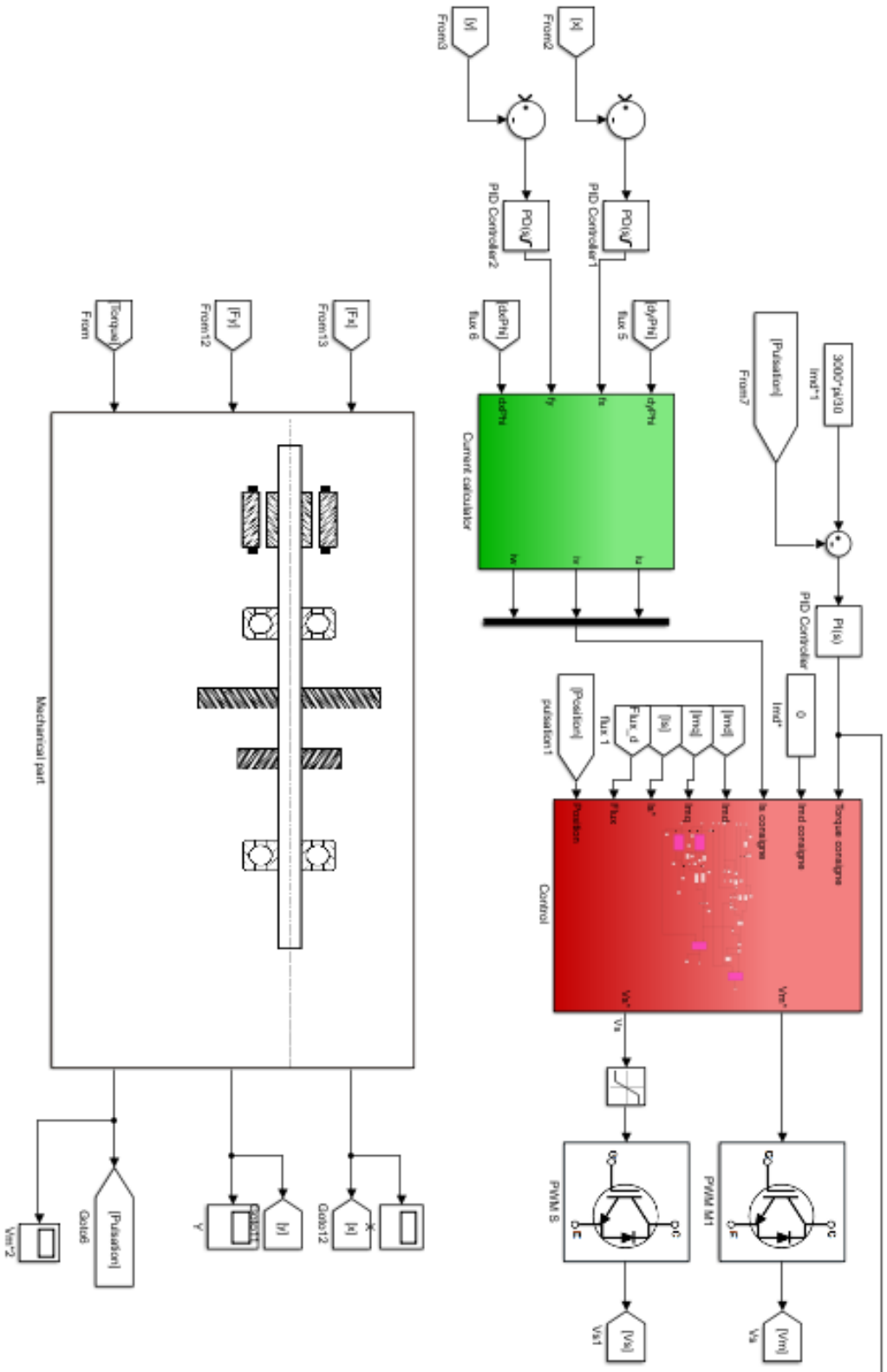


Fig. A.1 BLM control on Simulink

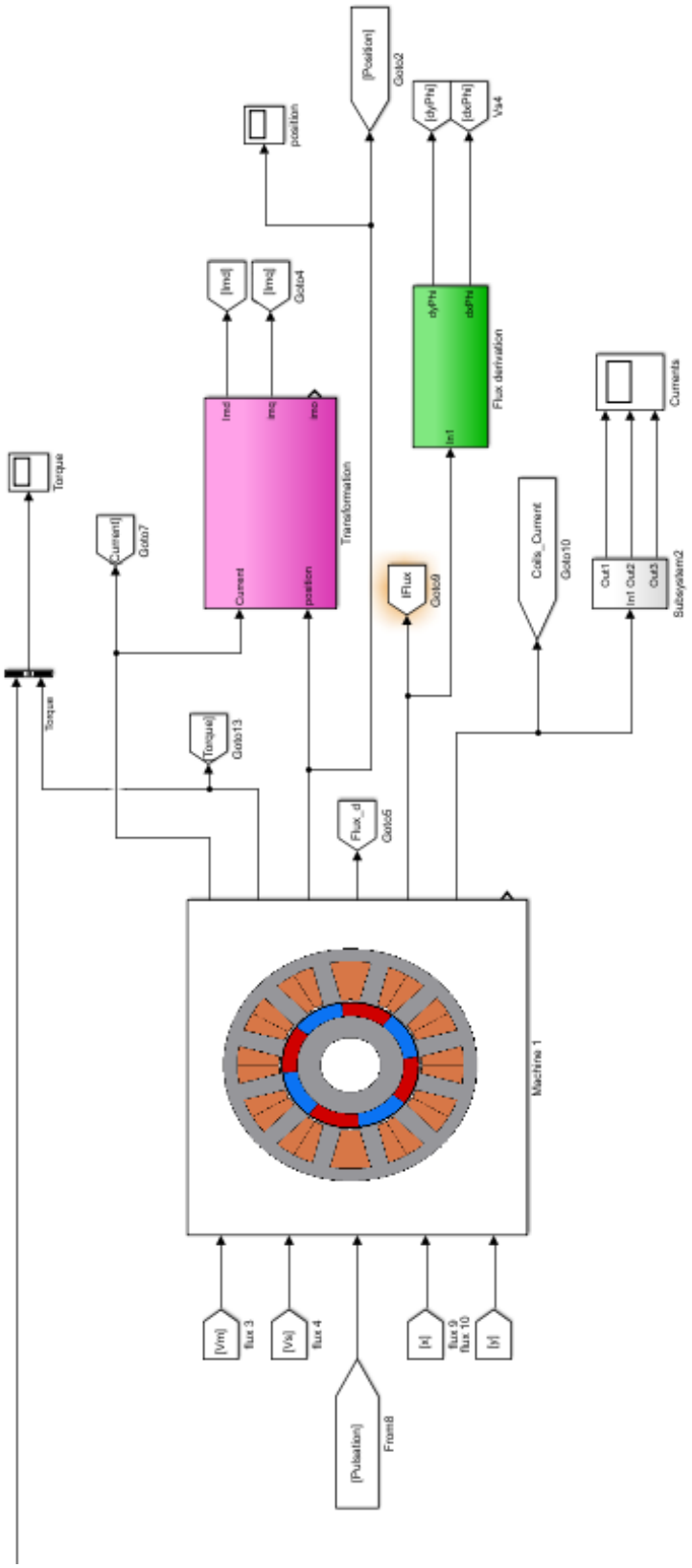


Fig. A.2 BLM control on Simulink

Appendix B

BLM rotodynamic interaction

B.1 Single shaft study

Table B.1 Critical speed value for both cases at divers stiffness

Data point	Case A		Case B	
	Stiffness	Critical speed	Stiffness	Critical speed
0	$0.00 \cdot 10^{0}\ N \cdot m^{-1}$	2030 rpm	$-8.00 \cdot 10^{5}\ N \cdot m^{-1}$	2584 rpm
1	$5.20 \cdot 10^{3}\ N \cdot m^{-1}$	2055 rpm	$-7.48 \cdot 10^{5}\ N \cdot m^{-1}$	2592 rpm
2	$1.10 \cdot 10^{4}\ N \cdot m^{-1}$	2078 rpm	$-6.97 \cdot 10^{5}\ N \cdot m^{-1}$	2600 rpm
3	$1.73 \cdot 10^{4}\ N \cdot m^{-1}$	2102 rpm	$-6.48 \cdot 10^{5}\ N \cdot m^{-1}$	2609 rpm
4	$2.43 \cdot 10^{4}\ N \cdot m^{-1}$	2126 rpm	$-6.01 \cdot 10^{5}\ N \cdot m^{-1}$	2619 rpm
5	$3.21 \cdot 10^{4}\ N \cdot m^{-1}$	2149 rpm	$-5.56 \cdot 10^{5}\ N \cdot m^{-1}$	2631 rpm
6	$4.07 \cdot 10^{4}\ N \cdot m^{-1}$	2172 rpm	$-5.12 \cdot 10^{5}\ N \cdot m^{-1}$	2644 rpm
7	$5.01 \cdot 10^{4}\ N \cdot m^{-1}$	2195 rpm	$-4.70 \cdot 10^{5}\ N \cdot m^{-1}$	2659 rpm
8	$6.06 \cdot 10^{4}\ N \cdot m^{-1}$	2216 rpm	$-4.30 \cdot 10^{5}\ N \cdot m^{-1}$	2677 rpm
9	$7.22 \cdot 10^{4}\ N \cdot m^{-1}$	2238 rpm	$-3.92 \cdot 10^{5}\ N \cdot m^{-1}$	2699 rpm
10	$8.50 \cdot 10^{4}\ N \cdot m^{-1}$	2258 rpm	$-3.56 \cdot 10^{5}\ N \cdot m^{-1}$	2725 rpm
11	$9.91 \cdot 10^{4}\ N \cdot m^{-1}$	2277 rpm	$-3.21 \cdot 10^{5}\ N \cdot m^{-1}$	2758 rpm
12	$1.15 \cdot 10^{5}\ N \cdot m^{-1}$	2296 rpm	$-2.88 \cdot 10^{5}\ N \cdot m^{-1}$	2800 rpm
13	$1.32 \cdot 10^{5}\ N \cdot m^{-1}$	2314 rpm	$-2.57 \cdot 10^{5}\ N \cdot m^{-1}$	2855 rpm
14	$1.51 \cdot 10^{5}\ N \cdot m^{-1}$	2331 rpm	$-2.27 \cdot 10^{5}\ N \cdot m^{-1}$	2931 rpm
15	$1.72 \cdot 10^{5}\ N \cdot m^{-1}$	2347 rpm	$-2.00 \cdot 10^{5}\ N \cdot m^{-1}$	3041 rpm
16	$1.95 \cdot 10^{5}\ N \cdot m^{-1}$	2362 rpm	$-1.74 \cdot 10^{5}\ N \cdot m^{-1}$	3212 rpm
17	$2.21 \cdot 10^{5}\ N \cdot m^{-1}$	2376 rpm	$-1.50 \cdot 10^{5}\ N \cdot m^{-1}$	3500 rpm
18	$2.50 \cdot 10^{5}\ N \cdot m^{-1}$	2390 rpm	$-1.28 \cdot 10^{5}\ N \cdot m^{-1}$	4009 rpm
19	$2.81 \cdot 10^{5}\ N \cdot m^{-1}$	2402 rpm	$-1.08 \cdot 10^{5}\ N \cdot m^{-1}$	4749 rpm
20	$3.16 \cdot 10^{5}\ N \cdot m^{-1}$	2414 rpm	$-8.89 \cdot 10^{4}\ N \cdot m^{-1}$	5316 rpm
21	$3.54 \cdot 10^{5}\ N \cdot m^{-1}$	2425 rpm	$-7.20 \cdot 10^{4}\ N \cdot m^{-1}$	828 rpm
22	$3.96 \cdot 10^{5}\ N \cdot m^{-1}$	2436 rpm	$-5.69 \cdot 10^{4}\ N \cdot m^{-1}$	1421 rpm
23	$4.44 \cdot 10^{5}\ N \cdot m^{-1}$	2458 rpm	$-4.36 \cdot 10^{4}\ N \cdot m^{-1}$	1669 rpm
24	$4.96 \cdot 10^{5}\ N \cdot m^{-1}$	2450 rpm	$-3.20 \cdot 10^{4}\ N \cdot m^{-1}$	1807 rpm
25	$5.53 \cdot 10^{5}\ N \cdot m^{-1}$	2464 rpm	$-2.22 \cdot 10^{4}\ N \cdot m^{-1}$	1894 rpm
26	$6.16 \cdot 10^{5}\ N \cdot m^{-1}$	2472 rpm	$-1.42 \cdot 10^{4}\ N \cdot m^{-1}$	1951 rpm
27	$6.87 \cdot 10^{5}\ N \cdot m^{-1}$	2480 rpm	$-8.00 \cdot 10^{3}\ N \cdot m^{-1}$	1989 rpm
28	$7.64 \cdot 10^{5}\ N \cdot m^{-1}$	2487 rpm	$-3.56 \cdot 10^{3}\ N \cdot m^{-1}$	2013 rpm
29	$8.49 \cdot 10^{5}\ N \cdot m^{-1}$	2494 rpm	$-8.89 \cdot 10^{2}\ N \cdot m^{-1}$	2026 rpm
30	$9.44 \cdot 10^{5}\ N \cdot m^{-1}$	2505 rpm	$-0.00 \cdot 10^{0}\ N \cdot m^{-1}$	2031 rpm

B.2 Mutiple shaft study

Table B.2 Components description for the first shaft of the system

Shaft 1							
Element	Nodes	Parameters					
		D_{outer}	D_{inner}	$\ell_{element}$	E	G	ρ
Shaft	1→3	10 mm	0 mm	15mm	$1.9 \cdot 10^{11}\ Pa$	$7.6 \cdot 10^{10}\ Pa$	$8000\ kg/m^3$
	3→7	30 mm	0 mm	13.75 mm			
	7→9	14 mm	0 mm	25.00 mm			
	9→11	20 mm	0 mm	23.00 mm			
	11→19	20 mm	0 mm	50.00 mm			
	19→27	20 mm	0 mm	10.00 mm			
	27→33	20 mm	0 mm	25.00 mm			
Discs		D_{outer}	D_{inner}	Thickness			ρ
	16	170 mm	20 mm	60 mm			$8000\ kg/m^3$
	31	170 mm	20 mm	30 mm			
Gears		D_{outer}	D_{inner}	Thickness	β	k_h	ρ
	20	152 mm	20 mm	25 mm	20°	$1 \cdot 10^8$	$8000\ kg/m^3$
Bearings		k_x and k_y			d_x and d_y		
	11	$1 \cdot 10^{10}\ N \cdot m^{-1}$			$300\ N \cdot s \cdot m^{-1}$		
	27	$1 \cdot 10^{10}\ N \cdot m^{-1}$			$300\ N \cdot s \cdot m^{-1}$		
BLM		k_{airgap}	max k_{BLM}		d_{BLM}		
	3→7	$-8 \cdot 10^5\ N \cdot m^{-1}$	$9.44 \cdot 10^5\ N \cdot m^{-1}$		$10\ N \cdot s \cdot m^{-1}$		

Table B.3 Components description for the second shaft of the system

Shaft 2							
Element	Nodes	Parameters					
		D_{outer}	D_{inner}	$\ell_{element}$	E	G	ρ
Shaft	1→10	20 mm	0 mm	38.00 mm	$1.9 \cdot 10^{11}$ Pa	$7.6 \cdot 10^{10}$ Pa	8000 kg/m^3
	11→21	20 mm	0 mm	10.00 mm			
	21→28	20 mm	0 mm	30.00 mm			
Discs		D_{outer}	D_{inner}	Thickness			ρ
	27	170 mm	20 mm	30 mm			8000 kg/m^3
Gears		D_{outer}	D_{inner}	Thickness	β	k_h	ρ
	14	54 mm	20 mm	25 mm	20°	$1 \cdot 10^8$	8000 kg/m^3
Bearings		k_x and k_y			d_x and d_y		
	1	$1 \cdot 10^{10}$ $N \cdot m^{-1}$			300 $N \cdot s \cdot m^{-1}$		
	21	$1 \cdot 10^{10}$ $N \cdot m^{-1}$			300 $N \cdot s \cdot m^{-1}$		

Table B.4 Critical speeds value for the 2 shaft system

Data point	2 shaft system				
	Stiffness	Critical speed			
		1	2	3	4
0	$0.00 \cdot 10^{0}\ N \cdot m^{-1}$	1728 rpm	1855 rpm	1957 rpm	2561 rpm
1	$5.20 \cdot 10^{3}\ N \cdot m^{-1}$	1730 rpm	1873 rpm	1978 rpm	2563 rpm
2	$1.10 \cdot 10^{4}\ N \cdot m^{-1}$	1731 rpm	1890 rpm	2000 rpm	2565 rpm
3	$1.73 \cdot 10^{4}\ N \cdot m^{-1}$	1732 rpm	1908 rpm	2021 rpm	2567 rpm
4	$2.43 \cdot 10^{4}\ N \cdot m^{-1}$	1733 rpm	1925 rpm	2042 rpm	2569 rpm
5	$3.21 \cdot 10^{4}\ N \cdot m^{-1}$	1733 rpm	1943 rpm	2063 rpm	2571 rpm
6	$4.07 \cdot 10^{4}\ N \cdot m^{-1}$	1734 rpm	1959 rpm	2083 rpm	2573 rpm
7	$5.01 \cdot 10^{4}\ N \cdot m^{-1}$	1734 rpm	1976 rpm	2102 rpm	2575 rpm
8	$6.06 \cdot 10^{4}\ N \cdot m^{-1}$	1735 rpm	1992 rpm	2121 rpm	2577 rpm
9	$7.22 \cdot 10^{4}\ N \cdot m^{-1}$	1735 rpm	2007 rpm	2139 rpm	2579 rpm
10	$8.50 \cdot 10^{4}\ N \cdot m^{-1}$	1735 rpm	2021 rpm	2157 rpm	2582 rpm
11	$9.91 \cdot 10^{4}\ N \cdot m^{-1}$	1736 rpm	2035 rpm	2173 rpm	2584 rpm
12	$1.15 \cdot 10^{5}\ N \cdot m^{-1}$	1736 rpm	2048 rpm	2189 rpm	2586 rpm
13	$1.32 \cdot 10^{5}\ N \cdot m^{-1}$	1736 rpm	2060 rpm	2204 rpm	2589 rpm
14	$1.51 \cdot 10^{5}\ N \cdot m^{-1}$	1736 rpm	2072 rpm	2219 rpm	2591 rpm
15	$1.72 \cdot 10^{5}\ N \cdot m^{-1}$	1736 rpm	2083 rpm	2232 rpm	2593 rpm
16	$1.95 \cdot 10^{5}\ N \cdot m^{-1}$	1736 rpm	2093 rpm	2245 rpm	2595 rpm
17	$2.21 \cdot 10^{5}\ N \cdot m^{-1}$	1736 rpm	2103 rpm	2257 rpm	2597 rpm
18	$2.50 \cdot 10^{5}\ N \cdot m^{-1}$	1737 rpm	2112 rpm	2268 rpm	2599 rpm
19	$2.81 \cdot 10^{5}\ N \cdot m^{-1}$	1737 rpm	2120 rpm	2278 rpm	2601 rpm
20	$3.16 \cdot 10^{5}\ N \cdot m^{-1}$	1737 rpm	2127 rpm	2288 rpm	2603 rpm
21	$3.54 \cdot 10^{5}\ N \cdot m^{-1}$	1737 rpm	2135 rpm	2297 rpm	2605 rpm
22	$3.96 \cdot 10^{5}\ N \cdot m^{-1}$	1737 rpm	2141 rpm	2306 rpm	2607 rpm
23	$4.44 \cdot 10^{5}\ N \cdot m^{-1}$	1737 rpm	2147 rpm	2314 rpm	2609 rpm
24	$4.96 \cdot 10^{5}\ N \cdot m^{-1}$	1737 rpm	2153 rpm	2321 rpm	2611 rpm
25	$5.53 \cdot 10^{5}\ N \cdot m^{-1}$	1737 rpm	2159 rpm	2328 rpm	2612 rpm
26	$6.16 \cdot 10^{5}\ N \cdot m^{-1}$	1737 rpm	2163 rpm	2335 rpm	2614 rpm
27	$6.87 \cdot 10^{5}\ N \cdot m^{-1}$	1737 rpm	2168 rpm	2341 rpm	2615 rpm
28	$7.64 \cdot 10^{5}\ N \cdot m^{-1}$	1737 rpm	2173 rpm	2347 rpm	2617 rpm
29	$8.49 \cdot 10^{5}\ N \cdot m^{-1}$	1737 rpm	2177 rpm	2352 rpm	2618 rpm
30	$9.44 \cdot 10^{5}\ N \cdot m^{-1}$	1737 rpm	2181 rpm	2357 rpm	2620 rpm

Appendix C

Test Study

C.1 Single shaft study description

Table C.1 Critical speeds value for shaft 1

Data point	shaft 1		
	Stiffness	Critical speed	
		1	2
0	$0.00 \cdot 10^{0}\ N \cdot m^{-1}$	2139 rpm	2202 rpm
1	$5.20 \cdot 10^{3}\ N \cdot m^{-1}$	2166 rpm	2230 rpm
2	$1.10 \cdot 10^{4}\ N \cdot m^{-1}$	2193 rpm	2258 rpm
3	$1.73 \cdot 10^{4}\ N \cdot m^{-1}$	2220 rpm	2286 rpm
4	$2.43 \cdot 10^{4}\ N \cdot m^{-1}$	2247 rpm	2314 rpm
5	$3.21 \cdot 10^{4}\ N \cdot m^{-1}$	2273 rpm	2342 rpm
6	$4.07 \cdot 10^{4}\ N \cdot m^{-1}$	2299 rpm	2369 rpm
7	$5.01 \cdot 10^{4}\ N \cdot m^{-1}$	2324 rpm	2395 rpm
8	$6.06 \cdot 10^{4}\ N \cdot m^{-1}$	2349 rpm	2421 rpm
9	$7.22 \cdot 10^{4}\ N \cdot m^{-1}$	2373 rpm	2446 rpm
10	$8.50 \cdot 10^{4}\ N \cdot m^{-1}$	2396 rpm	2471 rpm
11	$9.91 \cdot 10^{4}\ N \cdot m^{-1}$	2418 rpm	2494 rpm
12	$1.15 \cdot 10^{5}\ N \cdot m^{-1}$	2440 rpm	2517 rpm
13	$1.32 \cdot 10^{5}\ N \cdot m^{-1}$	2460 rpm	2538 rpm
14	$1.51 \cdot 10^{5}\ N \cdot m^{-1}$	2480 rpm	2559 rpm
15	$1.72 \cdot 10^{5}\ N \cdot m^{-1}$	2498 rpm	2578 rpm
16	$1.96 \cdot 10^{5}\ N \cdot m^{-1}$	2515 rpm	2597 rpm
17	$2.21 \cdot 10^{5}\ N \cdot m^{-1}$	2532 rpm	2614 rpm
18	$2.50 \cdot 10^{5}\ N \cdot m^{-1}$	2547 rpm	2630 rpm
19	$2.81 \cdot 10^{5}\ N \cdot m^{-1}$	2562 rpm	2646 rpm
20	$3.16 \cdot 10^{5}\ N \cdot m^{-1}$	2576 rpm	2661 rpm
21	$3.54 \cdot 10^{5}\ N \cdot m^{-1}$	2588 rpm	2674 rpm
22	$3.97 \cdot 10^{5}\ N \cdot m^{-1}$	2600 rpm	2687 rpm
23	$4.44 \cdot 10^{5}\ N \cdot m^{-1}$	2612 rpm	2699 rpm
24	$4.96 \cdot 10^{5}\ N \cdot m^{-1}$	2622 rpm	2711 rpm
25	$5.53 \cdot 10^{5}\ N \cdot m^{-1}$	2633 rpm	2721 rpm
26	$6.16 \cdot 10^{5}\ N \cdot m^{-1}$	2642 rpm	2732 rpm
27	$6.87 \cdot 10^{5}\ N \cdot m^{-1}$	2651 rpm	2741 rpm
28	$7.64 \cdot 10^{5}\ N \cdot m^{-1}$	2659 rpm	2750 rpm
29	$8.49 \cdot 10^{5}\ N \cdot m^{-1}$	2667 rpm	2759 rpm
30	$9.44 \cdot 10^{5}\ N \cdot m^{-1}$	2675 rpm	2767 rpm

C.2 Mutiple shaft study description

Table C.2 Components description for the first shaft of the system

Shaft 1							
Element	Nodes	Parameters					
		D_{outer}	D_{inner}	$\ell_{element}$	E	G	ρ
Shaft	1→3	10 mm	0 mm	15mm	$1.9 \cdot 10^{11}\ Pa$	$7.6 \cdot 10^{10}\ Pa$	$8000\ kg/m^3$
	3→7	30 mm	0 mm	13.75 mm			
	7→9	14 mm	0 mm	25.00 mm			
	9→11	20 mm	0 mm	23.00 mm			
	11→19	20 mm	0 mm	50.00 mm			
	19→27	20 mm	0 mm	10.00 mm			
	27→33	20 mm	0 mm	25.00 mm			
Discs		D_{outer}	D_{inner}	Thickness			ρ
	12	170 mm	20 mm	60 mm			$8000\ kg/m^3$
Gears		D_{outer}	D_{inner}	Thickness	β	k_h	ρ
	20	152 mm	20 mm	25 mm	20°	$1 \cdot 10^8\ N \cdot m^{-1}$	$8000\ kg/m^3$
Bearings		k_x and k_y				d_x and d_y	
	11	$1 \cdot 10^{10}\ N \cdot m^{-1}$				$300\ N \cdot s \cdot m^{-1}$	
	27	$1 \cdot 10^{10}\ N \cdot m^{-1}$				$300\ N \cdot s \cdot m^{-1}$	
BLM		k_{airgap}		max k_{BLM}		d_{BLM}	
	3→7	$-8 \cdot 10^5\ N \cdot m^{-1}$		$9.44 \cdot 10^5\ N \cdot m^{-1}$		$10\ N \cdot s \cdot m^{-1}$	

Table C.3 Components description for the second shaft of the system

Shaft 2							
Element	Nodes	Parameters					
		D_{outer}	D_{inner}	$\ell_{element}$	E	G	ρ
Shaft	1→10	20 *mm*	0 *mm*	38.00 *mm*	$1.9 \cdot 10^{11}$ *Pa*	$7.6 \cdot 10^{10}$ *Pa*	8000 kg/m^3
	11→21	20 *mm*	0 *mm*	10.00 *mm*			
	21→28	20 *mm*	0 *mm*	30.00 *mm*			
		D_{outer}	D_{inner}	Thickness			ρ
Discs	27	45 *mm*	20 *mm*	45 *mm*			8000 kg/m^3
	28	20 *mm*	20 *mm*	20 *mm*			2700 kg/m^3
		D_{outer}	D_{inner}	Thickness	β	k_h	ρ
Gears	11	64 *mm*	20 *mm*	25 *mm*	20°	$1 \cdot 10^8$ $N \cdot m^{-1}$	8000 kg/m^3
	14	54 *mm*	20 *mm*	25 *mm*			
		k_x and k_y				d_x and d_y	
Bearings	1	$1 \cdot 10^{10}$ $N \cdot m^{-1}$				300 $N \cdot s \cdot m^{-1}$	
	21	$1 \cdot 10^{10}$ $N \cdot m^{-1}$				300 $N \cdot s \cdot m^{-1}$	

Table C.4 Components description for the third shaft of the system

Shaft 3							
Element	Nodes	Parameters					
Shaft		D_{outer}	D_{inner}	$\ell_{element}$	E	G	ρ
	1→6	10 mm	0 mm	14.00mm	$1.9 \cdot 10^{11}\ Pa$	$7.6 \cdot 10^{10}\ Pa$	8000 kg/m^3
	6→13	44 mm	0 mm	20.00 mm			
	13→17	14 mm	0 mm	10.00 mm			
	17→21	20 mm	0 mm	10.00 mm			
	21→31	20 mm	0 mm	38.00 mm			
	31→41	20 mm	0 mm	10.00 mm			
	41→44	20 mm	0 mm	20.00 mm			
Discs		D_{outer}	D_{inner}	Thickness			ρ
	22	170 mm	20 mm	60 mm			8000 kg/m^3
Gears		D_{outer}	D_{inner}	Thickness	β	k_h	ρ
	31	128 mm	20 mm	25 mm	20°	$1 \cdot 10^8$	8000 kg/m^3
Bearings		k_x and k_y			d_x and d_y		
	5	$1 \cdot 10^{10}\ N \cdot m^{-1}$			$300\ N \cdot s \cdot m^{-1}$		
	14	$1 \cdot 10^{10}\ N \cdot m^{-1}$			$300\ N \cdot s \cdot m^{-1}$		
	21	$1 \cdot 10^{10}\ N \cdot m^{-1}$			$300\ N \cdot s \cdot m^{-1}$		
	41	$1 \cdot 10^{10}\ N \cdot m^{-1}$			$300\ N \cdot s \cdot m^{-1}$		
Generator		$airgap$		max B_{airgap}	d_{BLM}		
	3→7	5 mm		1.2 T	$10\ N \cdot s \cdot m^{-1}$		

Table C.5 Critical speeds value for the 3 shaft system

Data point	3 shaft system				
	Stiffness	Critical speed			
		1	2	3	4
0	$0.00 \cdot 10^{0}\ N \cdot m^{-1}$	4.449 rpm	2103 rpm	2187 rpm	2739 rpm
1	$5.20 \cdot 10^{3}\ N \cdot m^{-1}$	4.449 rpm	2128 rpm	2214 rpm	2742 rpm
2	$1.10 \cdot 10^{4}\ N \cdot m^{-1}$	4.449 rpm	2152 rpm	2241 rpm	2746 rpm
3	$1.73 \cdot 10^{4}\ N \cdot m^{-1}$	4.449 rpm	2177 rpm	2267 rpm	2749 rpm
4	$2.43 \cdot 10^{4}\ N \cdot m^{-1}$	4.449 rpm	2201 rpm	2294 rpm	2753 rpm
5	$3.21 \cdot 10^{4}\ N \cdot m^{-1}$	4.449 rpm	2225 rpm	2320 rpm	2757 rpm
6	$4.07 \cdot 10^{4}\ N \cdot m^{-1}$	4.449 rpm	2248 rpm	2346 rpm	2762 rpm
7	$5.01 \cdot 10^{4}\ N \cdot m^{-1}$	4.449 rpm	2270 rpm	2371 rpm	2767 rpm
8	$6.06 \cdot 10^{4}\ N \cdot m^{-1}$	4.449 rpm	2292 rpm	2395 rpm	2772 rpm
9	$7.22 \cdot 10^{4}\ N \cdot m^{-1}$	4.449 rpm	2312 rpm	2418 rpm	2777 rpm
10	$8.50 \cdot 10^{4}\ N \cdot m^{-1}$	4.449 rpm	2331 rpm	2441 rpm	2783 rpm
11	$9.91 \cdot 10^{4}\ N \cdot m^{-1}$	4.449 rpm	2350 rpm	2462 rpm	2789 rpm
12	$1.15 \cdot 10^{5}\ N \cdot m^{-1}$	4.449 rpm	2367 rpm	2483 rpm	2796 rpm
13	$1.32 \cdot 10^{5}\ N \cdot m^{-1}$	4.449 rpm	2382 rpm	2503 rpm	2802 rpm
14	$1.51 \cdot 10^{5}\ N \cdot m^{-1}$	4.449 rpm	2397 rpm	2521 rpm	2809 rpm
15	$1.72 \cdot 10^{5}\ N \cdot m^{-1}$	4.449 rpm	2411 rpm	2539 rpm	2816 rpm
16	$1.96 \cdot 10^{5}\ N \cdot m^{-1}$	4.449 rpm	2423 rpm	2555 rpm	2823 rpm
17	$2.21 \cdot 10^{5}\ N \cdot m^{-1}$	4.449 rpm	2434 rpm	2571 rpm	2830 rpm
18	$2.50 \cdot 10^{5}\ N \cdot m^{-1}$	4.449 rpm	2445 rpm	2586 rpm	2837 rpm
19	$2.81 \cdot 10^{5}\ N \cdot m^{-1}$	4.449 rpm	2454 rpm	2600 rpm	2844 rpm
20	$3.16 \cdot 10^{5}\ N \cdot m^{-1}$	4.449 rpm	2463 rpm	2613 rpm	2851 rpm
21	$3.54 \cdot 10^{5}\ N \cdot m^{-1}$	4.449 rpm	2471 rpm	2625 rpm	2857 rpm
22	$3.97 \cdot 10^{5}\ N \cdot m^{-1}$	4.449 rpm	2478 rpm	2637 rpm	2864 rpm
23	$4.44 \cdot 10^{5}\ N \cdot m^{-1}$	4.449 rpm	2484 rpm	2647 rpm	2870 rpm
24	$4.96 \cdot 10^{5}\ N \cdot m^{-1}$	4.449 rpm	2490 rpm	2658 rpm	2876 rpm
25	$5.53 \cdot 10^{5}\ N \cdot m^{-1}$	4.449 rpm	2496 rpm	2667 rpm	2882 rpm
26	$6.16 \cdot 10^{5}\ N \cdot m^{-1}$	4.449 rpm	2501 rpm	2676 rpm	2888 rpm
27	$6.87 \cdot 10^{5}\ N \cdot m^{-1}$	4.449 rpm	2505 rpm	2685 rpm	2894 rpm
28	$7.64 \cdot 10^{5}\ N \cdot m^{-1}$	4.449 rpm	2509 rpm	2693 rpm	2899 rpm
29	$8.49 \cdot 10^{5}\ N \cdot m^{-1}$	4.449 rpm	2513 rpm	2700 rpm	2904 rpm
30	$9.44 \cdot 10^{5}\ N \cdot m^{-1}$	4.449 rpm	2517 rpm	2708 rpm	2909 rpm